

Durham E-Theses

The coherent interaction of pions in deuterium at 11.7 GeV/c

Kemp, Denis

How to cite:

Kemp, Denis (1974) *The coherent interaction of pions in deuterium at 11.7 GeV/c*, Durham theses, Durham University. Available at Durham E-Theses Online: <http://etheses.dur.ac.uk/8238/>

Use policy

The full-text may be used and/or reproduced, and given to third parties in any format or medium, without prior permission or charge, for personal research or study, educational, or not-for-profit purposes provided that:

- a full bibliographic reference is made to the original source
- a [link](#) is made to the metadata record in Durham E-Theses
- the full-text is not changed in any way

The full-text must not be sold in any format or medium without the formal permission of the copyright holders.

Please consult the [full Durham E-Theses policy](#) for further details.

THE COHERENT INTERACTION OF PIONS

IN DEUTERIUM AT 11.7 GeV/c

by

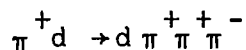
DENIS KEMP

A thesis presented at the University
of Durham for the degree of Ph. D.

February 1974.

A B S T R A C T

This thesis presents the results of the analysis of the reaction:



at 11.7 GeV/c incident momentum. The experiment from which the data were obtained is described and the method of selecting the sample of 1675 events belonging to the channel is discussed.

The reaction is found to be dominated by ρ^0 production with some f^0 production. There is also a d^{*++} non-resonant peak in the $d\pi^+$ mass spectrum. The three pion effective mass spectrum is dominated by threshold enhancements of the $\rho^0 \pi^+$ system, the A_1 , and the $f^0 \pi^+$ system, the A_3 .

A spin parity analysis indicates that the A_1 has $J^P = 1^+$ while the A_3 has $J^P = 2^-$. Neither of these enhancements are found to conserve s-channel helicity, but t-channel helicity is found to be compatible with the results on A_3 production and almost compatible with those on A_1 production.

A Longitudinal Phase Space analysis of the channel is described and the results of a kinematical model to explain A_1 and A_3 production are presented and critically discussed. The results of a search for coherent A_2 production are described and a small enhancement which may be identified with the η_N (1080) meson is studied.

T A B L E O F C O N T E N T S

	Page
ABSTRACT	i
TABLE OF CONTENTS	ii
CHAPTER ONE: <u>Introduction</u>	1
CHAPTER TWO: <u>Experimental Details and Total Cross Section</u>	6
2.1 The Experiment	6
2.2 The Scanning	7
2.3 The Measuring	8
2.4 The Programmes	10
2.5 The Check Scan	12
2.6 The Data Summary Tape	13
2.7 The Total Cross Section	14
2.8 The Stage of the Experiment	16
CHAPTER THREE: <u>Channel Separation</u>	18
<u>Introduction</u>	18
3.1 Four Prong Events	18
3.2 Three Prong Events	28
3.3 Contamination of Coherent Kaon Production	32
3.4 Channel Cross Section	33
CHAPTER FOUR: <u>General Features of the Data</u>	35
<u>Introduction</u>	35
4.1 The Differential Cross Section	35
4.2 The $d \pi^+$ Effective Mass Spectrum	36
4.3 The $d \pi^-$ Effective Mass Spectrum	38
4.4 The $\pi^+ \pi^+$ Mass Spectrum	39

	Page
4.5 The $\pi^+ \pi^-$ Mass Spectrum	39
4.6 $d^* \rho$ and $d^* f$ Associated Production	44
4.7 The $\pi^+ \pi^+ \pi^-$ Mass Spectrum	45
4.8 The $d \pi^+ \pi^-$ and $d \pi^+ \pi^+$ Mass Spectrum	49
4.9 Summary	50
CHAPTER FIVE: <u>Longitudinal Phase Space Analysis</u>	52
5.1 General Considerations	52
5.2 Three Body L.P.S.	53
5.3 Four Body L.P.S.	54
5.4 Transverse Momenta	56
5.5 Experimental L.P.S. Distributions	57
5.6 Production Mechanisms	61
CHAPTER SIX: <u>Analysis of Decay Angles of Mesonic Systems</u>	65
6.1 Introduction	65
6.2 Dipion Systems	65
6.2.1 The ρ^0 meson	65
6.2.2 The f^0 meson	69
6.2.3 The " η_N " region	71
6.3 Three Pion Systems	74
6.3.1 Spherical Harmonic Moments	74
6.3.2 The A_1 region	75
6.3.3 The A_3 region	81
6.3.4 The " $A_{2.5}$ " region	84
CHAPTER SEVEN: <u>Experimental Tests of Helicity Conservation</u>	86
<u>Introduction</u>	87
7.1 Density Matrix Elements Analysis	88
7.1.1 The A_1 meson	88
7.1.2 The A_3 meson	92

	Page
7.2 Spherical Harmonic Moments Analysis	95
7.2.1 The Method	95
7.2.2 The A_1 Region	97
7.2.3 The A_3 Region	98
7.2.4 Below the A_1 Region	98
7.2.5 Between the A_1 and A_3 region	98
7.2.6 Above the A_3 region	99
7.2.7 Summary	99
7.3 Longitudinal Phase Space Analysis	99
7.4 Conclusions	105
CHAPTER EIGHT: <u>Possible Kinematical Interpretation of Observed</u>	107
<u>Enhancements</u>	
Introduction	107
8.1 The d^* Enhancement	107
8.2 The A_1 and A_3 Enhancement	110
CHAPTER NINE: <u>Search for Coherent A_2 Production</u>	119
Introduction	119
9.1 Sample of Events Used	119
9.2 Results of the Search	121
9.3 Conclusions	126
CHAPTER TEN: <u>Comparisons and Conclusions</u>	127
APPENDIX A	
A.1 Peripheral Models	133
A.1.1 One pion exchange	133
A.1.2 Other particle exchanges	134
A.1.3 Form Factors	134
A.1.4 The Absorbtion Model	135
A.2. The Regge Pole Model	136

	Page
APPENDIX B:	
B.1. Reference Frames	139
B.1.1 The Gottfried Jackson Frame	139
B.1.2 The Helicity Frame	140
B.2 The Spin Density Matrix	141
B.3 The Method of Moments	142
B.4 The Spherical Harmonics	143
LIST OF TABLES	145
FIGURE CAPTIONS	146
ACKNOWLEDGEMENTS	151
REFERENCES	153

CHAPTER ONE

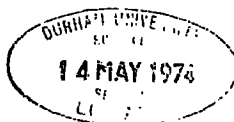
INTRODUCTION

In the absence of any complete theory of the strong interaction the role of experiment is particularly important in providing data on which theories or models can be based and tested. There are two main areas in which any experiment is essential:

- (1) To record what happens in a manner independent of any previous knowledge or model, and to determine the properties of short lived particles, or resonances, which, at relatively low energy, are found to form a large fraction of multi-particle final states.
- (2) To test any models or hypotheses which have been proposed on earlier data for compatibility with the results.

Many techniques have been used to detect the particles involved in strong interactions. One of the most useful of these at low energies has been the bubble chamber since it can give precision of measurement over a 4π solid angle on a wide variety of reactions. A proton target can be obtained by filling the chamber with hydrogen but many effects can better be studied by use of a neutron target, for example neutral meson production. No free neutron target is available, but the deuteron, consisting of a loosely bound proton-neutron pair, can be used as a quasi free neutron target and bubble chambers are often used filled with liquid deuterium. Heavy liquids have also been used as targets, since they give the possibility of detecting the decay products of uncharged pions, although they have the disadvantage of reduced precision of measurement.

It was in the study of interactions of pions with heavy nuclei that multi-particle production was found to occur without the nucleus



breaking up (Ref. 1.1). These interactions with the nucleus, were also soon discovered in deuterium (Ref. 1.2) and designated coherent reactions. A coherent reaction can be defined as one in which the target nucleus remains intact and in its ground state after the interaction.

This thesis is the report of a study of a coherent reaction of positive pions with the deuteron. The particular channel being investigated is:



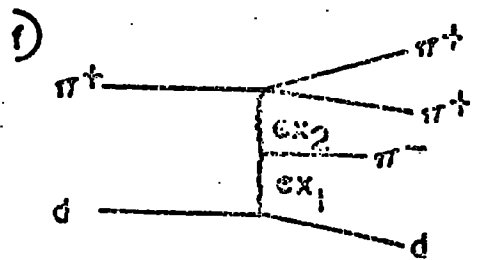
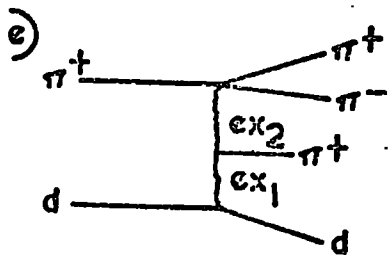
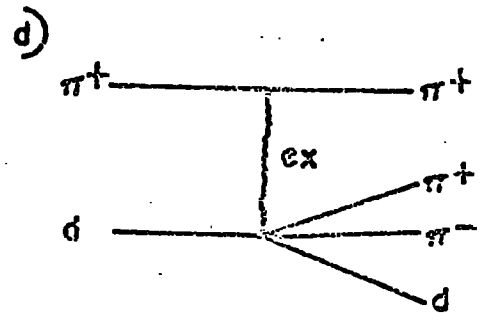
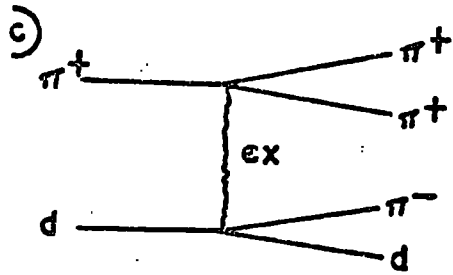
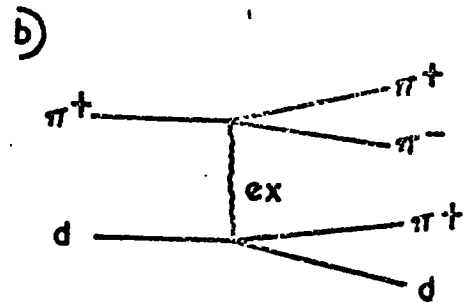
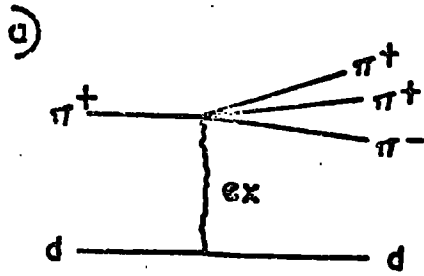
at 11.7 GeV/c incident pion momentum.

The advantage of a coherent interaction is that many exchange mechanisms which can occur with a nucleon target are forbidden. The zero isospin of the deuteron implies that it can exchange only objects which also have zero isospin. Three pion resonances produced by ρ exchange, for example, will not be produced in reaction 1.1. This can simplify the analysis of 3-pion states which are produced in this reaction.

The simplest set of quantum numbers that can be exchanged in this type of reaction are those of the vacuum ($I^G J^P = 0^+ 0^+$) or in Regge Pole terminology the Pomeron trajectory. (A brief description of the Regge Pole model and other exchange models is given in Appendix A). The pomeron is the exchange thought to dominate elastic scattering at energies above the isobar formation region (> 5 GeV/c). If reaction 1.1 does indeed proceed by pomeron exchange, then it may be expected to show similar features to the elastic reaction, the only difference being that the incident pion dissociates into a 3-pion state. This process is known as diffraction dissociation. It was first discussed by Good and Walker (Ref. 1.3).

There are other possible exchange mechanisms which may be expected to occur. Four simple exchanges are shown in figures 1.1 (a) - (d) and

FIG. 1.1 POSSIBLE EXCHANGE MECHANISMS



doubly peripheral mechanisms (fig. 1.1 (e) and (f)) may also contribute to the channel cross section. No diagrams are shown which would involve exotic exchanges or deuteron exchange since such processes are most unlikely to occur. In studying the reaction an attempt will be made to determine which of these diagrams occur, and the nature of the exchange involved.

Previous experiments have shown that, in the strong interaction, resonances are produced, in general, peripherally i.e. with only a small momentum transfer from the beam to the resonant state. In coherent reactions the momentum transfer from the target nucleus to the recoil nucleus is constrained to be very small, and, since this is equivalent to the momentum transfer from the beam to all other final state particles combined, resonance production in this combination may be enhanced.

This constraint to low momentum transfers can be understood in terms of the Uncertainty Principle: since it is required that the interaction be with the whole nucleus, it is necessary that the exchanged object cannot localise any one of the constituent nucleons i.e. the uncertainty in position must not be less than the nuclear diameter (a). The Uncertainty Principle states that:

$$\Delta p \Delta x > 1 \quad 1.2$$

(the units used throughout are such that $\hbar = c = 1$). Therefore, in order to localise a nucleon:

$$\Delta p > \frac{1}{a} \quad 1.3$$

and this corresponds to a momentum of ~ 220 MeV/c when the target is a deuteron. For momenta higher than this the probability of the reaction remaining coherent is reduced.

Low momentum transfers to the recoil deuteron result in non relativistic final state deuterons in the laboratory system and this results in the approximate relationship:

$$t_{\min}^{\frac{1}{2}} \approx \frac{M^{*2} - \mu^2}{2P_b} \quad 1.4$$

where M^* = the effective mass of the 3-pion system.

μ = the pion mass

P_b = the pion beam momentum in the lab. frame.

t_{\min} = the minimum value of the 4-momentum transfer squared from target to recoil deuteron, needed to produce this value of M^* .

Equation 1.4 shows that a given 3-pion mass can be produced with lower t (the square of the 4-momentum transfer from deuteron to deuteron) as the beam momentum is increased. The experiment reported here is at a higher beam momentum than all except one previously reporting studies of this channel and is, therefore, capable of studying higher 3-pion masses with more reasonable statistics, since they can be formed with lower t and do not result in break-up of the deuteron.

This thesis, then, describes the analysis performed on reaction 1.1. Chapter 2 presents briefly the details of the exposure together with an account of the scanning and measuring procedures and the calculation of the total π^+d cross section. In chapter 3 the method of selecting events which belong to the coherent channel is described and the channel cross section is computed. The general features of the channel, in terms of the resonances and enhancements produced, are presented in chapter 4, while in chapter 5 the channel is studied in terms of longitudinal phase space. Chapters 6 and 7 are concerned with the angular distributions of the decays of the produced states, the former describing the spin

states involved, and the latter testing the hypothesis of helicity conservation in either the s- or the t-channel. In chapter 8 models which attempt to explain some of the enhancements produced in the reaction are discussed and in chapter 9 a search for coherent production of the A_2 meson is described. The conclusions of the thesis are presented in chapter 10 together with a comparison of the results with previous work on this and similar channels.

The author is responsible for all the results presented, except for those in Chapter 2 or where explicitly stated in the text.

CHAPTER TWO

EXPERIMENTAL DETAILS AND TOTAL CROSS SECTION

2.1 THE EXPERIMENT

The data presented in this thesis is taken from an experiment performed by a collaboration of European laboratories comprising:

- (1) The University of Durham
- (2) The University of Genoa
- (3) The University of Milan
- (4) Ecole Polytechnique, Paris
- (5) Laboratoire de Physique Nucleaire et des Hautes Energies.

A beam of positive pions was used with a momentum of 11.7 GeV/c, extracted from the U3 beam line (Ref. 2.1) at the CERN proton synchrotron purified by two r-f separating cavities. The beam was incident on the CERN two metre bubble chamber (Ref. 2.2) filled with deuterium. The average number of beam particles entering the chamber was maintained at ~ 10 -15 per frame and they were timed to pass through the chamber during the sensitive time of the expansion-compression cycle of the liquid deuterium. The chamber was in a magnetic field of 17.5 kg. Photographs were taken on each expansion from 4 cameras positioned such that 3-dimensional reconstruction of the tracks is possible.

The experiment was performed in November and December of 1967 in two runs separated by one week. The beam momentum was determined, for each run, by measuring the curvature of a large number of primary tracks and taking the mean value, since the error on the measurement of individual tracks at this high momentum can be very large. The results were:

$$\text{Run 1: } 11.66 \pm 0.04 \text{ GeV/c}$$

$$\text{Run 2: } 11.74 \pm 0.04 \text{ GeV/c}$$

and these values were treated as fixed in the fitting procedures except for the known variation due to the energy loss down the

chamber and a slight weighting with the measured value of individual primaries.

A total of 150 thousand pictures were taken and the film was shared between the 5 collaborating laboratories for scanning, measuring and fitting. These procedures, as performed in Durham, are described in the subsequent sections of this chapter.

2.2 The Scanning

Only events in a certain volume of the chamber were treated as eligible for analysis, in order that a good measurement could be made of the curvature and direction of the secondary tracks and of the direction of the beam. This fiducial volume was 115cm long and situated near to the entrance of the chamber.

Each film was scanned for all events falling in this region of the chamber and relevant features of each event found were noted. These included.

- (1) The number of secondary tracks (prong size)
- (2) The presence of a stopping track (either a proton or a deuteron)
- (3) The presence of a stopping pion (recognisable by its decay)
- (4) The presence of a highly ionising track (grey proton)
- (5) The presence of kinks in the secondary tracks.
- (6) The presence of any interactions of the secondary tracks, particularly if these are near to the primary vertex.
- (7) The presence of associated V^0 's
- (8) The approximate position of the event.

The number of beam tracks entering the fiducial volume was counted and noted on every tenth frame and an average number was calculated for each film. Any frame which was too faint or had too many (> 25) or too

few (<5) beam tracks, was rejected and the number of these for each film was noted. From these two pieces of information the total number of beam tracks was calculated.

Several films were then rescanned independently and, by comparison of the two results, the efficiency of the scanning was calculated for each prong size. Table 2.1 shows the total number of events found for each prong size, together with the scanning efficiency and the corrected number of events.

2.3 Measuring

Only interactions of the beam with the neutron inside the deuteron or with the deuteron as a whole were required for measuring, since interactions with the proton can better be studied by use of a hydrogen filled bubble chamber. If the interaction is with the neutron then, in the impulse approximation, the proton is left with the Fermi momentum it had inside the deuteron, and this peaks at low momenta with only $\sim 1\%$ of events having the so-called 'spectator' proton with a momentum greater than $300 \text{ MeV}/c^2$. The vast majority of interactions on the neutron will be characterised by a proton which stops. Charge conservation demands that there be an even number of charged secondary tracks and so neutron events will either have an even number of prongs with a visible stopping proton or an odd number of prongs when the proton stops before it has travelled far enough to leave a visible track. This latter case arises for protons with a momentum less than $\sim 80 \text{ MeV}/c$.

Similarly, coherent deuteron events, as explained in Chapter 1, must have a low momentum deuteron in the final state and will result in either odd prong events (deuteron momentum $< \sim 140 \text{ MeV}/c$) or even prong events with a stopping deuteron. In general, a stopping deuteron cannot be distinguished from a stopping proton but a stopping track is known to be one or other of these.

TABLE 2.1

The Scanning Data

Prong size	No. of events	Scanning Efficiency (%)	Corrected No. of Events
1	5362	94.7	5662
2	21496	99.5	21604
3	14313	99.9	14327
4	26998	99.9	27025
5	9324	100	9324
6	12828	100	12828
7	2783	100	2783
8	3213	100	3213
> 8	886	100	886

The events selected for measurement, therefore, comprised all odd prong events and even prong events with at least one stopping track. It was further decided that only 3 and 4 prong events would be measured in the first instance, and then only if the events were non strange (i.e. no associated V^0 or kinked secondary track).

The measurement was performed on conventional IEP type machines. The machines were on line to an IBM 1130 computer which checked circle fits to the measured tracks and calculated the sagitta for the measured length of track. If the sagitta were less than 2mm in chamber space, immediate remeasurements was requested on a greater length of track. If the circle fit failed, the measurer was instructed to remeasure the track. Any event with a track which consistently failed to give a circle fit or a track for which a sagitta of 2mm could not be achieved was classified as unmeasurable. The computer processed the data and produced output in the required input format for the CERN fitting and reconstructing programmes. Any event failing in these programmes was remeasured, and a selection of events which failed again were measured for a third time.

2.4 The Programmes

Any distortion arising from the optical system of the cameras, was allowed for by measuring, on the film, the positions of several crosses (fiducial marks) whose positions on the chamber windows is well known. A polynomial fit of the measured positions to the known positions was made, using the CERN programme PYTHON (Ref. 2.3).

The results of this fit are used in the GERN geometrical reconstruction programme THRESH (ref. 2.4), which takes the measured data from three views and combines them to form a 3-dimensional picture of the event, fitting each track with a helix and noting its radius of curvature and

the direction in which it leaves the interaction vertex.

The information from THRESH is then passed through to the GERN fitting programme GRIND (ref. 2.5). This attempts to fit the event to a set of user supplied hypotheses, assigning a mass to each track and hence determining its momentum and trying to balance momentum and energy. The hypotheses tested for 3 and 4 prong events were:-

1. $\pi^+ d \rightarrow d\pi^+\pi^+\pi^-$
2. $\pi^+ d \rightarrow d\pi^+\pi^+\pi^-\pi^0$
3. $\pi^+ d \rightarrow pp\pi^+\pi^-$
4. $\pi^+ d \rightarrow pp\pi^+\pi^-\pi^0$
5. $\pi^+ d \rightarrow pn\pi^+\pi^+\pi^-$

For four pronged events there are no unseen final state particles in reactions 1 and 3. There are thus 4 constraint equations which must be satisfied before a fit is achieved, 3 due to conservation of momentum and one due to conservation of energy. An event which can satisfy all these constraints is known as a 4-C fit.

The remaining three reactions (2, 4 and 5) have a neutral particle in the final state, which, being unseen is unmeasured. The energy and momentum of the unseen particle can be deduced by balancing these two quantities before and after the interaction, and a fit to these channels will be given if the constraint:

$$E^2 - p^2 = m^2 \quad 2.1$$

can be satisfied with m equal to the mass of the neutral particle. The resulting fit is known as a 1C fit. Clearly the fitting procedure is less stringent for a 1C fit than for a 4C fit and it is likely that both the resolution and contamination by false fits will be worse for 1C than 4C reactions.

Events which give no fit to reactions 1-5 may belong to one of the following channels:

6. $\pi^+ d \rightarrow d \pi^+ \pi^+ \pi^- n (\pi^0)$
7. $\pi^+ d \rightarrow p p \pi^+ \pi^- n (\pi^0)$
8. $\pi^+ d \rightarrow p n \pi^+ \pi^+ \pi^- m (\pi^0)$

where $n > 2$ and $m > 1$.

These reactions are called NOFITs.

In the case of three prong events there is less information available from the measurement. It is known, however, for reactions 3, 4 and 5 that the unseen proton has a momentum less than ~ 80 MeV/c and so it has been treated in GRIND as a measured track with zero momentum and errors on P_x , P_y and P_z , the three components of momentum, of 30, 30 and 42 MeV/c respectively. In this way 4C-fits to reaction 3 and 1C fits to reaction 4 and 5 are still possible. It is found that this procedure works well for the 4-C fit but for the 1C's the final fitted quantities of the spectator are not meaningful, giving a fitted momentum which seldom differs more than 5 MeV/c from zero. For channel 1, the unseen deuteron cannot be constrained so strongly as the unseen proton since it can have a momentum as high as ~ 140 MeV/c before it leaves a visible track. It was decided, therefore, to treat the missing deuteron in the same way as a neutral particle. Three prong fits to reaction 1 are therefore 1C fits. It is impossible to follow this procedure in the case of reaction 2, because there would then be equivalently two neutral particles in the final state. Fits to reaction 2 were, therefore, not possible for three prong events.

Events which failed to be properly reconstructed by THRESH or GRIND were sent back to be remeasured.

2.5 The Check Scan

The degree of ionisation caused by a charged particle passing through a bubble chamber, corresponding to the density of bubbles along the track,

depends on β of the particle. Examination of the bubble density of the track can give information concerning the nature of the track. GRIND produces a table of the ionisation expected for each track assuming the track is a pion, a kaon and a proton. In general, a proton can be differentiated from a pion, if the proton has a momentum less than $\sim 1.3 \text{ GeV}/c$, since for these momenta proton tracks can be seen by eye to be less than minimum ionising, while pions are minimum ionising.

Every event passing grind was therefore subjected to a check scan, where every positively charged track was given a code as follows:

- 2: The track is definitely a proton or deuteron.
- 1: No differentiation is possible
- 0: The track is definitely a pion.

It was assumed that there is no difference between protons and deuterons since, in general, it is impossible to distinguish these by ionisation. The very few events with a track which was recognisable as a kaon were rejected from further analysis.

Any of the hypotheses giving a fit to an event was then checked for compatibility with the ionisation code and rejected if it were found to be incompatible.

2.5 The Data Summary Tape

After the check scan, the grind output was passed through the programme SLICE, which produced a data summary tape (D.S.T). This tape contains information on all the measured events. The χ^2 value and probability for any fitted hypothesis, together with the fitted and unfitted quantities for each track and the missing mass squared and missing energy squared and their errors are all stored on this tape. Any hypothesis which is compatible with ionisation but which does not give a fit are also stored on the D.S.T as the corresponding NOFIT

reaction, where, of course, only the unfitted quantities are available.

The D.S.T's from each collaborating laboratory were then circulated to the others for data analysis.

2.7 The Total Cross Section

The total cross section will be calculated in this section, for the Durham events only, from the formula:

$$\sigma_{\text{tot}} = \frac{n A}{L N_{\text{av}} d} \quad 2.2$$

where A = the atomic weight of the deuteron = 2

N_{av} = Avagadro's Number = 6.022×10^{23} mole⁻¹

d = the density of the liquid deuterium

L = the total beam track length.

n = the total number of interactions

The density of the deuterium (d) has been calculated by the French collaborators by measuring the decay length of muons in the chamber and knowing this length in hydrogen and the density of hydrogen under the conditions in which the chamber operates. The value found is 0.136 ± 0.005 gm/cc.

The total number of interactions can be calculated directly from table 2.1 by summing the number of each prong size, after correcting for scanning efficiency. This results in a value of 97652. There remains, however, a class of 1 prong events which are inaccessible to scanning, since the angle between the incident and emerging tracks is negligible, and these have not been allowed for in the 1 prong scanning efficiency. These events will be essentially elastic scatters with very small momentum transfers:

- (a) $\pi^+ d \rightarrow d \pi^+$ (deuteron unseen)
- (b) $\pi^+ p(n_{\text{sp}}) \rightarrow \pi^+ p(n_{\text{sp}})$ (proton unseen)
- (c) $\pi^+ n(p_{\text{sp}}) \rightarrow \pi^+ n(p_{\text{sp}})$ (proton unseen)

The subscript 'sp' in these reactions refers to the spectator nucleon. The cross section for each of these three processes has been calculated by the French collaborators, assuming values of the total cross section for π^+d, π^+p and π^+n collisions at this energy and using the optical theorem. Reactions (a) and (b) are then limited to certain maximum values of t by the necessity that the target remains unseen. For reaction (c) it was assumed that $2/3$ of the spectator protons remain unseen (as expected from the area under the proton momentum distribution for protons with momentum less than $80 \text{ MeV}/c$ as given by the Hulthen wave function), and the maximum value of t was calculated assuming that the angle between incoming and outgoing pions in the chamber remains less than 1° . The combined cross section for these processes, under these conditions, is found to be 2.8 mb . While the value of the total π^+d cross section (taken from counter experiments (ref. 2.6)) has been assumed in this calculation, it only results in a small correction term and the value of this quantity, to be calculated, is largely independent of this assumption.

The total track length L is given by:

$$L = n_1 \ell + \sum_{i=1}^n \ell_i' \quad 2.3$$

where $\ell =$ the total track length possible in the fiducial volume = 115 cm

$n_1 =$ the number of beam tracks entering the chamber which do not interact

$\ell_i' =$ the length of the track i before interacting and the sum runs over all interacting tracks.

The distribution of ℓ_i is found to be flat as would be expected, and so the mean value of ℓ_i can be written:

$$\ell_i = \ell/2 \quad 2.4$$

Equation 2.3 can then be written

$$L = n_1 \ell + \frac{n \ell}{2} \quad 2.5$$

or

$$L = N \ell \left(1 - \frac{n}{2N}\right) \quad 2.6$$

where N is the total number of beam tracks entering the chamber i.e. $N = n_1 + n$. N has been calculated from the scanning data and is equal to 501288 with an error of $\sim 3.5\%$. L can, therefore, be calculated if n is known, but n is 97652 plus the number of undetectable 1 prong events (n') for which $\sigma = 2.8 \text{ mb}$.

$$\text{i.e. } n = 97652 + n' \quad 2.7$$

and

$$\frac{n'}{N \ell \left(1 - \frac{n}{2N}\right)} \cdot \frac{A}{N_{\text{av}} d} = 2.8 \text{ mb} \quad 2.8$$

Equation 2.8 gives $n' = 5966$, yielding a value of n of 103591 and substituting this value into equation 2.6 results in a value of $L = 5169 \times 10^4 \text{ cm}$. Using these values of L and n in equation 2.2, the value for the total cross section is found to be:

$$\sigma_{\text{tot}} = 48.9 \pm 2.5 \text{ mb.}$$

This result is in good agreement with the result from counter experiments (Ref. 2.6) which give a value of $48.2 \pm 0.5 \text{ mb}$.

2.8 The Stage of the Experiment

At present all the three and four prongs have been measured and the published results, so far, are primarily on the channel

$$\pi^+ d \rightarrow pp \pi^+ \pi^- \quad (\text{Ref. 2.7})$$

A more general treatment of this channel together with the corresponding IC channel:

$$\pi^+ d \rightarrow pp \pi^+ \pi^- \pi^0$$

will be published shortly (Ref. 2.8).

Preliminary results on helicity conservation in the channel being considered in this thesis and also on the channel.

$$\pi^+ d \rightarrow p_{sp} n \pi^+ \pi^+ \pi^-$$

have also been published (Ref. 2.9). The results concerning this which are presented in Chapter 7 of this thesis, are more complete and supercede those of that publication.

The 5 and 6 prong data has also now been measured and analysis of these events has been started. It is hoped that a sample of 7 and 8 prong data will be measured soon, so that a comparison of different multiplicities may be possible.

CHAPTER THREE

CHANNEL SEPARATION

Introduction

The sample of events which give a fit to the coherent channel often also give a fit to one or more of the other channels listed in the previous chapter, and it is probable that some of the coherent fits are spurious. The ambiguity between coherent fits and other fits must be resolved in order to eliminate contamination of the coherent sample, if meaningful analysis is to be performed, and in this chapter the methods used to obtain a pure sample of the coherent channel are described. It was explained in the previous chapter that the types of fit to the coherent channel are different for 4-prong and 3-prong events i.e. 4C and 1C fits respectively. The methods of channel separations for these two samples will be described separately; for the 4-prong events in Section 1 and for the 3-prong events in Section 2. Section 3 gives a discussion of possible misidentification of the secondary pions and the channel cross section is computed in section 4.

3.1 Four Prong Events

Table 3.1 shows the total number of 4-prong events fitting the coherent channel together with the number of ambiguities with each of the other possible reactions. The only other 4C channel is reaction 3 and it can be seen that the number of ambiguities with that reaction is negligible. Since it is far easier for a 4C event to simulate a 1C than vice versa, the fits to reactions 2, 4 and 5 are expected to be largely spurious. Ambiguities with channel 2 can be neglected therefore, on the grounds that there are only a few such events. This is true also for an ambiguity with reaction 4. This ambiguity can be neglected

TABLE 3.1: The number of coherent fits
ambiguous with other channels.

	4 PRONGS		3 PRONGS	
	ALL	PROB > 1%	ALL	PROB > 1%
Total $\pi^+ d \rightarrow d \pi^+ \pi^+ \pi^-$	1534	1418	2139	2044
Unambiguous	123	100	4	2
AMB. and Reaction 2 $\pi^+ d \rightarrow d \pi^+ \pi^+ \pi^- \pi^0$	203	171	-	-
AMB. with Reaction 3 $\pi^+ d \rightarrow p p \pi^+ \pi^-$	3	2	33	28
AMB. with Reaction 4 $\pi^+ d \rightarrow p p \pi^+ \pi^- \pi^0$	326	223	1113	1048
AMB. with Reaction 5 $\pi^+ d \rightarrow p n \pi^+ \pi^+ \pi^-$	1411	1328	2135	2042
Accepted $\pi^+ d \rightarrow d \pi^+ \pi^+ \pi^-$		1230		445

for the further reason that it can only occur if the faster proton of reaction 4 has a momentum greater than $\sim 1.2 \text{ GeV}/c$ since otherwise it will be recognisable by ionisation and for such events it has previously been found that the majority of fits to reaction 4 are spurious (Ref. 3.1). The only important ambiguity is, therefore, that with reaction 5, since more than 90% of the events fitting reaction 1 also give a fit to that channel.

The χ^2 probability distribution for all 4-prong events fitting the coherent channel is shown in figure 3.1(a). Whilst, statistically, this is expected to be flat, there is a sharp peak of probabilities $\sim 1\%$, and an excess of events at high probabilities. The latter effect can be explained in terms of an overestimation in the fitting programme of the measured errors on the tracks. The former effect, however, is probably due to other channels contaminating the coherent one and events which fit with a probability less than 1% have been rejected in the subsequent analysis. The effect on the number of events and ambiguities can be seen in the second column of Table 3.1.

The high percentage of ambiguities with the reaction 5 remains after this selection and it is necessary to show that the whole coherent channel is not due to a sample of that reaction, termed the break-up channel, having a configuration which simulates coherent events. That this is not the case can be seen from figure 3.2(a) which shows the invariant mass spectrum of the proton-neutron combination $M(pn)$ for all 4-prong events fitting reaction 5. There is a strong peak at a mass $\sim 1.879 \text{ GeV}/c^2$ in this spectrum, which is due entirely to ambiguities with the coherent channel (hatched part of the histogram). The solid curve on the figure is the result of a Monte-Carlo calculation of this spectrum assuming:

- (i) The angle between the proton and neutron is isotropic
- (ii) One nucleon has a momentum spectrum given by the Hulthen wave function.

FIG 3.1

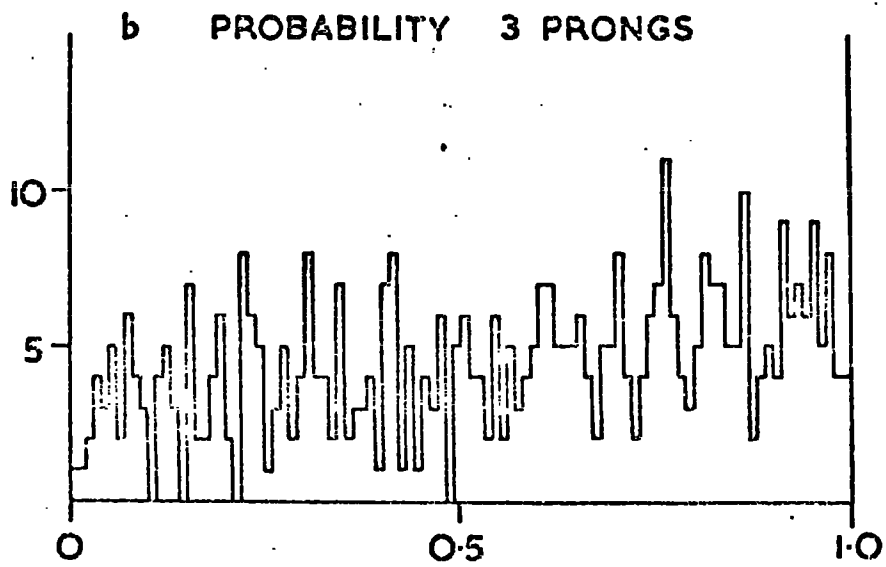
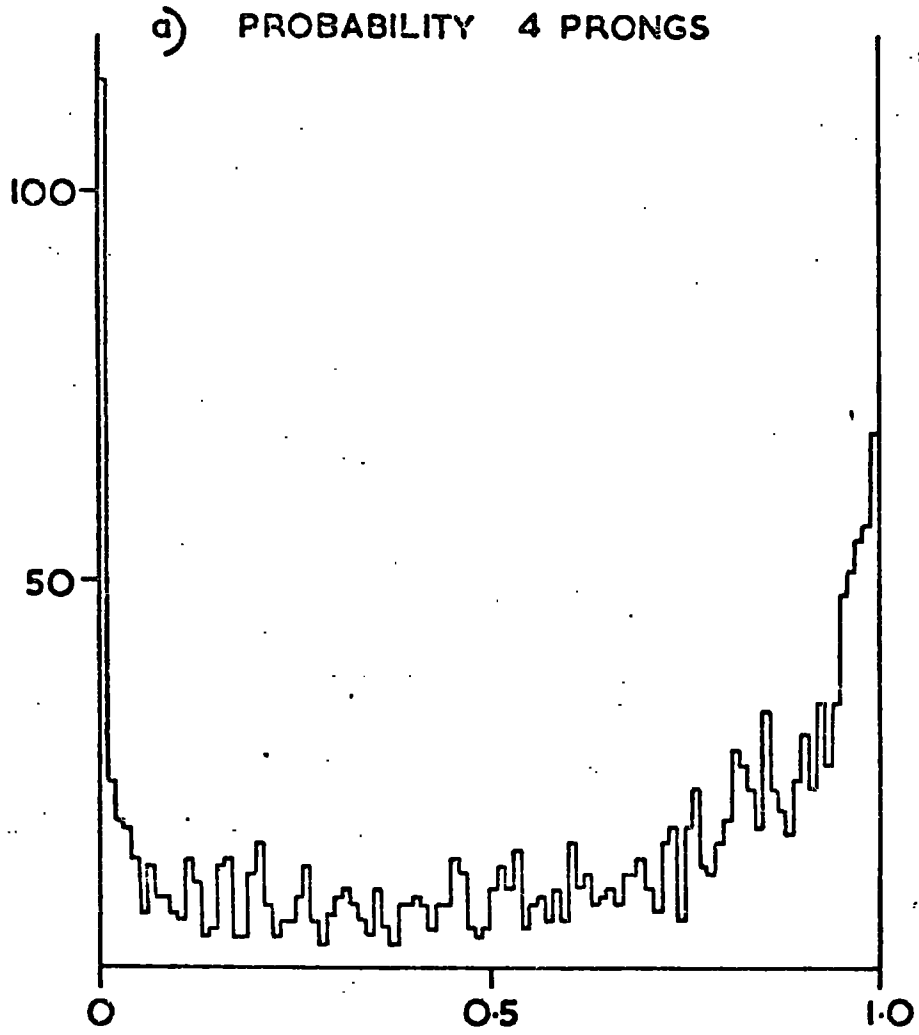
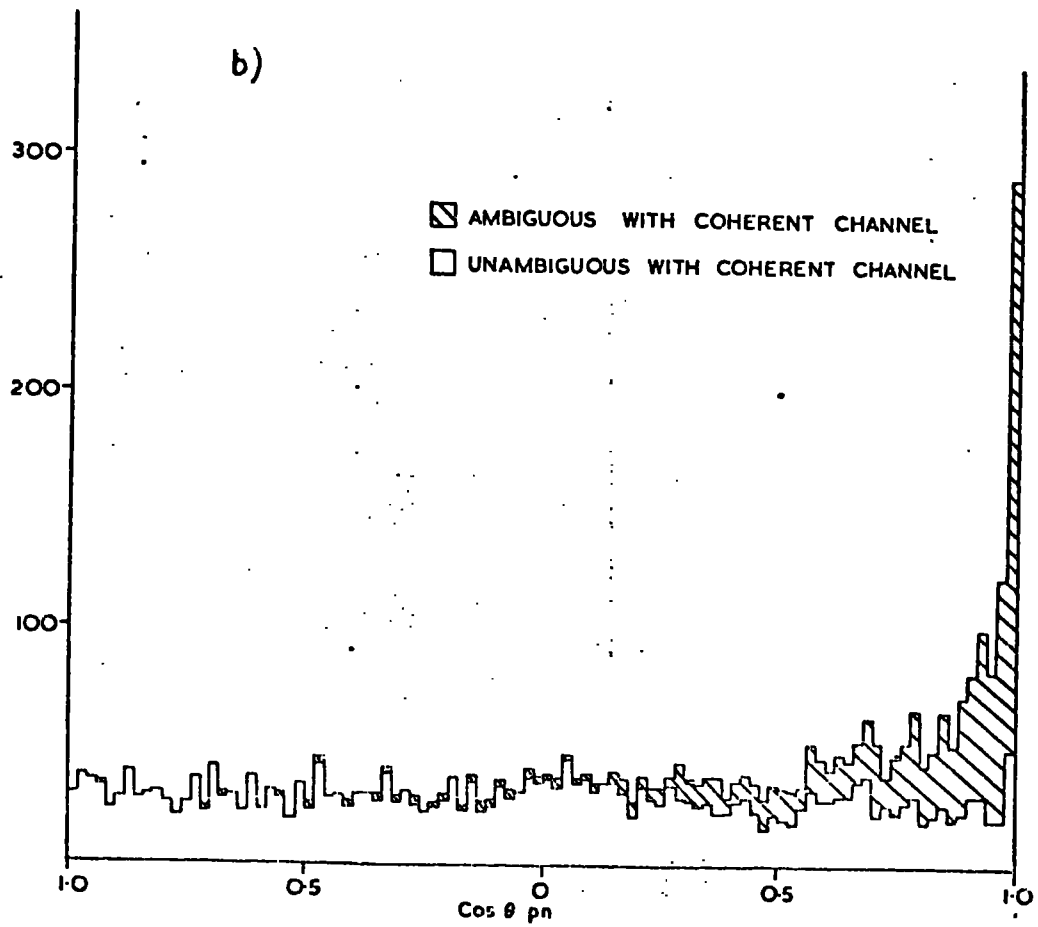
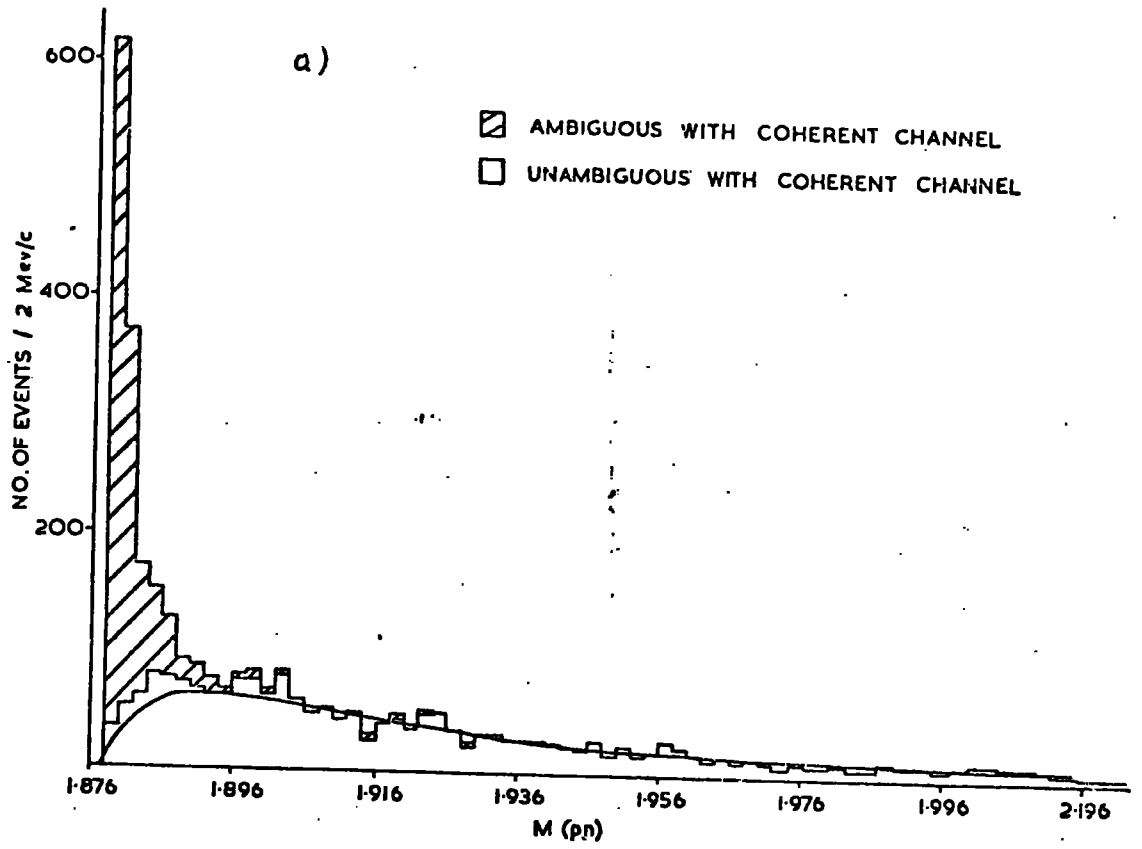


FIG 3.2



(iii) The other nucleon has a momentum spectrum similar to that of the non-spectator proton in reaction 4.

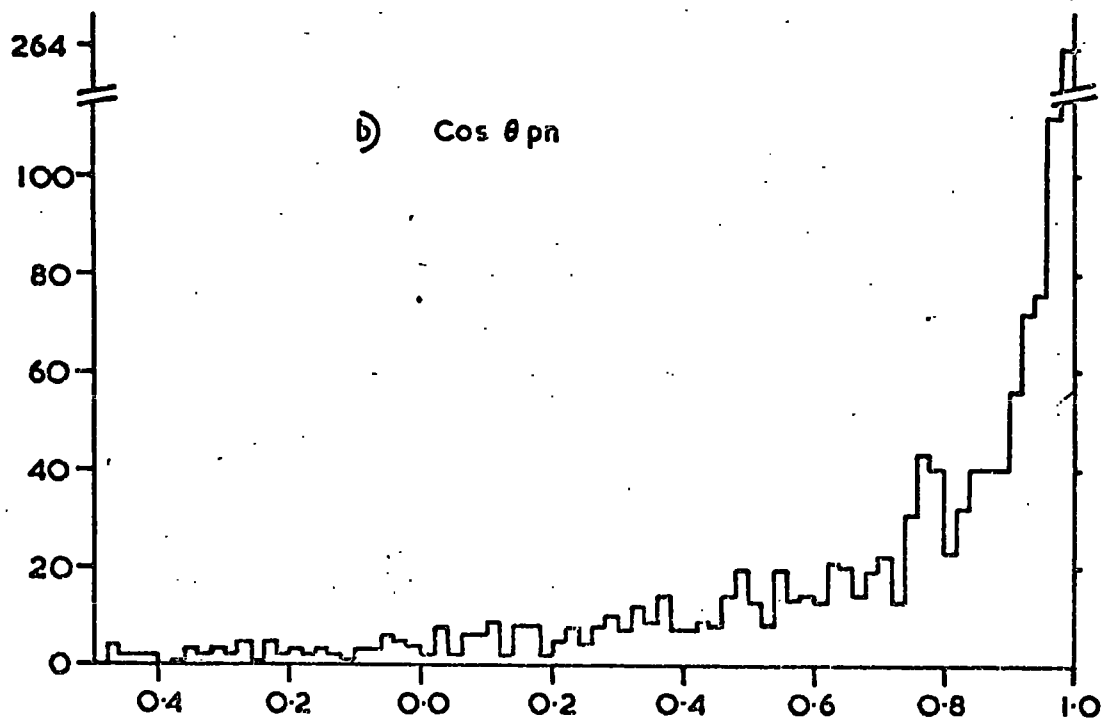
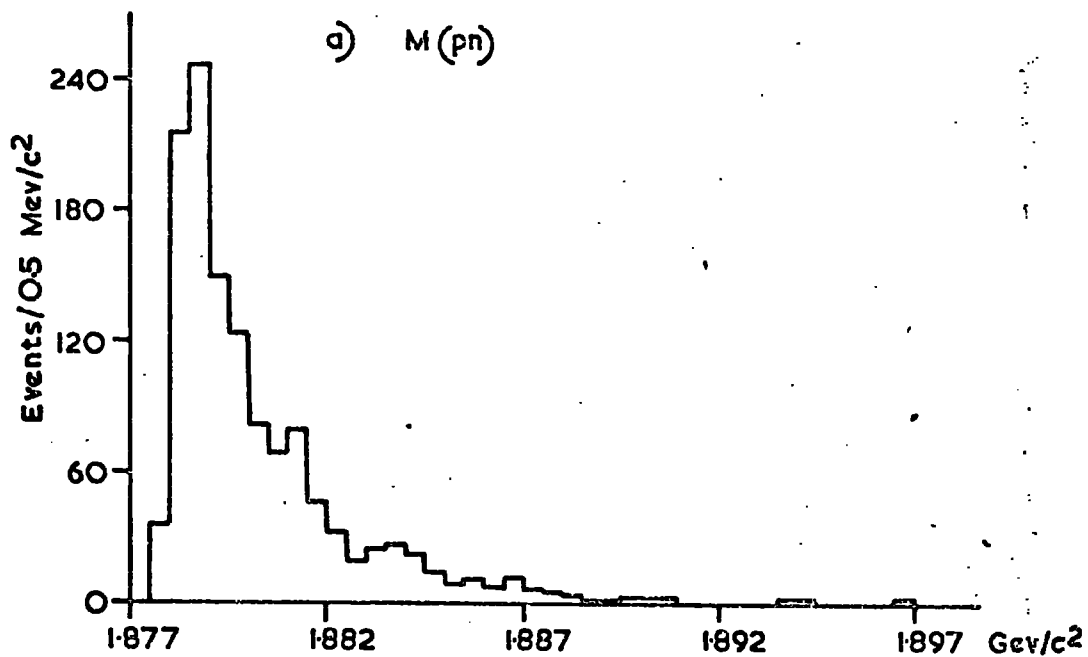
The curve is normalised to the upper part of the spectrum and by no means reproduces the coherent peak. Its failure to do so can be explained by the fact that assumption (i) above is patently in contradiction with the experimental data, as can be seen in figure 3.2 (b) which shows the distribution of the cosine of the angle between the proton and neutron ($\cos \theta_{pn}$) for all 4-prong events fitting channel 5 and for those ambiguous with reaction 1 (hatched histogram). There is a marked peak towards $\cos \theta_{pn}=1$ which is due entirely to channel $\pi^+d \rightarrow pn\pi^+\pi^+\pi^-$ events which also fit the coherent channel.

These features show that the majority of the fits to the coherent channel are due to coherent events. It is still probable, however, that some events which in fact should be assigned to the break-up channel ($\pi^+d \rightarrow pn\pi^+\pi^+\pi^-$) will give fits to the coherent channel. An estimate of the number of these events can be made from figure 3.2 (b). Assuming that for channel 5 events the distribution of $\cos \theta_{pn}$ is isotropic, as would be expected in the impulse approximation (and which is found to be the case for the angle between the two protons in channels 3 and 4), and assuming that those events with $\cos \theta_{pn} < 0$ are all break-up events, then the number of break-up events with $\cos \theta_{pn} > 0$ is known. The difference between this and the total number with $\cos \theta_{pn} > 0$ is equal to the number of true coherent events, and comparing this number with the number of fits to the coherent channel yields an estimate of the contamination. It is found that ~ 150 coherent fits should in fact be assigned to the break-up channel.

Figure 3.3 (a) shows $M(pn)$ for all events ambiguous between the two channels with a bin width of $0.5 \text{ MeV}/c^2$. The sharp peak centred

FIG 3.3

AMBIGUOUS 4 PRONGS



$\sim 1.878 \text{ GeV}/c^2$ and $2 \text{ MeV}/c^2$ wide, which is due to coherent events, is followed by a tail at higher masses. As the mass of the pn combination increases away from the mass of the deuteron, the hypothesis that the event is coherent becomes less probable. One way to remove contamination by the break-up channel is to reject all events with $M(pn)$ greater than some arbitrary limit.

A fit to the break-up channel of an event which in fact corresponds to the coherent channel ought to give parallel momenta to the proton and neutron. It is, therefore, possible to purify the sample by rejecting events for which Θ_{pn} is large. The distribution of this angle for events fitting the two competing channels is shown in figure 3.3 (b), where it can be seen that the angle is very large in some cases, although the majority of events are in the peak towards $\cos \Theta_{pn} = 1$.

A further method of selecting coherent events is by the ratio of the momenta of the neutron and proton. The momentum of a stopping track is derived from the range-energy relationship and the ratio of the momenta given to the track by interpreting it as a deuteron or proton has, therefore, a definite value:

$$\frac{P_d}{p_p} \approx 1.67 \quad 3.1$$

P_d = deuteron momentum p_p = proton momentum.

If it is assumed that the momenta of the three pions is the same in both fits, conservation of momentum implies:

$$\vec{P}_d = \vec{P}_n + \vec{P}_p \quad 3.2$$

P_n = neutron momentum

(The arrows signify that the quantities must be considered as vectors).

Since the angle between the proton and neutron should be zero for a coherent event then these quantities need not be considered as vectors and so, dividing eq. 3.2 by P_p :

$$\frac{P_n + P_p}{P_p} = \frac{P_d}{P_p} \approx 1.67 \quad 3.3$$

So $R = \frac{P_n}{P_p} = 0.67$ for a coherent event

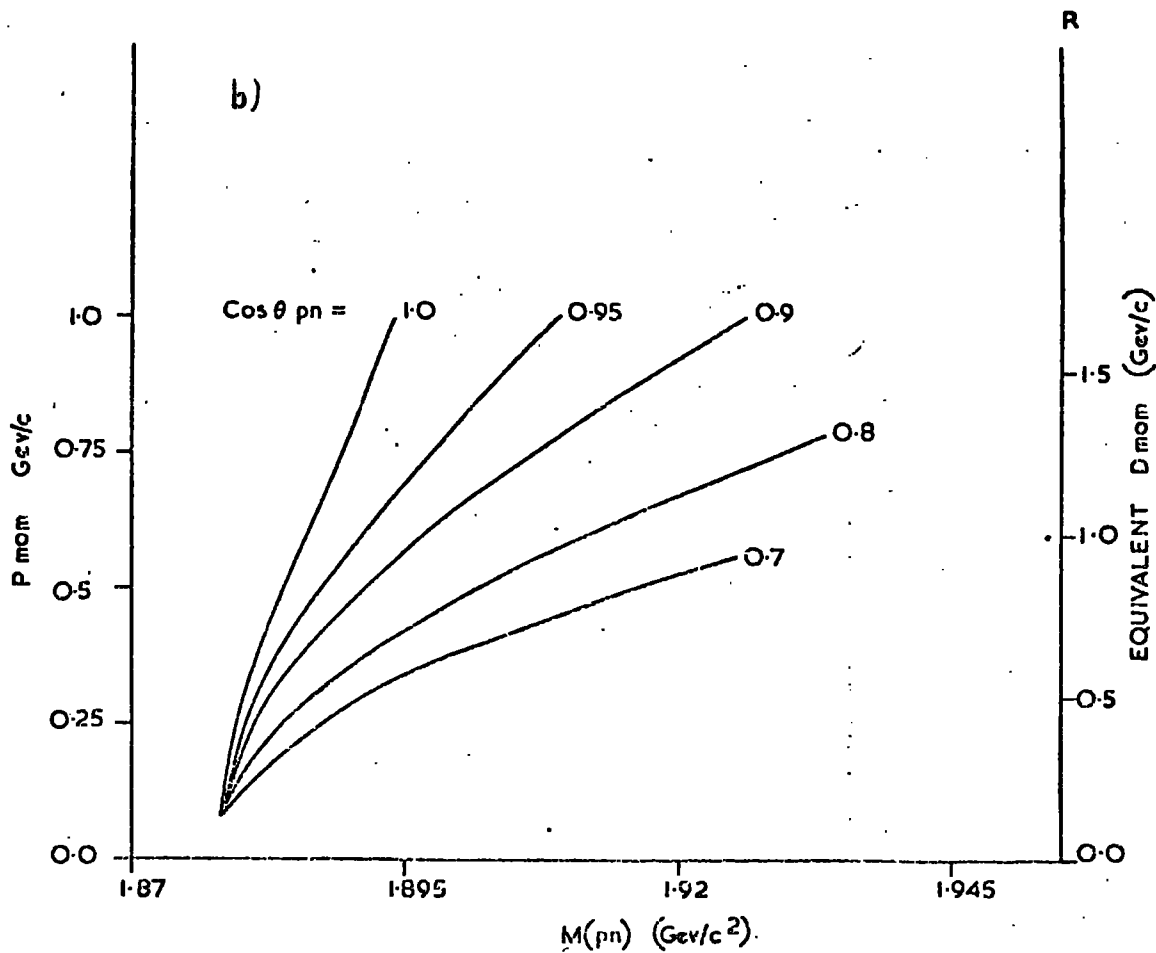
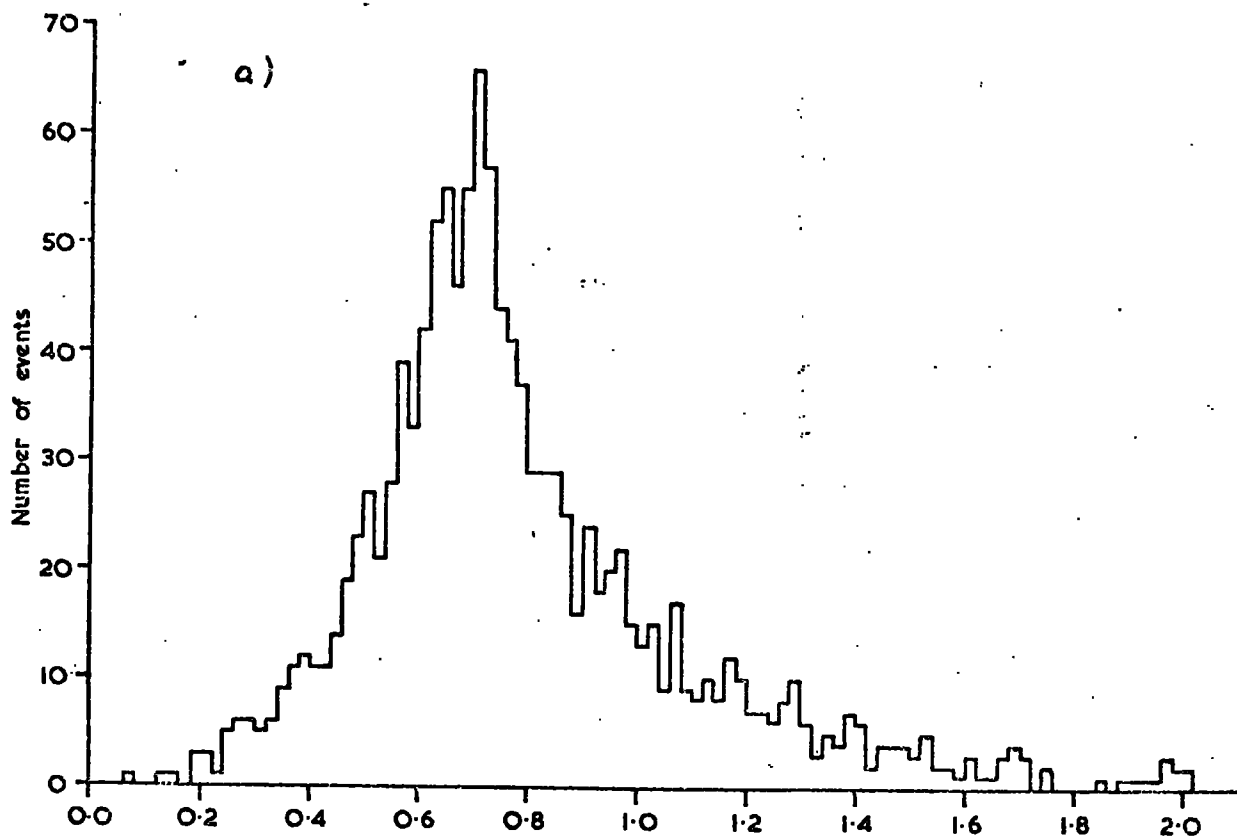
If, however, the event is not coherent, this ratio is not constrained. Figure 3.4 (a) shows the distribution of this ratio for all ambiguous events. The distribution peaks ~ 0.7 and is quite wide. The width is due largely to the error on the neutron momentum which is typically ~ 80 MeV/c and is large since it is an unseen particle.

If the ratio were correct in all cases then the relative momenta of the proton and neutron would increase as the momentum of the proton increased and this would lead to an increase in $M(pn)$. This effect can be seen in figure 3.4 (b) where the predicted value of $M(pn)$ is shown as a function of proton momentum under the assumption that $R = 0.67$. If θ_{pn} is not zero then the effect is even greater and this is also shown in figure 3.4 (b). for several values of this angle assuming that P_n has a projection of $0.67 P_p$ along the proton direction and the transverse component necessary to produce the specific angle. Thus to eliminate break-up events by anti-selecting high values of $M(pn)$ can lead to a biased sample, rejecting preferentially high momentum deuterons. For example to cut at $M(pn) = 1.885 \text{ GeV}/c^2$ would limit the deuteron momentum to be < 900 MeV/c if the ratio and $\cos \theta_{pn}$ were correct and < 350 MeV/c if $\cos \theta_{pn}$ were 0.7.

To reject events which have a large value of $\cos \theta_{pn}$ can also lead to a biased sample. The error on the fitted neutron track is due to the errors on the other tracks, since the neutron is unmeasured, and is, thus, independent of the neutrons momentum. If the error is in a direction perpendicular to the neutron direction then it will result in a change of the value of $\cos \theta_{pn}$ and this change will be greater for

FIG 3.4

THE DISTRIBUTION OF $R = \frac{N_{mom}}{P_{mom}}$ FOR ALL AMBIGUOUS 4 PRONG EVENTS.



smaller momentum neutrons. A coherent event, simulating a break-up event should give $\cos \theta_{pn} = 1$ but will deviate from this value because of the error on the neutron momentum and the deviation will be strongest for slow neutrons. Slow neutrons correspond to slow protons in the ambiguous sample as can be seen from the distribution of R and consequently, if the event is coherent, to slow deuterons. To reject events from the coherent sample by a cut on $\cos \theta_{pn}$ can, therefore, preferentially eliminate slow deuterons.

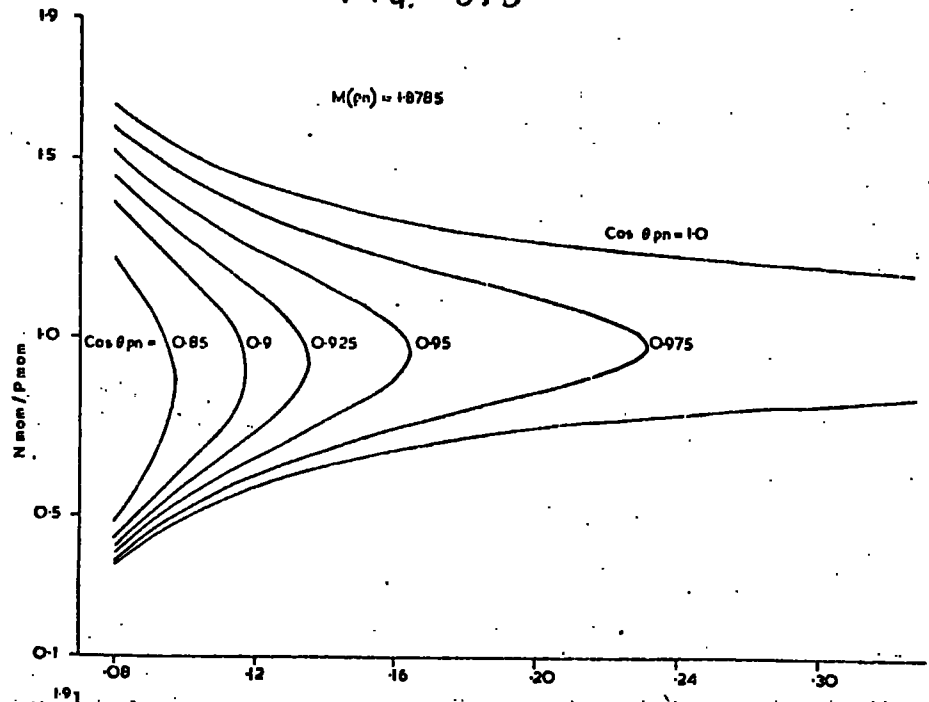
For any value of $M(pn)$ and P_p there are two possible values of P_n and hence of R and these depend only on the value of $\cos \theta_{pn}$. Figure 3.5 shows R as a function of P_p for 3 values of $M(pn)$ and several values of $\cos \theta_{pn}$. It can be seen that for slow protons, where the errors on R are large, the difference between the two solutions is also large, becoming smaller at higher proton momenta where the error on the ratio is smaller.

If an event were truly coherent then a spurious fit to the break up channel should give the lower ratio i.e. 0.67 in the ideal case. Even if $\cos \theta_{pn}$ is non-zero the lower ratio corresponds to a smaller component of the neutron momentum perpendicular to the proton direction as expected for coherent events.

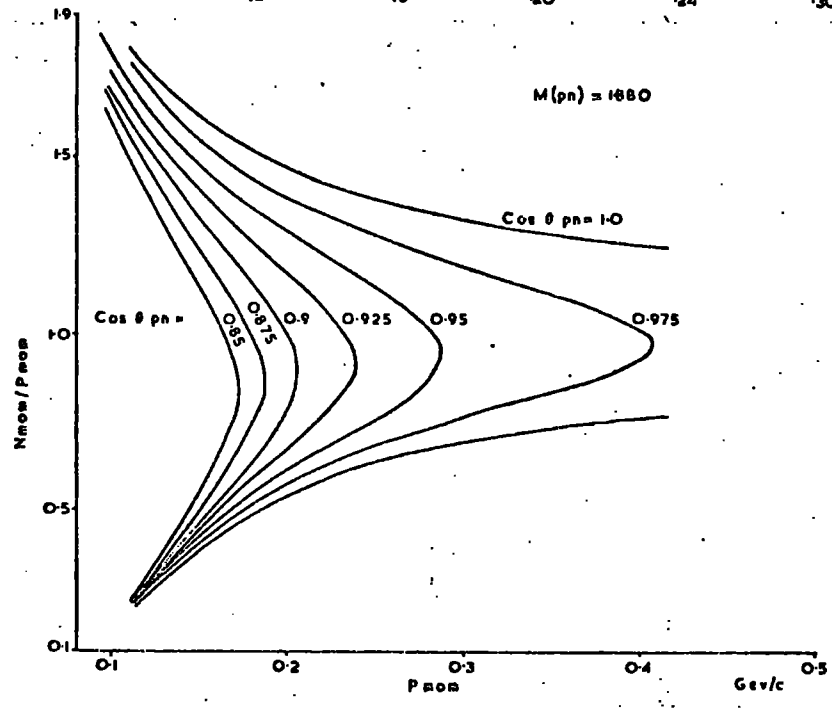
For a break up event simulating a coherent event, a high value of $R (> 1)$ will occur if the interaction takes place on the neutron with the proton as spectator, and a low value, if the reverse is true. The momentum distribution is peaked at low values of P_p for the ambiguous sample, indicating that they are probably spectators if they are really break-up events and hence it is expected that the higher solution for R will in fact occur for break-up events. In fact for the break up channel, the probability of spectator nucleon momentum falling in a certain region can be calculated from the Hulthen wave function, and the probability of the other nucleon falling in the same momentum region can be calculated

FIG. 3.5

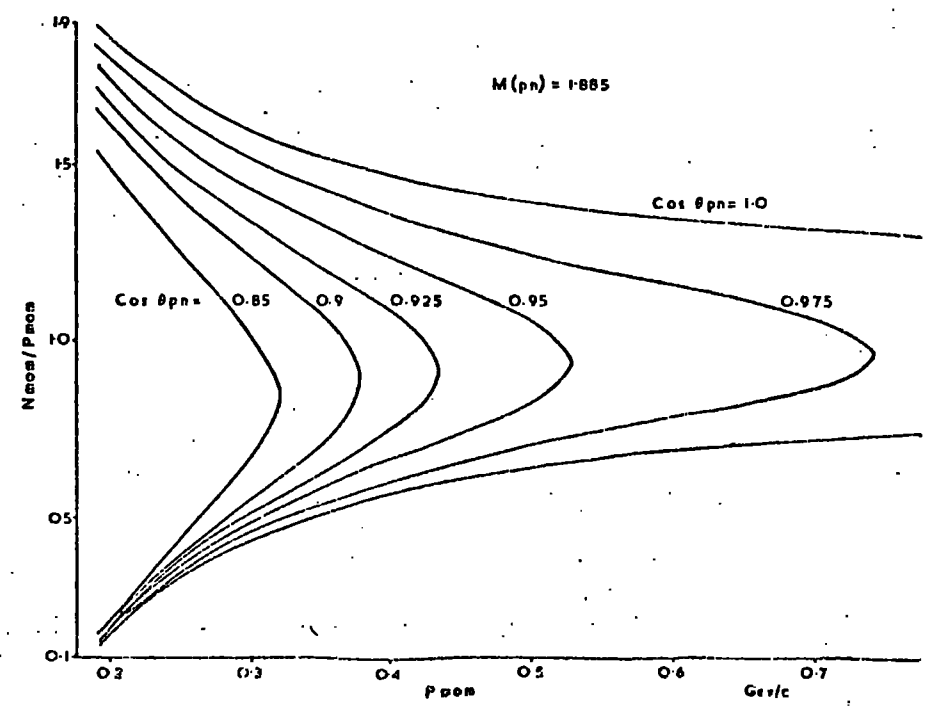
a)



b)



c)



assuming that its momentum distribution is similar to that of the non-spectator proton in Reaction 4. Dividing the experimental proton momentum spectrum according to the ratio of these two probabilities into two categories, spectator and participating nucleons, it is possible in both cases to calculate the probability that the neutron has a greater momentum. This has been done for every 20 MeV/c interval of the Pp spectrum for ambiguous events and combining the results it is found that ~90% of the events should have $R > 1$ if they belong to the break-up channel.

There is thus a distinct difference between the two competing channels: a real coherent event should yield the lower possible value of R, while a real break up events should yield the higher R value. The error on R must still be considered, but, as was seen earlier, in many cases the difference between the two solutions is very large. The sample of events was separated into 9 separate sub-samples:

1. $R + 3. \Delta R < RU$
2. $R + 2. \Delta R < RU < R + 3. R$
3. $R + \Delta R < RU < R + 2. R$
4. $R < RU_j < R + R$
5. $R - 3. \Delta R > RL$
6. $R - 2. \Delta R > RL > R - 3. R$
7. $R - \Delta R > RL > R - 2. R$
8. $R > RL > R - R$
9. $RL \text{ and } RU > 1$

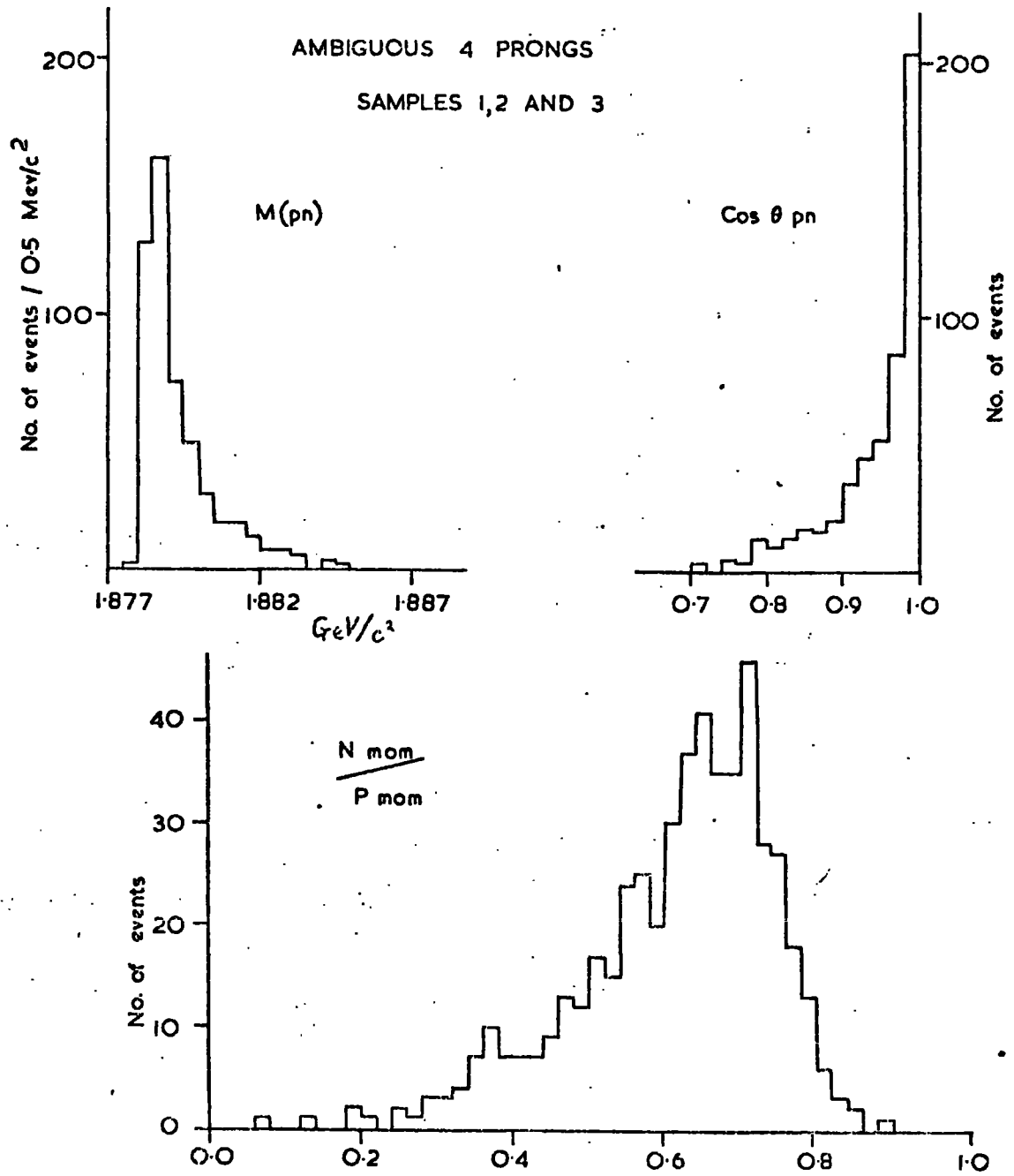
where RU = upper possible value of R for each event

RL = lower possible value of R for each event

ΔR = experimental error on R.

Samples 1, 2 and 3 take the lower value of R and are not within error of the other possible value. They are presumably, therefore, coherent. Figures 3.6 (a), (b) and (c) show respectively $M(pn)$, $\cos \theta_{pn}$ and R for these events. They show very markedly the features expected

FIG 3.6



of coherent events. The asymmetric shape of the R distribution is due to the sampling procedure and indicates that not all the coherent events are in this sample.

Samples 4 and 8 contain the events where the error on R is such that R is compatible with both possible values. When R takes the lower value (sample 4) there are no events with $M(p_n) > 1.88$ or with $\cos \theta p_n < 0.8$. These events have therefore been accepted as coherent. Similarly for sample 8, $M(p_n)$ is sharply peaked at ~ 1.879 and $\cos \theta p_n$ at 1. Furthermore, the distribution of R for these events is peaked towards 1. Errors on R for a coherent event can take it above 1 and indeed, if the R distribution is to be symmetric there must be some events with $R > 1$. Coherent events with $R > 1$ should peak at 1 and tail off above this value, and this is seen to be the case for sample 8 events, which have therefore been interpreted as coherent events.

Samples 5 and 6 consist of events which have a value of R not within 2 standard deviations of the lower possible value. They demonstrate no features expected for coherent events: no accumulation of events with low values of $M(p_n)$ or with $\cos \theta \sim 1$ and no peaking of the R distribution towards 1. These events have been rejected from the sample as belonging to reaction 5.

Events of sample 7 seem to mark the borderline between coherent and break-up events. There are some coherent features in the data: $M(p_n)$ low; $\cos \theta p_n$ tending towards 1 and some peaking of R towards 1. A further division of the sample was made as follows:

$$7(a) \quad R - \frac{3}{2} \Delta R > R_L > R - 2 \Delta R$$

$$7(b) \quad R - \Delta R > R_L > R - \frac{3}{2} \Delta R.$$

The events of sample 7(a) again show no coherent features and were rejected, while those of sample 7 (b) account entirely for the peaking towards 1 of the R distribution and were accepted.

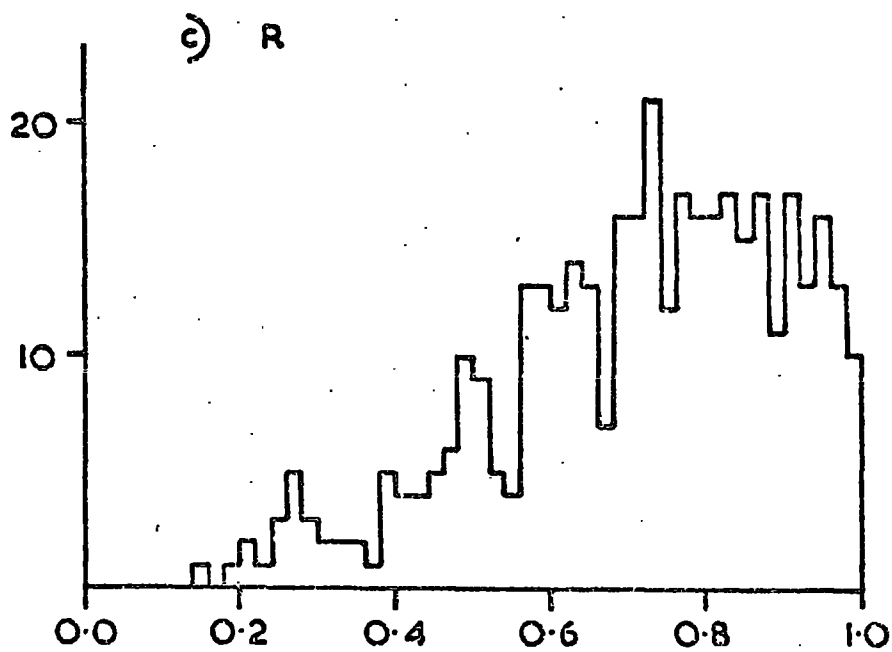
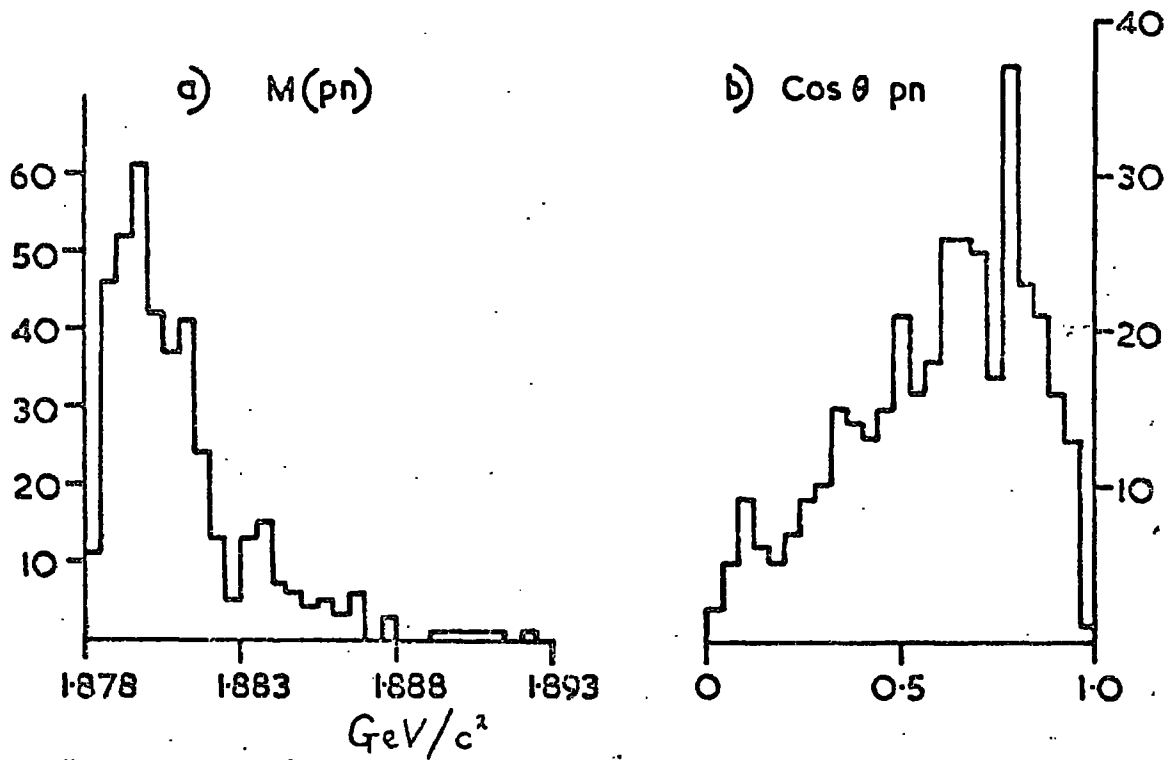
At this stage 173 events, all with $R > 1$, have been rejected. This number compares favourably with the estimated amount of contamination made earlier of ~ 150 events. Since $\sim 90\%$ of the break-up events are expected to have $R > 1$, an estimate of the contamination of the coherent sample by break-up events which have $R < 1$, can be made from this number. The result is ~ 19 events.

Sample 9 contains those events for which both possible values of R , (R_L and R_U) are smaller than 1. No decision about the coherence of the event can be made in this case from the actual value of R . Since R is necessarily less than 1, however, the contamination of this sample is likely to be small. Figures 3.7 (a) (b) and (c) show, respectively, $M(p_n)$, $\cos \theta_{pn}$ and R for these events. The distribution of $M(p_n)$ peaks strongly ~ 1.880 as expected for coherent events, and the $\cos \theta_{pn}$ distribution peaks ~ 0.8 . The reduction in the number of events above this value is due to the sampling procedure since if $\cos \theta_{pn}$ is 1 the two possible values of R cannot both be < 1 . It is possible that the break-up events with $R < 1$ will fall predominantly in this sample since these events will, in general, have a relatively high value of P_p and it is only for high values of P_p that R_U is < 1 as can be seen from figure 3.5. For this reason events with $M(p_n) > 1.887$ in this sample were rejected. While this selection is subject to the bias described above, it rejects only 13 events and it is found that no accepted event in any other sample has a value of $M(p_n)$ greater than this limit.

While it is hoped that this latter selection criterion will reduce the number of break-up events with $R < 1$, it cannot be proved categorically that it does so and the figure of 19 events for this contamination must remain as an upper limit. There may also be some contamination resulting from the acceptance of sample 8 events and part of sample 7. The total number of events accepted from these two samples, however, is only 116 and a study of the distributions of $M(p_n)$, $\cos \theta_{pn}$ and R for these shows

FIG 3.7

SAMPLE 9 EVENTS



that the contamination is unlikely to be more than 10%. Thus, the total contamination is ≤ 30 events in 1130 ambiguities. The 100 unambiguous events have been accepted as coherent, giving a final 4-prong sample of 1230 coherent events with $\leq 2.5\%$ contamination.

Table 3.2 gives the total number of events in each sample, together with the numbers accepted and rejected from them. In summary, the criteria used to select the 4 prong coherent events were:

- (i) Probability of fit $> 1\%$
- (ii) If ambiguous with reaction 5: then
 - (a) if $RU > 1$ $R - \frac{3}{2} \Delta R < RL$
 - (b) If $RU < 1$ $M(pn) < 1.887$

3.2 Three Prong Events

The 3-prong data consists of events where the deuteron, or proton, in the final state, has such a low momentum that it leaves no visible track in the bubble chamber. In fitting an event to reaction 1 the deuteron was treated in the same way as an unseen neutral particle and results, therefore, in a 1-C fit. The data is likely, therefore, to be more contaminated for the 3-prongs than was the case for the 4-prong events.

Table 3.1 shows the total number of 3-prong events giving a fit to reaction 1, together with the number of these ambiguous with each of reactions 3-5. No fit is possible to reaction 2 since this channel contains two unseen particles. Fits to reactions 4 and 5 were possible, as explained in the chapter 2, by treating the unseen proton as a measured track with zero momentum and suitable errors. Fits to reaction 3 are 4-C fits and are, therefore, more probable than any 1C fit and events ambiguous between this channel and the coherent channel were rejected from the coherent sample.

TABIE 3.2: Number of events accepted and rejected in each subsample of the 4-prong data.

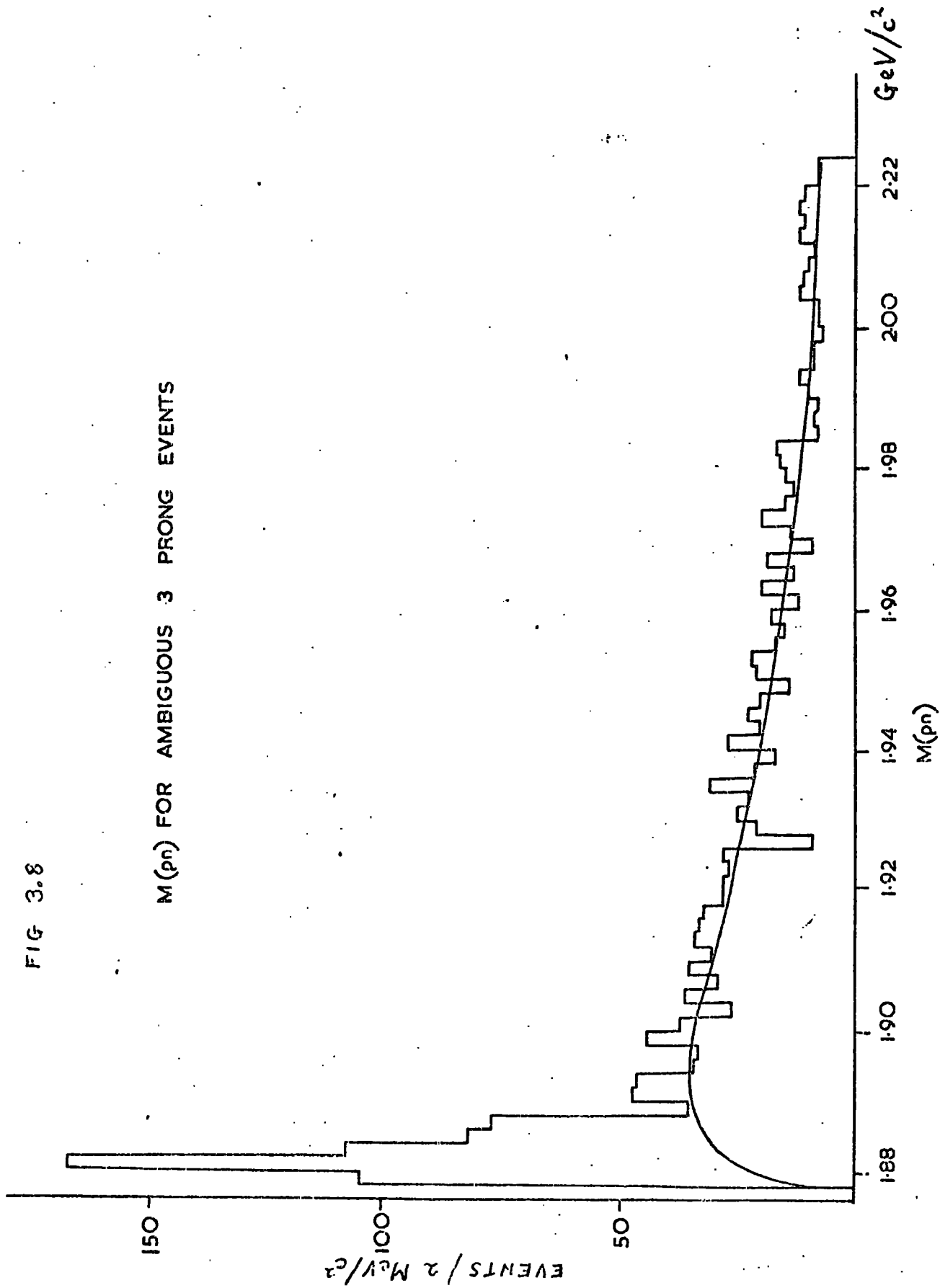
SAMPLE	NO. ACCEPTED	NO. REJECTED	TOTAL
1	255	0	255
2	122	0	122
3	136	0	136
4	110	0	110
5	.0	80	80
6	0	63	63
7	56	32	88
8	60	0	60
9	391	13	404
Unambiguous	100	0	100
TOTAL	1230	188	1418

The largest ambiguity is between the coherent channel and reaction 5, the break-up channel, as was the case in the 4-prong data. In this case, essentially every event which fits one of these also fits the other. While, in principle, it is possible to resolve this ambiguity by studying for example, the angle between the proton and neutron ($\cos \theta_{pn}$) in the fit to reaction 5, in practice, such a method proves useless since the method of treating the unseen proton is unsatisfactory when a further neutral particle is involved in the interaction. The fit, in fact, gives almost zero momentum to the proton thus yielding all quantities which depend upon its intrinsic properties meaningless. Properties of the proton-neutron combination, such as their combined effective mass $M(pn)$ can be used, however, since these depend on the measured quantities of the three seen pions.

The distribution of $M(pn)$ for all 3-prong events fitting both reactions 1 and 5 is shown in figure 3.8 (a). This shows a large peak, centred $\sim 1.88 \text{ GeV}/c^2$. The smooth curve shown in this figure is the result of a similar Monte-Carlo calculation to that performed for the 4-prong sample, with the added criterion that the spectator proton must have a momentum less than the visibility limit ($\sim 80 \text{ MeV}/c$). This curve by no means reproduces the threshold peak, which is therefore interpreted as being due to coherent events. A cut was made at a value of $M(pn) = 1.885 \text{ MeV}/c^2$ and events above this value were rejected from the coherent sample. It should be noted that this selection is free from the bias described for the 4-prong events, which was due to the range-momentum relation for stopping measured tracks. An estimate of the contamination present in the remaining 447 events can be made from the curve in figure 3.7 (a) and the result is $\sim 20\%$. The figure suggests that coherent events are present up to a value of $M(pn)$ of ~ 1.888 but to include events up to this mass results in an increase

FIG 3.8

$M(p\bar{p})$ FOR AMBIGUOUS 3 PRONG EVENTS



in the contamination to 25%.

A further reason for the choice of $1.885 \text{ MeV}/c^2$ as the limit arises from the fact that the unseen proton in reaction 5, is fitted with zero momentum. This results in all the momentum not taken by the 3-pions being given to the neutron, while this momentum is given to the deuteron in reaction 1. The neutron momentum is related, thus, to both the deuteron momentum and to $M(pn)$, which are therefore related to each other. The deuteron momentum visibility limit $\sim 140 \text{ MeV}/c$ corresponds to a value of $M(pn)$ of ~ 1.885 thus to cut at this value ensures that deuterons are not fitted with momenta such that they should leave a visible track.

The sample of events remaining has a flat probability distribution as can be seen in fig. 3.1 (b). This is in contradiction to the 4-prong sample. It has been shown in the study of reactions 3 and 4, however, that to overestimate the errors on the fitted tracks by a factor of 1.5 would successfully explain both distributions (Ref. 3.1). Events with a probability less than 1% have been rejected for compatibility with the 4-prong sample. The remaining number of 3-prong events is then 445.

No attempt has been made to resolve the ambiguity between reactions 1 and 4 since 3-prong fits to reaction 4 have been found to be mostly spurious, particularly if the fast proton is not recognizable by ionisation, as must be the case of an ambiguity with the coherent channel is to occur. Moreover, it seems unlikely that an event which should in fact be assigned to channel 4 will simulate the break-up channel in such a way that the break-up channel simulates the coherent channel.

In summary the selections made were:

- (i) $M(pn)$ for ambiguous fit $< 1.885 \text{ GeV}/c^2$
- (ii) Probability $> 1\%$
- (iii) No simultaneous 4C fit.

A check can be made that the 3-prong sample is compatible with the 4-prongs by trying to match the deuteron momentum spectra for the two sets of data. In order to do this only the data from Durham and the two French laboratories have been used, since the Italian laboratories only measured three prong events with a more than minimum ionizing track. The pion tracks in the coherent channel all tend to be fast and therefore minimum ionising and this selection, therefore, effectively filters out 3-prong coherent events. The deuteron laboratory momentum spectrum is shown in figure 3.9 for the other 3 laboratories, with the 3-prong sample hatched. The matching is quite good. If, $M(pn)$ is limited to a smaller value than $1.885 \text{ GeV}/c^2$ then a dip becomes apparent in this distribution at the join between the two samples and, similarly, if higher values of $M(pn)$ are allowed, an enhancement appears in the spectrum.

3.3 Contamination by Coherent Kaon Production

Having selected a sample of events which are coherent, there remains the possibility that the pions have been misidentified and are in fact kaons. The reaction may be:

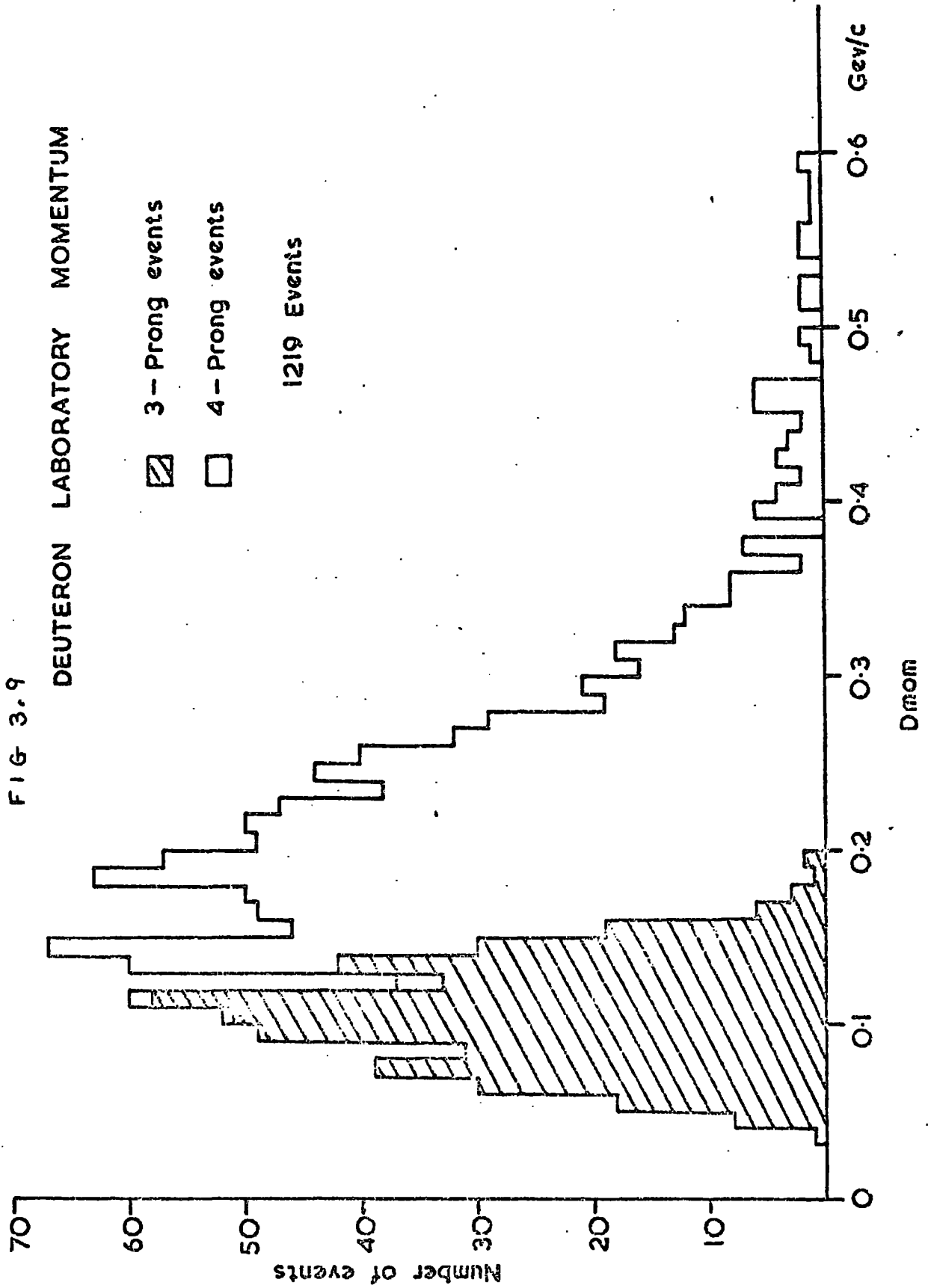


Events with a kinked secondary track, which may be due to a kaon decaying, were not measured and events where the ionisation was not compatible were rejected, but the meson tracks are very fast in this channel, in general, and the kaons may not decay in the chamber and their ionisation will in general be indistinguishable from that of the pions.

In order to investigate this possibility, a sample of 300 4-prong events, which were accepted as coherent, were passed through the program GRIND and fits attempted to this channel. About 50% of these gave a 4-C fit to reaction 6. This is understandable since for a fast track to change its mass from that of a pion to that of a kaon without changing

FIG 3.9

DEUTERON LABORATORY MOMENTUM



its momentum results in a negligible change in its energy and both momentum conservation and energy conservation can be maintained. However, only 14 events give a χ^2 probability for this fit which is of comparable magnitude to that for reaction 1. This gives an upper limit of 5% to the contamination of reaction 1 by reaction 6. The contamination is likely to be much less than that, however, as can be seen by the fact that of the events which give a fit to reaction 6 ~ 90% fit the reaction twice, by successively interpreting both positive non stopping tracks as the positive kaon. This fact indicates the ease with which spurious fits to reaction 6 can arise. (If events are accepted as belonging to reaction 6 only if they give a probability > twice that of the fit to reaction 1 then the resulting amount of contamination is less than 2%.

In the case of the 3-pronged events ~ 75% gave at least one fit to reaction 6 and 40% had probabilities of comparable magnitude to that of reaction 1. These, however, are the results of less reliable IC fits and can therefore more easily be spurious. There is no reason to believe that the cross section for reaction 6 is relatively greater for 3-prong events than for 4-prong and it is assumed that the contamination here is the same as for the 4-prongs.

3.4 Channel Cross Section

The channel cross section is given by:

$$\sigma = \sigma_{\text{tot}} \frac{n}{N}$$

where n = the number of events in the channel

and N = the total number of events

The number of events in the channel must be corrected for any losses which may occur between the scanning and the DST stages of the experiment. These losses can be due to immeasurability of the event, or to failures of the system. The corrected number of events from Durham is 770 ± 85

yielding a value for the channel cross section of $360 \pm 45 \mu\text{b}$. This value has been combined with the values given by the two French laboratories and the final value is $353 \pm 30 \mu\text{b}$.

CHAPTER FOUR

GENERAL FEATURES OF THE DATA.

Introduction

In this chapter the general characteristics of the reaction will be examined in terms of effective mass plots and differential cross sections. The purpose of the chapter is to determine the parameters, such as mass, width and production cross section, of the resonances and enhancements which occur. These parameters will be determined in a manner which is as model independent as possible. The first section briefly describes the overall differential cross section and, thereafter, the various mass spectra are examined sequentially. Characteristics of resonances produced are discussed in the appropriate sections.

4.1. The Differential Cross Section.

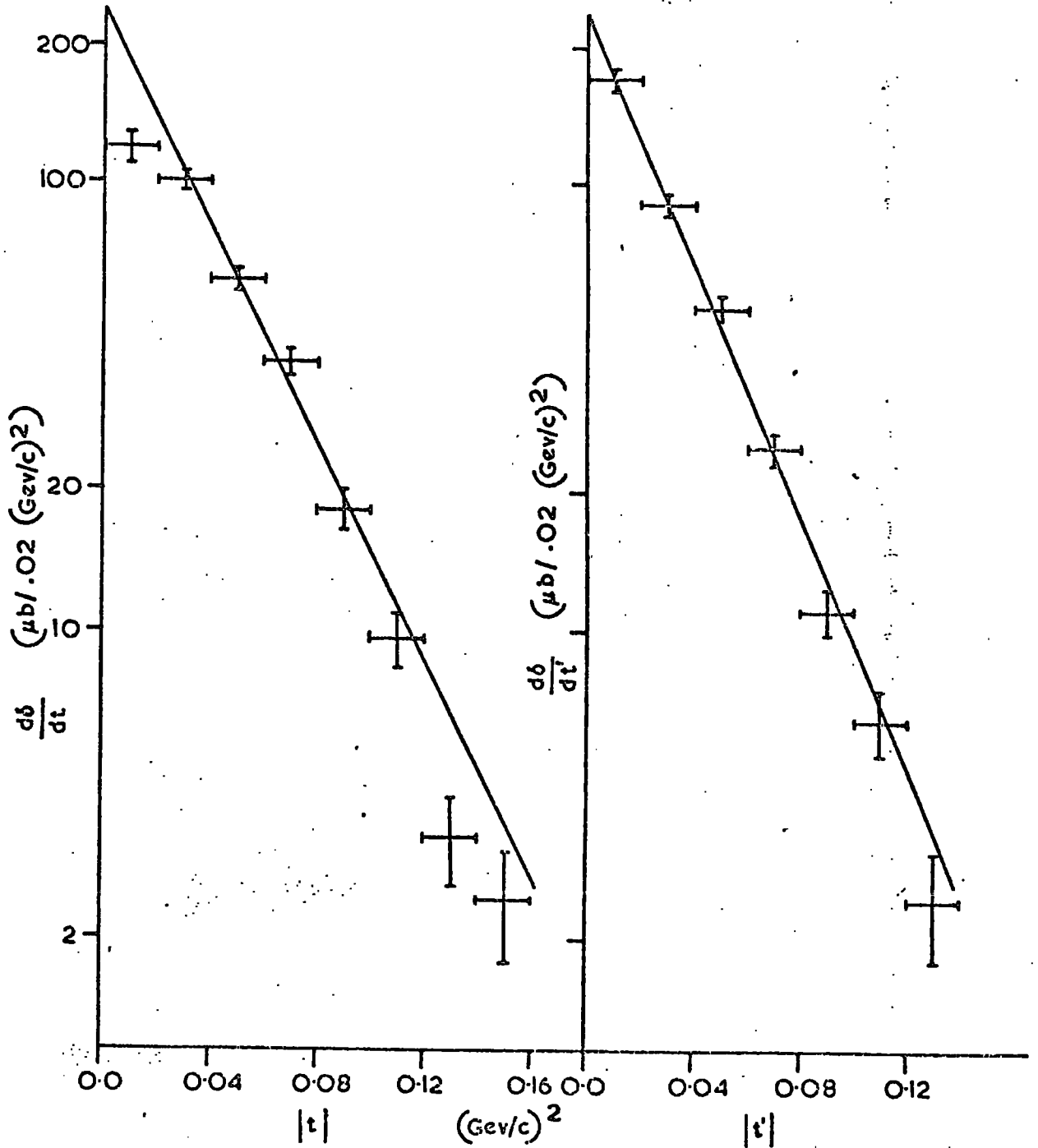
The differential cross section for the reaction is shown in figure 4.1 (a) in terms of the relativistically invariant variable t defined as the square of the 4-momentum transfer from the initial to the final state deuteron ($d\sigma/dt$ vs. t) and in figure 4.1 (b) in terms of t' ($d\sigma/dt'$ vs. t') where t' is defined as:

$$t' = t - t_{\min} \quad 4.1$$

and t_{\min} is the minimum kinematically allowed value of t for each individual event. It can be seen that the distributions are strongly peaked towards 0, corresponding to the configuration where the angle between the incoming and outgoing deuterons is very small in the centre of mass reference frame. The reaction is thus very peripheral as would be expected for coherent deuteron events since less peripheral collisions (higher values of t) are more likely to result in deuteron break-up as explained in Chapter 1.

FIG. 4.1

DIFFERENTIAL CROSS SECTIONS



Weighted least square fits have been made to these distributions in the t and t' range $0.02-0.12$ $(\text{GeV}/c)^2$ using the parametrizations:

$$\frac{d\bar{r}}{dt} = K \exp(-At) \quad 4.2$$

and

$$\frac{d\bar{r}}{dt'} = k' \exp(-Bt') \quad 4.3$$

A difficulty encountered in this procedure was the effect of the reduced sample of 3-prong events since these correspond to very low values of t . The 3-prong data is weighted, in the figures by the ratio of the total number of 4-prongs to the number of 4 prongs from the three collaborating laboratories which also contributed three prong events, and it is this resulting distribution which was fitted to Equations 4.2 and 4.3. The results were found to be compatible with the results of fitting only the events from the laboratories which measured all three prongs, as would be expected since the effect of the 3-prong sample is small except in the first t region $(0.0-0.02 (\text{GeV}/c)^2)$ and this was not used in the fitting.

The fitted parameters were:

$$A = 27.6 \pm 3.0 (\text{GeV}/c)^{-2}$$

$$B = 32.6 \pm 1.9 (\text{GeV}/c)^{-2}$$

and the results of the fitting are shown as the solid lines in figure 4.1. The fit to the $d\bar{r}/dt$ distribution overestimates the number of events below $|t| = 0.02 (\text{GeV}/c)^2$. This dip at 0 is probably due to the production in this reaction of high mass three pion states for which t_{\min} is significantly different from zero, an interpretation supported by the fact that the extrapolated line from the fit to the $d\bar{r}/dt'$ distribution passes directly through the experimental point.

4.2 The $d\pi^+$ effective mass spectrum

Since there are two identical positive pions in the final state of

this reaction, two combinations of the $d\pi^+$ effective mass for each event are plotted in the mass spectrum shown in fig. 4.2. The only structure visible in this distribution is the peak near threshold. If the positive pions are labelled fast (π_f^+) and slow (π_s^+) according to their momentum in the laboratory frame then a plot of the $d\pi_s^+$ effective mass (hatched histogram in fig. 4.2) shows that the peak is formed entirely in this combination.

A fit to this spectrum in the region $M(d\pi) < 2.6 \text{ GeV}/c^2$ of a simple s-wave Breit-Wigner function:

$$BW(M) = \frac{(\Gamma_0/2)^2}{(M-M_0)^2 + (\Gamma_0/2)^2} \quad 4.3$$

where M_0 is the central mass value and Γ_0 is the width, together with a hand drawn background, yields the following parameters:

$$M_0 = 2210 \text{ MeV}/c^2$$

$$\Gamma_0 = 300 \text{ MeV}/c^2$$

The fit is very poor, however, irrespective of the shape used for the background.

In estimating the cross section for production of this peak care must be taken over the assumed form of the background. There is, moreover, a marked difference in the relative amount of production between the 4-prong data and the 3-prong data, as can be seen in figures 4.3 (a) and (b) which show the $d\pi_s^+$ mass spectrum for these two samples respectively, and this difference must be allowed for when correcting for the missing 3-prongs. A lower limit to the cross section has been calculated by counting only events which fall above a horizontal line extrapolated from the $d\pi$ mass region $2.4 - 3.2 \text{ GeV}/c^2$. The value found is $42 \mu\text{b}$ or 12% of the data. An upper limit can be determined by examination of figure 4.3 (c) which shows, for the 4 prong sample,

FIG 4.2 THE ($d\pi^+$) EFFECTIVE MASS 2×1675 COMBINATIONS.

 $d\pi^+$ SLOW COMBINATION ONLY.

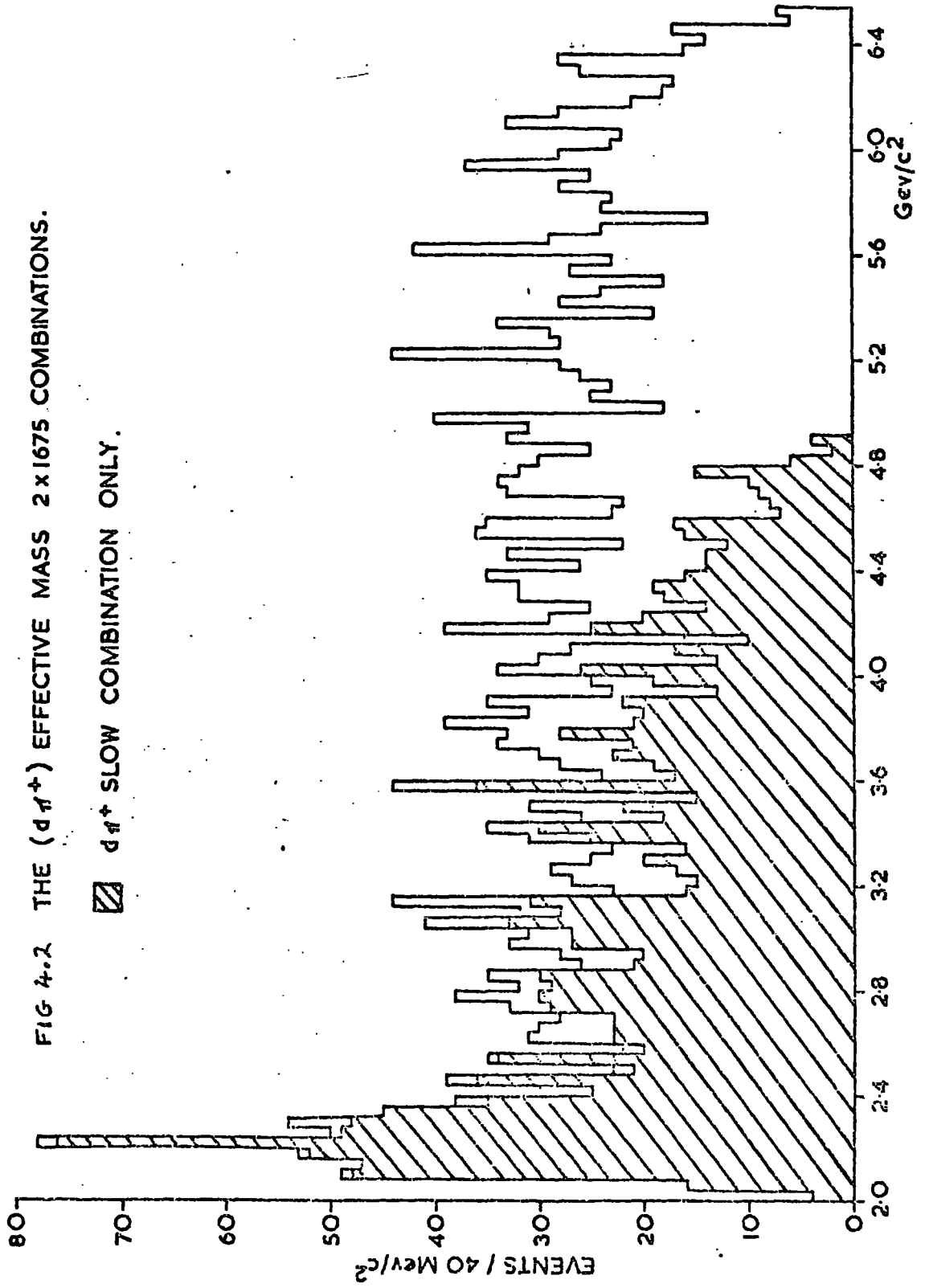
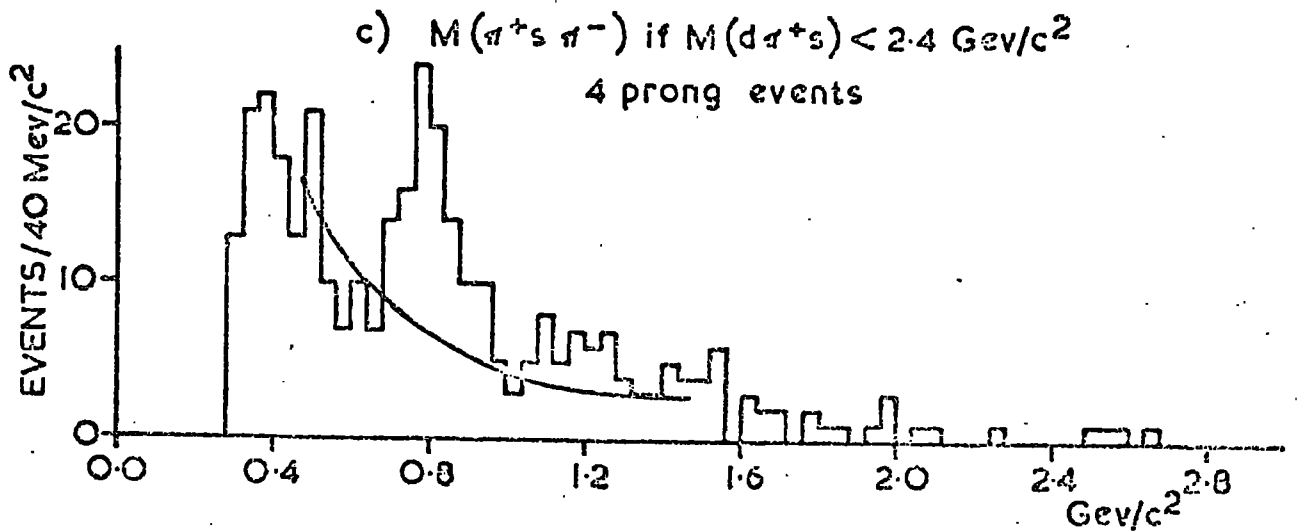
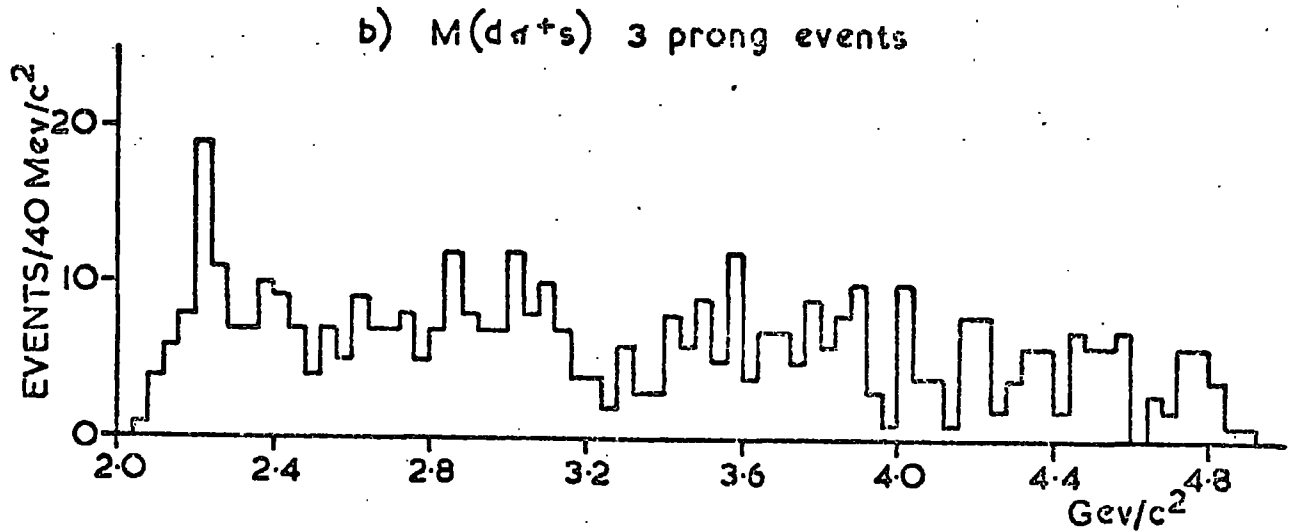
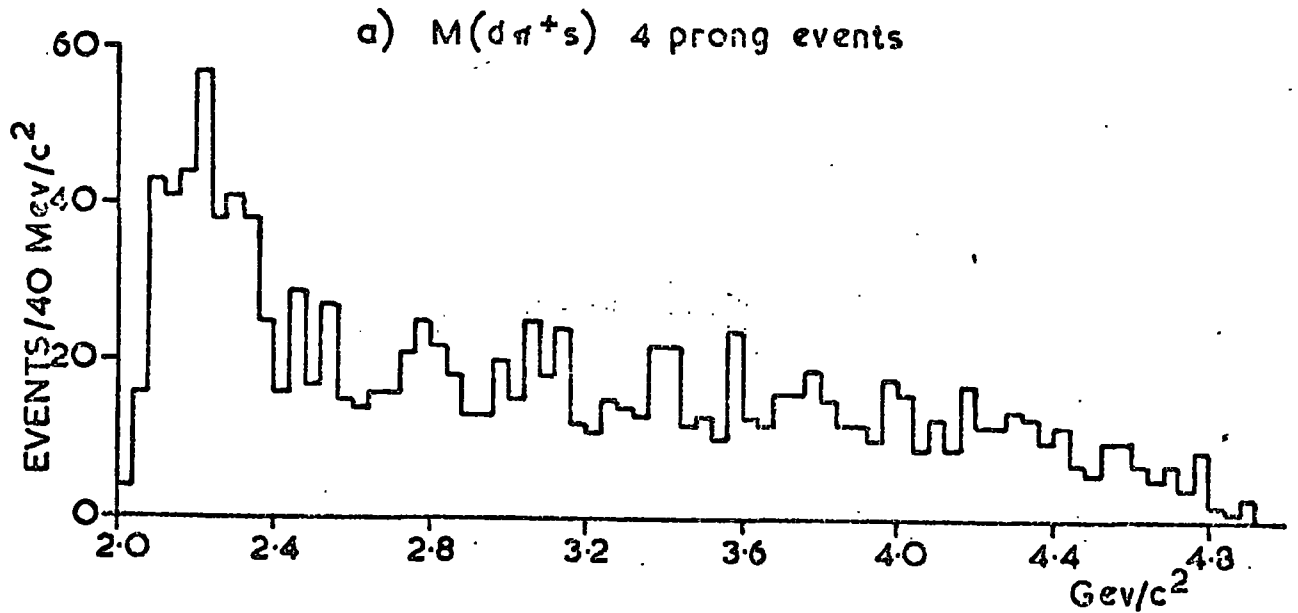


FIG 4.3



the $\pi_s^+ \pi^-$ effective mass spectrum of those events for which the $\pi_s^+ d$ mass falls in the peak ($M(\pi_s^+ d) < 2.4 \text{ GeV}/c$). There is a prominent ρ^0 signal and some indication of an f^0 in the distribution, and these must contribute to the background below the $d\pi_s^+$ peak. The number of ρ^0 and f^0 events has been estimated by use of a hand-drawn background to this spectrum and, assuming all other events are due to the $d\pi_s^+$ mass peak, a value of $55 \mu\text{b}$ or 15.5% of the channel, is found for the production cross section of this peak. The best estimate for this cross section can thus be written as the average $48 \pm 7 \mu\text{b}$.

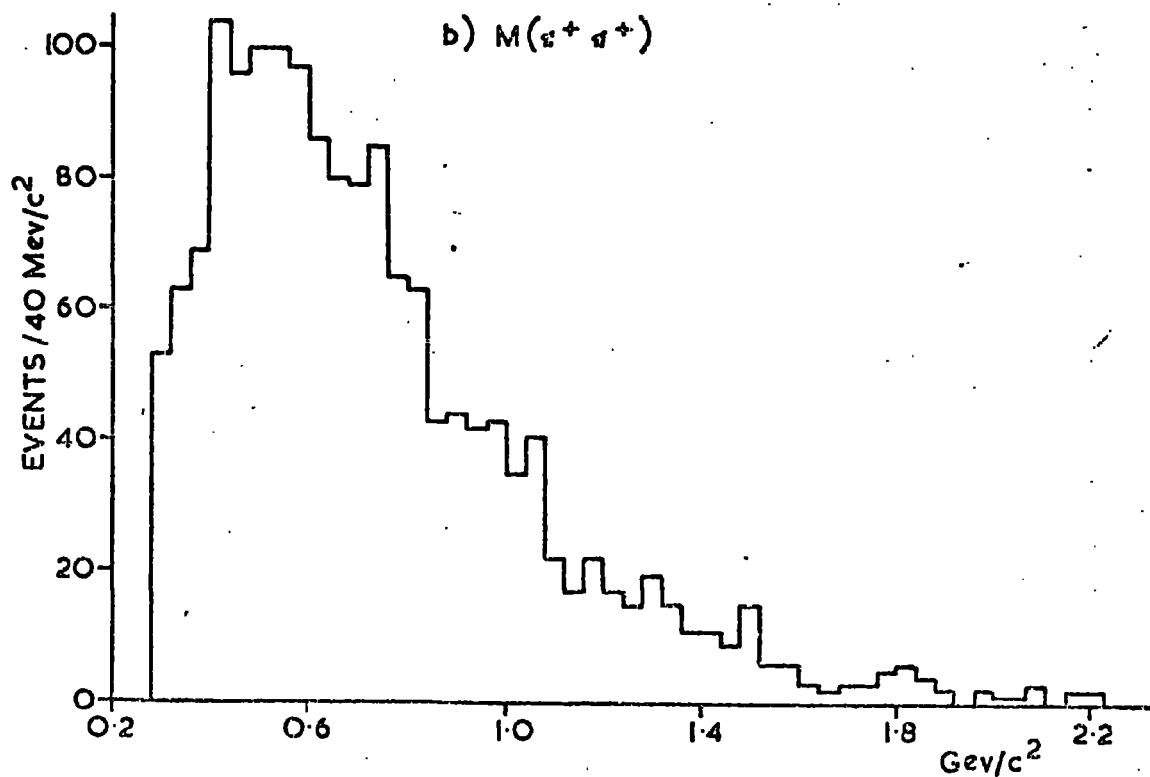
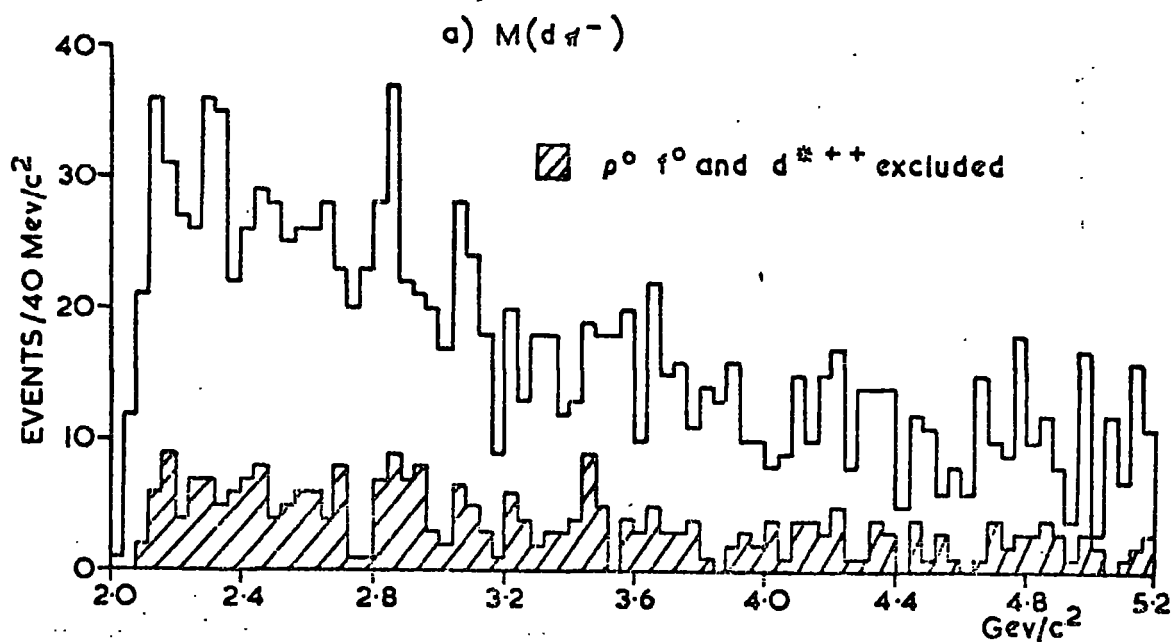
This peak has been seen in many other coherent deuteron experiments and is usually known as the d^{*++} (Ref. 4.1). It is not interpreted as a resonance of the pion-deuteron system, however, and a model to explain its production mechanism will be discussed in Chapter 8.

4.3 The $d\pi^-$ mass spectrum

The effective mass distribution of the $d\pi^-$ combination is shown in figure 4.4 (a). There is no clear evidence for any structure, merely a broad maximum from 2.0 to 3.0 GeV/c^2 followed by a gradual tailing off. There is no evidence for a neutral enhancement (d^{*0}) to correspond to the d^{*++} observed in the previous section.

As will be seen later there is a great deal of ρ^0 and some f^0 production in this channel, both of which will contribute only background to this spectrum. The d^{*++} will also lead to background in this distribution, so, if any d^{*0} is produced it may be hidden in the high background level. The hatched histogram in fig. 4.4 (a) shows the $d\pi^-$ spectrum when there is no simultaneous production of ρ^0 ($0.665 < M(\pi^+ \pi^-) < 0.865 \text{ GeV}/c^2$), f^0 ($1.12 < M(\pi^+ \pi^-) < 1.36 \text{ GeV}/c^2$) or d^{*++} ($M(d\pi_s^+) < 2.4 \text{ GeV}/c^2$). The remaining statistics are severely limited but still there is no evidence for a d^{*0} signal and it is concluded that production of d^{*0} does not occur.

FIG 4.4



4.4 The $\pi^+\pi^+$ mass spectrum

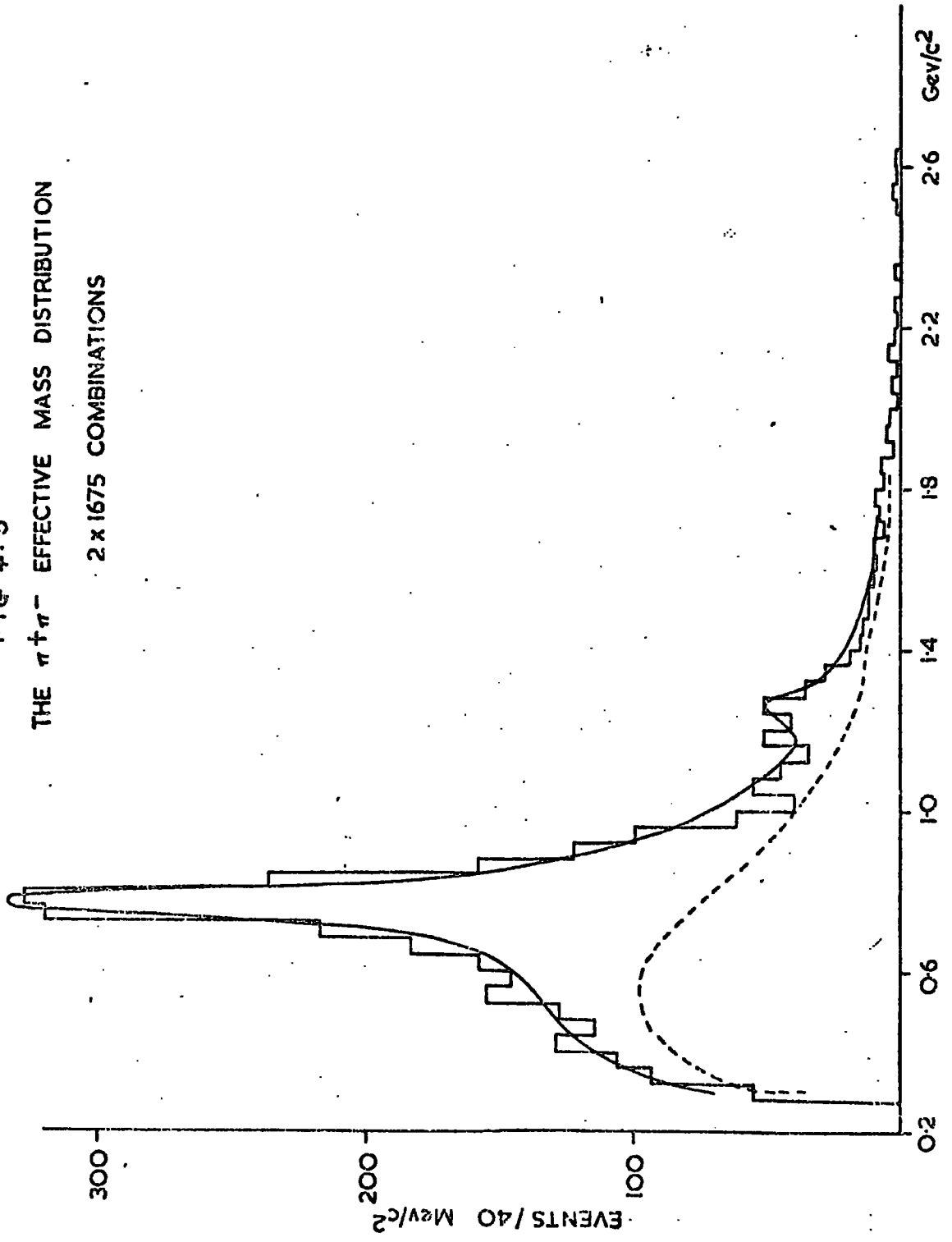
This distribution is shown in figure 4.4 (b). Its shape is quite smooth and there is no evidence of any narrow enhancements whether of kinematic or dynamic origin.

4.5 The $\pi^+\pi^-$ mass spectrum

The invariant mass distribution of the $\pi^+\pi^-$ system is shown in figure 4.5, where both neutral dipion combinations have been plotted for each event. The main feature of this spectrum is the very strong ρ^0 signal. There is also some indication of f^0 production, but there is no evidence for any higher mass dipion resonances such as the g^0 .

Since two dipion combinations are plotted for every event, even if every event has a dipion resonance in the final state there will be 50% background in figure 4.5. In fitting Breit-Wigner functions to the spectrum it is necessary to know the shape of the background distribution. It has been assumed that the background will have the same shape as the $\pi^+\pi^+$ spectrum since that contains no resonances and is subject to all the kinematical effects (such as resonance production in the 3-pion system and reflections of the d^{*++} enhancement) as is the $\pi^+\pi^-$ background. A smooth curve drawn through the $\pi^+\pi^+$ spectrum (shown in figure 4.5 as the dashed curve) was therefore taken as the background shape. The advantages of this procedure is that the shape is determined directly from the data and is in no way model dependent, the only assumption involved being that in the absence of resonance production the $\pi^+\pi^-$ and $\pi^+\pi^+$ distributions are identical. A possible objection to this assumption arises from the fact that the distribution of the angle between the beam pion and the positive pion resulting from the ρ^0 , in the ρ^0 reference frame is asymmetric, as will be seen in chapter 6; if the other positive pion has a preference for one direction in this frame, a difference between the $\pi^+\pi^+$ and $\pi^+\pi^-$ background will result and,

FIG 4.5
THE $\pi^+\pi^-$ EFFECTIVE MASS DISTRIBUTION
2 x 1675 COMBINATIONS



since there is clearly strong ρ^0 production, this difference could be significant. To check this possibility the cosine of the angle between the two positive pions in the ρ^0 rest system has been examined. An asymmetry in the distribution of this angle would imply that the assumption made was incorrect. The distribution is shown in figure 4.6 (a), where if both $\pi^+\pi^-$ masses fall in the ρ^0 region ($0.665 < M(\pi^+\pi^-) < 0.865 \text{ GeV}/c^2$) both angles have been plotted weighted by a factor of $\frac{1}{2}$. The distribution is almost isotropic and there is no obvious asymmetry. It is concluded that the assumption made is valid.

The spectrum of figure 4.5 has been fitted, by the method of minimising χ^2 , to the function:

$$N_{\text{pre}}^{(i)} = a \cdot \text{BW}^{(i)}(\rho) + b \cdot \text{EW}^{(i)}(f) + (\text{Tot} - a - b) \cdot \text{BG}^{(i)} \quad 4.4$$

where $N_{\text{pre}}^{(i)}$ = predicted number in the i^{th} bin

Tot = total number of combinations in the spectrum

$\text{BG}^{(i)}$ = fraction of the background in the i^{th} bin defined such

that:

$$\sum_i \text{BG}^{(i)} = 1 \quad 4.5$$

and the summation runs over all bins.

a = total number of ρ^0 's produced

b = total number of f^0 's produced.

$\text{BW}^{(i)}(\rho)$ is predicted fraction of ρ^0 's in the i^{th} bin according

to the relativistic P-wave Breit-Wigner functions:

$$\text{BW}^{(i)}(\rho) = \frac{\Gamma(m)}{(m^2 - m_0^2)^2 + m_0^2 \Gamma^2} \cdot \frac{m}{q} \quad 4.6$$

where

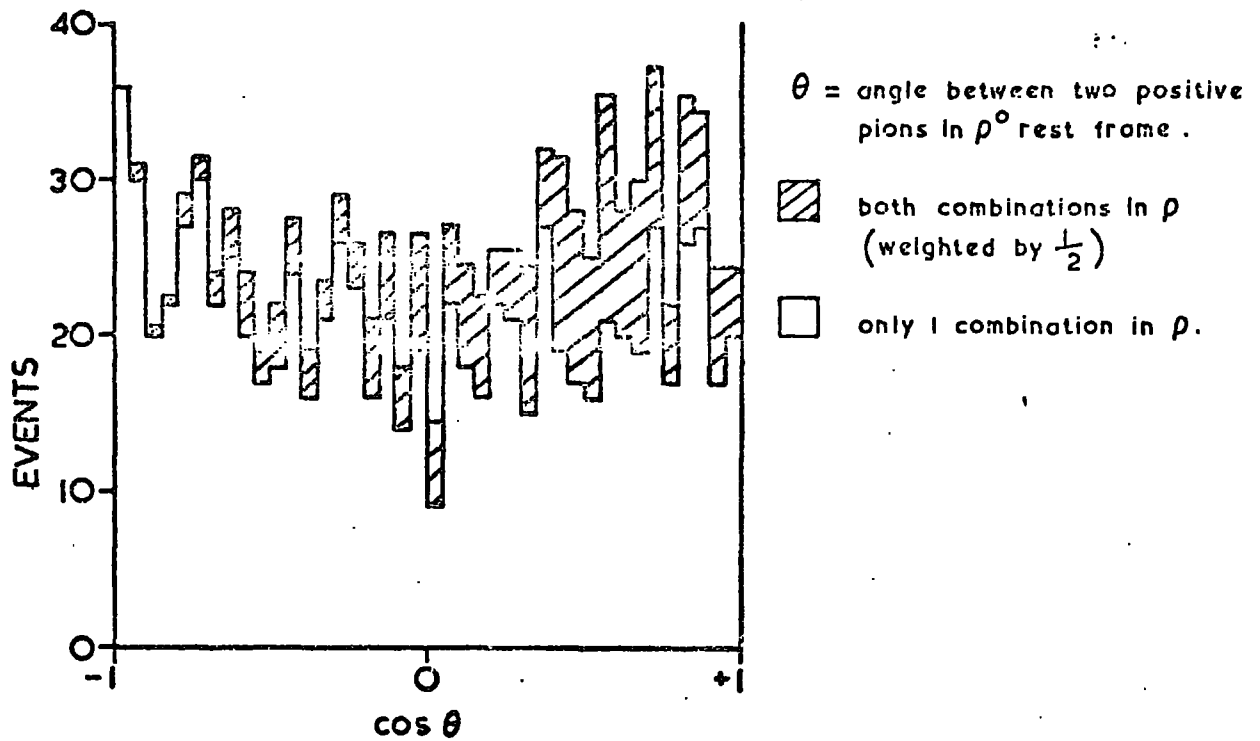
m = dipion mass at centre of i^{th} bin

m_0 = central ρ^0 mass

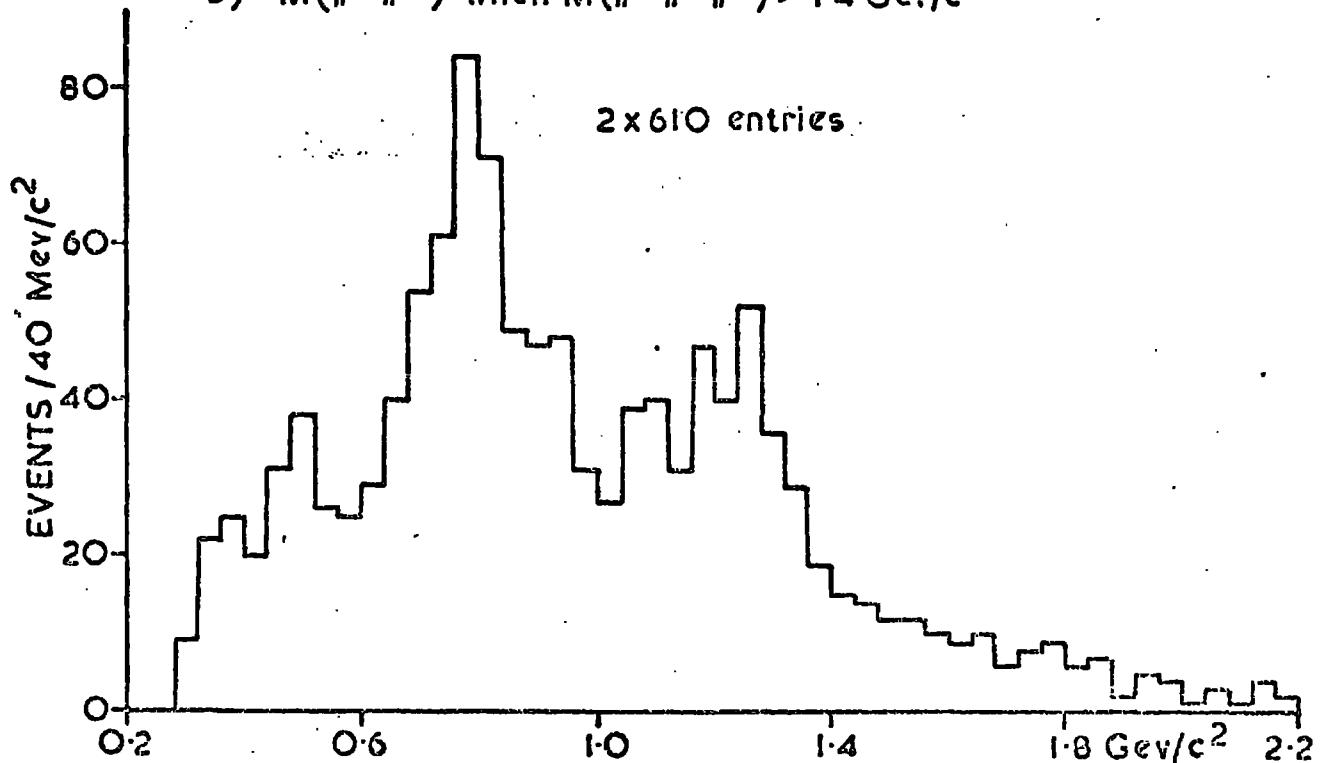
$$\Gamma(m) = \Gamma_0 \left(\frac{q}{q_0} \right)^3 \frac{\rho(m)}{\rho(m_0)} = \text{the mass dependent width} \quad 4.7$$

FIG 4.6

a) $\cos \theta$ distribution of ρ^0 events



b) $M(\pi^+\pi^-)$ when $M(\pi^+\pi^+\pi^-) > 1.4 \text{ GeV}/c^2$



and $\Gamma = \rho^0 \text{ width} = \Gamma(m_0)$
 $q =$ pion momentum in dipion rest frame
 $q_0 =$ value of q at $m = m_0$

and the $\rho(m)$ are rather arbitrary slowly varying functions given by Jackson (ref. 4.2) as:-

$$\rho(m) = m^{-1} \quad 4.8$$

The factor m/q in equation 4.6 is introduced to reduce the 4-body phase space to 3-body phase space. Due to lack of statistics in the f^0 region an s-wave non relativistic form of the Breit-Wigner function (Eq. 4.3) was used for $BW^{(i)}(f)$. Both $BW^{(i)}(\rho)$ and $BW^{(i)}(f)$ were normalised as:-

$$\sum_i BW^{(i)}(\text{res}) = 1 \quad 4.9$$

The fitted parameters were the central mass values of the ρ^0 and f^0 mesons together with their widths and the total number of each (a and b). Since the fit was performed on the spectrum in $40 \text{ MeV}/c^2$ bins the Breit-Wigner functions were integrated numerically over the bin in the fitting in order not to produce any distortion in the regions where they are quickly varying. Overall normalisation is built into the function.

The result of the fit is shown as the solid curve in fig. 4.5. The fit in the higher statistics region (up to $1 \text{ GeV}/c^2$) is excellent but above this, and particularly in the f^0 region the fit is poor. This is due partly to the poor shape of the f^0 produced in this experiment but may also be due to errors in the background estimation or an overestimation of the tail of the ρ^0 , as may occur if an incorrect form for the mass dependent width of the ρ^0 has been used (Note that the fit overestimates the number of events in the range $0.96 - 1.04 \text{ GeV}/c^2$). The f^0 parameters found in this fit are, therefore, unreliable and have large errors; a more reliable estimation of these will be made later.

The ρ^0 fit is excellent and the fitted parameters are:

$$M_{\rho} = 762 \pm 4 \text{ MeV}/c^2$$

$$\Gamma_{\rho} = 116 \pm 8 \text{ MeV}/c^2$$

Number of ρ^0 's = 1078 ± 50 .

The cross section for ρ^0 production is thus $\sigma = 227 \pm 20 \mu\text{b}$. No significant difference in the number of ρ^0 's produced relatively in the 3 and 4 prong samples is seen.

In figure 4.5 the signal in the f^0 region is not very prominent. In order to see it more clearly, figure 4.6 (b) shows all $\pi^+\pi^-$ combinations for events where the three pion effective mass is greater than $1.4 \text{ GeV}/c$ i.e above threshold for f^0 production. The effect of this is to greatly reduce the ρ^0 signal and thus to enhance the f^0 . Fits of the type of Eq. 4.3 have been attempted to this spectrum and the results for the f^0 parameters are:

$$M_f = 1235 \pm 15 \text{ MeV}/c^2$$

$$\Gamma_f = 130 \pm 20 \text{ MeV}/c^2$$

Number of f^0 's = 120 ± 30

corresponding to a cross section of $25 \pm 6 \mu\text{b}$, where this is calculated assuming that no f^0 production occurs in the 3 prong data, as indicated by the data. The fit in the f^0 region is poor again and the fitted value of the mass is $\sim 30 \text{ MeV}/c^2$ smaller than the currently accepted value (Ref. 4.3). These features can be explained partly by the presence in fig. 4.6 (b) of the small bump at $\sim 1080 \text{ MeV}/c^2$. This is also present in fig. 4.5 (b) although the fit there suggests that it is due to the tail of the ρ^0 . While this bump is small and may easily be statistical in origin, it is interesting to note that its central mass value and width ($\sim 80 \text{ MeV}/c^2$) are identical with those of a previously reported dipion enhancement known as the $\eta_{\text{N}}(1080)$ meson (Ref. 4.4). Further discussion of this signal will be deferred until

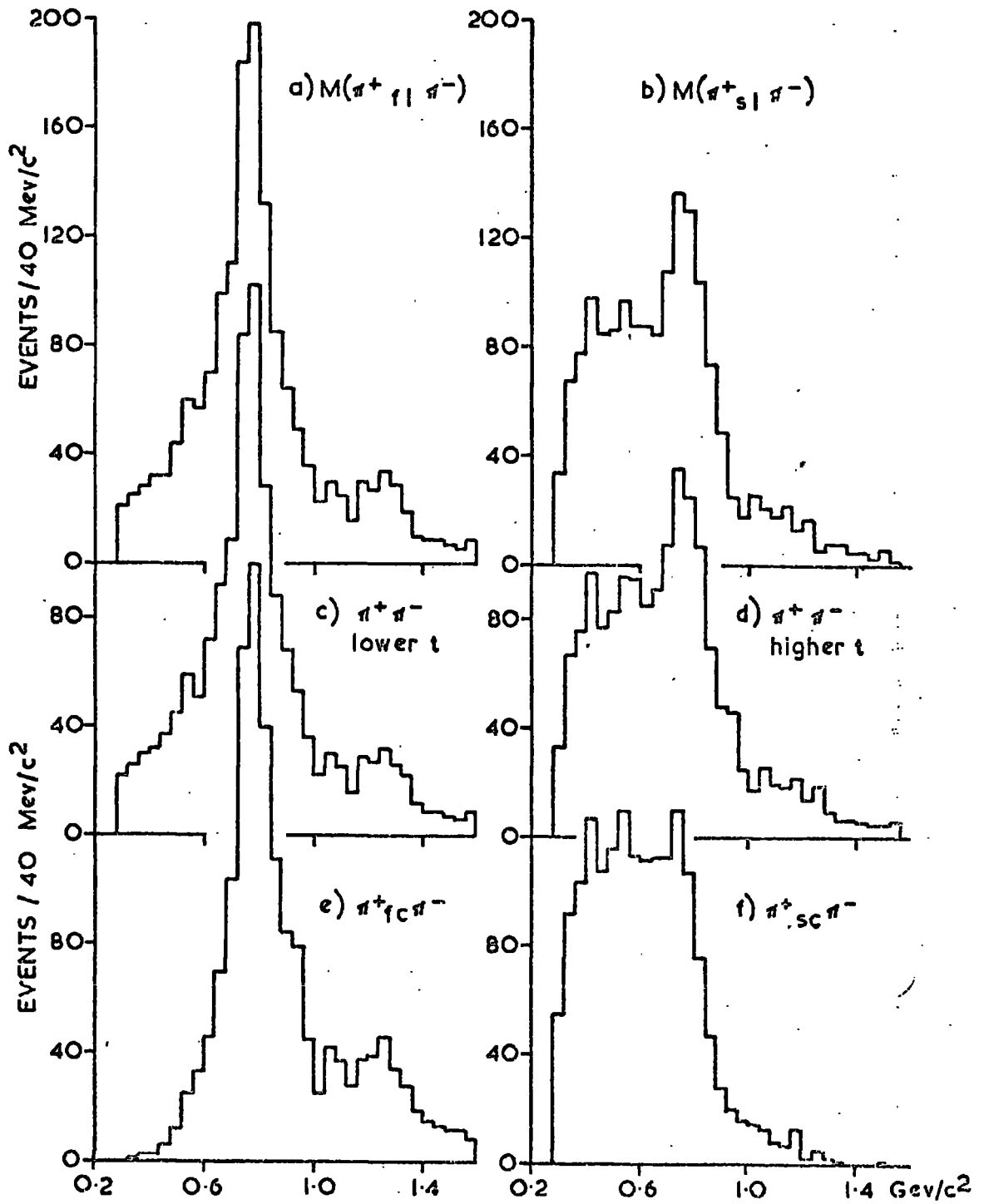
Chapter 6.

When considering dipion properties, it would clearly be advantageous if the background below the signal could be reduced. This can be done by using some criterion for distinguishing between the two positive pions, as can be seen in figure 4.7 which shows the $\pi^+ f \pi^-$ and $\pi^+ s \pi^-$ combinations, (4.7(a) and (b) respectively) where $\pi^+ f$ and $\pi^+ s$ refer to the π^+ with greater and smaller momentum in the lab system, and the $\pi^+ \pi^-$ combination formed with smaller (4.7c) and greater (4.7d) momentum transfer from the beam, and, finally, the $\pi^+ fc \pi^-$ and $\pi^+ sc \pi^-$ combinations (4.7e and f) where fc and sc refer to the greater and smaller momentum in the rest system of the 3-pions. The effects of labelling the pions by their laboratory momentum and t to the dipion system are very similar; they result in a strong clearance of background in both the ρ^0 and f^0 regions in one combination, although a distinct ρ^0 signal and a possibility of an f^0 signal remains in the other combination. The best differentiation between resonant signal and background occurs when distinguishing between the positive pions by their momenta in the 3-pion rest system, but, even here, some possibility of ρ^0 production in the "wrong" combination cannot be ruled out.

The reduction in background in fig. 4.7 (a),(c) and (e) is useful for the determination of the mass and width of the resonances without so much dependence on the form of the background used, but not so useful for determining their production cross sections because of the uncertainty in the number of resonant combinations in figs. 4.7 (b),(d) and (f). The results for the masses and widths (compatible from each sample) are:

$$\begin{aligned}
 M_{\rho} &= 764 \pm 3 \text{ MeV}/c^2 \\
 \Gamma_{\rho} &= 149 \pm 10 \text{ MeV}/c^2 \\
 M_f &= 1255 \pm 12 \text{ MeV}/c^2 \\
 \Gamma_f &= 131 \pm 10 \text{ MeV}/c^2.
 \end{aligned}$$

FIG 4.7



The f^0 parameters are here more in agreement with the currently accepted value. The width of the ρ^0 is here rather larger than that determined previously and compares well with the Particle Data Group estimate of $146 \pm 10 \text{ MeV}/c^2$.

A dependence of the width of the ρ^0 on t' from the beam to the dipion system was noted in the channel

$$\pi^+ d \rightarrow pp \pi^+ \pi^-$$

in this experiment (Ref. 2.8) and also in Ref. 4.5. No such dependence is observed in this channel, as can be seen in figure 4.8 which shows the dipion mass spectra for four regions of t' . Fits to these distributions indicate that the ρ^0 width is independent within errors of the t' region used. It can be seen that the background level increases as t' increases in both the ρ^0 and f^0 regions. The slopes of the $d\sigma/dt'$ distributions for ρ^0 events have been determined by maximum likelihood fits to the distributions of expressions of the type of Eq. 4.2 and the resulting parameters are:-

$$B_{\rho} = 7.7 \pm 0.7$$

$$B_f = 7.0 \pm 2.3$$

4.6 d^* and $d^* f$ associated production

Figure 4.9 shows the scatterplot of $M(d\pi^+s)$ vs $M(\pi^+ f \pi^-)$, where the labels f and s refer to the fast and slow positive pions in the laboratory system. This criterion has been used to distinguish between the positive pions since, as was seen in section 4.2 of this chapter, the d^{*++} is formed entirely with the π_s^+ defined in this way. In the scatterplot there is a distinct ρ^0 band and a less obvious f^0 band, in both of which there is an accumulation of events in the region of overlap with the d^{*++} . There is little evidence for a d^* band in the figure; the accumulation of events in the d^* region of the projection of this plot seems to come largely from the ρ^0 and f^0 overlap regions.

FIG. 4.8

DIPION MASS FOR VARIOUS REGIONS OF t' .

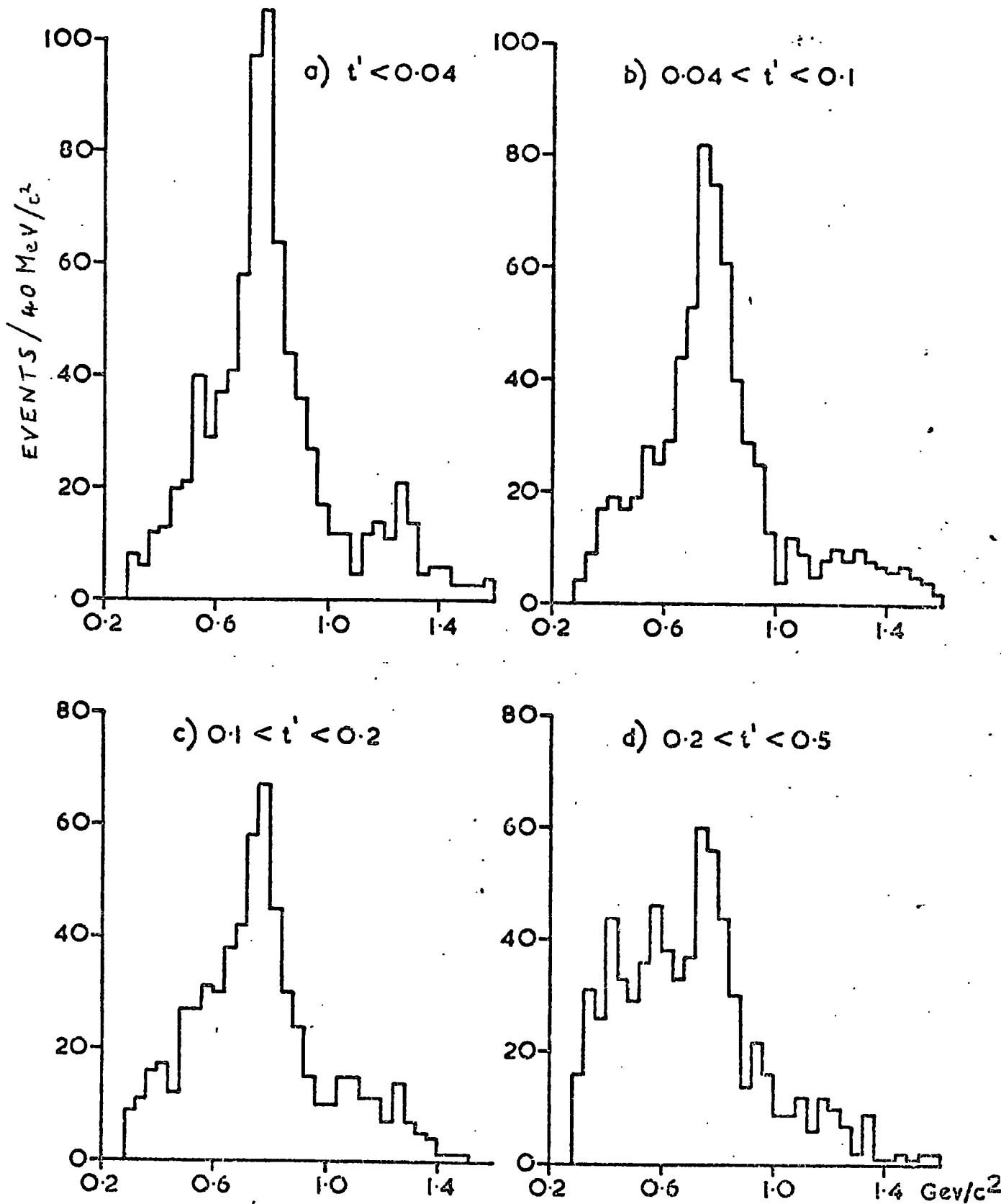


FIG 4.9

$M(d\pi^+)$ vs. $M(\pi^+\pi^-)$

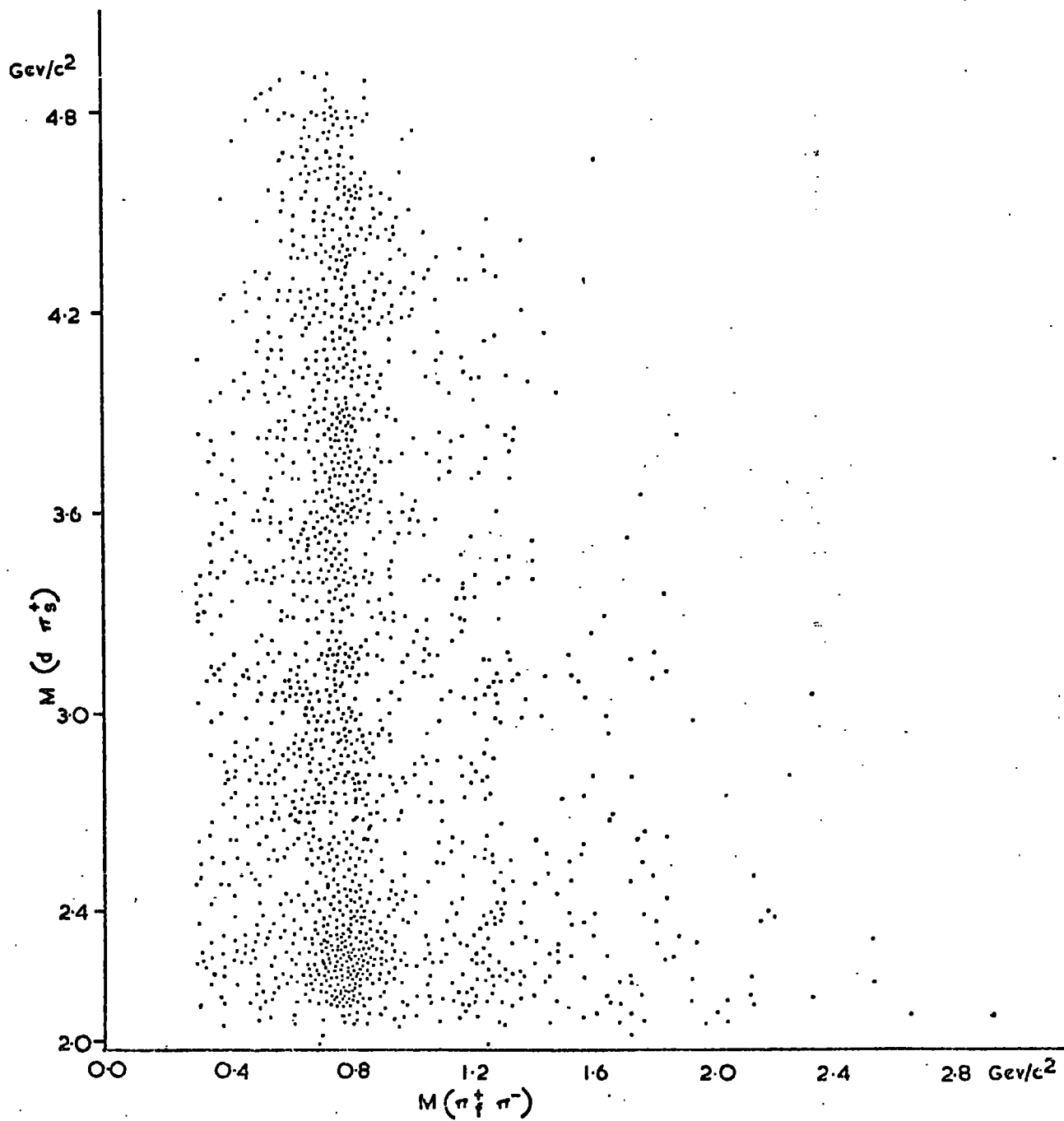


Figure 4.10 (a) shows the dipion mass spectrum ($\pi^+ f \pi^-$ only) for events in the d^* region, while figs. 4.10(b) and (c) show the $d\pi_s^+$ mass spectrum for events with $M(\pi_f^+ \pi^-)$ in the ρ^0 and f^0 regions respectively. Clear ρ^0 and f^0 signals are present when $M(d\pi_s^+)$ is in the d^* region, while a clear d^* signal is seen for $M(\pi_f^+ \pi^-)$ in the ρ^0 region. There is also an indication of a d^* signal when $M(\pi_f^+ \pi^-)$ is in the f^0 region. From these projections, and from the scatterplot an estimate can be made of the number of events corresponding to associated production of $d^* \rho$ and $d^* f$ final states by making estimates of the background below the relevant signals. This method is rather rough and the resulting errors are rather large. The results are:

$$\pi^+ d \rightarrow d^* \rho : 143 \pm 25 \text{ events: } \sigma = 30 \pm 5 \mu\text{b}$$

$$\pi^+ d \rightarrow d^* f : 28 \pm 10 \text{ events: } \sigma = 6 \pm 2 \mu\text{b}$$

and this implies that 75% of d^{*++} produced in this channel is produced in association either with a ρ^0 or an f^0 meson.

4.7 The $\pi^+ \pi^+ \pi^-$ spectrum

The distribution of the three pion combination is shown in figure 4.11. The main features of this spectrum are a strong broad enhancement in the mass range $0.95 - 1.35 \text{ GeV}/c^2$, followed by a weaker enhancement in the region $1.5 - 1.9 \text{ GeV}/c^2$.

The former of these enhancements encompasses the mass region where both the A_1 meson (Mass $\sim 1100 \text{ MeV}/c^2$) and the A_2 region (Mass $\sim 1300 \text{ MeV}/c^2$) may occur. There is no evidence, however, for two distinct peaks and the central mass $\sim 1120 \text{ MeV}/c^2$ and the approximate width ($\sim 300 \text{ MeV}/c^2$) suggests that the effect may be due entirely to A_1 production. This is true also when only 4 pronged events are considered (hatched histogram in fig. 4.11) and this sample, being the result of 4-G fits, has a mass resolution substantially smaller than the bin-width used in the figure. If A_2 production occurs in this channel, then its cross section is markedly

FIG 4.10

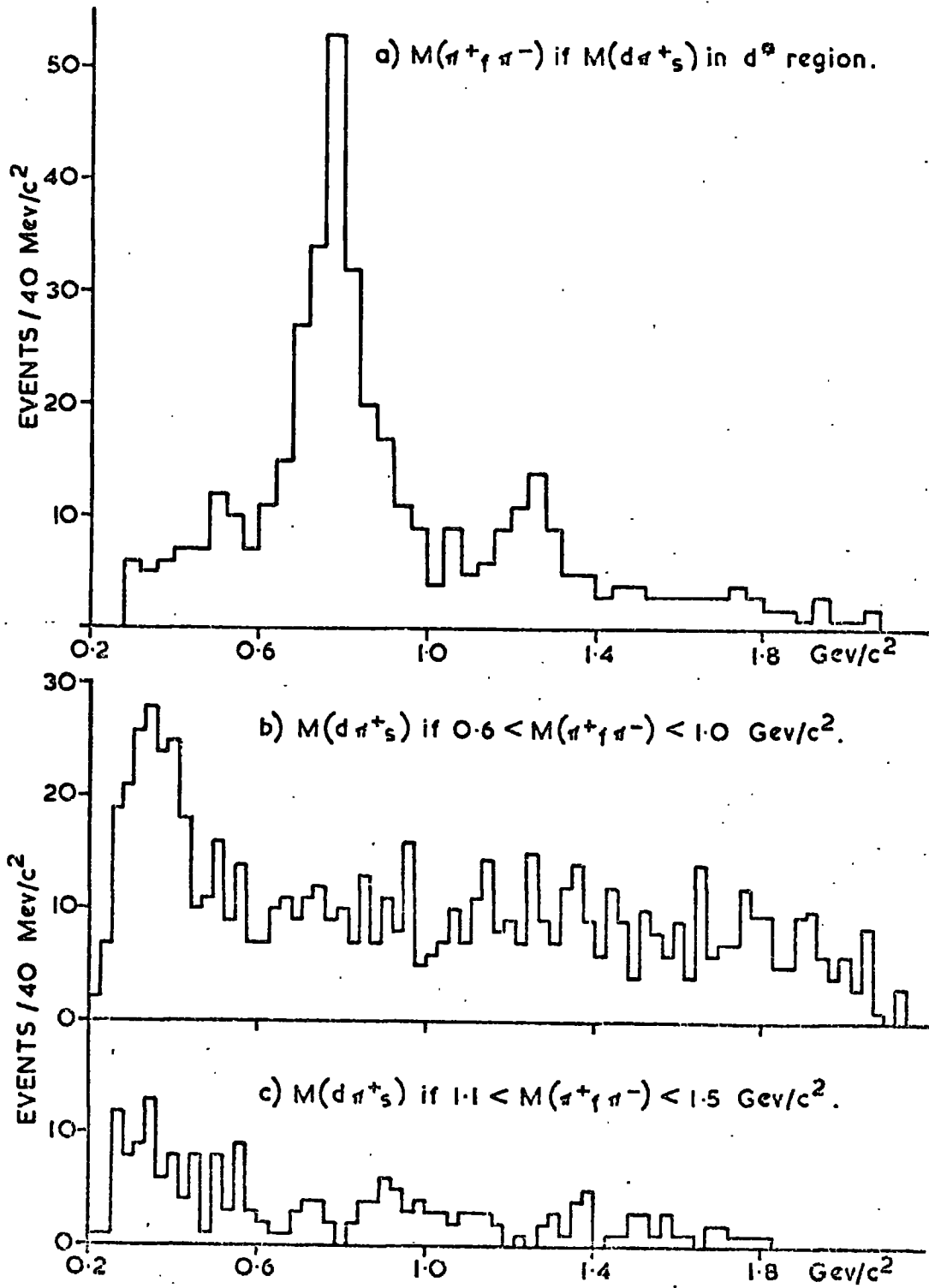
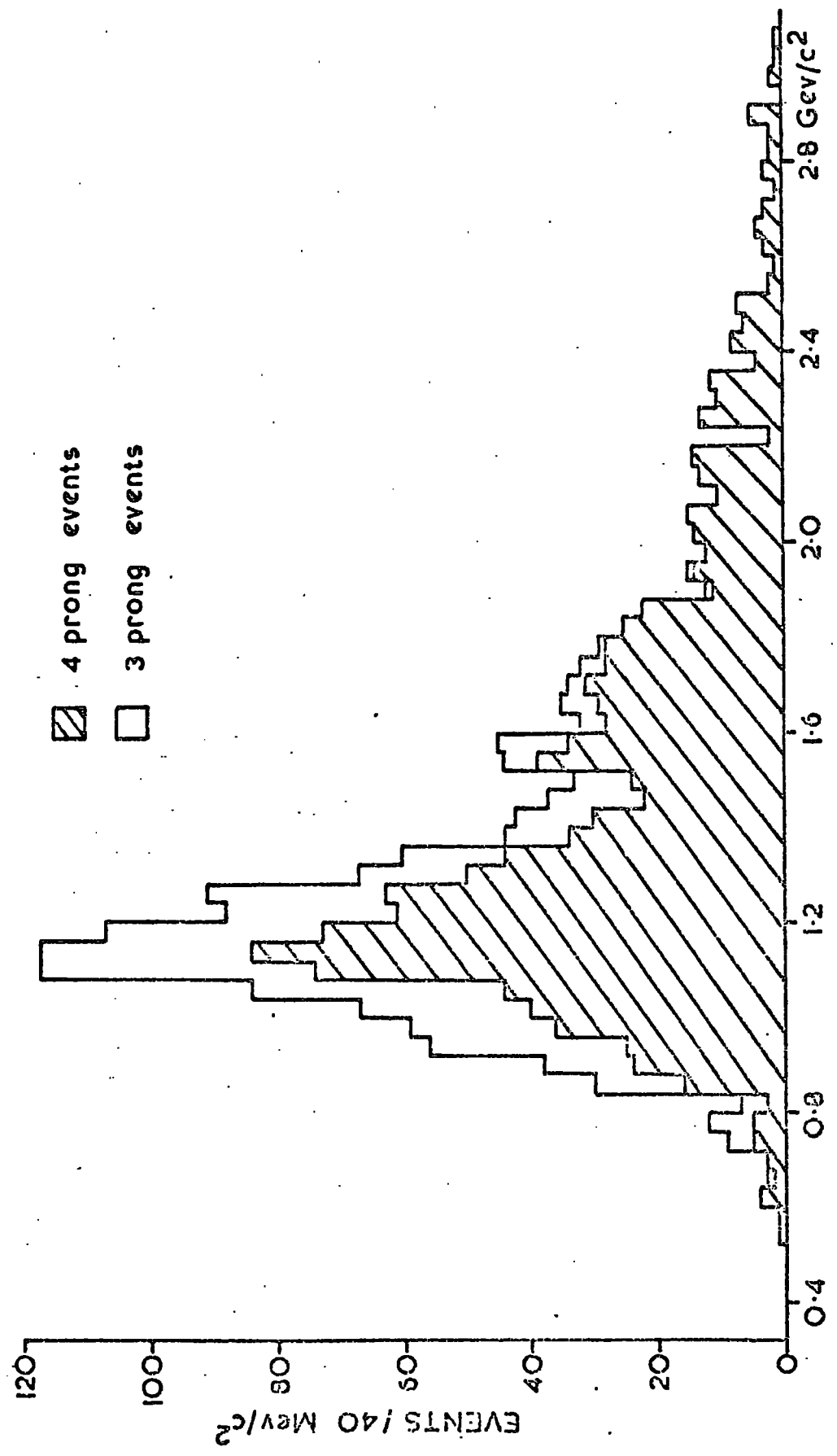


FIG 4.11
EFFECTIVE MASS OF THE $\pi^+\pi^+\pi^-\pi^-$ SYSTEM.



smaller than that for A_1 production. Chapter 9 gives the results of a search for A_2 production.

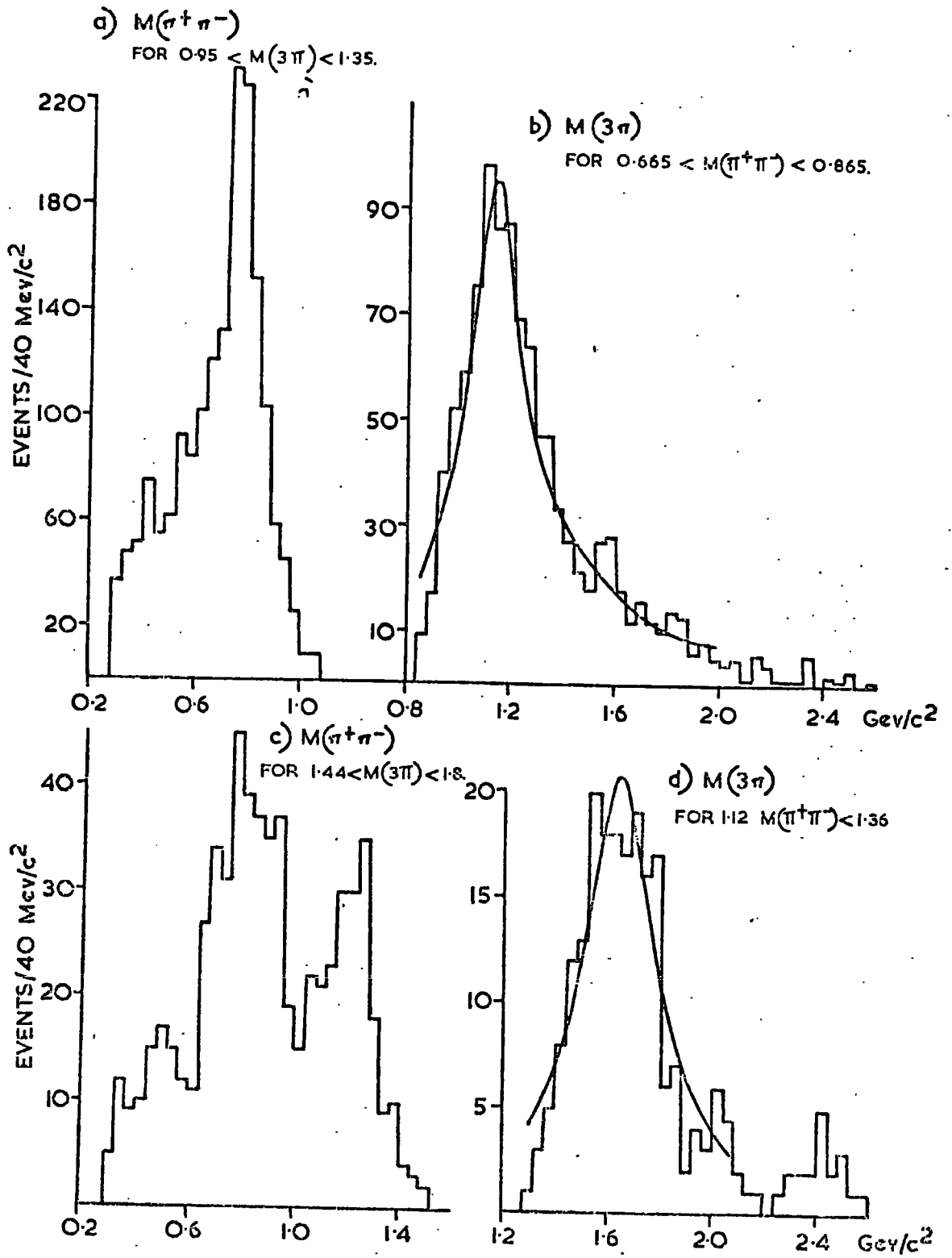
The higher enhancement has a central mass $\sim 1.7 \text{ GeV}/c^2$ which is in the region of the A_3 meson. The width is difficult to determine from this distribution since the shape of the background is unknown, but it seems to be in the range $300\text{-}400 \text{ MeV}/c^2$. As can be seen from the figure, the enhancement occurs only in the four prong sample. This is because t_{\min} from beam to 3 π 's is quite high in this mass region and 3 prong events necessarily have very small values of t .

The dipion mass spectrum for events in the A_1 region is shown in figure 4.12 (a) and shows that the A_1 meson decays dominantly into $\rho\pi$. This distribution is compatible with 100% decay of the enhancement into the two body channel $\rho\pi$. This fact is emphasised in figure 4.12 (b) where the three pion mass is plotted for all events which have a neutral dipion mass in the ρ^0 region. ($0.665 < M(\pi^+ \pi^-) < 0.865 \text{ GeV}/c^2$). It shows that ρ^0 events account entirely for the A_1 enhancement.

Figure 4.12 (c) shows the dipion mass spectrum for events in the A_3 region (defined here as $1.44 - 1.8 \text{ GeV}/c^2$). There is a strong ρ^0 and strong f^0 signal in this distribution. The ρ^0 signal does not imply a $\rho^0\pi$ decay mode of the A_3 , however, as can be seen from fig. 4.12 (b) where no peak in the A_3 region is apparent in the $\rho^0\pi$ system. In fact, the A_3 enhancement is very much correlated with f^0 production, as is clear from fig. 4.12 (d) which shows the $f^0\pi$ mass spectrum (f^0 defined as $1.12 < M(\pi^+ \pi^-) < 1.36 \text{ GeV}/c^2$). This distribution consists of a broad enhancement near threshold, followed by a small, featureless tail. With the present statistics no detailed calculations of the A_3 decay branching ratios are possible. Studies of the dipion mass spectra from various regions of 3-pion mass, however, indicate that the data is compatible with 100% decay into $f^0\pi$.

Fits of simple S-wave Breit-Wigner functions have been made to

FIG 4.12



the $\rho^0\pi$ mass spectrum and to the $f^0\pi$ spectrum. A linear background was assumed in both cases. The fitted parameters given were:-

$$\begin{aligned} M_{A_1} &= 1134 \pm 8 \text{ MeV}/c^2 \\ \Gamma_{A_1} &= 260 \pm 21 \text{ MeV}/c^2 \\ M_{A_3} &= 1636 \pm 15 \text{ MeV}/c^2 \\ \Gamma_{A_3} &= 335 \pm 43 \text{ MeV}/c^2 \end{aligned}$$

and the fitted curves are shown in figures 4.12(b) and (d) respectively. The fit to the A_1 is quite good, although the sharp rise and the slightly convex sides of the enhancement are not well described by the Breit-Wigner function. The fit to the A_3 is very poor: the steep sides and flat top of the enhancement are in contradiction with the predictions of a simple Breit-Wigner shape. Possible interpretation of these two peaks by Deck-type mechanisms will be discussed in chapter 8.

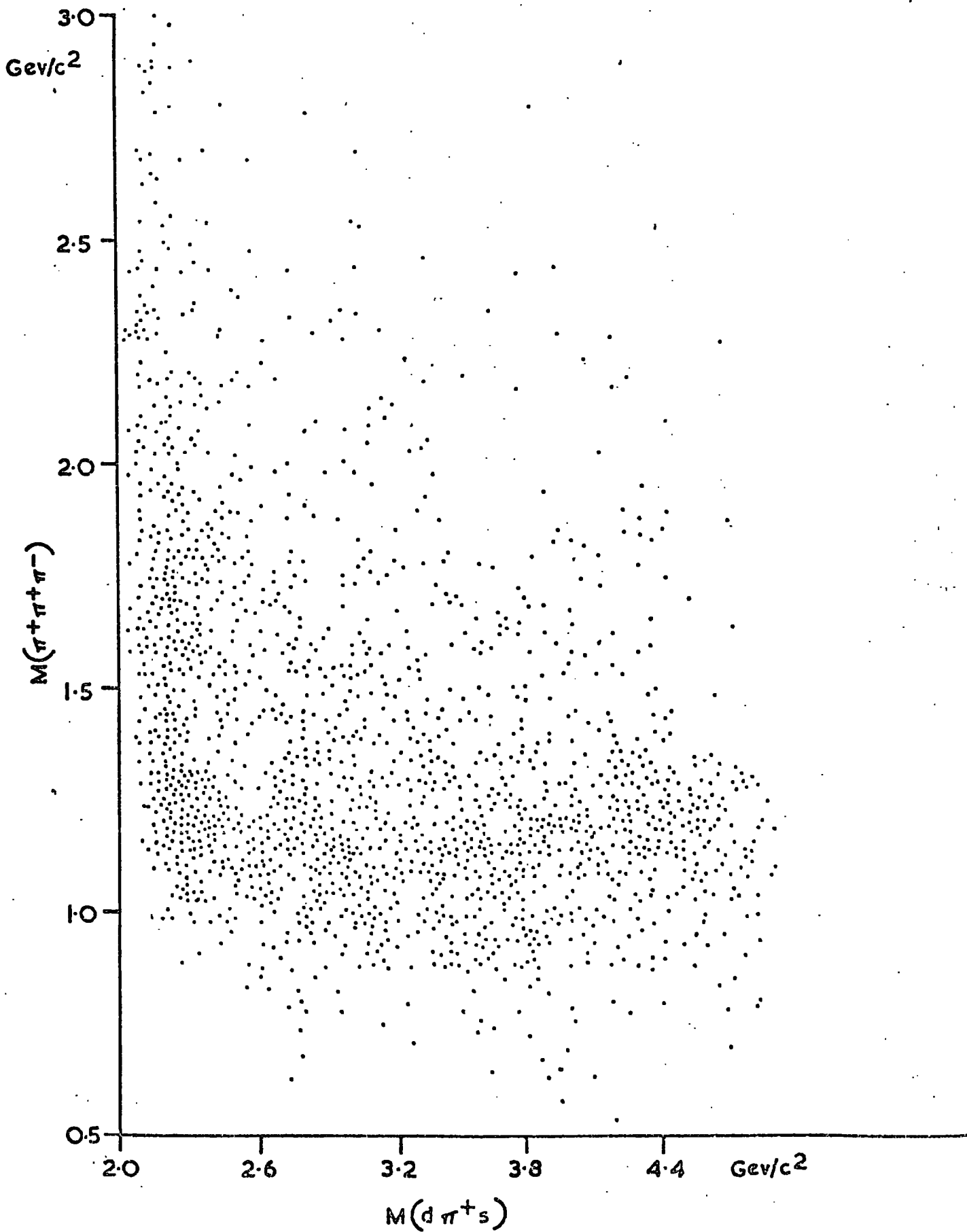
In figure 4.11 there is a small narrow peak in the mass range 1.52-1.6 GeV/c^2 which, though hardly statistically significant, can be seen to be due to $\rho^0\pi^+$ combinations in fig. 4.12 (b) and, thus is unlikely to be due to a statistical fluctuation of the A_3 signal, since the A_3 decays $f^0\pi^+$. This peak, which will hereafter be called the " $A_{2.5}$ " for reference purposes, without implying any resonant interpretation, has a central mass value $\sim 1560 \text{ MeV}/c^2$ and a width which is less than $80 \text{ MeV}/c^2$. More discussion of this effect is given in chapter 6, where examination of the decay angles of the " $A_{2.5}$ " shows that the peak is most unlikely to be resonant.

The slope of the $d\theta/dt$ distribution for events in the A_1 region has been determined as 34.8 ± 2.8 , while, for events in the A_3 region the corresponding figure is 29.4 ± 3.4 .

The effect of d^* production on the three pion spectrum can be seen in figure 4.13, which shows the scatterplot of the $d\pi_s^+$ effective mass vs. that of the three pions. The strong A_1 band on this plot overlaps

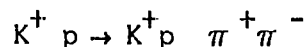
FIG 4.13

$M(3\pi)$ vs. $M(d\pi^+s)$

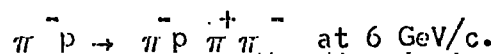


the d^* band only a little and d^* contamination of the A_1 signal is not very important. A weaker A_3 band is also apparent in this figure but here the overlap region with the d^* band is not so small. These effects can be seen in figures 4.14 (a) and (b) where the mass spectrum of the 3 pions is plotted separately for those events which have a d^* and those which do not. The vast majority of the A_1 signal is formed without a d^* while a clear A_3 signal is seen when d^* events are chosen. The A_3 signal cannot be explained as a kinematical reflection of the d^* , however, since there is A_3 production when d^* events are antiselected, particularly when a neutral dipion mass lies in the f^0 region, as can be seen in the hatched histogram of fig. 4.14 (a). The peak in the A_3 region for events with $M(d\pi^+)$ $< 2.4 \text{ GeV}/c^2$ is, therefore, probably due to A_3 production and must contribute to the background below the d^{*++} signal.

Since the main features of the three pion spectrum are an enhancement of the $\rho^0\pi$ system just above threshold and an enhancement of the $f^0\pi$ system just above threshold, it is possible that the whole spectrum can be explained by threshold enhancements of one dipion combination with the remaining pion. This continuous threshold enhancement effect was found to be the case in the reaction:

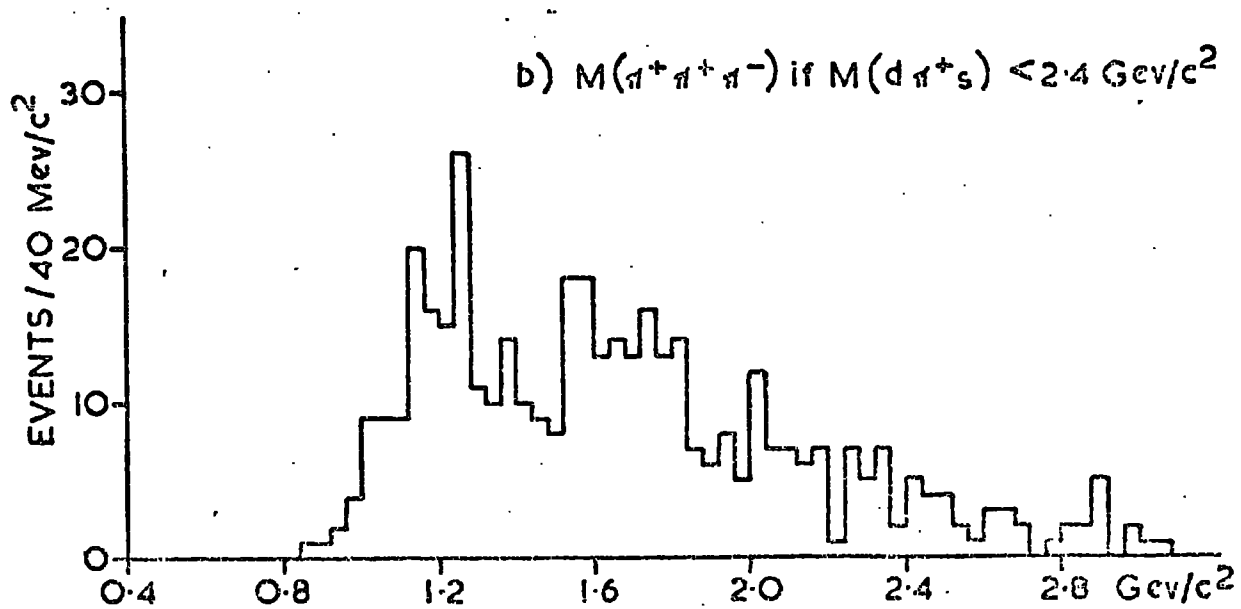
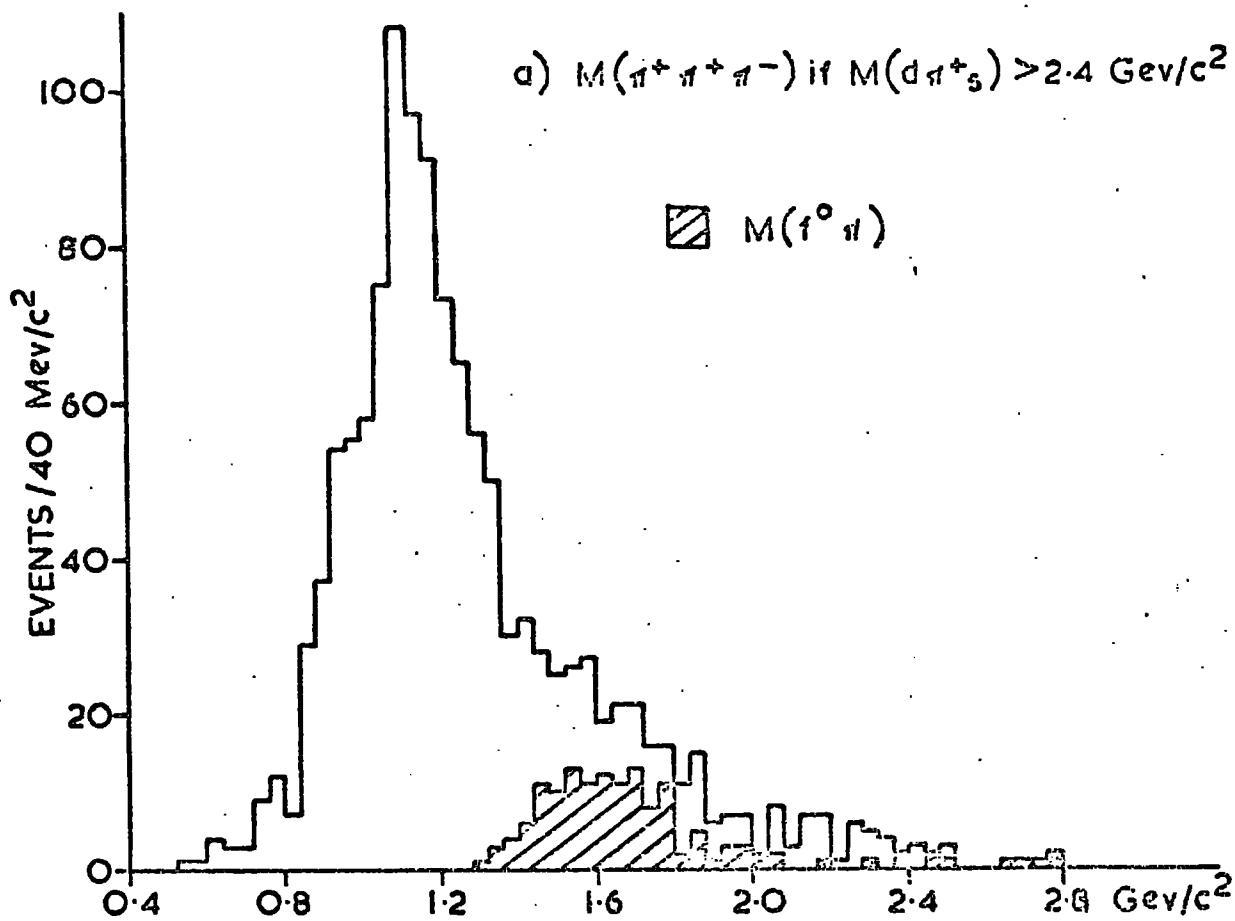


at 1.2 GeV/c incident momentum (Ref. 4.6). Crennel et al. (Ref. 4.7), however, in the reaction:



found that the 3-pion spectrum was not due to a threshold effect except in the A_1 and A_3 regions. In order to test whether the channel being studied here is of the continuous threshold type, it is necessary first to decide which dipion combination to study. Since the two threshold effects observed, the A_1 and the A_3 , are of a $\pi^+ \pi^-$ combination, it seems likely that other threshold effects will also be of this type.

FIG 4.14



The three pion mass spectra from various regions of $M(\pi^+\pi^-)$ are shown in figure 4.15. In these plots only events which have neither neutral dipion mass combination in the ρ^0 region have been used, since these events are known to contribute to the A_1 enhancement. There is no strong evidence that threshold effects are dominant: in the first region ($0.4 < M(\pi^+\pi^-) < 0.6 \text{ GeV}/c^2$) there is a peak at low 3π mass ($\sim 0.8 \text{ GeV}/c^2$), but this accounts only for a small fraction of the data (< 30%) and may be due to a diminution of events in the A_1 region, the second dipion mass range ($0.92 - 1.04 \text{ GeV}/c^2$) has a sharp peak at threshold which again accounts for <30% of the data and may be caused by the high mass tail of the A_1 , since this dipion mass region contains the high mass tail of the ρ^0 meson; at higher dipion masses there is no sign of threshold enhancements. It is concluded that, while for low dipion masses there may be a small amount of threshold enhancement in the three pion system, the effect is not so strong outside the ρ^0 and f^0 regions. The possibility of threshold enhancements of the $\pi^+\pi^+$ system has been examined and no evidence for the effect discovered. It seems, therefore, that the effect is only important when the dipion combination is in a definite spin-parity state.

A further point of interest in figure 4.15 is in the third dipion mass region ($1.04 - 1.12 \text{ GeV}/c^2$), which is the position of the small bump which was mentioned above and tentatively identified with the $\eta_N(1080)$ meson. This signal does not result in a threshold enhancement and in particular, it is by no means correlated with the tripion signal $\sim 1.56 \text{ GeV}/c^2$, the " $A_{2.5}$ ".

4.8 The $d\pi^+\pi^-$ and $d\pi^+\pi^+$ mass spectra

The remaining possible particle combinations $d\pi^+\pi^-$ and $d\pi^+\pi^+$ are shown in figure 4.16 (a) and (b) respectively. They have very similar shapes which show no sign of any dynamical effects. The peaking of both these distributions at very high mass reflects the strongly

FIG 4.15

$M(\pi^+\pi^+\pi^-)$ FOR SEVERAL REGIONS OF $M(\pi^+\pi^-)$
 ρ EVENTS EXCLUDED

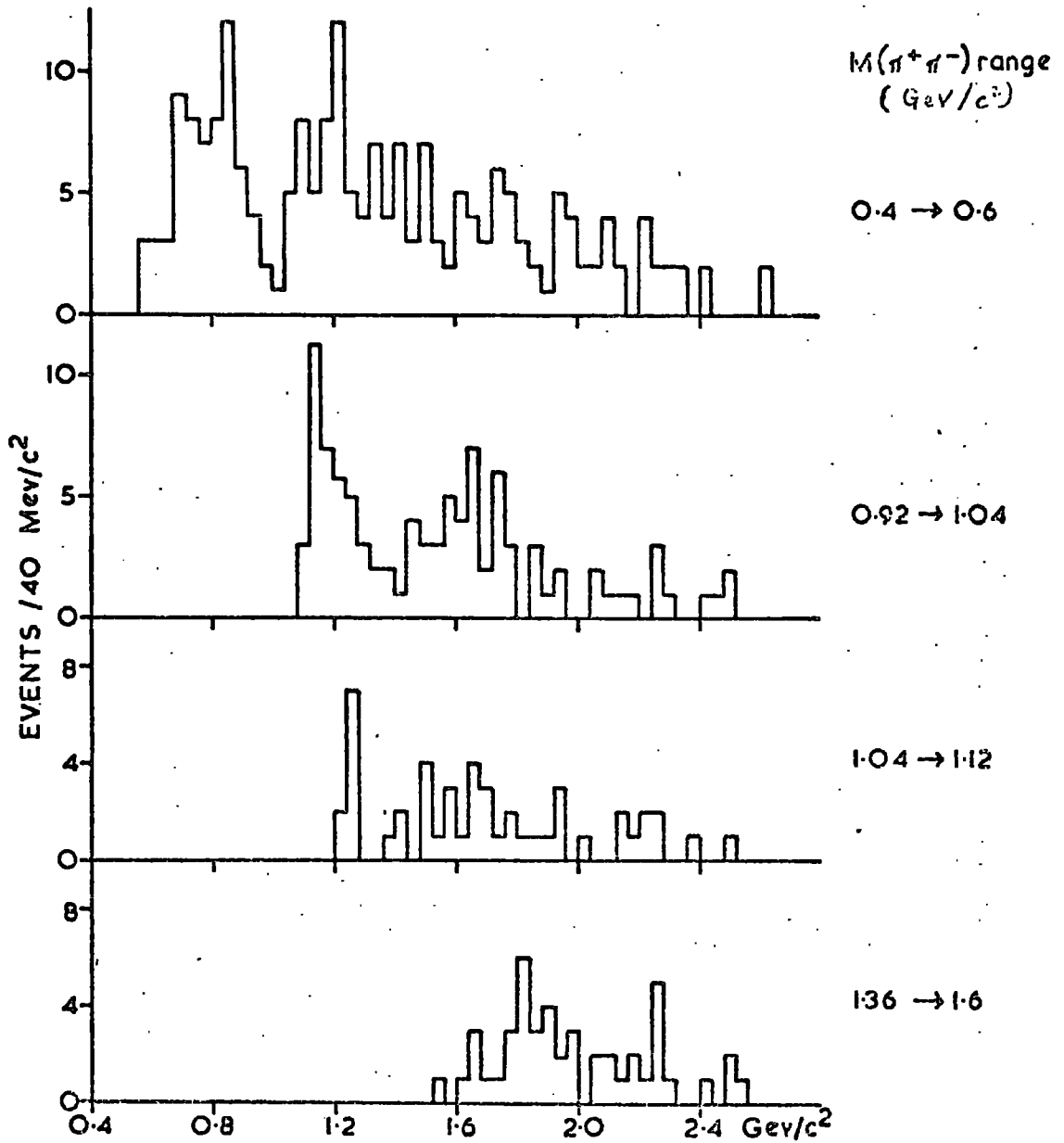
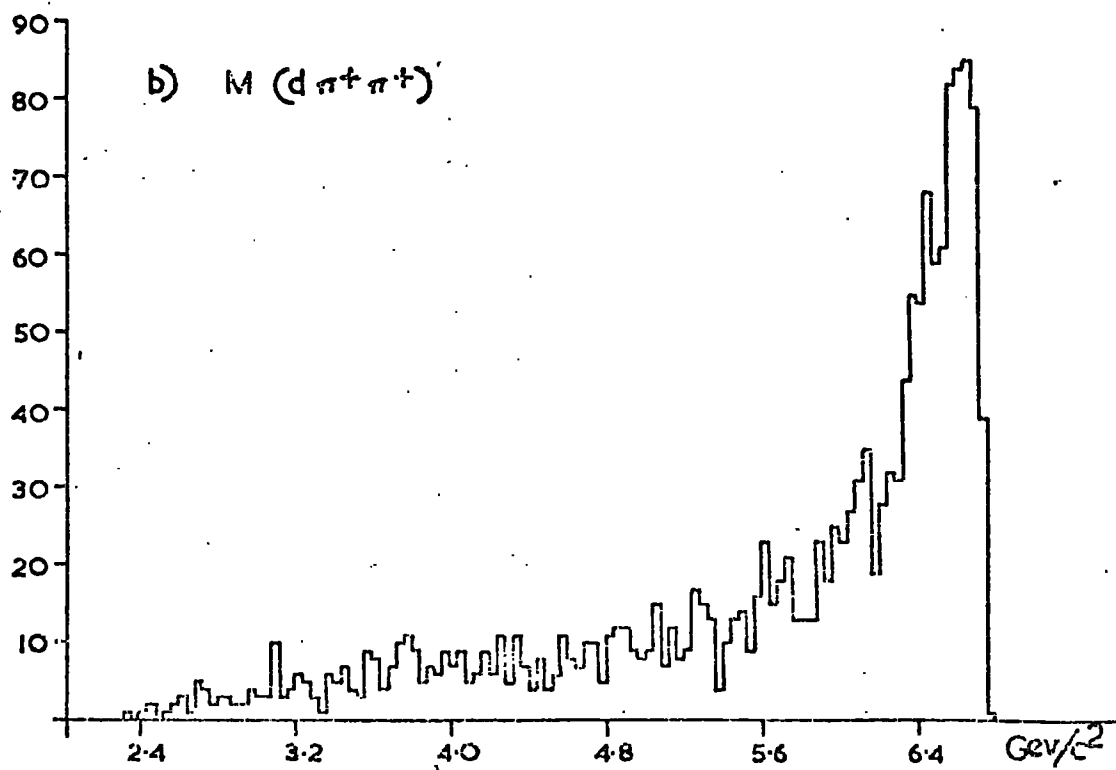
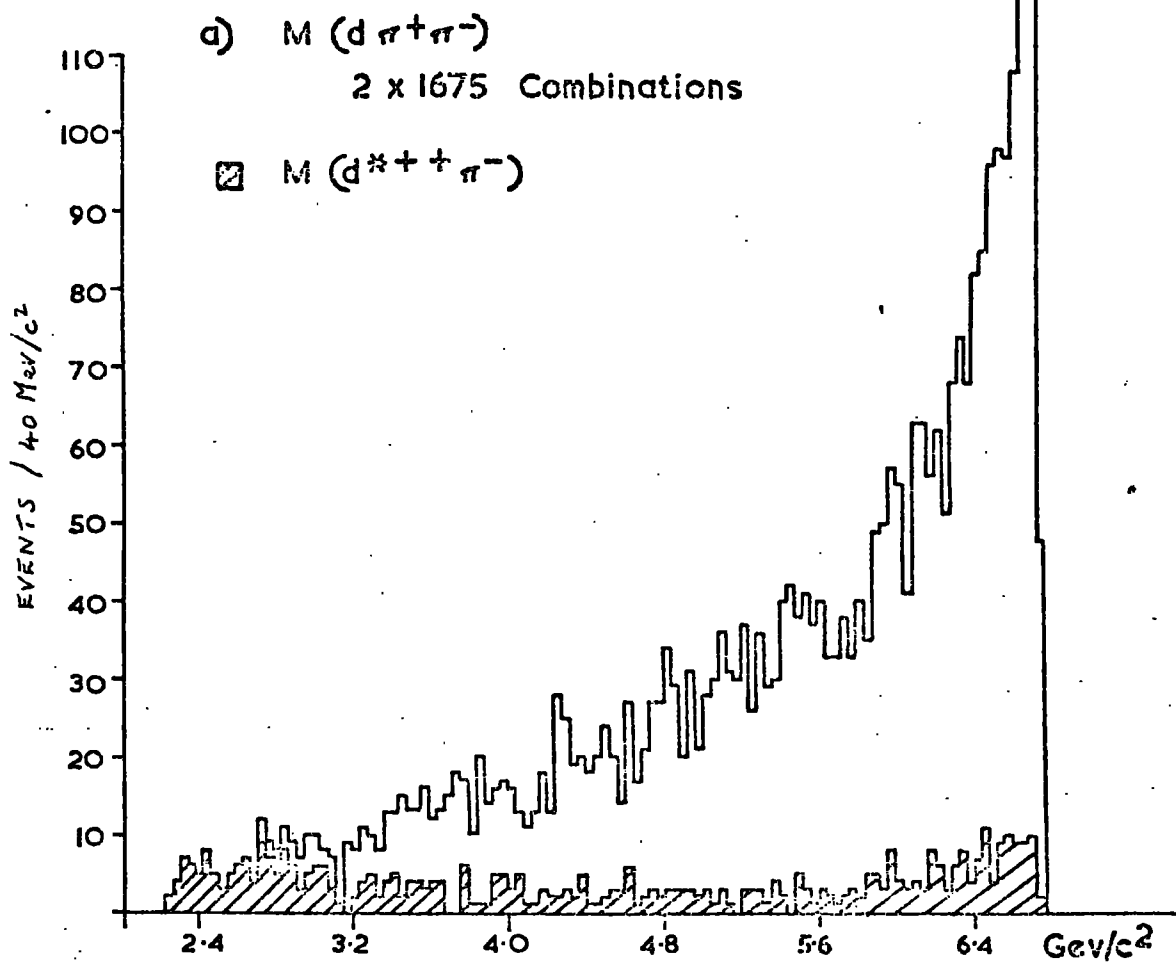


FIG 4.16



peripheral nature of the interaction.

Examination of the $d \rho^0$ and df^0 mass spectra, also shows no structure; their distributions are very similar to those in figure 4.16 (a). The result of combining d^{*++} with the π^- is shown in the hatched histogram of fig. 4.16 (a). This distribution shows a small accumulation of events at high mass and, perhaps, an accumulation in the low mass region ($< 3.2 \text{ GeV}/c^2$). The lack of statistics, however, prevent further study of this effect, except to comment that it is also present to some extent when the d^{*++} is combined with the remaining π^+ and this may indicate a kinematic origin.

4.9 Summary

The channel being studied is dominated by ρ^0 production, with some f^0 production. There is also an enhancement in the $d \pi^+$ mass spectrum $2.2 \text{ GeV}/c^2$, the d^* , which is often produced in association with the ρ^0 or f^0 meson. The cross sections for the various final states involving these combinations are contained in table 4.1. The three pion spectrum is dominated by a $\rho^0 \pi$ enhancement, the A_1 , and an $f^0 \pi$ enhancement, the A_3 , both produced just above threshold. The remainder of the 3 pion spectrum cannot be explained by threshold enhancements. The masses and widths of all these effects are summarized in table 4.2. In addition there is a small bump in the $\pi^+ \pi^-$ spectrum which may be identified with the $N(1080)$ meson, and an accumulation of $\rho^0 \pi^+$ events $\sim 1.56 \text{ GeV}/c^2$.

TABLE 4.1

Cross sections for the various final states

final state	N ^o of events	cross section (nb)	% of channel
$d\pi^+\pi^+\pi^-$	422	89 ± 21	24.7
$d\pi^+\rho^0$	935	197 ± 20	56.5
$d\pi^+f^0$	92	19 ± 6	5.3
$d^{*++}\pi^+\pi^-$	55	12 ± 9	3.3
$d^{*++}\rho^0$	143	30 ± 5	8.5
$d^{*++}f^0$	28	6 ± 2	1.7

TABLE 4.2

Parameters of Resonances and Enhancements produced

Resonance	Mass (MeV/c ²)	Width (MeV/c ²)	Decay Mode
ρ^0	764 ± 3	149 ± 10	$\pi^+\pi^-$
f^0	1255 ± 12	131 ± 10	$\pi^+\pi^-$
d^{*++}	~ 2210	~ 300	$d\pi^+$
A_1^+	1134 ± 8	260 ± 21	$\rho^0\pi^+$
A_3^+	1636 ± 15	335 ± 43	$f^0\pi^+$

C H A P T E R F I V E

LONGITUDINAL PHASE SPACE ANALYSIS

5.1 General Considerations

The purpose of studying an interaction is to discover by what mechanism or mechanisms the reaction occurs, or, more generally to discover the form of the transition matrix element M . The cross section for the interaction can be written:

$$\sigma = \frac{1}{P_{cm}} s^{-\frac{1}{2}} \int |M|^2 dV \quad 5.1$$

with
$$dV = \delta_3(\sum_i p_i) \delta(s^{\frac{1}{2}} - \sum_i E_i) \prod_i \frac{d^3 p_i}{E_i} \quad 5.2$$

where P_{cm} = the incident momentum in the centre of mass system

s = the square of the centre of mass energy

dV = the element of phase space

p_i = the centre of mass momentum of the i^{th} particle

E_i = the centre of mass energy of the i^{th} particle

and the summations and product run over all the i final state particles.

The matrix element M depends in general on the energy, momentum, spin etc. of the outgoing particles and for a many body final state, this leads to a plethora of variables and it becomes difficult to visualise the structure of M .

Some information on the form of M can be gained by study of invariant mass spectra and $\frac{d\sigma}{dt}$ distributions. For example, the lack of any structure in the $d\pi^-$ and $d\pi^+\pi^-$ mass spectra, demonstrated in the previous chapter, indicates that exchange mechanisms of the types shown in figures 1.1 (c) and (d) are not important in this channel. The $d\pi^+$ peak (d^*) may be due to a mechanism of the form of figure 1.1 (b) while the A_1 and A_3 peaks can be formed by exchanges corresponding to figure

1.1 (a). The differential cross sections show that the reaction is very peripheral.

Van Hove (ref. 5.1) has suggested a new way of presenting experimental data, which can show more explicitly the form of M . It arises from the empirical fact that, at high energies, the momenta of the final state particles in a direction perpendicular to that of the incident particles in the centre of mass system (transverse momenta) are small and independent of the incident energy. The momenta along the direction of the incident particles (longitudinal momenta), therefore, contain all the information about the variation of the matrix element, which can therefore, be studied in terms of longitudinal momenta alone.

For an N body final state reaction there are N longitudinal momenta of which only $N - 1$ are independent because of the constraint:

$$\sum_i q_i = 0 \quad 5.3$$

where q_i is the longitudinal momentum of the i^{th} particle and the sum runs over all final state particles. Conservation of energy can be written:

$$\sum_i (q_i^2 + m_i^2 + r_i^2) = s \quad 5.4$$

where m_i and r_i are, respectively, the mass and transverse momentum of the i^{th} final state particle. At high energies, since the r_i 's are small, this can be written approximately as:

$$\sum_i |q_i| \approx s^{\frac{1}{2}} \quad 5.5$$

thus forming another approximate constraint on the q_i 's, leaving only $N-2$ of them independent.

5.2 Three Body L.P.S.

For a 3-body final state, for example, constraint (5.3) causes all the events to lie in a plane bounded by a hexagon, while constraint (5.5) causes them to fall near its boundary. An example of this is shown in

figure 5.1 (a) for the reaction:



This plot, called the longitudinal phase space plot, falls into six separate sectors according to which particles are going forward or backwards in the centre of mass system. The Feynman diagrams shown by the sectors in the figure are intended as guides to the possible exchange mechanisms responsible for any population of the particular sector and merely indicate which particles are forward (upper vertex) or backward (lower vertex). In the high energy limit, the sectors would indeed correspond to the appropriate simple exchange mechanism, but at lower energies events may be expected to spill over into an adjacent sector. Multiperipheral diagrams of the types shown in figures 1.1 (e) and (f), moreover, need not correspond to any one particular sector.

5.3 Four Body L.P.S.

The full longitudinal phase space representation for a 4-body final state reduces to a cuboctahedron (figure 5.1 (b)), due to equation (5.3). In this figure each q_i is measured perpendicularly to a hexagon at $q_i = 0$. Constraint (5.5) causes the events to fall towards the surface of this figure so that the representation is essentially completely specified by the polar and azimuthal angles defined with respect to a right-handed co-ordinate system in the figure.

A more useful way of presenting the data is in terms of the reduced longitudinal momenta (X_i) defined as:

$$X_i = \frac{2 \cdot q_i}{\sum |q_j|} \quad 5.7$$

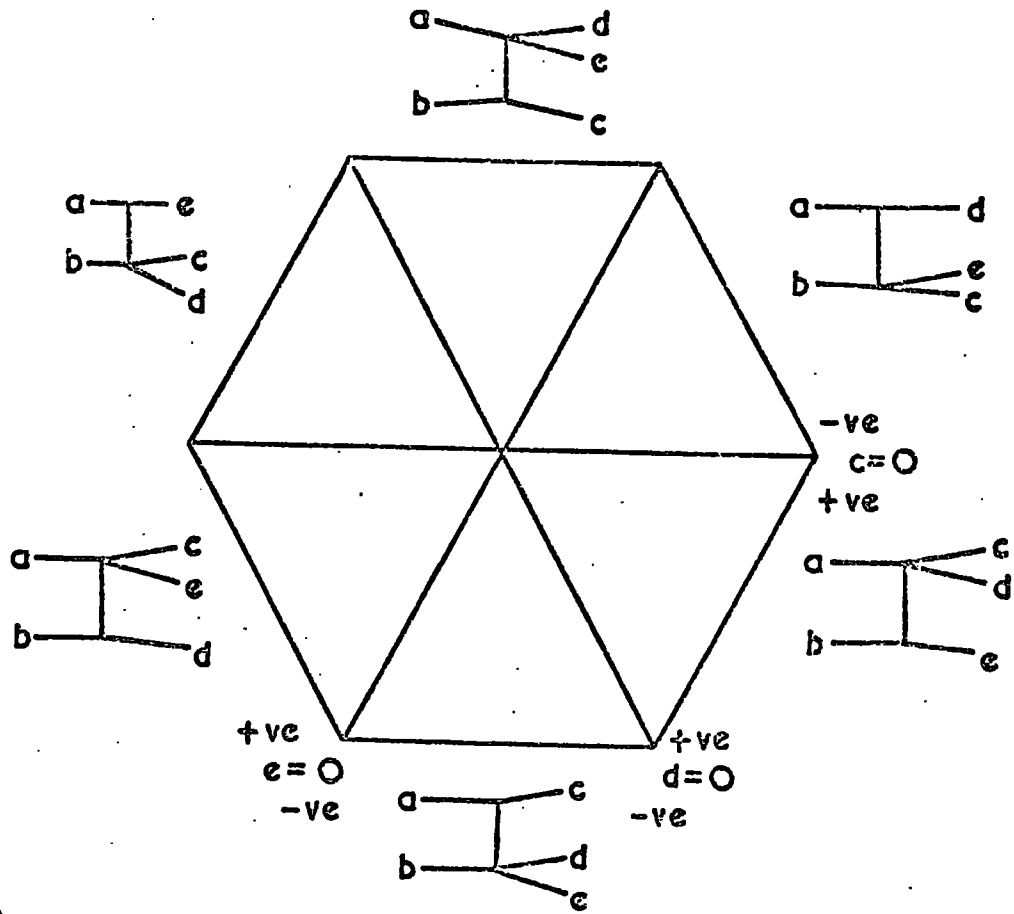
The X_i 's have the advantage of being independent of incident energy and obeying exactly the two constraint equations:

$$\sum_i X_i = 0 \quad 5.8 (a)$$

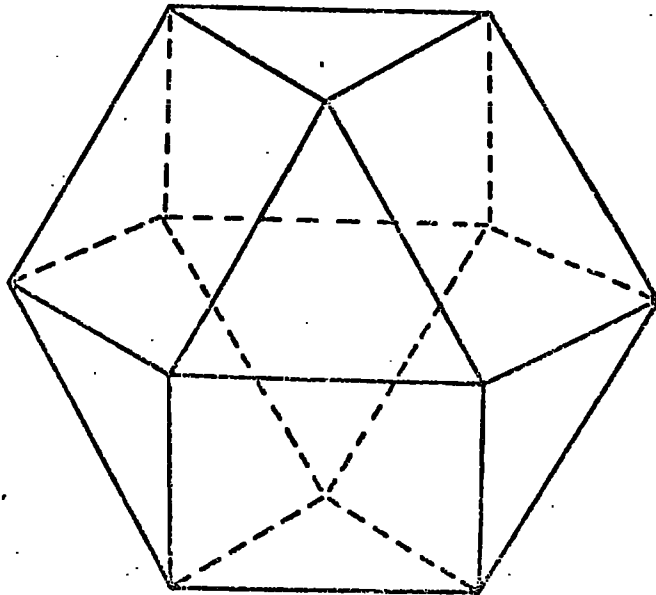
and
$$\sum_i |X_i| = 2 \quad 5.8 (b)$$

FIG 5.1

a) 3-body L.P.S. hexagon for the reaction $a+b \rightarrow c+d+e$



b) General 4 body L.P.S. cuboctahedron.



There are, therefore, for $N = 4$, only two X_i 's which are independent and to plot any two X_i 's against each other, completely defines the event.

For a 4-body final state there are in general 14 different possible forward-backward configurations. There are, however, in the coherent channel, two identical pions and this reduces the number of configurations to 10. It is found, empirically, that the final state deuteron is backwards in every event leaving only 5 possible configurations and if the identical pions are labelled fast (f) and slow (s) by the criterion:

$$X_f > X_s \quad 5.9$$

then in the present experiment the fast pion goes forward in all except 5 events and so for the remaining events there are only 4 possible configurations. When X_s and X_- , the reduced longitudinal momenta of the slow positive pion and of the negative pion respectively, are chosen as the two independent parameters, each possible configuration populates a separate sector of the $X_s - X_-$ plane.

It is possible to write the energies and momenta of the particles as functions of X_i and r_i and s , and so dV can be written as a function of these. Defining dV_0 as :

$$dV_0 = \delta_2 \left(\sum_i r_i \right) \delta \left(\sum_i x_i \right) \delta \left(1 - \frac{1}{2} \sum_i |x_i| \right) \prod_i dx_i d^2 r_i \quad 5.10$$

and

$$\omega = \left[\sum_{i=1}^n (x_i^2 E_i^{-1}) \right] \cdot \left[\frac{1}{2} \sum_{i=1}^n |q_i| \right]^{3-n} \left[\prod_{i=1}^n E_i \right] \quad 5.11$$

$$\text{Then } dV = \omega^{-1} dV_0 \quad 5.12$$

and dV_0 is a phase space volume element which is independent of s .

Distributions Δ and $\Delta\omega$ can be defined as:

$$\Delta = \sigma N_t^{-1} \sum_y 1 \quad 5.13$$

and

$$\Delta\omega = \sigma N_t^{-1} s^{-1} \sum_y \omega_y$$

where σ is the total channel cross section

N_t is the number of events in the channel and ω_y is the weight for an event y defined by equation (5.11) and the sum runs over all events y in the region δV of phase space, defined in terms of the variables X_i and r_i . Δ is therefore the partial cross section for the region δV and the value of $\Delta\omega$ in this region is given by:

$$\begin{aligned} \Delta\omega &= P_{cm}^{-1} s^{-\frac{3}{2}} \int_{\delta V} |M|^2 \omega dV \\ &= P_{cm}^{-1} s^{-\frac{3}{2}} \int_{\delta V} |M|^2 dV_0 \end{aligned} \quad 5.14$$

$\Delta\omega$ is, thus, equivalent to the integral of $|M|^2$ over the energy independent variables X_i and r_i with the energy independent volume element dV_0 .

If δV is defined as that region of phase space enclosed in a certain region of the X_i variables with no restriction on the values of r_i , then the bin volume δx is given by:

$$\delta x = \int_{bin} \delta \left(\sum_{i=1}^n X_i \right) \delta \left(1 - \frac{1}{2} \sum_{i=1}^n |X_i| \right) \prod_{i=1}^n dx_i \quad 5.15$$

$$\text{then } \frac{\Delta\omega}{\delta x} = P_{cm}^{-1} s^{-\frac{3}{2}} \int |M|^2 \prod_{i=1}^{n-2} d^2 r_i \quad 5.16$$

Thus this distribution gives the value of $|M|^2$ integrated over transverse momenta, in an energy independent way, without the phase space effects involved by the use of the variables X_i . A direct comparison of data at various energies is therefore possible.

5.4 Transverse Momenta

If the distribution of r_i is independent of energy and of the values of q_i then the integration in equation (5.16) will result only in a constant and the distribution of $\Delta\omega$ will be directly proportional to $|M|^2$ if δx is constant. To check this the mean value of r_i has been calculated in bins of the $X_s - X_-$ plane of longitudinal phase space (L.P.S) for

each of the final state particle. The bin size used here, and throughout the analysis is 0.125×0.125 , except in some cases, where the statistics are small, in which case larger bins have been used. The results are shown in figure 5.2(a).

(d). These are the unweighted averages given by:-

$$\langle \bar{r}_i \rangle = \frac{\int_{\delta V} |M|^2 r_i dV}{\int_{\delta V} |M|^2 dV} \quad 5.17$$

but the weighted averages, given by:

$$\langle \bar{r}_i \omega \rangle = \frac{\int_{\delta V} |M|^2 r_i \omega dV}{\int_{\delta V} |M|^2 \omega dV} \quad 5.18$$

have also been calculated and the effect of the weighting is small, changing the calculated values by less than 5%. It can be seen that the values of $\langle r_i \rangle$ are remarkably constant over L.P.S. at $\sim 150 \text{ MeV}/c$ for the deuteron and $\sim 300\text{-}350 \text{ MeV}/c$ for the pions. In the case of the π^- there is a small variation in that there seems to be a dip in the distribution near the $X_- = 0$ axis, irrespective of the value of X_s . This dip cannot be explained statistically since the errors on the values are typically less than 20% and the dip is greater than this. The variation, however, is small when compared to that of the $\Delta\omega$ distribution, as will be seen, and it is concluded that the $\Delta\omega$ distribution is almost directly proportional to $|M|^2$.

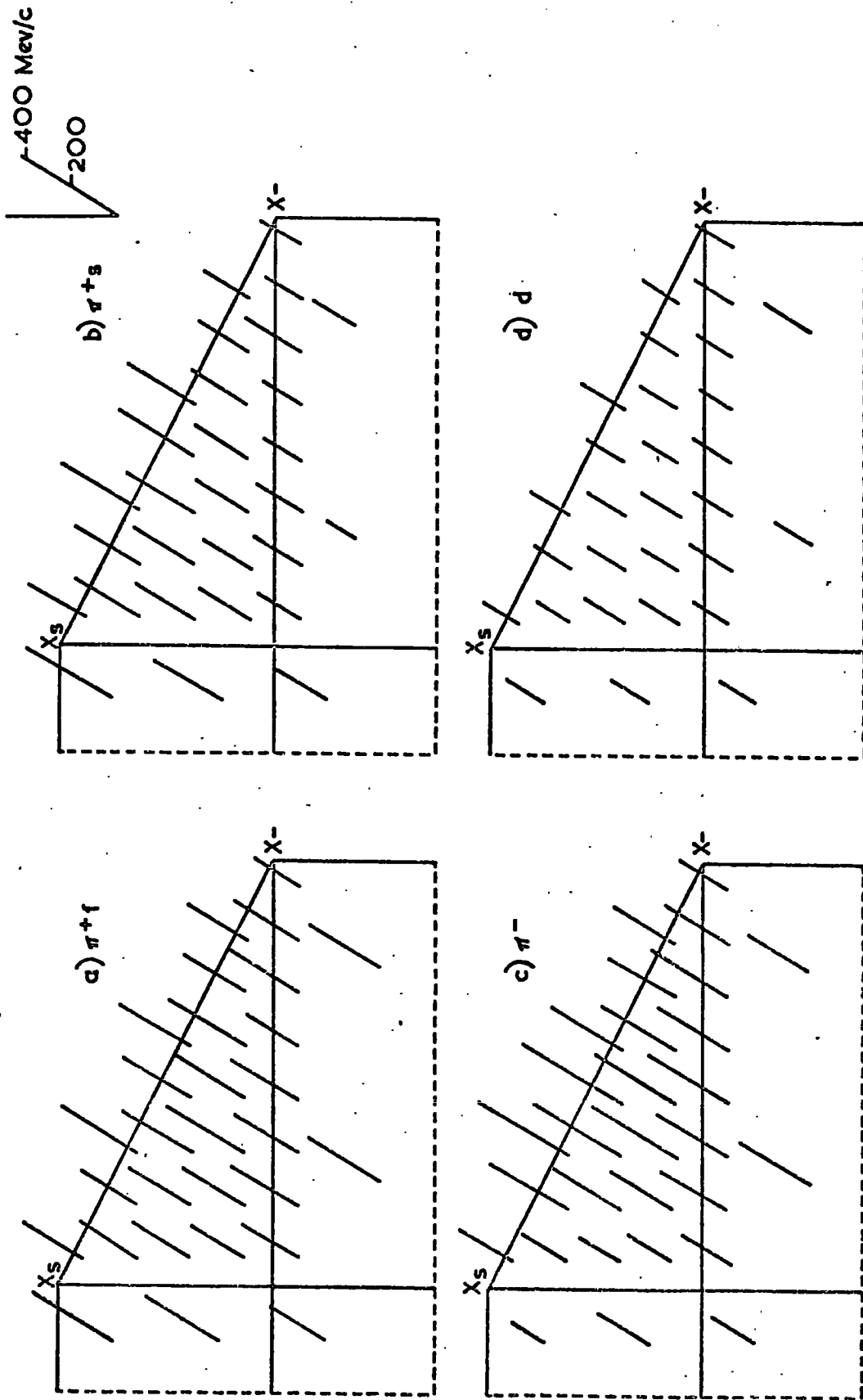
5.5 Experimental L.P.S. distributions

The experimentally determined values of the Δ and $\Delta\omega$ distributions in the $X_s - X_-$ plane are shown in figures 5.3 (a) and (b) respectively. The outline shape of these figures is due to the definition of X_s and the constraints 5.8 (a) and (b). The regions are labelled in the figure as:-

$$\text{Region 1: } X_s > 0 \quad X_- > 0$$

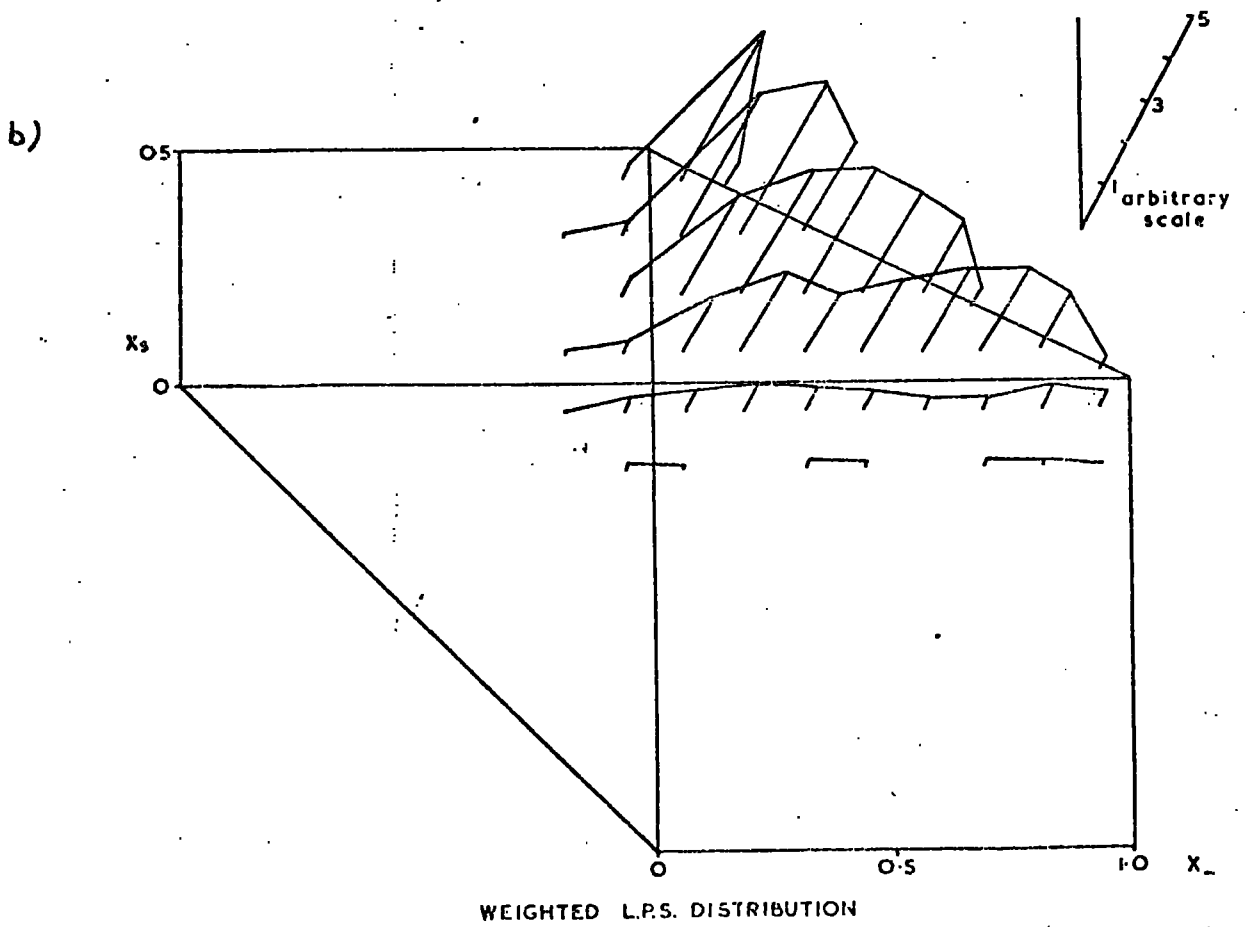
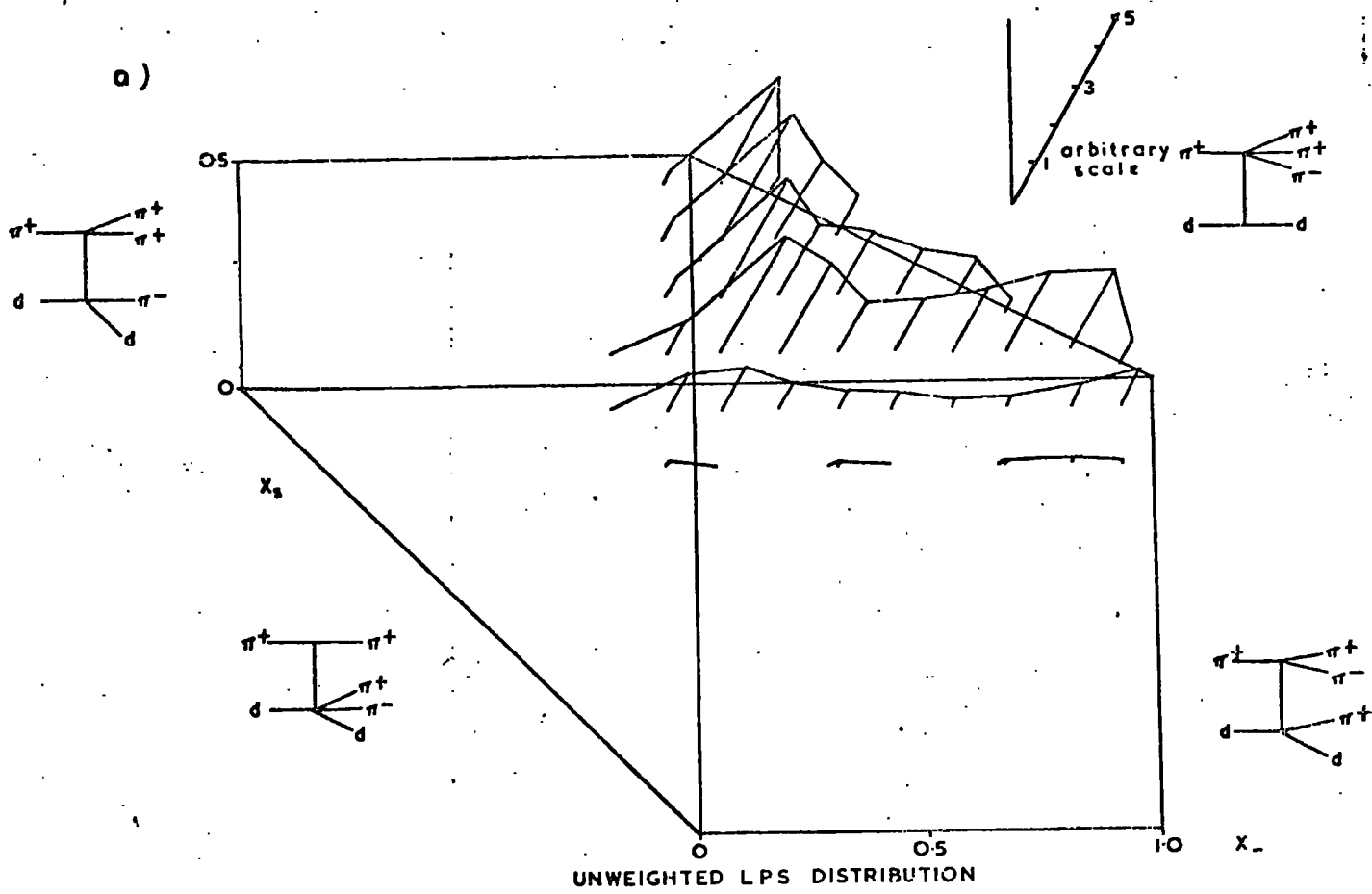
$$\text{Region 2: } X_s > 0 \quad X_- < 0$$

FIG 5.2



MEAN TRANSVERSE MOMENTA

FIG 5.3



Region 3: $X_s < 0$ $X_- < 0$

Region 4: $X_s < 0$ $X_- > 0$.

It is clear that the channel is dominated by a mechanism which populates Region 1 corresponding to the configuration in which all three pions go forwards. This is the region where diffraction dissociation events would be expected to occur. Although there are some events in region 2, (π^- backwards), the shape of the distribution suggests that this is merely the tail of the dominant mechanism, spilling over the boundary. The only other sector which has any appreciable population is Region 4 (π_s^+ backwards). While this too could be due to spillover from the main peak, it is more strongly populated than Region 2, suggesting that a secondary mechanism may be responsible. The strong peaking along sector boundaries in the unweighted distribution can be seen to be an effect of the choice of variables X_i , since it is not present in the weighted $\Delta\omega$ distribution, where these effects have been removed.

In order to discover whether different regions of L.P.S. do, in fact correspond to different production mechanisms, it is interesting to plot effective mass spectra from the different regions separately. If the Feynman diagrams corresponding to each region are correct, then resonances would only be expected to occur in combinations of particles, emitted from the same vertex. In Region 1, for example, tripion or dipion resonances can be expected, while in Region 4 there should be no 3-pion resonances and dipions should be formed only in the $\pi_f^+ \pi^-$ combination. High mass resonances, however, formed going forward in the centre of mass system, upon decaying, may give sufficient momentum to one decay product in the backward direction to cause it to travel backwards in the centre of mass system, and, if this is the case, the event will fall in the 'wrong' L.P.S. region. This effect is not

important for lower mass resonances, since the momentum available in the resonance rest system for the decay products is not very great and, unless the resonance has only a small c.m.s longitudinal momentum, the decay products will travel in the same direction as the resonance. Low mass resonances can only cross over to the 'wrong' L.P.S. sector, therefore, if produced with a high momentum transfer from the beam, and since this is not the case either for 3-pion or 2-pion resonances, there should be no problem.

In figure 5.4 (a) and (b) the $\pi^+ \pi^-$ and $\pi^+ \pi^-$ effective mass distributions are shown for events falling in Region 1. There is evidence of ρ production in both combinations although there is no clear f^0 signal. The 3 pion mass spectrum for events from the same region is shown in fig. 5.4 (c); there is a clear A_1 signal but the number of events in the A_3 region is significantly reduced from that of the whole sample. The $\pi^+ \pi^-$ mass spectrum for Region 4 events is presented in figure 5.4 (d). There is little evidence for any resonant state in the distribution although a small amount of ρ^0 and some f^0 production cannot be dismissed. In the $\pi^+ \pi^-$ mass spectrum from this region (fig. 5.4(e)) there is a strong ρ^0 signal and a small enhancement in the f^0 region, while the 3-pion mass distribution for Region 4 events, shown in fig. 5.4(f) shows no A_1 production at all, merely a broad enhancement in the A_3 region. Of the 96 events which fall in Region 2, the only evidence for any resonance production is in the $\pi^+ \pi^-$ mass spectrum, where there is a clear peak in the f^0 region (fig. 5.5 (a)). The 3-pion mass spectrum from this region has a large proportion of events in the A_3 region but the lack of statistics make it impossible to recognise this as a definite enhancement. There is no sign of any mesonic resonance production in the events from Region 3. These features are summarised in table 5.1 which gives the number of events falling in each region,

FIG 5.4

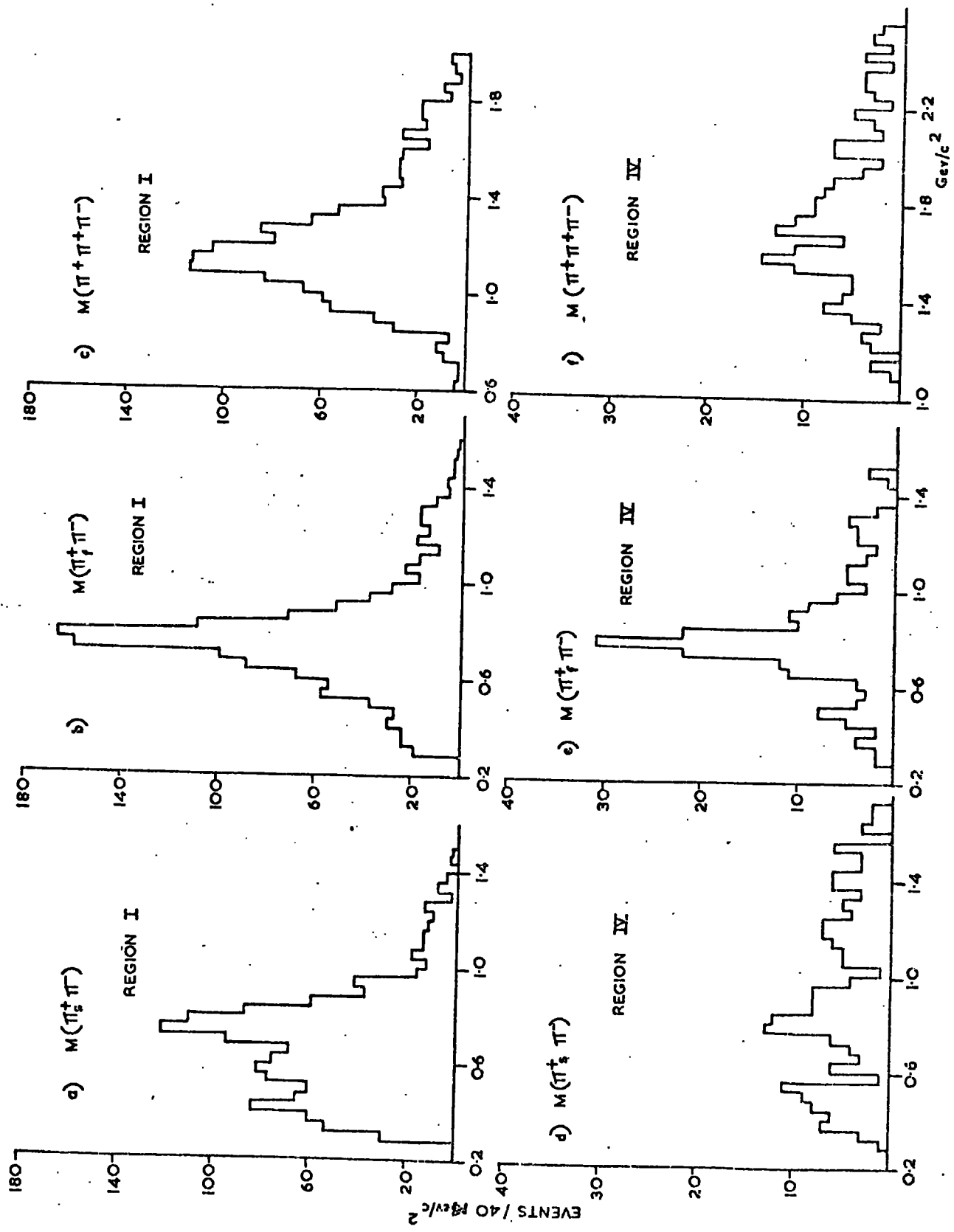
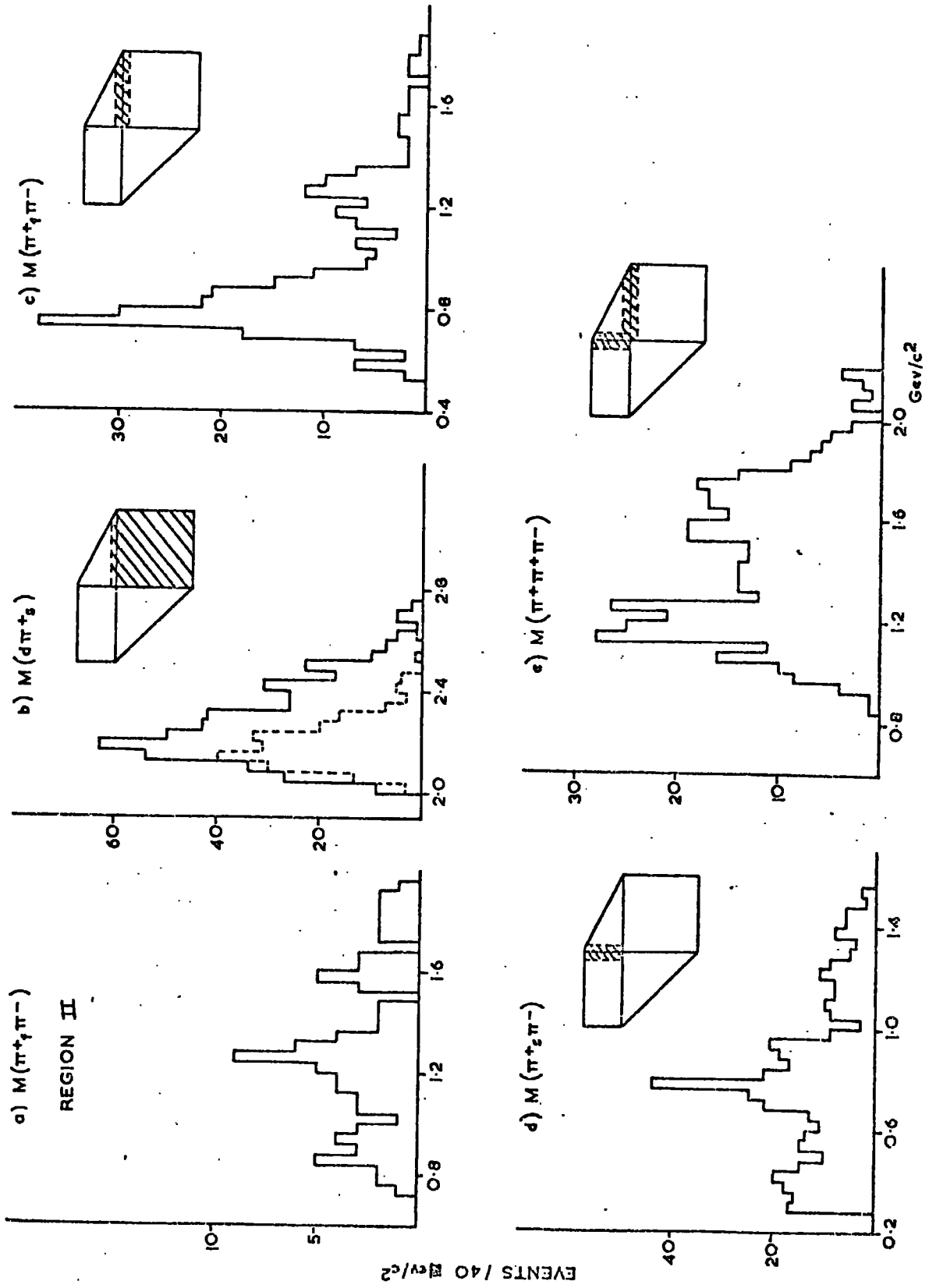


FIG 5.5



Region	Number of events		Resonances Produced		
	Forward	Backward	$\pi^+ s \pi^-$	$\pi^+ f \pi^-$	$\pi^+ s \pi^-$ $\pi^+ f \pi^-$
1	$\pi^+ f \pi^+ s \pi^-$	d	ρ	$\rho(f?)$	$A_1 (A_3?)$
2	$\pi^+ f \pi^+ s$	$\pi^- d$	-	f	$(A_3?)$
3	$\pi^+ f$	$\pi^+ s \pi^- d$	-	-	-
4	$\pi^+ f \pi^-$	$\pi^+ s d$	$\rho?$ (f?)	$\rho(f?)$	A_3

TABLE 5.1: Resonances produced in the separate regions of L.P.S.

together with the resonances produced in each particle combination.

5.6 Production Mechanisms

The resonances produced in Region 1 are compatible with the expected exchange diagram; the ρ^0 and A_1 , as low mass enhancements are produced and some evidence for f^0 and A_3 is present. The enhancements in Region 2, f^0 and perhaps some A_3 , can be explained in terms of the mechanism which corresponds to Region 1 spilling over the boundary and populating Region 2 for high mass resonances. In Region 4, however, the strong ρ^0 production in the $\pi^+ f \pi^-$ combination, cannot be explained in this way since the ρ^0 must be considered a low mass resonance as otherwise it should be seen in Region 2. This feature of Region 4 is, however, compatible with the exchange diagram which would be expected to populate this region and it must be concluded that Region 4 is not populated merely by the tail of the dominant mechanism but by a separate mechanism. This is emphasised by the fact that the d^{*++} is produced in Region 1 but only for events close to the $X_s=0$ border. Figure 5.5 (b) shows the $d\pi^+$'s effective mass spectrum for events in Region 4 together with those which fall in Region 1 but satisfy the condition $X_s < 0.05$. The whole of the d^{*++} peak lies in this region of L.P.S. The dashed histogram in fig. 5.5 (b) shows only those events falling in Region 4 and it can be seen that these events correspond to the low mass end of the enhancement. The higher mass part of the enhancement, spills over the boundary although it is only a little above threshold. This effect is caused by the high mass of the deuteron.

The high mass enhancements (f^0 and A_3) which do not fall entirely in the regions of L.P.S. where they would be expected can be seen quite clearly when the events which lie around the boundary of the expected region are plotted. For this purpose the area around the border $X_1=0$ has been defined as $|X_1| < 0.05$. The f^0 can be seen in the $\pi^+ f \pi^-$ combination near the $X_s=0$ border (fig. 5.5(c)) and, to some extent, in the $\pi_s^+ \pi^-$ combination near the $X_s=0$ border (fig. 5.5(d)) and while the former of these may be

partly correlated with the secondary mechanism responsible for d^* production, the latter cannot be explained in this way. A clear A_3 signal is seen in the tripion mass spectrum around both these borders, shown combined in figure 5.5(e).

It can be seen in figure 5.3 that there is some evidence of a double peak structure in the Δ distribution near the boundary $X_s=0$. This is clearer in the unweighted distribution but is not an effect of the choice of variables X_i since it can also be seen in the weighted distribution (Δw). It is of interest to attempt to determine whether the double peak is statistical or represents a physical variation of the matrix element, particularly since it is in the area where the two competing mechanisms seem to overlap. To this end the L.P.S. plot been divided into three areas defined as follows:

Area 1 : $X_s > 0.125$

Area 2 : $0 < X_s < 0.125$; $X_- < 0.375$

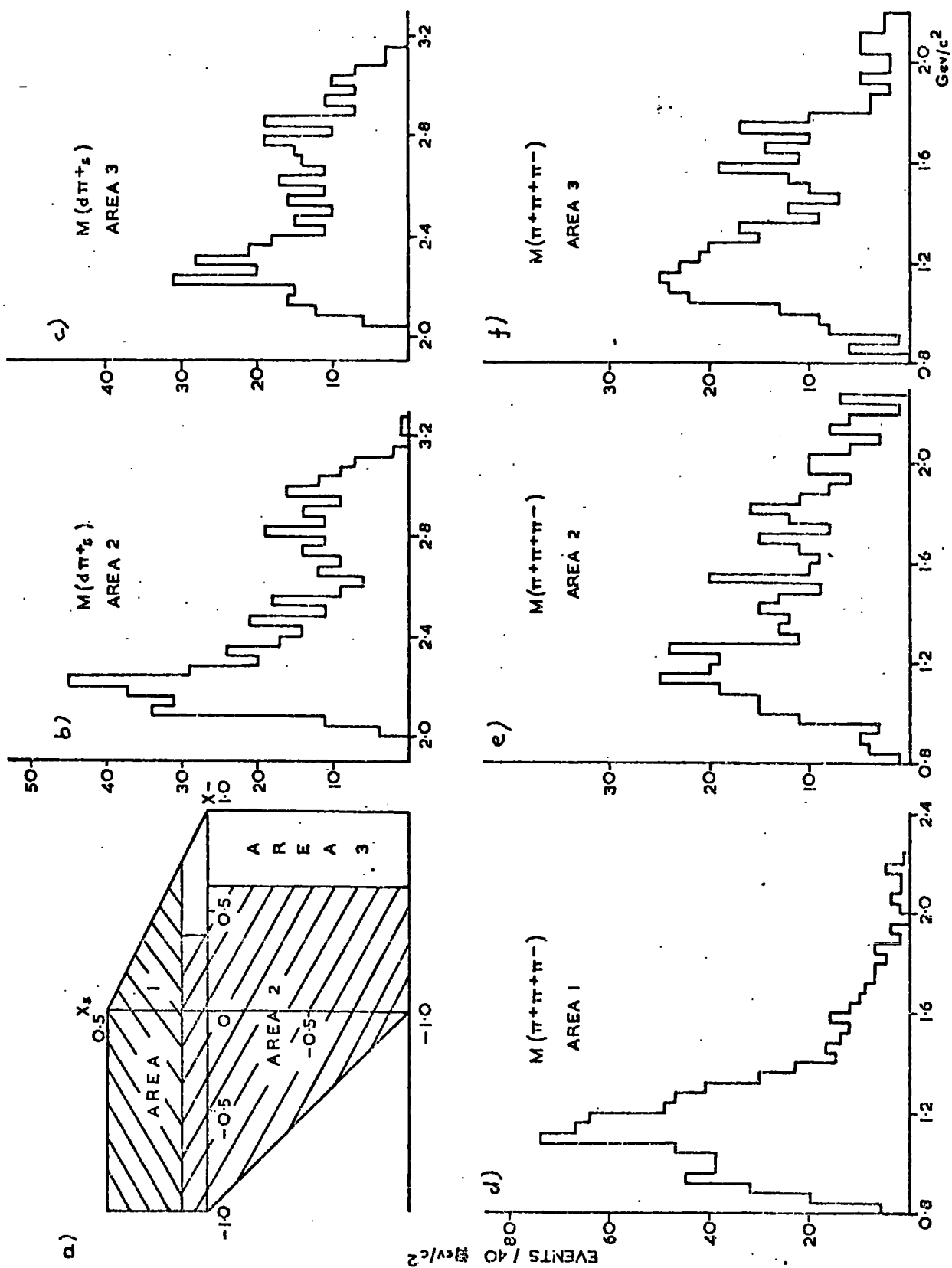
and $X_s < 0$; $X_- < 0.675$

Area 3 : the remainder.

These are shown schematically in figure 5.6 (a) and correspond to the part of the L.P.S. where there is no double peak (Area 1), the left hand peak (Area 2) and the right hand peak (Area 3).

Figures 5.6 (b) and (c) show the $d\pi^+$ mass distribution for events in areas 2 and 3 respectively. While there is evidence for d^{*++} production in both these areas, the proportion of events in the d^* peak is greater in area 2, where $\sim 53\%$ of the combinations have a mass less than $2.4 \text{ GeV}/c^2$, than in area 3, where only $\sim 44\%$ fall in this mass region. This difference of d^* production cross section is further emphasised if allowance is made for the background below the d^* peak; subtracting a hand drawn background from both distributions, the proportions of d^{*++} production in the two areas becomes 34% and 22% respectively. In area 1 no events have a $d\pi^+$

FIG 5.6



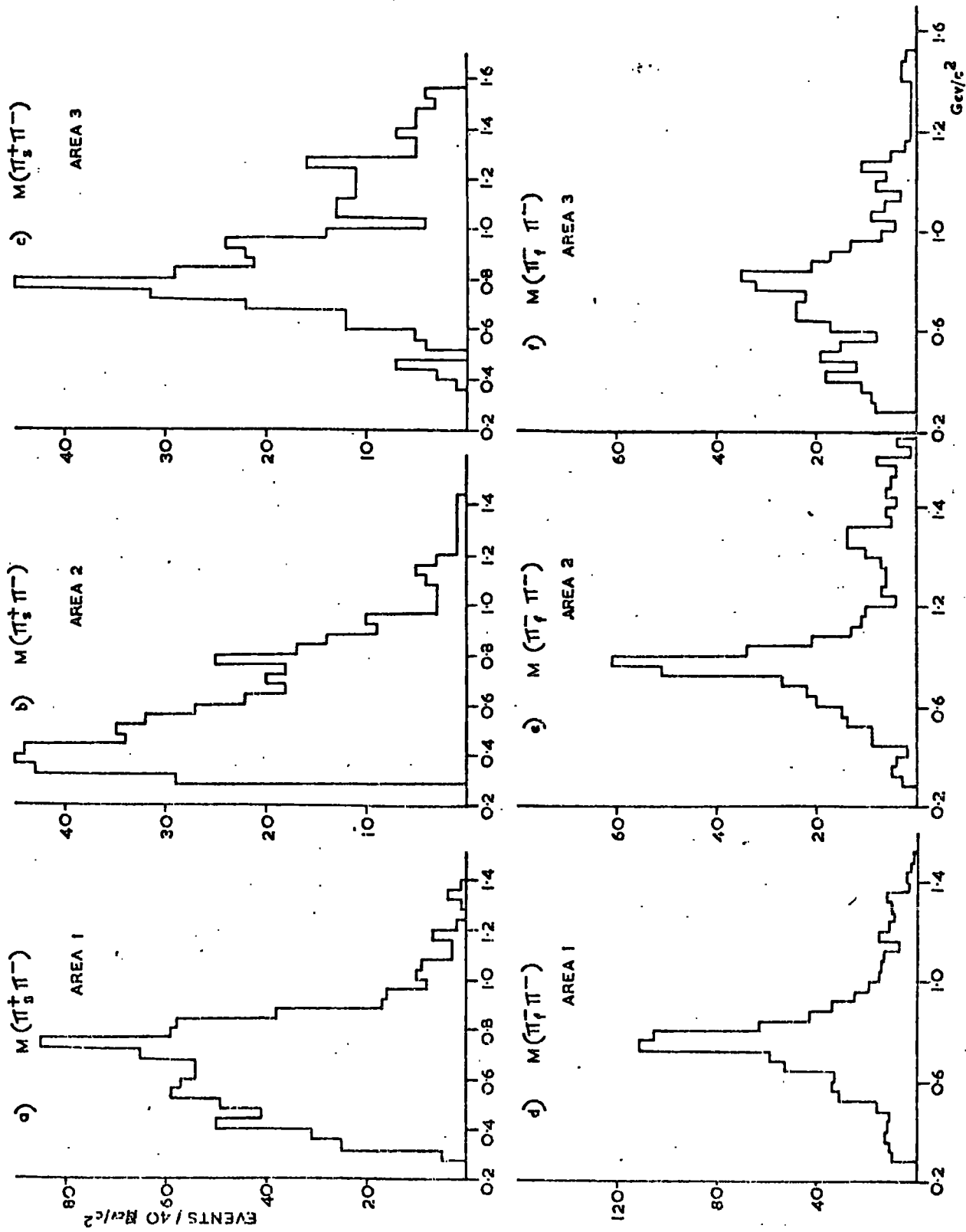
effective mass less than $3.0 \text{ GeV}/c^2$.

The three pion effective mass distribution for each area are shown in figure 5.6 (d), (e) and (f). The A_1 peak is apparent in each of the three areas, but, while there are events in the A_3 mass region in every case, it is only in area 3 that a clear A_3 peak can be seen.

The clearest difference between areas 2 and 3 can be seen in figures 5.7 (b) and (c) where the $\pi^+ \pi_s^-$ mass spectra are shown for the two areas. There is strong ρ^0 and f^0 production for the right hand peak, while the left hand peak shows neither of these resonances in this combination. The inverse is true for the $\pi^+ f\pi^-$ mass spectra, as can be seen in figures 5.7 (e) and (f), although here there is some ρ^0 and f^0 production even in the right hand peak. Also shown in figure 5.7 for comparison are the $\pi^+ \pi_s^-$ mass spectrum (fig. 5.7(a)) and the $\pi^+ f\pi^-$ mass spectrum (fig. 5.7 (d)) for area 1. These differences in the dipion mass spectra may arise partly kinematically. For example, in area 2, where the π_s^+ and π^- are both, in general, moving relatively slowly in the longitudinal direction of the c.m.s. their combined effective mass is constrained to take low values unless their transverse momenta are high. There is, however, no such kinematic explanation of the differences in the three pion spectrum or the $d\pi_s^+$ mass distribution and it is concluded that the double peak structure cannot be disregarded as a physical effect, the left hand peak being more associated with d^* production and the right hand peak more with A_3 production. It would be interesting to see the results of a similar analysis on this channel at different energies to see if this double peak is present there also.

In conclusion, the longitudinal phase space analysis shows that the channel is dominated by a mechanism which populates Region 1 of L.P.S. with a secondary mechanism populating Region 4. In the area

FIG 5.7



where these two mechanisms would be expected to overlap the L.P.S. distribution shows two peaks which seem to have different characteristics.

C H A P T E R S I X

ANALYSIS OF DECAY ANGLES OF MESONIC SYSTEMS

6.1 Introduction

In this chapter the decay angular distributions of the resonances and enhancements presented in Chapter 4 will be discussed. The discussion falls into two sections. The first deals with resonances in the dipion system, ρ^0 and f^0 , whose spins are well known and the analysis involves computation of the spin density matrix elements for these in order to gain information on their production mechanisms. This section also contains some discussion of the ' η_N ' enhancement. The second section contains an analysis of the spins of the A_1 and A_3 enhancements and here the point of view taken is the determination of the spin-parity since the overall spin structure of these states is not so well known. Throughout the chapter the reference frame used to define the decay angles is the Gottfried-Jackson frame, which is described in Appendix B.

6.2. Dipion Systems

6.2.1 The ρ^0 meson

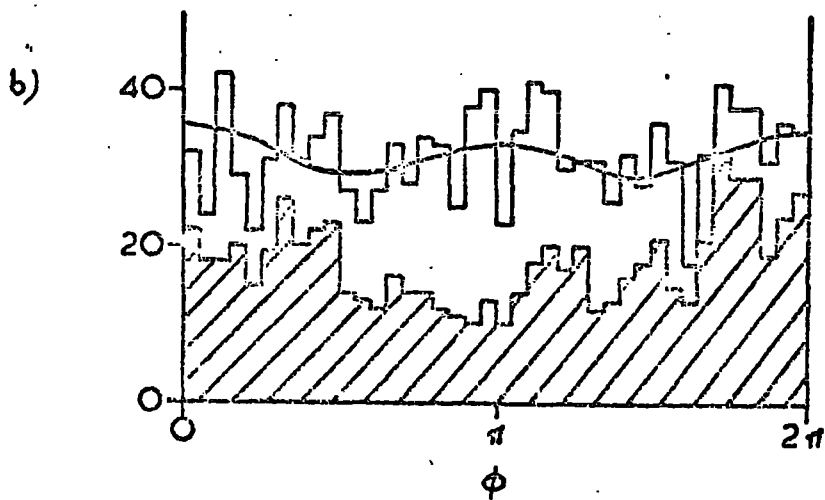
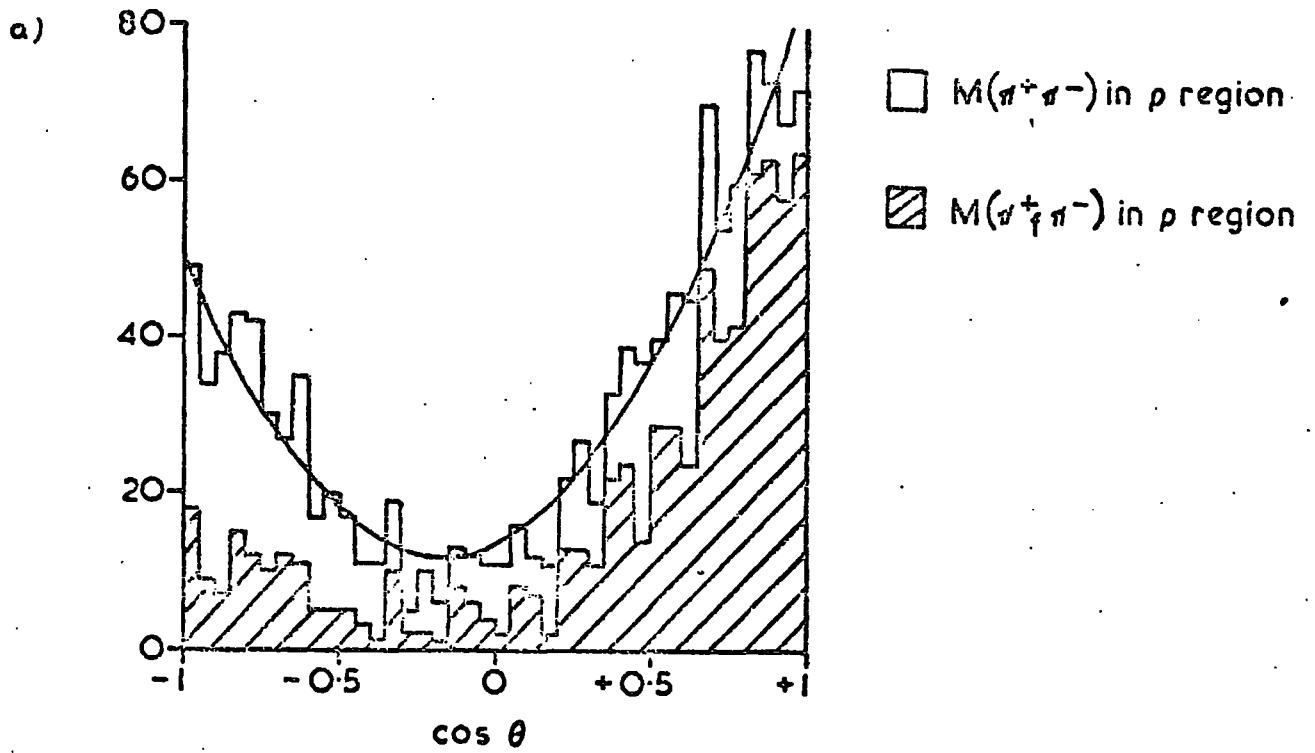
The ρ meson is known to have spin (J) equal to 1 and odd parity ($J^P = 1^-$). The decay angular distribution for such a dipion resonance is given by:-

$$W(\theta, \phi) = \frac{3}{4\pi} \left\{ \frac{1}{2} (1 - \rho_{00}) + \frac{1}{2} (2\rho_{00} - 1) \cos^2 \theta - \rho_{1-1} \sin^2 \theta \cos 2\phi - \sqrt{2} \operatorname{Re} \rho_{10} \sin 2\theta \cos \phi \right\} \quad 6.1$$

(For definitions of the quantities involved see Appendix B).

Figure 6.1 shows the distribution of $\cos \theta$ and ϕ for all $\pi^+ \pi^-$ combinations with an effective mass in the ρ^0 region, defined as 0.665-0.865 GeV/c². Recalling (from Chapter 4) that the result of the fit to the dipion mass spectrum indicates that this mass region contains ~35% background, it would be advisable to reduce this back-

FIG. 6.1 ρ DECAY ANGLES



ground if possible. As pointed out in chapter 4, a marked improvement in the signal to background ratio can be achieved by using only one dipion combination per event, for example $\pi_f^+ \pi^-$ (where π_f^+ indicates the π^+ with the greater momentum in the laboratory system) or the $\pi^+ \pi^-$ combination formed with lower momentum transfer from the beam. The result of such a criterion, however, is not wholly satisfactory, since there is still a ρ^0 signal in the "wrong" combination. This signal can be seen to correspond preferentially to a certain configuration of the decay in figure 6.1 (hatched histogram, where only $\pi_f^+ \pi^-$ combinations falling in the ρ^0 region have been plotted). It is clear that there is a much stronger reduction in the number of events $\sim \cos \theta = -1$ than elsewhere. This is unlikely to be the result of reduced background since it would imply that the background has more events in the backward hemisphere ($\cos \theta < 0$) than in the forward, while plots of the decay angles for events just below and just above the ρ^0 region show the opposite to be true. It is concluded, therefore, that to select one π^+ by any such criterion leads to a biased angular distribution.

Another possible way of reducing the background arises from the fact that $\sim 17\%$ of the events have both neutral dipion effective masses in the ρ^0 region. Such events can be weighted by a factor of a half but, while this reduces the background to some extent, it also reduces the amount of signal.

In general, therefore, the subsequent analysis is based on all mass combinations falling in the given mass region. The results to be presented however have been checked by using a sample defined as follows: t' , the square of the 4-momentum transfer from the beam to the dipion system minus its minimum value, was determined for

both combinations and hence the quantity $T = |t_1^i - t_2^i|$ was calculated. It was found that there is essentially no resonant signal in the combination formed with higher t^i for events with $T > 0.2 \text{ GeV}/c$ and only the other combination was used. The remainder of events ($T < 0.2 \text{ GeV}/c^2$) have signals in both combinations, and these were also used weighted by 0.5. The results obtained by using this sample agreed within errors with those obtained by using the entire sample except at the highest values of t^i where the background is particularly strong.

It can be seen from figure 6.1 that the distribution of $\cos \theta$ is not symmetric around 0 and this is in contradiction with the assignment of $J^P = 1^-$ since equation 6.1 cannot produce such an asymmetry. Defining the asymmetry parameter A by:

$$A = \frac{F - B}{F + B} \quad (6.2)$$

where F = the number of combinations with $\cos \theta > 0$

B = the number of combinations with $\cos \theta < 0$,

it is found that $A = 0.30 \pm 0.03$. That this is not due to background can be seen from the fact that A is smaller than this value in both the mass region immediately below the ρ^0 region ($A = 0.28 \pm 0.10$) and immediately above it ($A = 0.04 \pm 0.05$). If it is assumed that the asymmetry of the background is smoothly varying through the ρ region, then the true value of A for ρ events will be higher than that calculated above.

This asymmetry of the neutral ρ^0 is generally attributed to the P-wave ρ signal interfering with an S-wave $I = 0$ state in the same mass region, known as the ϵ . If this is the case then the decay angular distribution must be modified to take into account the S-P

interference. It becomes:

$$\begin{aligned}
 W(\theta, \phi) = \frac{3}{4\pi} & \left\{ \rho_{00} \cos^2 \theta + \rho_{11} \sin^2 \theta - \sqrt{2} \operatorname{Re} \rho_{10} \sin 2\theta \cos \phi \right. \\
 & \left. - \rho_{1-1} \sin^2 \theta \cos 2\phi \right\} + \frac{\sqrt{3}}{4\pi} \left\{ -2\sqrt{2} \operatorname{Re} \rho_{10}^{\text{int}} \sin \theta \cos \phi \right. \\
 & \left. + 2 \operatorname{Re} \rho_{00}^{\text{int}} \cos \theta \right\} + \frac{1}{4\pi} \rho_{00}^{\text{s}} \quad (6.3)
 \end{aligned}$$

where the interference terms are marked with the superscript 'int' and the pure S-wave with 's'. The density matrix condition of trace unity is now written:

$$2\rho_{11} + \rho_{00} + \rho_{00}^{\text{s}} = 1. \quad (6.4)$$

and can be used to eliminate ρ_{00}^{s} from the above expression.

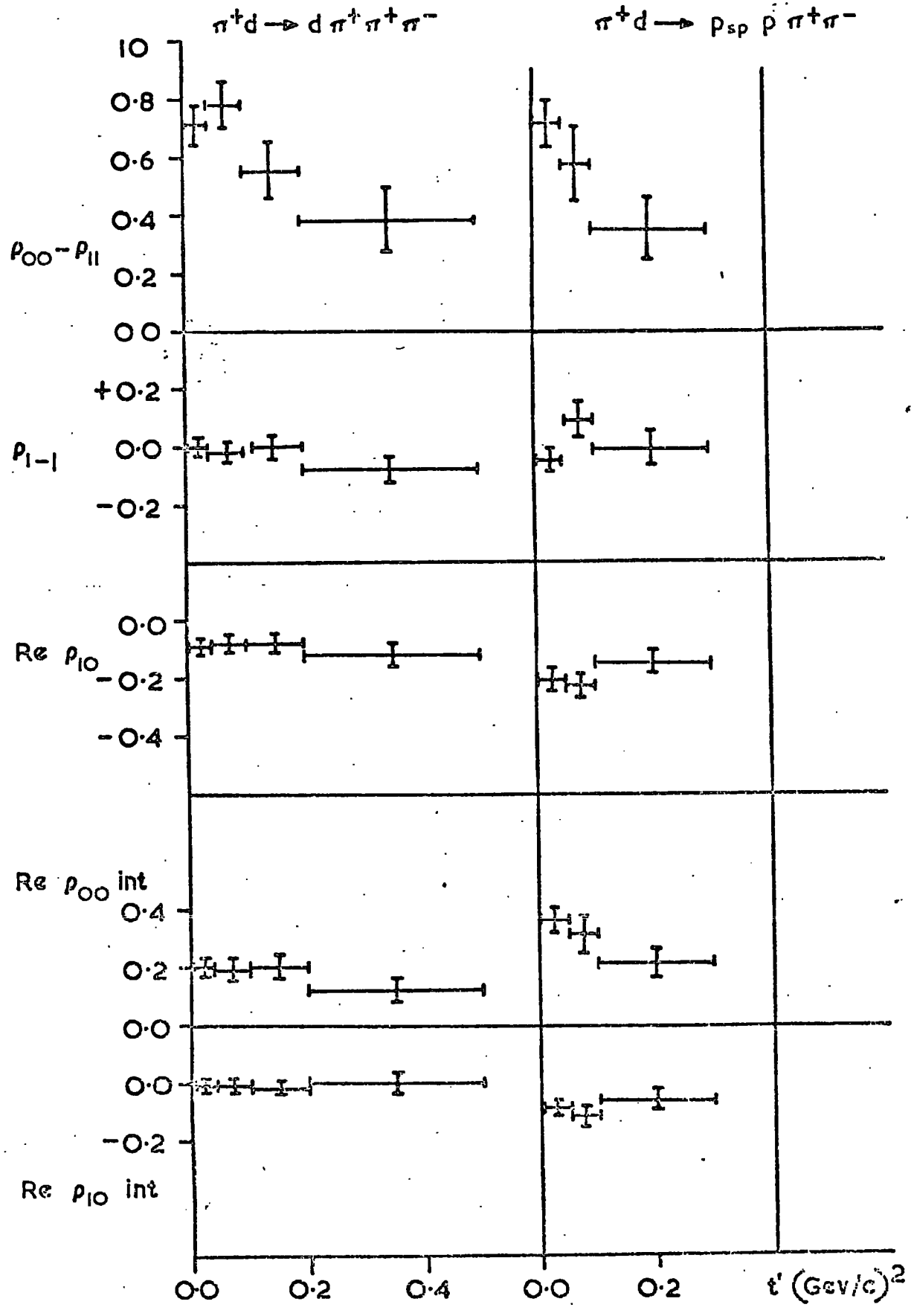
Using this expression, the values of the density matrix elements for the ρ^0 mass region have been calculated by the method of moments (see appendix B) and are given in table 6.1. There is insufficient information in the data to determine ρ_{00} and ρ_{11} separately. Only the value of a linear combination of these ($\rho_{00} - \rho_{11}$) can be found. The calculated curves, assuming these values, for the $\cos \theta$ and ϕ distributions are shown as the curves in figure 6.1 where it can be seen that the agreement with the data is quite good.

Since the density matrix elements can, in general vary as a function of t or t' , the values determined above must be considered as average values over the whole t range. More explicit information is given in the other columns of table 6.1 and in figure 6.2, where the variation of the density matrix elements is given as a function of t' . For comparison the values obtained in this experiment for the channel:

$$\pi^+ d \rightarrow p p \pi^+ \pi^- \quad 6.5$$

are also shown.

FIG 6.2 ρ DENSITY MATRIX ELEMENTS



There is a marked similarity between the results obtained in the two channels. Simple One-Pion-Exchange predicts that ρ_{1-1} , $\text{Re } \rho_{10}$ and $\text{Re } \rho_{10}^{\text{int}}$ should be zero but this is not the case in either channel (N.B. $\text{Re } \rho_{10}$). For the reaction 6.5, however, the density matrix elements have been shown to be compatible with the hypothesis of one-pion-exchange with absorption (OPEA) (Ref.) and, therefore, it can be assumed that in the present channel ρ^0 production is also compatible with the hypothesis. It is interesting, nonetheless, to note the difference between the two channels: a slower decrease of $\rho_{00} - \rho_{11}$ with t' in this channel than in channel 6.5; a much smaller value of $\text{Re } \rho_{10}$ and $\text{Re } \rho_{10}^{\text{int}}$ in this channel, especially at low t' and, particularly, the fact that $\text{Re } \rho_{00}^{\text{int}}$ shows no tendency to decrease with increasing t' (except perhaps, above $t' = 0.2 \text{ (GeV/c)}^2$) in contrast not only to channel 6.5 in this experiment but also to other experiments which have been interpreted with the OPEA model (Ref. 6.2.) Predictions of the values of the ρ^0 density matrix elements, assuming diagrams of the type shown in figure 1.1a, cannot be made.

6.2.2 The f^0 meson

The f^0 meson has spin-parity $J^P = 2^+$ and the expected decay distribution for such an object decaying into two pions is given by:

$$\begin{aligned}
 W(\theta, \phi) = \frac{15}{16\pi} \left\{ \sin^4 \theta \left(\rho_{22} + \rho_{2-2} \cos^2 \phi \right) + \sin^2 2\theta \left(\rho_{11} - \rho_{1-1} \cos 2\phi \right) \right. \\
 + 3\rho_{00} \left(\cos^2 \theta - \frac{1}{3} \right)^2 - 4 \sin^3 \theta \cos \theta \left(\text{Re } \rho_{21} \cos \phi - \text{Re } \rho_{2-1} \cos 3\phi \right) \\
 + 2/\sqrt{6} \text{Re } \rho_{20} \sin^2 \theta \left(\cos^2 \theta - \frac{1}{3} \right) \cos 2\phi + 2/\sqrt{6} \text{Re } \rho_{10} \sin 2\theta \\
 \left. \times \left(\cos^2 \theta - \frac{1}{3} \right) \cos \phi \right\} \quad 6.6
 \end{aligned}$$

CHANNEL :		$\pi^+ d \rightarrow d \pi^+ \pi^-$					$\pi^+ d \rightarrow pp \pi^+ \pi^-$		
T' RANGE (GeV/c) ² :	ALL	0.0-0.04	0.04-0.1	0.1-0.2	0.2-0.5	0.0-0.05	0.05-0.1	0.1-0.3	
Element									
$\rho_{00} \rho_{11}$	0.57±0.04	0.71±0.07	0.78±0.08	0.55±0.10	0.38±0.11	0.71±0.08	0.57±0.13	0.35±0.11	
ρ_{1-1}	-0.04±0.02	0.0 ±0.03	0.02±0.03	0.0 ±0.04	-0.08±0.04	-0.05±0.04	0.08±0.06	-0.01±0.06	
Re ρ_{10}	-0.09±0.01	-0.09±0.03	-0.08±0.03	-0.08±0.03	-0.12±0.03	-0.21±0.04	-0.23±0.04	-0.15±0.04	
Re ρ_{00}	0.17±0.02	0.20±0.03	0.19±0.03	0.20±0.04	0.12±0.04	0.36±0.04	0.31±0.06	0.21±0.05	
Re ρ_{10}	-0.01±0.01	-0.01±0.02	-0.01±0.02	-0.01±0.02	0.0 ±0.02	-0.09±0.02	-0.12±0.03	-0.06±0.03	

TABLE 6.1

The ρ^0 spin density matrix elements

The distribution of $\cos \theta$ and ϕ for all combinations of the neutral dipion mass in the f^0 region (defined as $1.12 < M(\pi^+ \pi^-) < 1.36$) are shown in figure 6.3. The f^0 density matrix elements were computed by the method of moments, using the above expression, and the results obtained are given in the first column of table 6.2. The curves shown in the figure are those calculated using the results. The fits are quite good except in the $\cos \theta$ distribution $\sim \cos \theta = 0$. This and the negative, non-physical value of $\rho_{22} (-0.11 \pm 0.03)$ have been observed before in the f^0 region and are usually attributed to the presence of an S-wave background interfering with the dominant D-wave resonant signal. (Ref. 6.3).

The values of the density matrix elements as a function of t' are presented in table 6.2, together with the values obtained in this experiment for the channel 6.5. The diagonal elements for both channels are shown in figure 6.3b. The agreement between the two channels is excellent. This implies that the mechanism for the production of the f^0 may be the same in both channels. One pion exchange which is thought to dominate reaction 6.5 cannot therefore, be ruled out for this reaction.

6.2.3 The " η_N " region

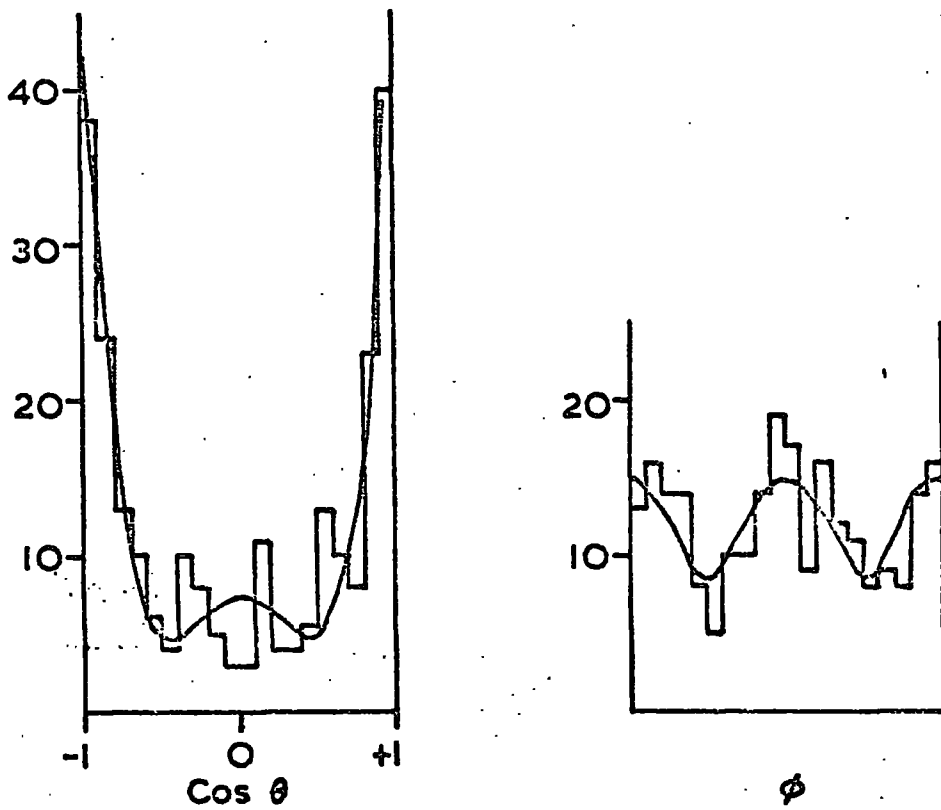
If the small enhancement (see Chapter 3) in the mass region ~ 1.08 GeV/c² is identified with the previously observed η_N dipion resonance, then it is of interest to investigate its spin characteristics. Previous direct observations of this enhancement have been in the channel:-



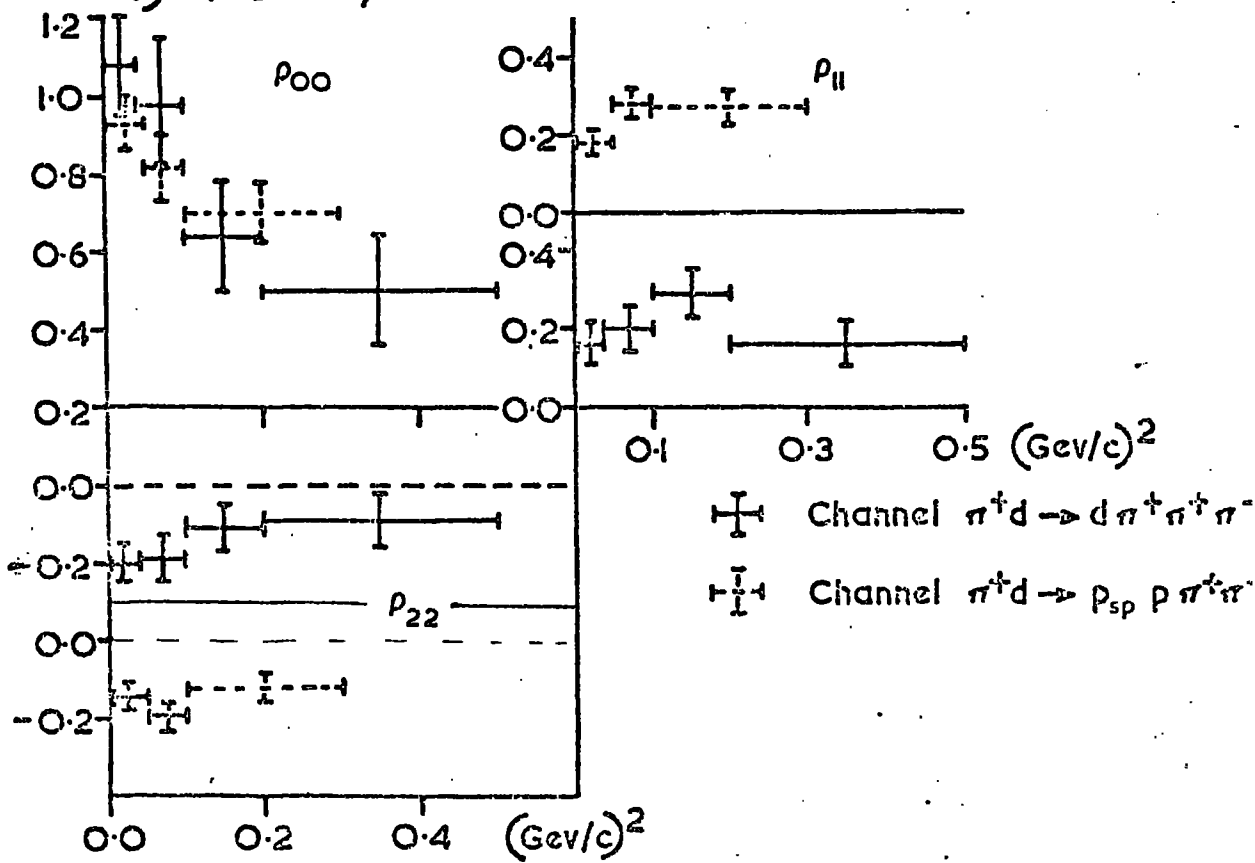
The results obtained have suggested that the spin of this enhancement is not zero, thus ruling out the hypothesis that the effect is a $\pi\pi$ decay mode of the S^* resonance which has been observed to decay into $K \bar{K}$. A difficulty has been, however, that a clear signal in the dipion mass spectrum is only seen when $\cos \theta < -0.75$ and this, coupled with the fact

FIG 6.3

a) f Decay angles



b) f Density matrix elements

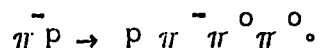


CHANNEL; t' RANGE;	$\pi^+ d \rightarrow d \pi^+ \pi^+ \pi^-$					$\pi^+ d \rightarrow pp \pi^+ \pi^-$		
	ALL	0.0-0.04	0.04-0.1	0.1-0.2	0.2-0.5	0.0-0.05	0.05-0.1	0.1-0.3
ELEMENT								
ρ_{00}	0.81 \pm 0.07	0.10 \pm 0.13	0.98 \pm 0.17	0.64 \pm 0.14	0.50 \pm 0.14	0.93 \pm 0.07	0.82 \pm 0.10	0.70 \pm 0.08
ρ_{11}	0.20 \pm 0.03	0.16 \pm 0.05	0.20 \pm 0.06	0.29 \pm 0.06	0.16 \pm 0.06	0.18 \pm 0.03	0.28 \pm 0.04	0.27 \pm 0.04
ρ_{22}	-0.11 \pm 0.03	-0.20 \pm 0.05	-0.19 \pm 0.06	-0.11 \pm 0.06	0.09 \pm 0.07	-0.14 \pm 0.03	-0.19 \pm 0.04	-0.12 \pm 0.03
ρ_{1-1}	-0.13 \pm 0.04	-0.02 \pm 0.06	-0.13 \pm 0.09	-0.10 \pm 0.07	-0.23 \pm 0.07	0.04 \pm 0.04	0.03 \pm 0.06	-0.02 \pm 0.04
$\rho_{2.2}$	-0.02 \pm 0.03	0.0 \pm 0.04	-0.01 \pm 0.05	-0.05 \pm 0.06	0.0 \pm 0.08	0.06 \pm 0.03	0.06 \pm 0.03	0.0 \pm 0.04
Re ρ_{21}	-0.08 \pm 0.02	0.02 \pm 0.04	0.02 \pm 0.05	-0.19 \pm 0.04	-0.14 \pm 0.06	-0.04 \pm 0.02	-0.09 \pm 0.03	-0.04 \pm 0.03
Re ρ_{2-1}	-0.01 \pm 0.02	-0.07 \pm 0.04	0.06 \pm 0.05	-0.06 \pm 0.05	0.12 \pm 0.06	0.0 \pm 0.02	0.02 \pm 0.03	0.01 \pm 0.03
Re ρ_{20}	0.01 \pm 0.02	0.05 \pm 0.03	0.03 \pm 0.04	-0.03 \pm 0.04	0.01 \pm 0.06	0.03 \pm 0.02	0.51 \pm 0.02	-0.01 \pm 0.02
Re ρ_{10}	-0.19 \pm 0.04	-0.06 \pm 0.07	-0.19 \pm 0.08	0.29 \pm 0.07	0.28 \pm 0.07	0.05 \pm 0.04	-0.16 \pm 0.05	-0.12 \pm 0.04

TABLE 6.2

The f^0 spin density matrix elements

that the channel is peripheral, implies that the positive pion is very fast in the laboratory system and cannot be recognised by ionization. It has been suggested that the effect may be due to misidentified reactions of the type:-



In the present channel this difficulty is not important but the low statistics and two possible combinations of $\pi^+ \pi^-$ make analysis rather complex and subject to misinterpretation.

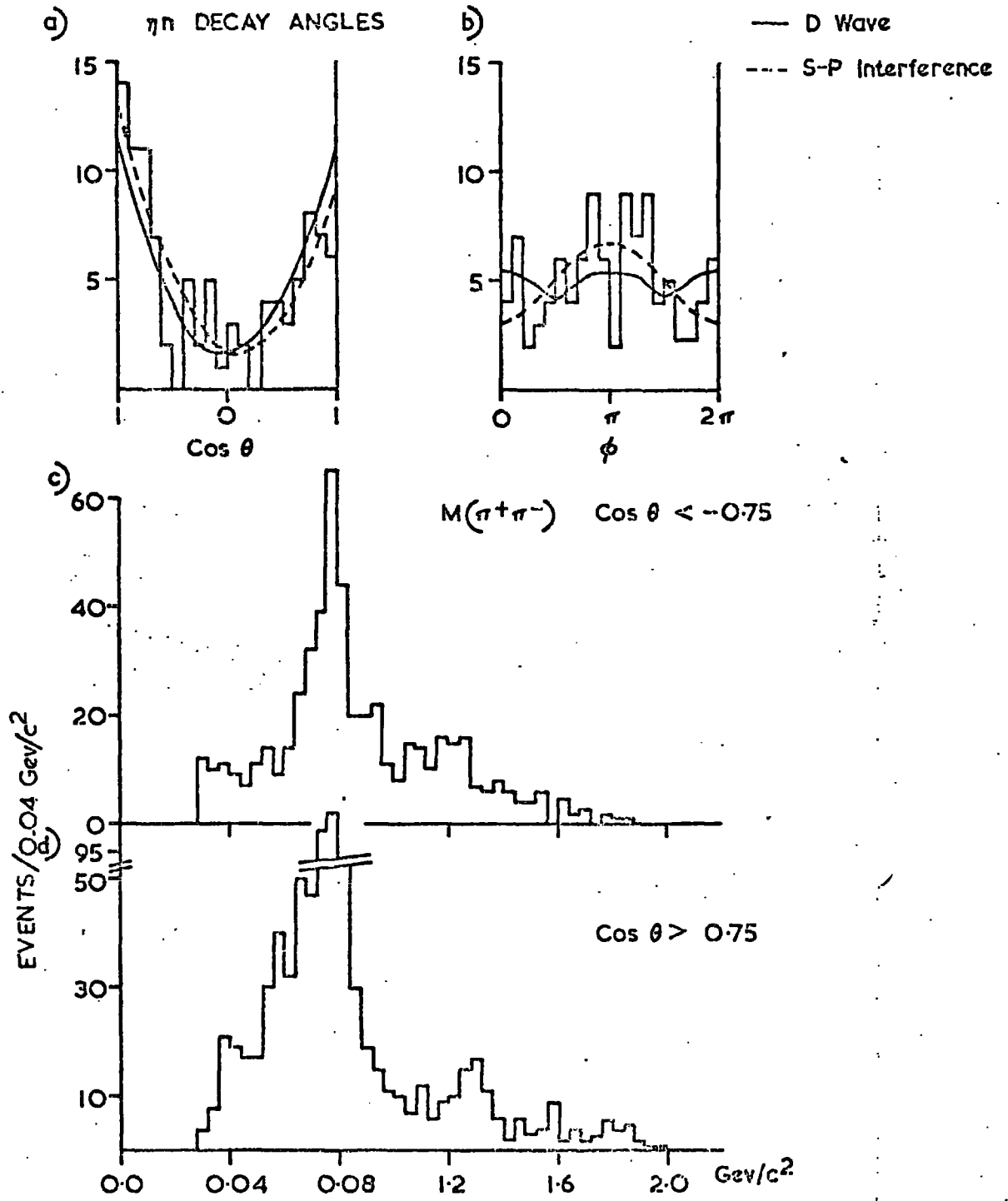
The decay angles of all dipion mass combinations falling in the η_N region (1.04 - 1.12 GeV/c²) are shown in figure 6.4. A pure S-wave can immediately be ruled out since this would imply isotropy of the $\cos \theta$ distribution. Assuming the isospin of the enhancement is 0 (no evidence for an enhancement in this mass region in any charged mode has been seen), then the symmetry of the dipion wave function implies that only spin parity assignments in the series:

$$J^P = 0^+, 2^+, 4^+, \dots \text{ are possible.}$$

Fits to a pure D-wave distribution and to an S-wave interfering with a P-wave from the ρ^0 tail have been made and are shown in figure 6.4. Both are adequate and fits to higher spins or including P-D interference have not been attempted.

It is interesting to note that the signal is stronger when $\cos \theta < -0.75$ (fig. 6.4c) than when $\cos \theta > 0.75$ (Fig. 6.4d) in this reaction as was the case in the previous experiments (Ref. 6.4). and if it is accepted that this enhancement is indeed due to production of the η_N meson, then this result tends to discredit the suggestion that earlier results were due to misidentification of events and support their conclusions that the spin is not zero.

FIG 6.4



6.3 Three Pion Systems

The decay angles of a three pion system are not uniquely defined as in the case of dipions, since different directions can be used as the analyser and a complete discription of the spin state cannot be achieved by using only one. In this section three directions have been used. These are:

(i) The normal to the decay plane of the 3-pion system in its own rest frame. This is defined as

$$\vec{N} = \vec{P}_{\pi s} \times \vec{P}_{\pi f}$$

where P refers to the momentum vector of the particle and the subscripts s and f refer to the slower and faster pions in the 3 pion rest frame.

(ii) The direction of one of the pions in the 3-pion rest frame. In order to eliminate the ambiguity between the identical positive pions, the negative pion has been chosen for this purpose.

(iii) Since the 3-pion enhancements to be discussed decay by a two step process, firstly into a pion and a dipion resonance, the direction of the resonance can be used as the analyser, thus treating the decay as a two body one.

6.3.1 Spherical Harmonic Moments

Since the spherical harmonics form a complete orthonormal set of functions, the decay distributions can be expressed as a sum of terms of the form:-

$$W(\theta, \phi) = \sum_{\ell=0}^{\ell_{\max}} \sum_{m=0}^{\ell} \alpha_{\ell m} Y_{\ell}^m(\theta, \phi)$$

where $\alpha_{\ell m}$ is the coefficient of each term. The average value of any particular harmonic is given by:

$$\langle Y_{\ell}^m \rangle = \frac{\int W(\theta, \phi) Y_{\ell}^{m*}(\theta, \phi) d \cos \theta d \phi}{\int W(\theta, \phi) d \cos \theta d \phi}$$

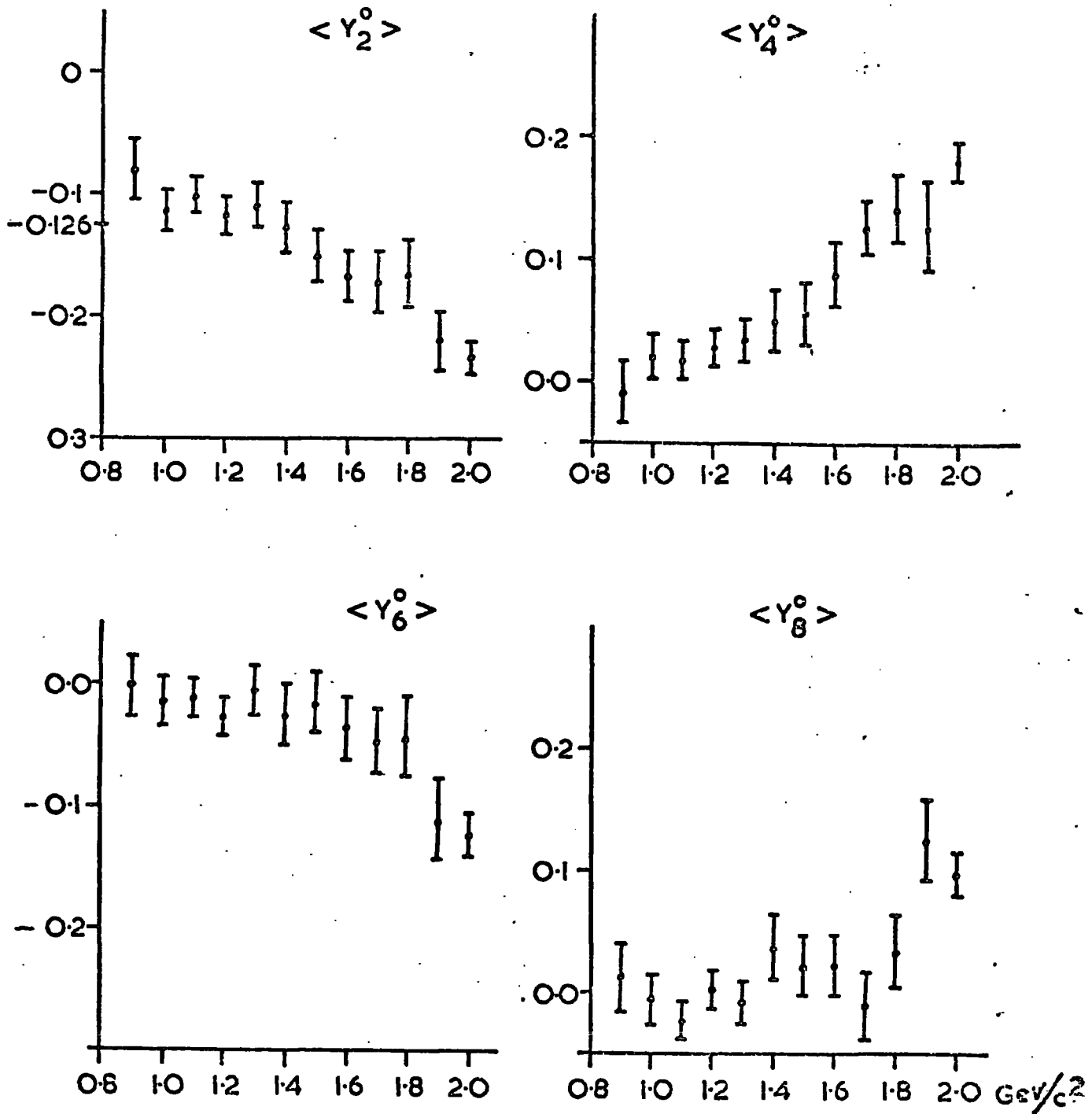
and this is equal to α_{ℓ}^m , due to the orthogonality of the spherical harmonics, (see appendix B for definitions). Thus, the values of α_{ℓ}^m can be determined directly from the data by taking the experimental average of the function. It is expected that only terms up to $\ell = 2J$ will be important for a resonance with spin J . When the normal to the decay plane is used, parity conservation implies that $\text{Re} Y_{\ell}^m = 0$ if ℓ is odd and this is found to be the case. The values of $\langle Y_{\ell}^m \rangle$ with m not equal to zero show no significant deviations from zero. This does not imply that m of the produced state is zero but does imply that its spin density matrix is diagonal. In the A_1 region only $\langle Y_2^0 \rangle$ is important implying that $J > 1$ is unlikely to have very much effect. If the A_1 is a pure $J^P = 1^+$ state with $m = 0$ then $\langle Y_2^0 \rangle$ is constrained to take the value -0.126 since the polar angle distribution is proportional to $\sin^2 \theta$. The data, although slightly below this value, is not incompatible with it.

The spherical harmonic moments with $\ell > 4$ remains small up to a mass value $\sim 1.85 \text{ GeV}/c^2$ implying that in the A_3 region only $J \leq 2$ occur. If $J = 2$ no direct prediction of the values of the moments can be made.

6.3.2 The A_1 Region

The A_1 region is defined as the 3π effective mass range $1.0 - 1.24 \text{ GeV}/c^2$. Greater values of the mass have been excluded because of the possibility of A_2 production, to be discussed in Chapter 9. The decay angular distributions of the normal to the decay plane are shown in figure 6.6. The $\cos \theta_N$ distribution is approximately described by $\sin^2 \theta_N$ while the ϕ_N distribution is compatible with isotropy. Assuming that the spin of the A_1 is less than 2, as indicated by the spherical harmonic

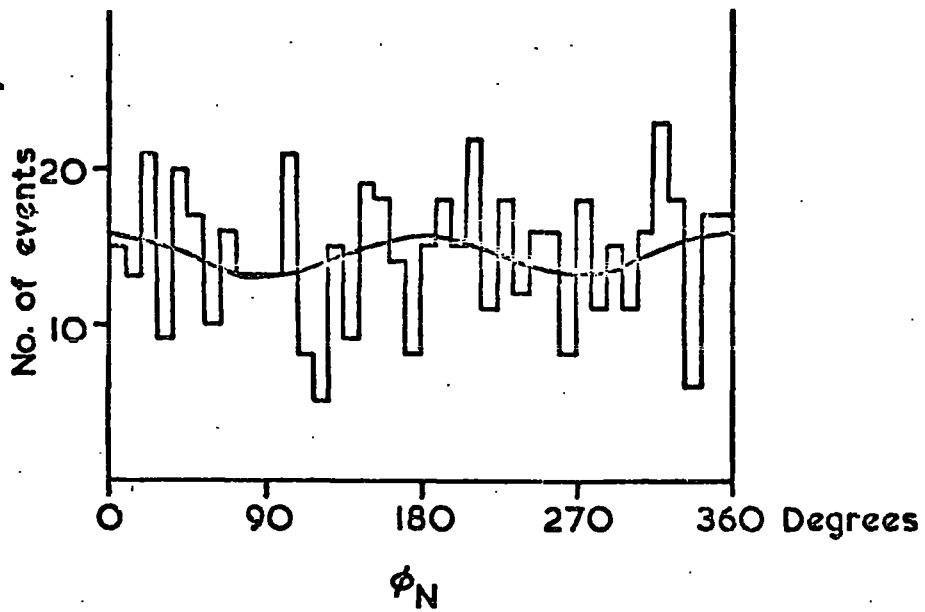
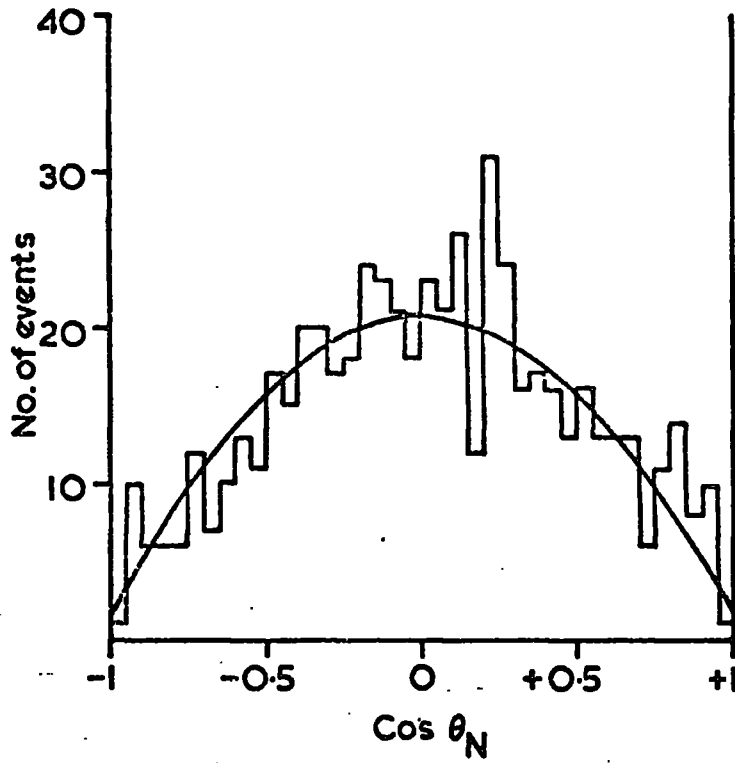
FIG 6.5



SPHERICAL HARMONIC MOMENTS OF THE NORMAL TO THE 3π DECAY PLANE AS A FUNCTION OF 3π MASS.

FIG 6.6

DECAY ANGLES OF THE NORMAL TO THE
PRODUCTION PLANE IN THE A_1 REGION.



moments, then the two possible J^P assignments are $J^P = 1^+$ or 1^- . Spin zero is incompatible with the $\cos\theta_N$ distribution, predicting isotropy. The decay distribution for $J^P = 1^-$ is described by:

$$W(\theta, \phi) = \frac{3}{8\pi} \left\{ \sin^2\theta + \rho_{00}(3\cos^2\theta - 1) - 2\sqrt{2} \sin 2\theta \cos\phi \operatorname{Re} \rho_{10} - 2 \sin^2\theta \cos 2\phi \rho_{1-1} \right\} \quad 6.10$$

while that for $J^P = 1^+$ is described by:

$$W(\theta, \phi) = \frac{3}{8\pi} \left\{ \frac{1 + \cos^2\theta}{2} + \rho_{00} \left(\frac{1 - 3\cos^2\theta}{2} \right) + \operatorname{Re} \rho_{10} 2\sqrt{2} \sin\theta \cos\theta \cos\phi + \rho_{1-1} \sin^2\theta \cos 2\phi - \lambda \operatorname{Im} \rho_{10} 2\sqrt{2} \sin\theta \cos\theta \right\} \quad 6.11$$

where $\lambda = R_1^- / R_1^+$ and R_1^- and R_1^+ contain the angle independent parts of the two possible decay amplitudes. λ is real and limited to the range:

$$|\lambda| < 1 \quad 6.12$$

and is zero when two of the decay particles are identical due to symmetry properties if one of the identical particles is chosen randomly. If, however, the two identical particles are labelled f and s as described above, a process equivalent to using only a half of the Daltiz Plot, then λ may not be zero (Ref. 6.5).

Both the relations 6.10 and 6.11 can give a $\sin^2\theta$ distribution of $\cos\theta_N$; the former if $\rho_{00} = 0$ and the latter if $\rho_{00} = 1$. Fits to this distribution of the two functions in fact yield $\rho_{00} = 0.08$ and $\rho_{00} = 0.85$ respectively and fit with equal probabilities.

The Morrison Rule (Ref. 6.6) for diffractively produced systems states that the change in spin (ΔJ) and parity (ΔP) between the initial and final states are related by:

$$\Delta P = (-1)^{\Delta J}$$

implying that the only possible J^P assignments when a pion beam is used are in the series $J^P = 0^- 1^+ 2^- \dots$. If the A_1 is produced diffractively this suggests that $J^P = 1^+$. Moreover, the value of $\rho_{00} - \rho_{11}$ for the ρ -mesons resulting from the decay of the A_1 is 0.72 ± 0.06 implying a very high value of ρ_{00} . It seems unlikely that an A_1 with a large longitudinal alignment (ρ_{00} small) would decay into a ρ^0 with such a large transverse alignment. It is concluded, therefore, that the A_1 region is predominantly $J^P = 1^+$.

The density matrix elements of the A_1 , assuming it is a pure $J^P = 1^+$ state, have been calculated by the method of moments and the results are presented in table 6.3. The curves in figure 6.6 are those calculated using the values found and it can be seen that the agreement between the experimental data and the curves is good. No discussion of the variation of the density matrix elements with t will be given here since this is directly concerned with the question of helicity conservation. A complete discussion of this is given in the next chapter.

A $J^P = 1^+$ object decaying into a 0^- and 1^- system can do so either through an S-wave ($L=0$) or a D-wave ($L=2$). Since the A_1 is near threshold of the $\rho\pi$ system, it might be expected that the S-wave is predominant. To test this assumption, the distribution of the ρ^0 direction in the Gottfried-Jackson frame can be examined. A pure 1^+ state decaying entirely to $\rho\pi$ gives for these angles (Ref. 6.7).

$$W(\theta, \phi) = \frac{1}{4\pi} + \frac{\mu}{4\pi} \left\{ \frac{1}{2} (3\rho_{00} - 1)(3 \cos^2 \theta - 1) - 3\rho_{1-1} \sin^2 \theta \cos 2\phi - 3\sqrt{2} \operatorname{Re} \rho_{10} \sin 2\theta \cos \phi \right\} \quad 6.13$$

In this expression μ is related to the amount of D-wave present in the decay and is 0 if D-wave is absent. Using the method of moments, values of $\mu\rho_{00}$ can be found from this expression and, since ρ_{00} in 6.13 should be the same here as when the normal was used as the analyser, μ

can be determined.

Figure 6.7a shows the distribution of $\cos \Theta$, using the ρ direction as the analyser. In the figure, if both $\pi^+ \pi^-$ combinations have an effective mass in the ρ region, both values of $\cos \Theta$ have been plotted with weight 1 (outer histogram and with weight $\frac{1}{2}$ (inner hatched histogram). It is clear that the distribution is not flat, indicating that D-wave decay is present to some extent. It must be noted, however, that the anisotropy is less marked when the two ρ events are weighted by $\frac{1}{2}$. This implies that the peaking of the distribution $\sim \cos \Theta \pm 1$ is correlated with the $\rho\rho$ overlap region and may be due to interference between the two possible $\rho\pi$ decays. Assuming this not to be the case μ has been determined as 0.29 ± 0.02 from the weighted histogram. μ has also been determined throughout the mass range $0.95 \rightarrow 1.35$ in mass bins of $50 \text{ MeV}/c^2$ in order to determine where the D-wave becomes important, and the results are given in table 6.4 It is clear that the D wave contribution is important only above $1.1 \text{ GeV}/c^2$, i.e. in the upper half of the A_1 .

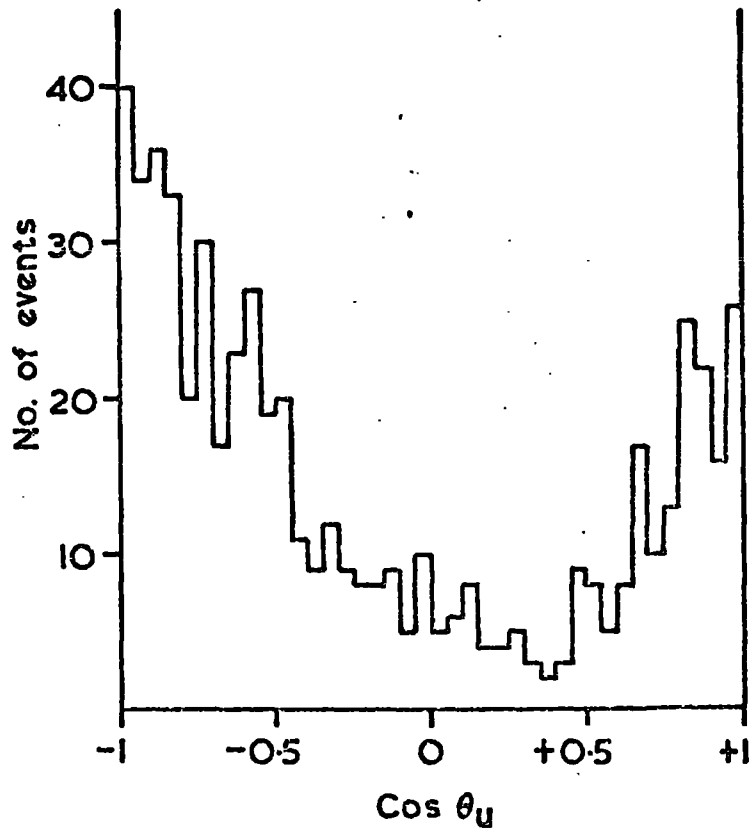
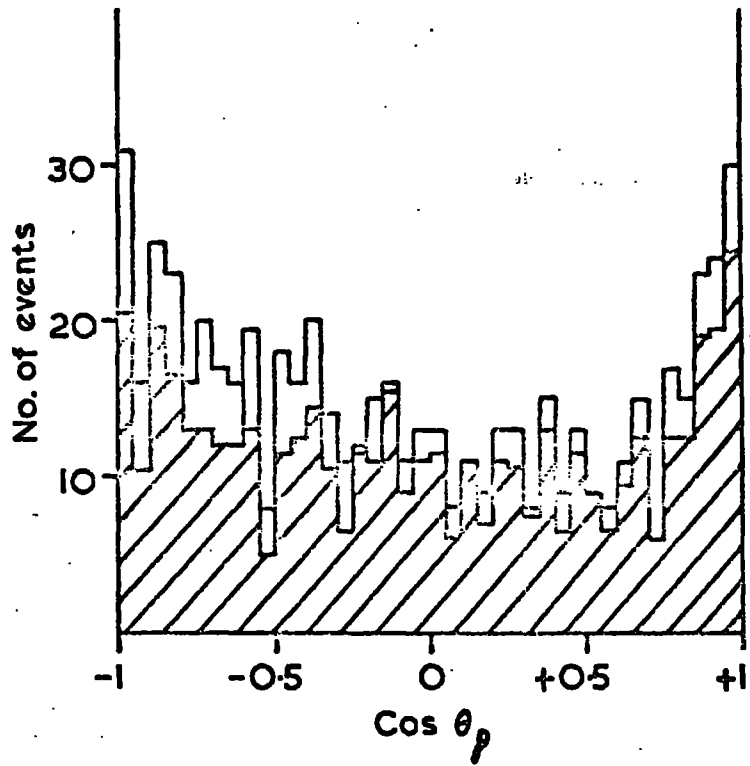
The above discussion is based on the hypothesis that the A_1 is a pure $J^P = 1^+$ state. Evidence that this is not the case is given in figure 6.7b) where the distribution of $\cos \Theta_U$ (the polar angle of the unambiguously charged pion) is shown. For a 1^+ object the predicted distribution of this angle is given by:-

$$W(\cos \Theta, \phi) = \frac{3}{8\pi} \left[2A + (1-3A) \left\{ \frac{1 + \cos^2 \Theta}{2} + \rho_{00} \frac{(1-3 \cos^2 \Theta)}{2} + 2\sqrt{2} \sin \Theta \cos \Theta \cos \phi \operatorname{Re} \rho_{10} + \sin^2 \Theta \cos 2\phi \rho_{1-1} \right\} \right]$$

where $A = \frac{R_0}{2R_1^+ + R_0}$ and $0 < A < 1$.

FIG 6.7

A₁ DECAY DISTRIBUTIONS



This expression is unable to account for the strong asymmetry present in the data. The asymmetry is indicative of a state of opposite parity interfering with the dominant 1^+ state. It can be related to the fact that the ρ^0 , resulting from the decay of the A_1 , decays asymmetrically due to interference with an S-wave, dipion state, the ϵ . Thus the A_1 can be thought of as a mixture of $\rho\pi$ and $\epsilon\pi$. If the $\epsilon\pi$ is in an S-wave state, the spin parity will be 0^- and would cause an asymmetry. If this is the case then Equation 6.14 above should contain extra terms of the form.

$$\alpha \cos \theta + \beta \sin \theta \cos \phi .$$

The resulting expression can explain an asymmetry in both the $\cos \theta$ distribution and the ϕ distribution. There is no experimental evidence for an asymmetry in the ϕ distribution. The values of α and β have been determined by the method of moments and the results given:

$$\alpha = -0.20 \pm 0.04$$

$$\beta = -0.05 \pm 0.03.$$

In order to determine any variation of these parameters throughout the mass range 0.95 - 1.35, they were recalculated in mass bins of 50 MeV/c² and the results are given in table 6.4. α reaches a maximum in the central A_1 mass region while β is never more than two standard deviations away from 0 and is particularly small in the central A_1 region.

In conclusion the A_1 seems to be predominantly an S-wave $\pi\rho$ state ($J^P = 1^+$) but there is also some admixture of opposite parity which may be an S-wave $\pi\epsilon$ state ($J^P = 0^-$). There is also some indication of D-wave $\pi\epsilon$ decay but the evidence for this is rather speculative.

ELEMENT :	ρ_{00}	ρ_{1-1}	$\text{Re}\rho_{10}$	$\lambda\text{Im}\rho_{10}$
VALUE :	0.91	0.08	-0.05	0.02
ERROR :	0.07	0.06	0.04	0.02

TABLE 6.3

The A_1 spin density matrix elements

3π mass region. (GeV/c ²)	μ	α	β
0.95 - 1.00	0.07 ± 0.31	-0.36 ± 0.11	-0.21 ± 0.08
1.00 - 1.05	0.12 ± 0.28	-0.14 ± 0.09	-0.13 ± 0.07
1.05 - 1.10	0.20 ± 0.25	-0.26 ± 0.08	-0.08 ± 0.05
1.10 - 1.15	0.25 ± 0.25	-0.23 ± 0.07	-0.0 ± 0.04
1.15 - 1.20	0.43 ± 0.25	-0.17 ± 0.08	-0.02 ± 0.04
1.20 - 1.25	0.50 ± 0.30	-0.17 ± 0.08	-0.12 ± 0.06
1.25 - 1.30	0.59 ± 0.31	-0.16 ± 0.08	-0.02 ± 0.05
1.30 - 1.35	0.43 ± 0.38	-0.03 ± 0.08	-0.09 ± 0.07

TABLE 6.4

The values of μ , α and β through the A_1 region

6.3.3 The A_3 region

The distributions of $\cos \theta_N$ and ϕ_N , the decay angles of the normal to the production plane, for events in the A_3 region are shown in figure 6.8a. The A_3 region is defined here as all those events which have a 3-pion mass in the range $1.44 - 1.8 \text{ GeV}/c^2$ and at least one neutral dipion mass in the f^0 region, together with those other events in the same 3-pion mass range which have neither neutral dipion mass in the ρ^0 region. These rejected events account for the $\rho^0\pi$ peak $1.56 \text{ GeV}/c^2$ which may not be due to A_3 production. While the ϕ_N distribution is compatible with isotropy, that of $\cos \theta_N$ is peaked $\sim \cos \theta_N = 0$ and this implies a low value of ρ_{00} if the spin parity of the A_3 is in the series:

$$J^P = 1^-, 2^+, 3^-, 4^+ \dots$$

The value of ρ_{00} of the f^0 resulting from the decay of the A_3 has been evaluated as 0.74 ± 0.08 which, as in the case of the A_1 , would imply that ρ_{00} of the A_3 is also high. This, together with the Morrison Rule if the A_3 is diffractively produced, suggests that the J^P assignment for the A_3 is in the series:

$$J^P = 1^+, 2^-, 3^+ \dots$$

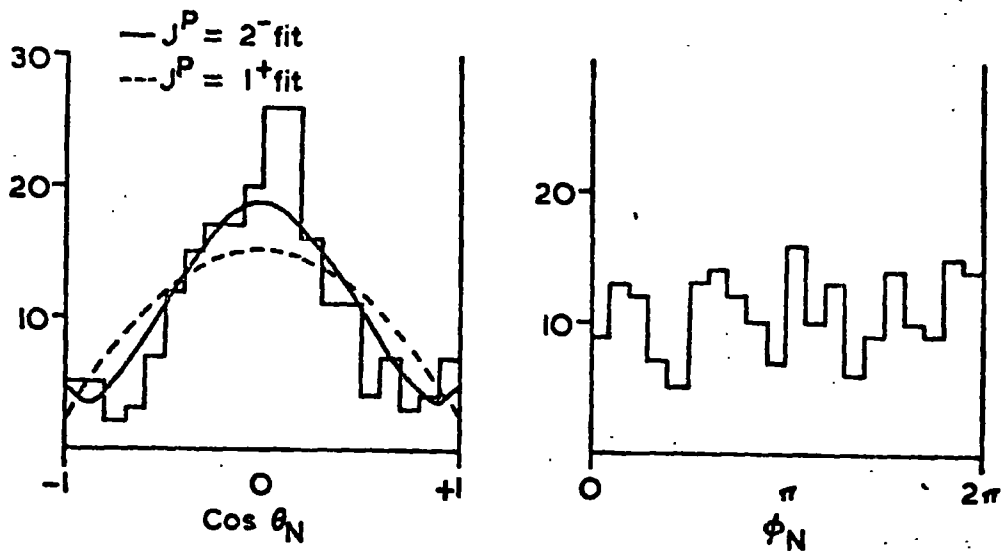
If $J^P = 1^+$ then the polar angle distribution should be described by Equation 6.11 integrated over ϕ , i.e.:-

$$W(\theta) = \frac{3}{4} \left\{ \frac{1 + \cos^2 \theta}{2} + \rho_{00} \left(\frac{1 - 3 \cos^2 \theta}{2} \right) \right\} \quad 6.15$$

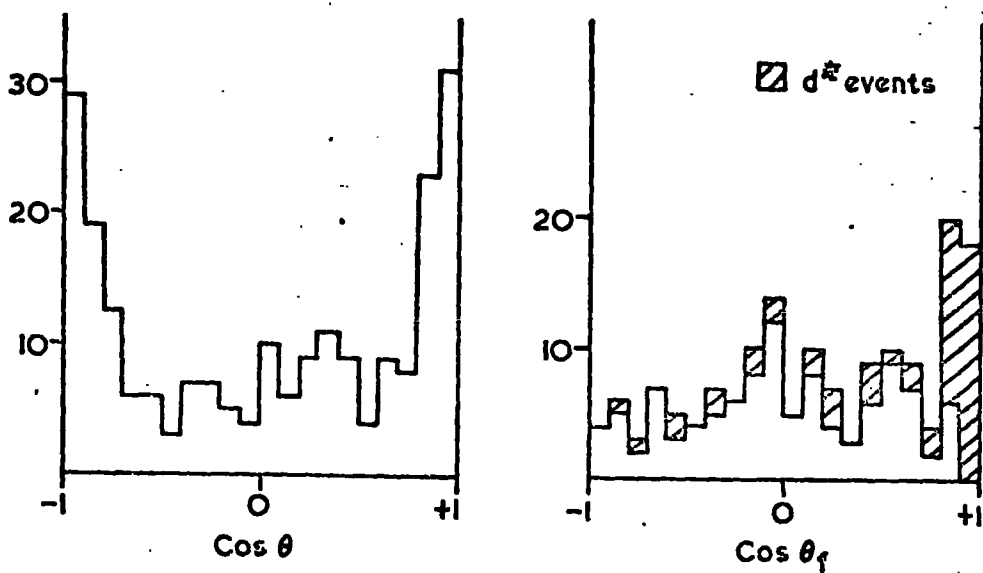
This expression has been fitted to the data and the best fit ($\rho_{00} = 0.87$) is shown in figure 6.8a as the dashed curve. The fit is very poor with a χ^2 probability of less than 1%. The distribution for $J^P = 2^-$ is given by:

FIG 6.8

d) A_3 DISTRIBUTIONS OF THE NORMAL TO THE DECAY PLANE



b) POLAR ANGLE OF π^- FOR A_3 EVENTS. c) POLAR ANGLE OF ρ^0 FOR A_3 EVENTS.



$$\begin{aligned}
 W(\theta) = & (\alpha + 6) \left\{ \frac{5}{8} \rho_{00} - \frac{5}{4} \rho_{11} + \frac{1}{3} \right\} \sin^4 \theta \\
 & + \left\{ \rho_{00} (\alpha - 6) + \rho_{11} (4\alpha + 6) - \alpha \right\} \sin^2 \theta \\
 & + \rho_{00} (2 - \alpha) - 2 \alpha \rho_{11} + \alpha
 \end{aligned} \tag{6.16}$$

where $\alpha = \frac{R_2^+}{R_0}$ > 0 and R_2^+ and R_0 are independent of the decay angles as in the previous section.

The result of fitting this expression is shown as the solid curve in figure 5.8a. The fitted parameters are:

$$\rho_{00} = 0.91 \pm 0.06$$

$$\rho_{11} = 0.01 \pm 0.05$$

$$\alpha = 20.$$

with a χ^2 confidence level of ~30%. The fit was very insensitive to the value of α .

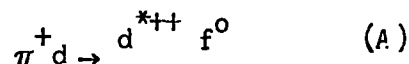
The distribution has also been fitted to the expression for $J^P = 3^+$ and an equally adequate confidence level achieved, but the small value of the spherical harmonic moment $\langle Y_6^0 \rangle$ in this region renders such a spin assignment unlikely.

In conclusion, the most likely J^P value of the A_3 meson produced in this experiment is 2^- . This result, moreover, is unaltered when every event in the given mass range is used, and when only $f_{\pi^+}^0$ events are used.

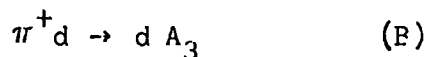
Interference between the dominant 2^- state with some other spin-parity is not necessarily clear when the normal to the decay plane is used as the analyser, as was the case in the A_1 region. To test for this the direction of the unambiguously charged pion has been used as the analyser and the polar angle distribution is shown in figure 6.8b. Interference with a state of opposite parity would manifest itself

in this figure as an asymmetry around $\cos \theta_u = 0$. No clear asymmetry is apparent in the data. The asymmetry parameter A , as defined in equation 6.2, is found to be 0.10 ± 0.07 which is not significantly different from 0, and no evidence for such an interference is present. If the interfering state had the same parity, then the effect on this distribution would be more subtle and the present statistics are not sufficient to investigate this hypothesis.

An $f^0 \pi^+$ state with spin parity $J^P = 2^-$ can decay via an S-wave or D-wave. Since the A_3 is near threshold the S-wave may be expected to dominate and this would lead to an isotropic distribution of the polar angle when direction of the f^0 is used as analyser. The experimental distribution of this angle is shown in figure 5.8c. It is quite isotropic except for a peak above $\cos \theta_f = 0.8$. This peak cannot be interpreted as evidence for a D-wave decay of the A_3 , however, since this would lead to a symmetric distribution. The peak is due to contamination of the A_3 sample by events of the type:



as can be seen from the hatched histogram which corresponds to events with at least one $\pi^+ d$ mass in the d^* region. If a weight of $\frac{1}{2}$ is given to such events the resulting spectrum does not deviate strongly from isotropy. Although this procedure is rather arbitrary there is no more rigorous way of separating events of type A above from those of the type



There is, thus, no evidence for a D-wave decay of the A_3 .

In summary, the A_3 produced in this reaction is compatible with a pure S-wave $J^P = 2^- f^0 \pi$ system.

6.3.3 The " $A_{2.5}$ " region

In this section the decay angles of the $\rho\pi$ enhancement ~ 1.56 GeV/c^2 , tentatively named the $A_{2.5}$ in chapter 4 are examined. The events used are those in the mass range $1.52 < M(3\pi) < 1.6$ GeV/c^2 which have at least one neutral dipion combination in the ρ^0 region. The purpose of this is twofold.

(i) To determine whether the enhancement has a well defined spin-parity, since any resonant interpretation of the peak depends upon this criterion.

(ii) To attempt to find any differences between this enhancement and the A_3 , for otherwise it may be the result of a statistical fluctuation within the A_3 .

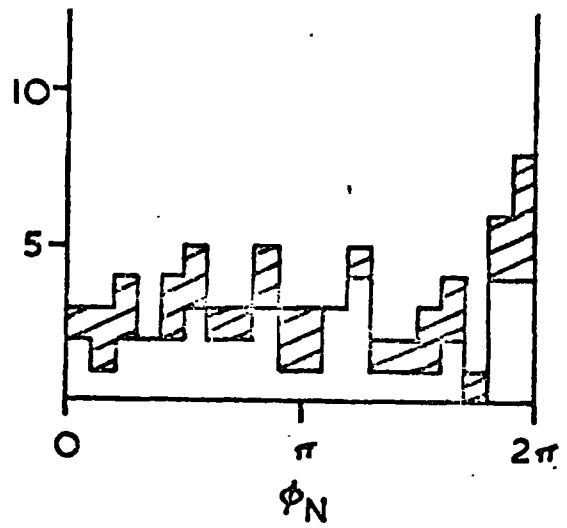
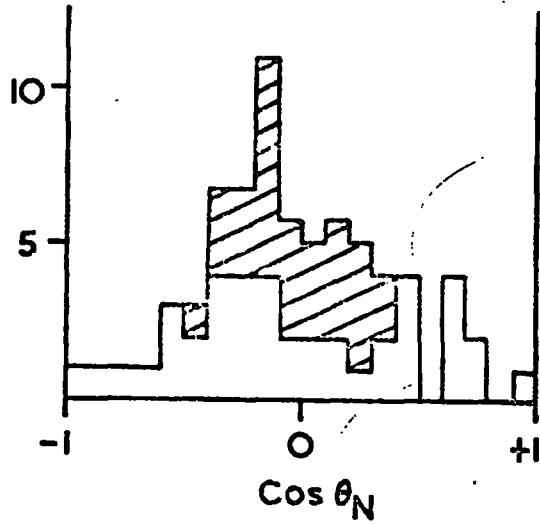
The lack of statistics makes any fitting of decay distributions impossible and the discussion must remain, at best, qualitative.

The distribution of the decay angles of the normal to the decay plane for " $A_{2.5}$ " events are shown in figure 6.9a, together with the polar angles of the unambiguously charged pion (fig. 6.9b) and of the direction of the ρ^0 (fig. 6.9c). The most noticeable difference between these distributions and those of the A_3 is in the final one, where the large anisotropy cannot be dismissed by weighting d^* events by $\frac{1}{2}$ as in the case of the A_3 . It is necessary to remove all d^* events (hatched regions of the histograms), and even then a small anisotropy remains. After removal of d^* events the sample is too small to be able to compare even qualitatively with the A_3 . Furthermore, since 43% of the " $A_{2.5}$ " events are also d^* events (c.f. 24% in the A_3 region) removal of these will reduce the signal into total insignificance. In order to accept this enhancement as more than a kinematical effect of d^* production it is also necessary to accept asymmetries in the $\cos \theta_\rho$ and the $\cos \theta_u$ distributions, together with a small anisotropy in the ϕ_N distribution,

FIG 6.9

"A₂₅" DECAY DISTRIBUTIONS

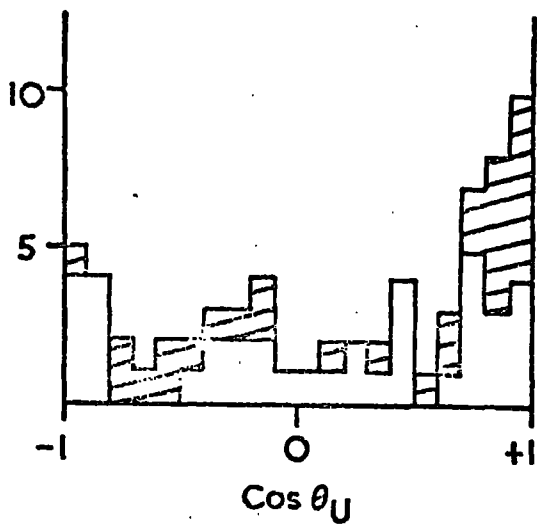
a) Normal to decay plane



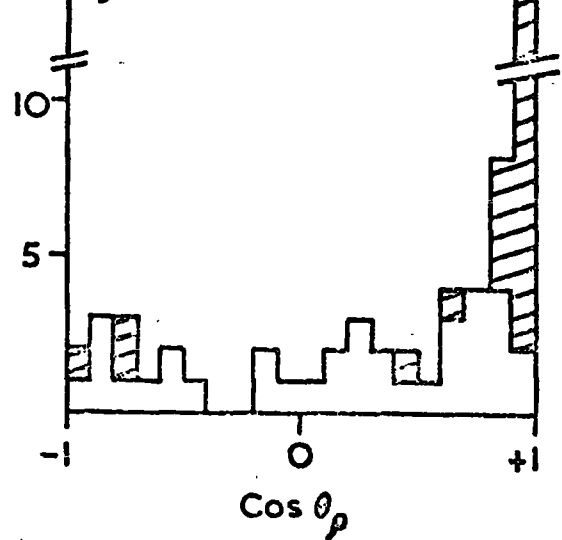
▨ d* included

□ d* excluded

b) π^-



c) ρ^0



all of which suggest that it is not in a pure spin state.

The small size of the signal, coupled with the high d^* background and the asymmetric decay distributions indicate that the signal is most unlikely to be resonant.

CHAPTER SEVEN

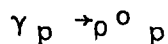
EXPERIMENTAL TESTS OF HELICITY CONSERVATION

Introduction

There has been considerable interest recently in the question of conservation of helicity in reactions which are thought to be diffractive i.e. which are dominated by Pomeron exchange. The problem is to discover, for such events, if helicity is conserved either in the s-channel or in the t-channel or in neither of these.

The helicity of a particle is defined as the projection of the particles spin along the direction of motion, and information about this can be found by studying the decay angular distribution of the state produced. If s-channel helicity conservation (S.C.H.C) is to be investigated then the frame of reference used is the helicity frame (see Appendix B) where the polar axis is equivalent to the direction of motion of the produced state in the overall centre of mass system, On the otherhand if t-channel helicity conservation (TCHC) is being studied, the Gottfried-Jackson reference frame is used since here the polar axis is equivalent to the direction of the produced state in the centre of mass system of the t-channel.

Evidence has been presented (Ref. 7.1) in the study of elastic πN interactions, which are thought to proceed by Pomeron exchange, suggesting that helicity is conserved in the s-channel rather than the t-channel. SCHC has been shown to hold (Ref. 7.2) in the ρ -photo-production reaction:



and this reaction is also diffractive. Gilman et al (Ref. 7.3) consequently made the hypothesis that all diffractive processes conserve helicity in the s-channel and not in the t-channel. If this is the case

then A_1 and A_3 production, (and also Q and L production), which are thought to be produced diffractively; ought to show SCHC and not TCHC.

Several experiments on A_1 and Q production (Ref. 7.4) however, have shown a strong discrepancy with SCHC and suggest that in these reactions helicity is conserved in the t-channel, thus contradicting the Gilman hypothesis if the A_1 and Q enhancements are indeed produced diffractively. Production of these states shows the characteristics of diffractive dissociation reactions: steep slope of $d\sigma/dt$, cross section independent of incident energy etc. and their spin-parity assignments agree with the Morrison Rule (Chap. 6.) for diffractive processes. Frautschi (Ref. 7.5) however, has proposed an alternative rule for diffractive processes, based on the SU(6) quark model, which suggest that the A_1 and Q mesons cannot be produced in this way and hence need not show SCHC. A_3 production, however, can proceed by a diffractive mechanism according to both the Frautschi Rule and the Morrison Rule. Observation of SCHC in A_3 production would thus support the Frautschi Rule and Gilman hypothesis at the expense of the Morrison Rule while TCHC would disprove the Gilman hypothesis and support the Morrison Rule. Paler et al. (Ref. 7.6) have presented some evidence for TCHC in A_3 production.

Furthermore a slight indication of non-conservation of TCHC as well as SCHC, in diffractive A_1 production has been observed by some authors (Ref. 7.7).

In this chapter, an investigation is made of the conservation of helicity for both the A_1 and A_3 enhancement. The reaction being studied has an advantage over non-coherent channels in that the coherence of the deuteron acts as a filter to other processes (such

as ρ exchange) which can occur with a nucleon target, and gives a cleaner sample of diffractive events. For example, the A_1 does not suffer from the complication of a large background due to nearby A_2 production. There is a disadvantage in the channel, however, since the momentum transfer to the deuteron is necessarily small to ensure coherence, and this implies that the angle between the s-channel and t-channel polar axes remains small. In spite of this disadvantage, differences between distributions in the two reference frames can be clearly seen.

Section 1 gives a discussion of the density matrix elements of the A_1 and A_3 in the Gottfried-Jackson and helicity reference frames. In section 2 a spin-independent method of testing helicity conservation based on the use of spherical harmonic moments is discussed, while section 3 makes use of a method based on the longitudinal phase space plot. Section 4 gives a brief conclusion.

7.1 Density Matrix Elements Analysis

The prediction of helicity conservation for the spin density matrix elements of the produced state when a pion beam is used is particularly simple. Since the incident pion has spin zero, its helicity is necessarily zero and thus, if SCHC holds, the helicity of the produced A_1 or A_3 must also be zero i.e. ρ_{00} of the meson in the helicity frame must be 1 and all other elements must be zero, implying total alignment of the spin, in a direction perpendicular to the direction of motion. Similarly, if TCHC holds, the same predictions are made for the density matrix elements in the Gottfried-Jackson frame.

7.1.1 The A_1 meson

Assuming that the A_1 enhancement is a pure $J^P = 1^+$ state then the decay distribution of the normal to the decay plane is described by Eq. 6.11 of the previous chapter. Defining the A_1 region to be

$1.0 < M(3\pi) < 1.24 \text{ GeV}/c^2$ as previously, the density matrix elements of the A_1 have been determined, by the method of moments, for various regions of the square of the 4-momentum transfer to the $A_1(t)$, in both the helicity and G-J frames. The results of this are presented in table 7.1 and are plotted in fig. 7.1. It can be seen that all the elements except ρ_{00} are compatible with zero in both reference frames. In the G-J frame ρ_{00} is compatible with 1 up to $t = 0.04 \text{ (GeV}/c)^2$ becoming smaller by slightly more than one standard deviation above this. Its value in the highest region ($0.08-0.12 \text{ (GeV}/c)^2$) of ~ 0.7 is rather low but the error on this is large due to the small statistics in this t region. In general then, no clear evidence for a non-conservation of helicity in the t -channel is apparent. In the helicity frame, ρ_{00} is compatible with 1 only in the very lowest t region; between $t = 0.02$ and $0.08 \text{ (GeV}/c)^2$ it is not strongly in disagreement with the predicted value of 1 (within 2 standard deviations) although it is consistently lower than the corresponding value in the G-J frame; in the highest t region the value of 0.26 ± 0.26 is strongly incompatible with unity in spite of the large error and presents firm evidence for non-conservation of helicity in the s -channel in this reaction.

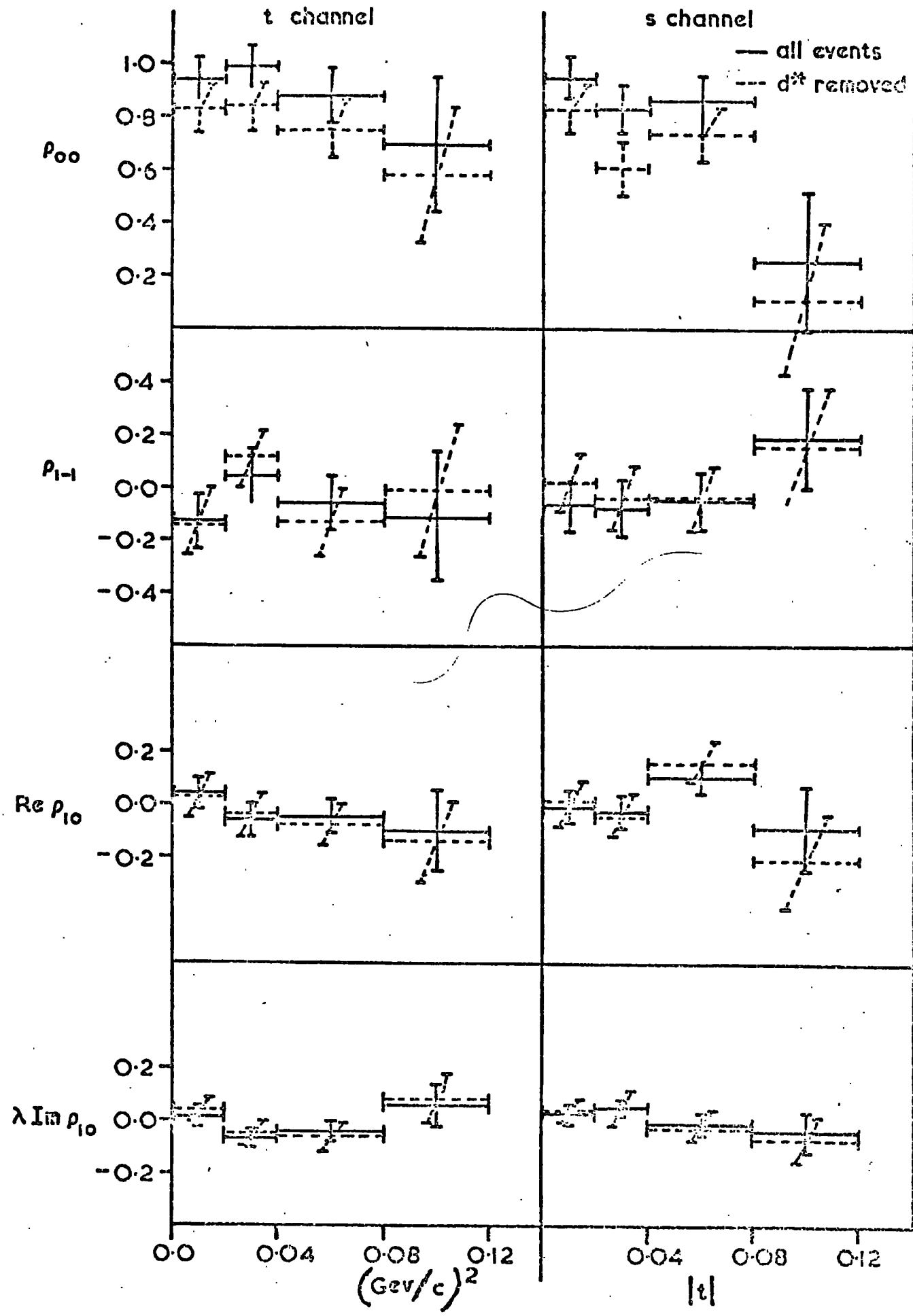
A possible source of error in the above calculations is that all events in the given mass region have been included in the analysis, irrespective of whether there is simultaneous production of the d^* . Since the d^* is not produced diffractively, its effects may lead to biased results. On the other hand, there is background below the d^* signal which may correspond to a particular configuration of the 3π system and to exclude all events in the d^* region ($M(c\pi^+) < 2.4 \text{ GeV}/c^2$) may lead to a bias in the decay angular distribution of the tripion state. The density matrix elements, however, have been recalculated

FIG 7.1

A_1 Density Matrix Elements

G-J FRAME

HELICITY FRAME



t range (GeV/c) ²	G-J FRAME				HELICITY FRAME			
	ρ_{00}	ρ_{1-1}	$\text{Re } \rho_{10}$	$\lambda_{\text{Im} \rho_{10}}$	ρ_{00}	ρ_{1-1}	$\text{Re } \rho_{10}$	$\lambda_{\text{Im} \rho_{10}}$
0.0-0.02	0.94±0.08	-0.13±0.10	0.04±0.06	0.01±0.03	0.95±0.08	-0.06±0.10	-0.01±0.06	0.03±0.03
0.02-0.04	0.99±0.08	0.04±0.10	-0.06±0.06	-0.07±0.03	0.82±0.10	-0.08±0.10	-0.03±0.06	0.05±0.03
0.04-0.08	0.88±0.10	-0.06±0.10	-0.05±0.06	-0.04±0.03	0.86±0.10	-0.05±0.11	0.10±0.06	-0.01±0.04
0.08-0.12	0.70±0.25	-0.11±0.24	-0.10±0.15	0.06±0.08	0.26±0.26	0.19±0.19	-0.09±0.15	-0.04±0.07
0.0 -0.02	0.83±0.10	-0.12±0.12	0.03±0.08	0.04±0.04	0.82±0.10	0.02±0.11	0.01±0.08	0.04±0.04
0.02-0.04	0.84±0.10	0.11±0.12	-0.04±0.08	-0.05±0.05	0.61±0.10	-0.04±0.12	-0.04±0.08	0.05±0.06
0.04-0.08	0.75±0.11	-0.13±0.13	-0.08±0.08	-0.06±0.05	0.74±0.10	-0.04±0.12	0.16±0.08	-0.03±0.06
0.08-0.12	0.58±0.26	-0.01±0.25	-0.14±0.15	0.08±0.10	0.11±0.29	0.16±0.22	-0.21±0.18	-0.07±0.09

TABLE 7.1

The A_1 spin density matrix elements for several t regions

excluding d^* events and the results are presented in table 7.1 and figure 7.1 (dashed lines). There is little change in any of the density matrix elements except for ρ_{00} , where the effect of the cut is systematically to reduce the value by ~ 0.1 or 0.2 . The fact that the effect is so systematic implies that those events which have both a d^* and a A_1 signal do in fact correspond to a particular configuration of the 3π system with a clustering of events $\sim \cos \theta = 0$, thus raising the value of ρ_{00} and a bias is inherent in the result, whether or not d^* events are included, if it is assumed that some of the background below the d^* signal is due to diffractive A_1 production. However it can be safely assumed that the true values of the density matrix elements fall somewhere between the two calculated ones. With this assumption, the conclusion of non-conservation of s-channel helicity is strengthened and the tendency, noted above, for ρ_{00} in the G-J frame to decrease with increasing t becomes more noticeable.

The above discussion is based on the assumption that the state is a pure $J^P = 1^+$. In fact it was demonstrated in the previous chapter that there is some admixture of another state of opposite parity. If it is assumed that the admixture is an s-wave $\pi\pi$ state ($J^P = 0^-$) then the calculated values of the density matrix elements are not the true values of the $J^P = 1^+$ state but some combination of these with modifications due to the interfering state. Defining δ to be the relative cross section for production of the 0^- to the 1^+ state then:

$$\rho'_{00} = \frac{\rho_{00} + \delta/3}{1 + \delta}$$

$$\text{and } \rho'_{ij} = \frac{\rho_{ij}}{1 + \delta} \quad i = j$$

where ρ'_{ij} are the experimentally determined values and ρ_{ij} are the true values of the 1^+ state.

Thus the calculated value of ρ_{00} will be smaller than the true value if the calculated value is greater than .33 and vice versa. The effect on the other elements will be small if δ is not very large. In the s-channel the value of ρ_{00} will thus be smaller than the observed value of 0.26 in the highest t-region and non-conservation of helicity in the s-channel is clearer. In the t-channel the true value of ρ_{00} will be higher than the measured value throughout the t range and TCHC will become even more compatible with the results.

7.1.2 The A_3 meson

The A_3 meson has been shown to have spin and parity $J^P = 2^-$ in the preceding chapter. The distribution of the polar angle of the normal to the production plane for such a state is described by Eq.6.16 of that chapter. A maximum likelihood fit of the experimental distributions in three intervals of t' has been made to this expression with the values of ρ_{00} and ρ_{11} being allowed to vary. The value of α the part of the function independent of the angles, equal to R_2^+/R_0 , was fixed at 20 in the fitting since its value was found to have little effect on the fit even when the complete A_3 sample was used (see chapter 6). A problem was found in that in the lowest t' interval very large non-physical values were given for ρ_{00} and large negative values were found for ρ_{11} . This was true also to a lesser extent in the second t' interval. In the highest and, from the point of view of testing helicity conservation, the most important t' range no such problem occurred. In order to counteract this effect ρ_{11} was restricted to positive values and likelihoods of comparable magnitude were obtained.

The A_3 region was defined, as in the previous chapter, as $1.44 < M(3\pi) < 1.8 \text{ GeV}/c^2$, except for those events with at least one dipion mass combination in the ρ^0 region and neither dipion mass in the f^0 region. This anti-selects the $\rho^0\pi$ peak, $A_{2.5}$, which was considered

to be statistical and not due to A_3 production. The effect of retaining these events in the sample has been checked, however, and found to have little effect on the values obtained for the density matrix elements.

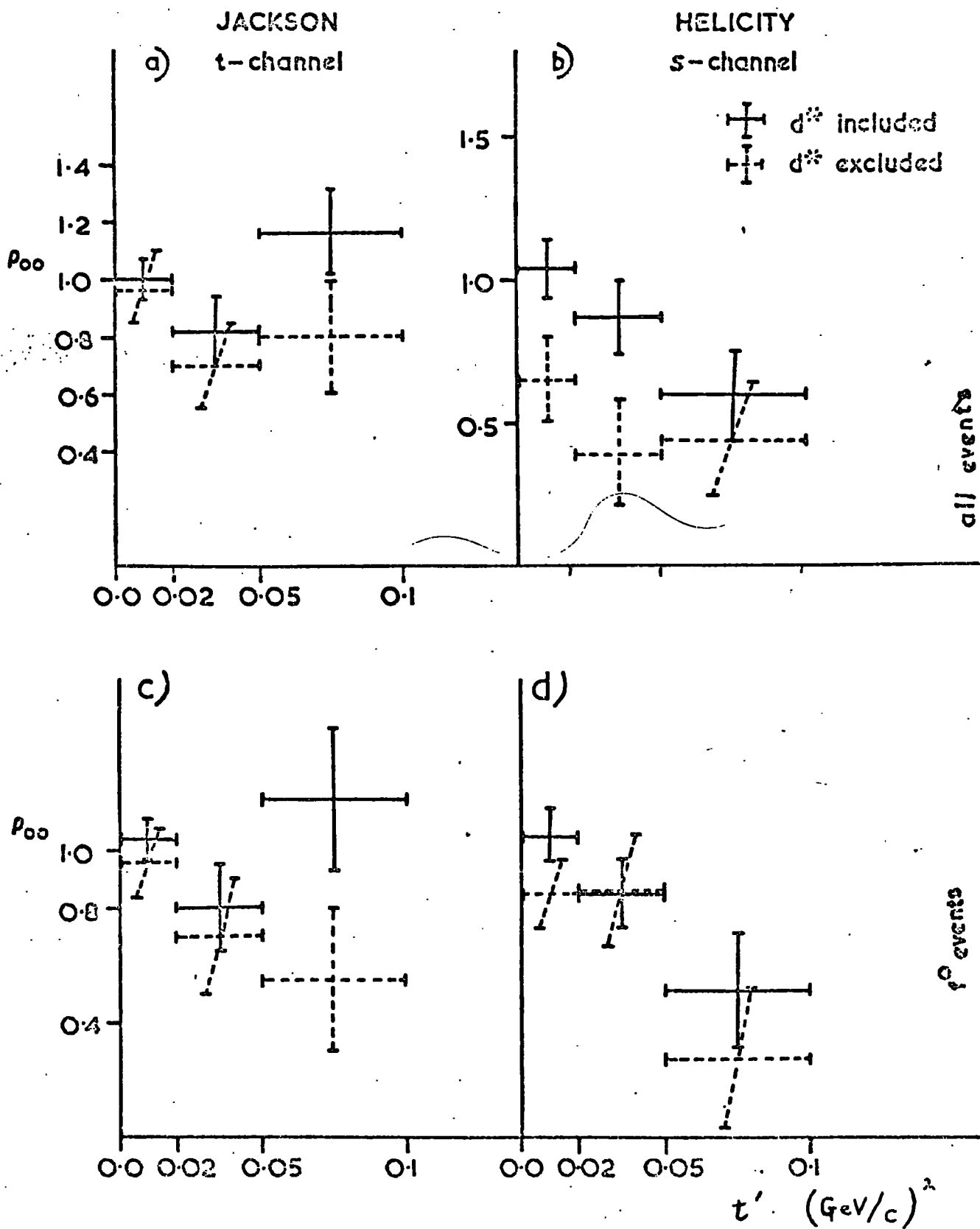
Figures 7.2(a) and (b) and table 7.2 show the values of ρ_{00} in the G-J frame and the helicity frame respectively. In the G-J frame ρ_{00} is compatible with 1 throughout the whole range of t' , while in the helicity frame, there is a distinct tendency for it to decrease as t' increases. The value of ρ_{00} in the helicity frame for the highest t' interval is 0.60 ± 0.15 and is incompatible with unity.

This result has been checked by using only f^0 events as the sample since non f^0 events may correspond only to background and not to the true A_3 signal. The results of this are also given in Table 7.2 and shown diagrammatically in fig. 7.2 (c) and (d). The results are quite compatible with those obtained above, the main difference being an increase in the errors due to the smaller statistics. In fact in the highest t' range the value found for ρ_{00} in the helicity frame (0.50 ± 0.21) is even more incompatible with unity than previously.

The above analysis was repeated excluding those events which had a $d\pi^+$ mass combination in the d^* region and the results of the fitting can be seen in table 7.2 and figure 7.2 as the dashed lines. As was the case for the A_1 meson, the effect of excluding d^* events is to reduce ρ_{00} , in general and to increase the errors since the already rather low statistics are further reduced. No clear incompatibility with TCHC is seen; the value of ρ_{00} in the highest t' region when only f^0 events are used of 0.55 ± 0.25 is within 2 standard deviations of 1. SCHC, however, is dramatically in contradiction with the data.

These results, that the A_3 meson in this reaction, conserves helicity in the t -channel and not in the s -channel, are in agreement with those of Paler et al (Ref. 7.6)

FIG 7.2 ρ_{00} OF THE A_3 vs t'



t' range (GeV/c) ²	G.J FRAME				HELICITY FRAME			
	ALL EVENTS		f ⁰ EVENTS		ALL EVENTS		f ⁰ EVENTS	
	d*inc	d*exc	d*inc	d*exc	d*inc	d*exc	d*inc	d*exc
0.0 - 0.02	1.00±0.07	0.96±0.10	1.04±0.08	0.96±0.12	1.04±0.08	0.65±0.15	1.05±0.10	0.85±0.12
0.02 - 0.05	0.82±0.12	0.70±0.15	0.80±0.15	0.70±0.20	0.87±0.14	0.39±0.18	0.85±0.12	0.86±0.20
0.05 - 0.10	1.16±0.15	0.80±0.20	1.18±0.25	0.55±0.25	0.60±0.15	0.44±0.20	0.51±0.22	0.27±0.25

TABLE 7.2

ρ_{00} of the A_3 meson for several t' regions

7.2 Spherical Harmonic Moments Analysis

In this and the following sections a method of testing helicity conservation in a way which is independent of the spin of the produced state will be discussed. The purpose of this is partly to check the results of the previous section, since, particularly in the A_1 region the complete spin structure is not known and the results depend on various assumptions, and partly, since it is possible that the whole channel is dominated by Pomeron exchange, to examine helicity conservation in regions of 3-pion mass other than the A_1 and A_3 regions although their spin structures are completely unknown.

7.2.1 The Method

The method used is that of Beaupre et al (Ref. 7.8) and relies on the fact that the spherical harmonic moments, $\langle Y_{\ell}^m \rangle$ with $m \neq 0$ must be zero if the density matrix is diagonal. If helicity is conserved in any reference frame then ρ_{00} in that frame should be one and all other elements zero, which is a special case of diagonal density matrix.

The procedure is to calculate the quantity (χ^2) defined as:

$$\chi^2 = \sum_{\ell=1}^{\ell_{\max}} \sum_{m=1}^{\ell} \frac{|\langle Y_{\ell}^m \rangle|^2}{\sigma^2} \quad 7.2$$

where $\langle Y_{\ell}^m \rangle$ is the experimentally determined spherical harmonic moment and σ is its error. χ^2 is calculated in the G-J frame and then the decay angles are redefined for every event by rotating the polar axis of the reference frame by an angle β in the production plane. The result of this rotation is to redefine the previous polar angle (θ) and azimuthal angle (ϕ) as follows:

$$\begin{aligned} \cos \theta' &= \cos \theta \cos \beta + \sin \theta \sin \beta \cos \phi \\ \tan \phi' &= \frac{\sin \theta \sin \phi}{-\cos \theta \sin \beta + \sin \theta \cos \phi \cos \beta} \end{aligned} \quad 7.3$$

where θ' and ϕ' are the polar and azimuthal angles in the new reference

frame. It is then possible to calculate χ^2 as a function of the rotation angle β and find the value of β where χ^2 becomes minimum (β_{\min}). This angle, β_{\min} , then defines the reference frame in which helicity is most likely to be conserved. For TCHC this frame should be the G-J frame and β_{\min} should be zero, while for SCHC β_{\min} should be equal to the crossing angle from the G-J frame to the helicity frame (δ) given by:-

$$\cos \delta = \frac{t - \mu_0^2 + m^2}{\left\{ (t - \mu_0^2 - m^2)^2 - 4\mu_0^2 m^2 \right\}^{\frac{1}{2}}} \quad 7.4$$

where μ_0 is the pion mass.

and m is the tripion mass.

In principle the normal to the decay plane or any of the pions from the decay can be used as the reference direction. Parity conservation, however, restricts the possible values of the spherical harmonic moments as follows:-

$$I_m(\langle Y_{\ell}^m \rangle) = 0 \text{ if } \ell \text{ is even}$$

$$R_e(\langle Y_{\ell}^m \rangle) = 0 \text{ if } \ell \text{ is odd,}$$

when the normal to the decay plane is used as the analyser and:-

$$I_m(\langle Y_{\ell}^m \rangle) = 0 \text{ for all } \ell \text{ when the momentum of one of the}$$

pions is used as the analyser. To use one of the pion momenta will give more information, therefore, and will be a more sensitive test.

Beaupre et al have argued that the unambiguously charged pion, in this case the π^- , constitutes the best analyser, and this has been chosen since it removes the difficulty of distinguishing between the two positively charged pions.

A difficulty inherent in the method is in the choice of ℓ_{\max} in eq. 7.2. A study of the $m=0$ harmonic moments of the π^- shows that,

in general, $l > 6$ does not contribute and the value of l_{\max} normally used was 6. β_{\min} was determined, however, in each region for l_{\max} up to 10 in order to detect any effect of higher moments and in some cases they were found to considerably alter the value of β_{\min} . This will be commented on below.

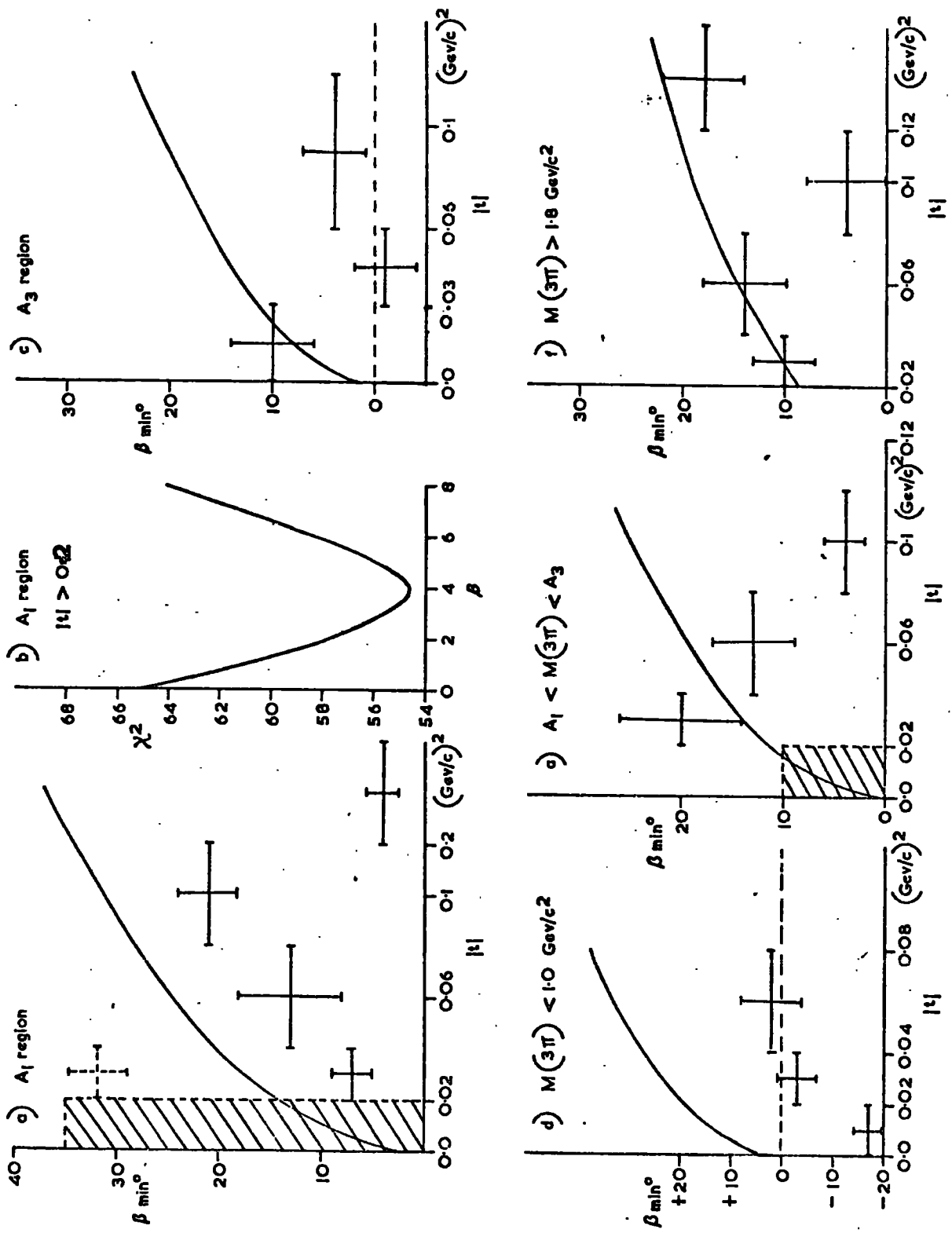
7.2.2 The A_1 region

The results of the analysis for events in the A_1 region are shown in fig. 7.3 (a). This is for non d^* events although the inclusion of d^* events has no effect, within error, on the results. In the lowest t region the value of χ^2 varies little with β when l_{\max} is 6 and as l_{\max} is increased minima appear but in no stable way. It was decided, therefore, to treat β_{\min} in this region as underdetermined. In the second t region there was, similarly, no variation of χ^2 with β when l_{\max} was 6 but at $l_{\max} = 8$ two distinct minima occurred at $\beta = 7 \pm 2$ and $\beta = 32 \pm 3$, both of which were equally prominent when l_{\max} was raised to 10. For higher t -regions excellent minima were found with $l_{\max} = 6$ which did not change significantly as l_{\max} was increased.

The highest t interval used in this analysis ($t > 0.12 (\text{GeV}/c^2)$) was not used in the study of the density matrix elements, since it contains only 15 events. The reason it is included here is shown in figure 7.3(b) which shows the variation of χ^2 with β ($l_{\max} = 10$). There is a very steep and prominent minimum at $\beta = 4^\circ$.

The results show an incompatibility with both TCHC ($\beta_{\min} = 0$) and SCHC ($\beta_{\min} = \delta$ where δ is shown as the smooth curve in figure 7.3(a)) for all values of t . This result, however, is not so conclusive as it may appear since the χ^2 confidence level for $\beta_{\min} = 0$ in the t range 0.08 - 0.12, where the result seems most inconsistent with TCHC, is $\sim 30\%$ i.e. still an acceptable level. Nonetheless, the confidence level

FIG 7.3



for minimum χ^2 is a factor of 2 greater and the possibility of non-conservation of helicity in the t-channel cannot be ignored. Similarly, acceptable confidence levels are found for SCHC in each t range, except for the very highest where SCHC can be ruled out.

7.2.3 The A_3 region

Figure 7.3(c) shows the value of β_{\min} for A_3 events. The results here above $|t| = 0.03 \text{ (GeV/c)}^2$ are quite compatible with TCHC and incompatible with SCHC. In the lowest t interval it seems that SCHC is more likely, but it must be noted that the confidence level for $\beta_{\min} = 0^\circ$ is $\sim 60\%$ even here and it must be concluded that TCHC is an acceptable hypothesis throughout the whole t range.

7.2.4 Below the A_1 region

β_{\min} is compatible with 0° above $|t| = 0.02 \text{ (GeV/c)}^2$ as can be seen in fig. 7.3 (d). The value of β_{\min} in the lowest t range ($-17 \pm 3^\circ$) is quite incompatible with both s- and t-channel helicity conservation, but, again, the confidence level for $\beta = 0^\circ$ is 16%, a value which must be regarded as acceptable. The confidence level for $\beta = 13.5^\circ$, the value expected if SCHC holds in this region is negligible.

7.2.5 Between the A_1 and A_3 regions

The sample of events used here are all those with a three pion effective mass in the range $1.24 - 1.44 \text{ GeV/c}^2$, together with those events in the range $1.44 - 1.6$ which are not accepted as A_3 events, i.e. those with no dipion mass in the f^0 region and at least one in the ρ^0 region. The results of the analysis are shown in figure 7.3(e). The t range $0.0 - 0.02 \text{ (GeV/c)}^2$ gave no clear minimum, just a broad shallow dip between $\beta = -10^\circ$ and $+10^\circ$. Increasing l_{\max} had no effect on this dip. It can be seen that neither SCHC or TCHC seem to hold, although the former of these is a better candidate up to a value of $|t| = 0.08 \text{ (GeV/c)}^2$. Above this value the latter hypothesis is favoured.

7.2.6 Above the A_3 region

For events with $M(3\pi) > 1.8 \text{ GeV}/c^2$ ℓ_{max} was set to 10, because the effects of the higher moments on the value of β_{min} was not negligible. The results are shown in figure 7.3(f). For this 3π mass t_{min} is greater than 0.02 and so no events fall in the first range. The points fall quite well on the line $\beta_{\text{min}} = \delta$ and, therefore, support the hypothesis of SCHC, except in the t range $0.08-0.12 (\text{GeV}/c)^2$, where the value is compatible with TCHC. The χ^2 confidence level for $\beta = \delta (=19^\circ)$ in this t region, however, is $\sim 70\%$ (c.f. 90% for $\beta = 0^\circ$) and it is concluded that SCHC is compatible with the data.

7.2.7 Summary

The results of the spherical harmonic moments analysis are not very conclusive, since often, while suggesting helicity conservation in one channel, the hypothesis of helicity conservation in the other channel cannot be excluded. The results, however, indicate:

1. s-channel helicity is not conserved in this reaction except, perhaps, when the 3 pion mass is $> 1.8 (\text{GeV}/c)^2$.
2. t-channel helicity is conserved for A_3 production and possibly also when the 3-pion mass is $< 1.0 \text{ GeV}/c^2$.
3. The A_1 region seems to conserve neither s- nor t-channel helicity, but, while TCHC cannot be dismissed in any t region, SCHC is incompatible with the data for $t > 0.12 (\text{GeV}/c)^2$.
4. There is no evidence either for TCHC or for SCHC in the 3-pion mass range between the A_1 and the A_3 regions.

7.3 Longitudinal Phase Space Analysis

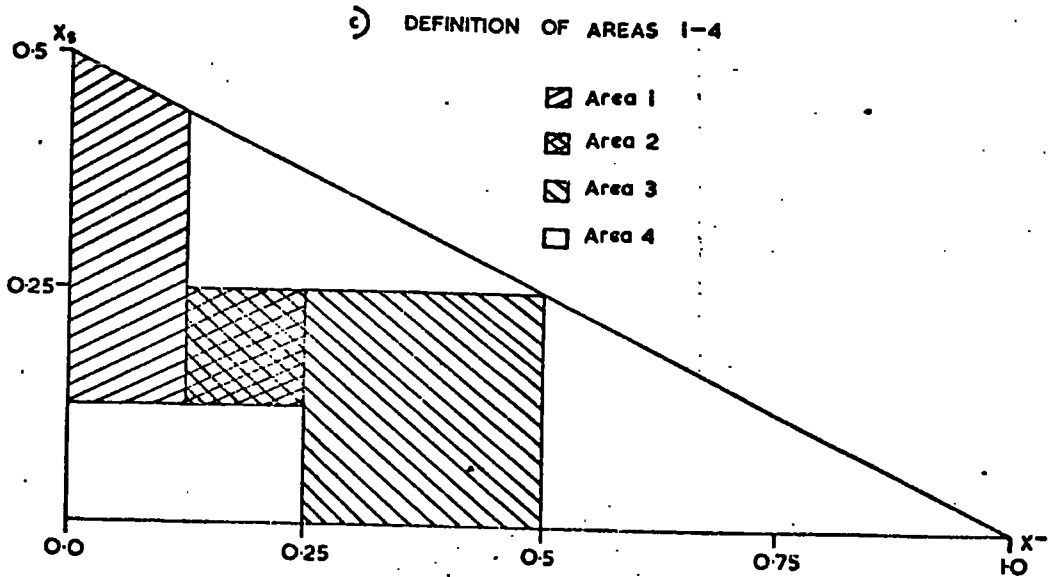
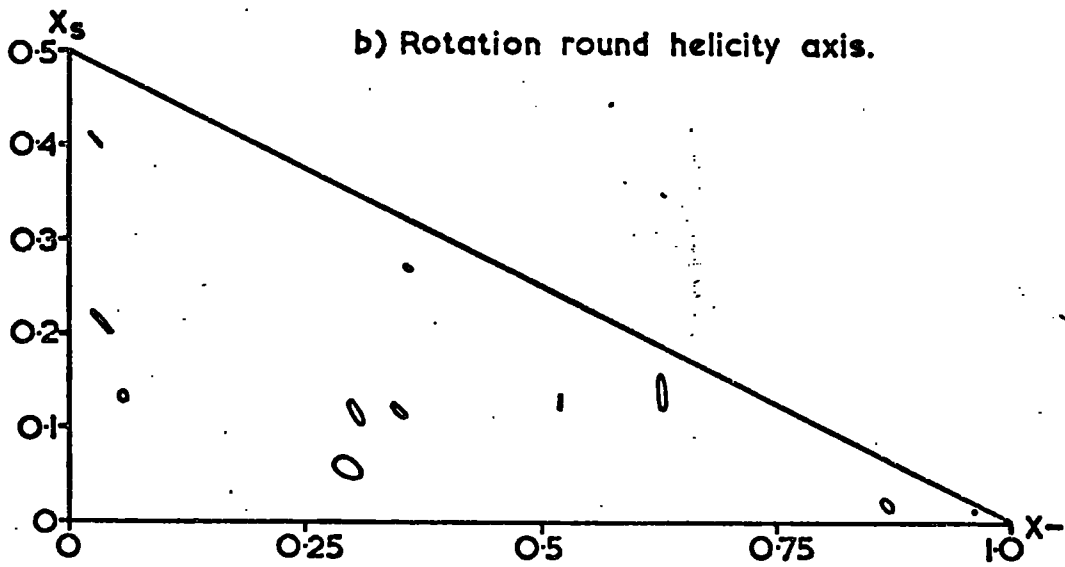
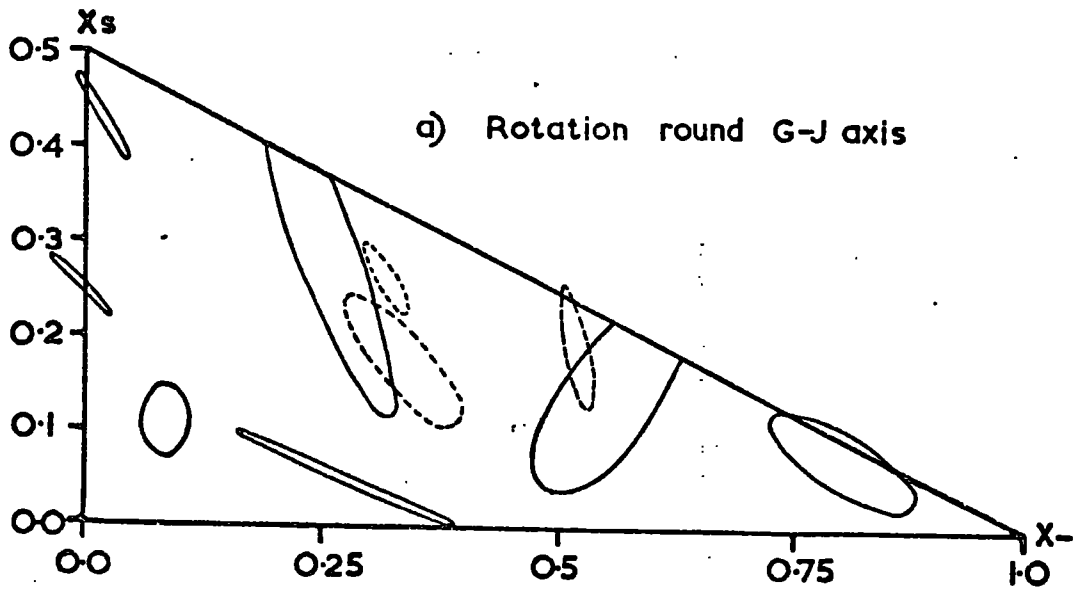
One problem in testing helicity conservation is the selection of diffractively produced events. This was done in section 7.1 by choosing only the A_1 and A_3 enhancements, both of which are thought to be produced

diffractively, and in section 7.2 by assuming that the whole channel is diffractive. In this section diffractive events are selected by looking at the appropriate region of longitudinal phase space, i.e. the region where all three pions are going forwards in the c.m.s. system. The method used is that of Beaupre et al (Ref. 7.9).

Helicity conservation implies isotropy around the relevant polar axis for all kinematical configurations of the final state. This implies that the diffractive region of L.P.S. ought to show no variations in population under rotations of events around the G-J polar axis for TCHC or around the helicity frame polar axis for SCHC. If an event is selected and all three pions are simultaneously rotated around one of these axes, then the point which represents this event in the X_s-X_- plane of L.P.S. (see chapter 5 for definitions) traces out a path which depends on the particular kinematic features of the event e.g. t , the decay angles, the particle momenta etc. These paths are shown for several randomly chosen events in fig. 7.4 (a) under rotation around the t-channel axis and in fig. 7.4 (b) under rotation around the s-channel axis. It can be seen that, while for the t-channel axis an event can move quite a long way from its starting point, when the s-channel axis is used the loops are small. This implies that to look for invariance of the L.P.S. population under such rotations will be a sensitive test of t-channel helicity conservation but will be relatively insensitive to non-conservation of s-channel helicity.

Different events will, in general, be at their maximum distance from their starting points in L.P.S. for different values of the rotation angle ϕ . Since the loops are not circular, the maximum distance clearly depends on the starting point. The maximum possible distance, however, occurs for $\phi = \pi$ radians and it has been assumed that any change in the L.P.S. distributions under a rotation will be

FIG 7.4



most evident if every event has been rotated by this amount.

Figure 7.5 (a) shows diagrammatically the number of events in each bin of L.P.S. originally (centre), after rotation of each event by π radians around the G.J polar axis (left) and after a similar rotation around the helicity polar axis (right). The same data is shown numerically in figure 7.6(a). As would be expected, there is very little difference between the unrotated and the helicity rotated distributions. The distribution after rotation around the G-J polar axis shows a reduction of events in the top left hand corner of the diffractive region and an increase of events in the lower central area of the region. While these differences are hardly statistically significant, it is interesting to note that the very same effect was seen by Beaupre et al (Ref. 7.9) in both π^+p and π^-p experiments at 8 GeV/c and 12 GeV/c. It seems that the effect, though small is persistent and, in the light of this, it can be argued that it represents evidence for a slight non-conservation of t-channel helicity.

In an attempt to enhance the effect the process was repeated using only events with $t > 0.02 (\text{GeV}/c)^2$, since for value of t smaller than this the G-J polar axis and helicity axis are not very well separated and the sensitivity of the test to a non-conservation of t-channel helicity may be reduced. The results of this are shown in fig. 7.5 (b) diagrammatically and 7.6(b) numerically, where it can be seen that, although the same trends are apparent, they are not significantly enhanced. The reason for this may be that the effect is largely due to A_1 production, and the cut on t greatly reduces the number of A_1 events. Figure 7.5(c) and 7.6(c) show the distributions when only A_1 events are used. It is clear that A_1 production contributes strongly to the above effects.

If it is assumed that the noted differences in the L.P.S. distributions

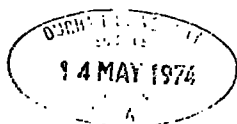


FIG 7.5

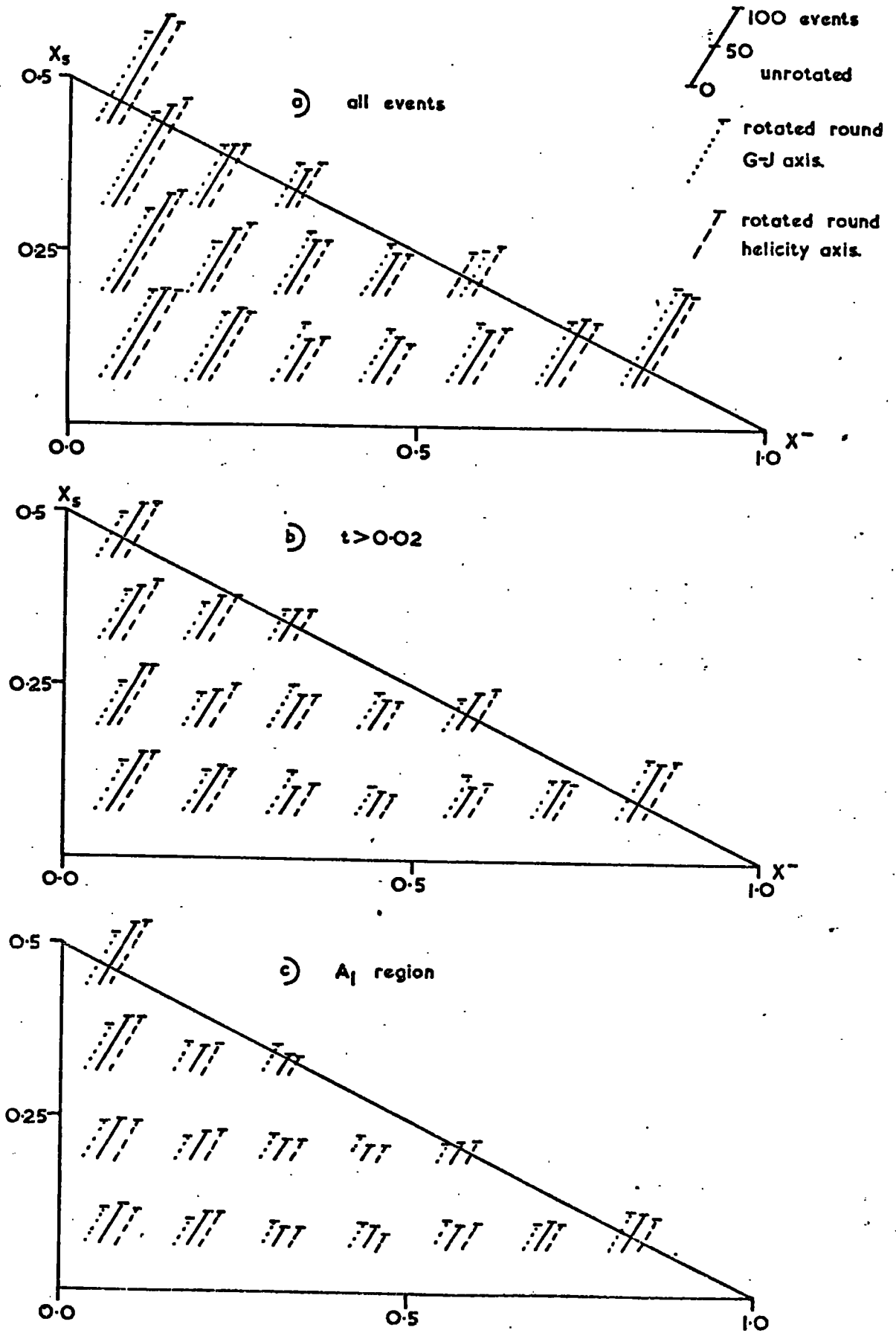
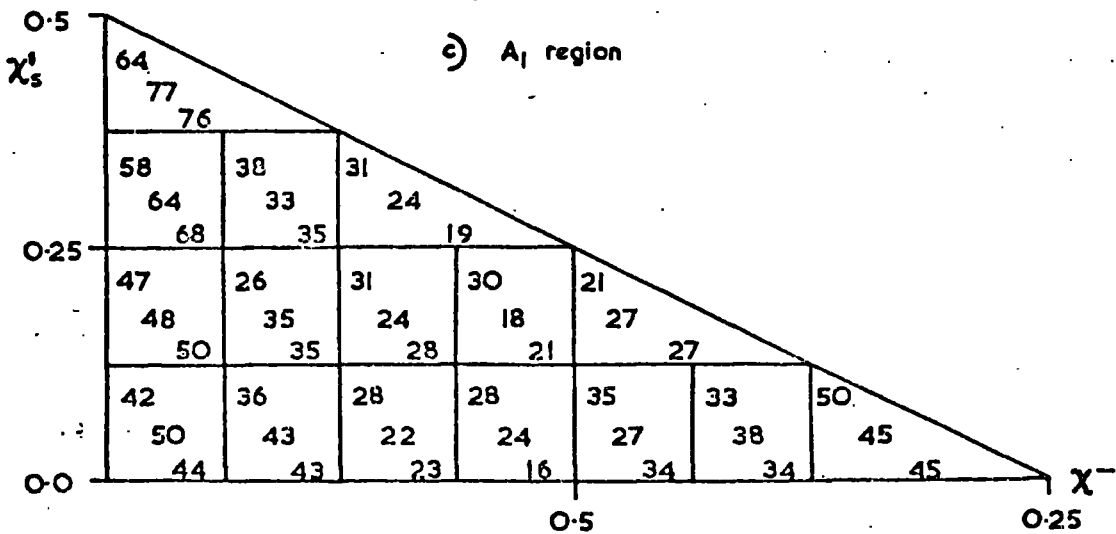
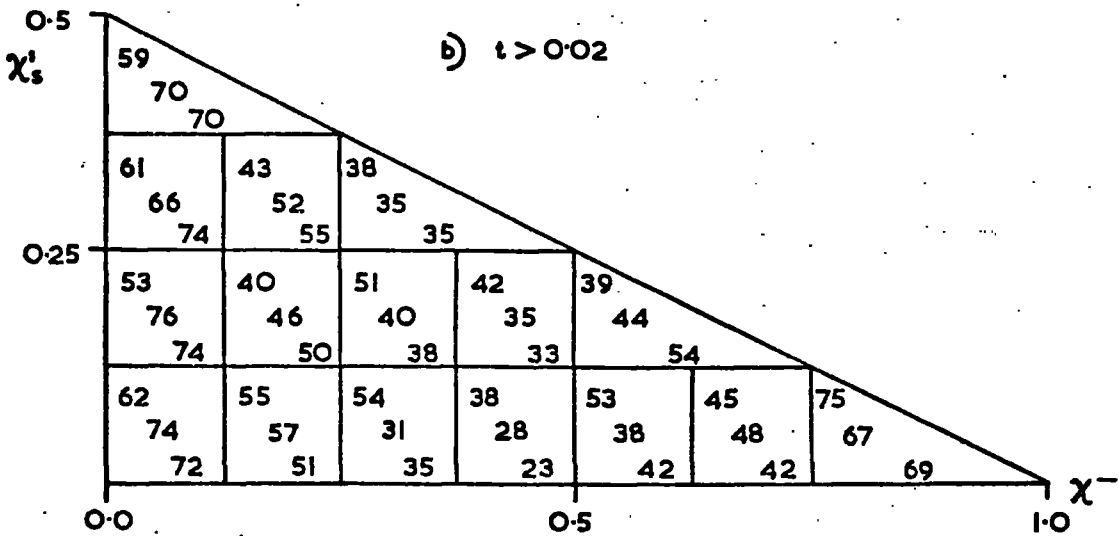
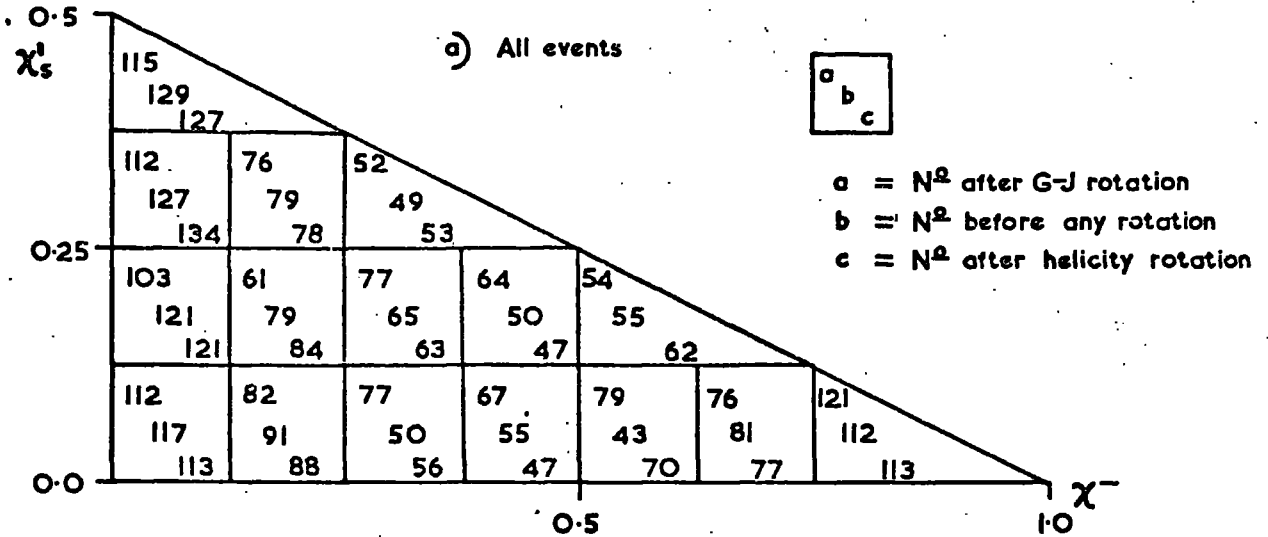


FIG 7.6

THE NUMBERS OF EVENTS PER L.P.S. REGION BEFORE AND AFTER ROTATION OF PIONS BY π AROUND THE G-J AND HELICITY AXES.



are indeed due to non-conservation of t-channel helicity, then it is possible to find the characteristics of the responsible events by selecting those regions of L.P.S. which change most. To this end the diffractive region of L.P.S. has been divided into 4 areas defined as:

Area 1 : $X_s > 0.125$ and $X_- < 0.125$

Area 2 : $0.125 < X_s < 0.25$
and $0.125 < X_- < 0.25$

Area 3 : $X_s < 0.25$
and $0.25 < X_- < 0.5$

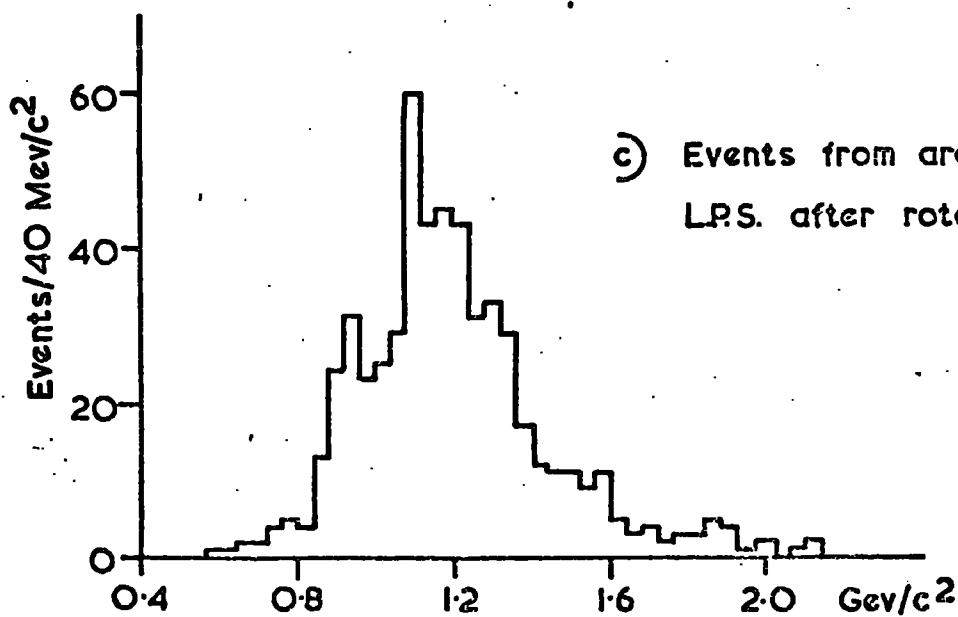
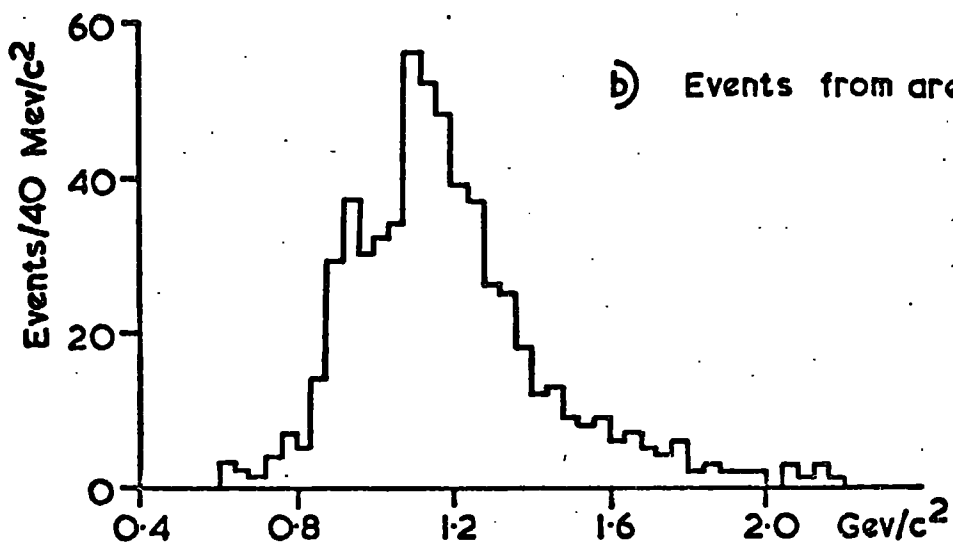
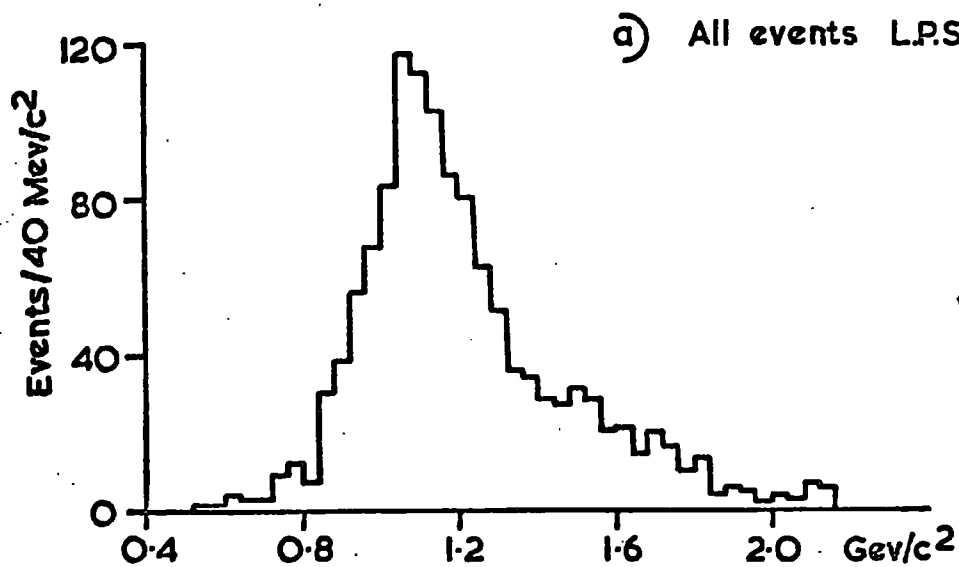
Area 4: The remainder.

Thus areas 1 and 2 correspond to those regions which give a decreased population after rotation around the t-channel axis, while area 3 is that which increases in population. Area 4 is that which remains relatively invariant. These areas are shown schematically in figure 7.4(c).

Figure 7.7 shows the 3 pion effective mass spectrum for (a) the whole of the diffractive region and (b) areas, 1, 2 and 3 only. The scales are such that the areas under the two histograms are almost the same to make comparison easier. The A_1 signal is quite clear in fig. 7.7 (b), indicating that A_1 production accounts for part of the apparent non-conservation of t-channel helicity. Although a large part of the observed A_3 production does not fall in the diffractive region of L.P.S. it can be seen that the number of events in the A_3 region in areas 1-3 is reduced relatively to the whole region. This is in agreement with the previous result of TCHC for A_3 production, although it does not prove that hypothesis: it is possible, for example, that A_3 events may account for the increase in the population of area 3

FIG 7.7

$M(3\pi)$



after the rotation. To check this, the events which fall in areas 1, 2 and 3 after rotation around the t-channel polar axis have been plotted in figure 7.7 (a) where there is still relatively fewer events in the A_3 region than would be expected by a random choice of events. While this does not prove that A_3 production gives an invariant population in L.P.S. under such rotations it demonstrates that no evidence to refute that hypothesis is present in the data. Lack of statistics prevents any direct study of the L.P.S. distribution for A_3 events.

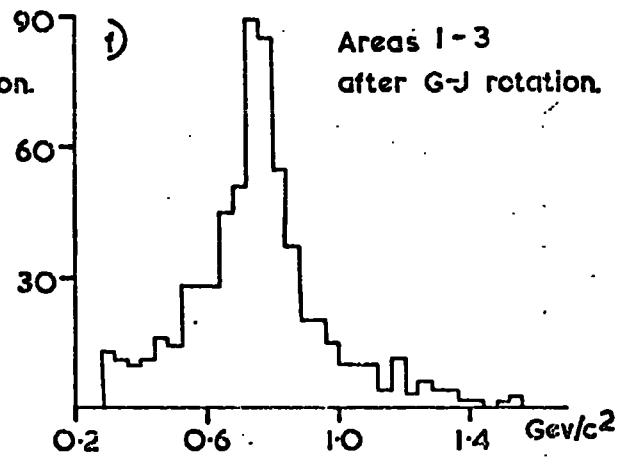
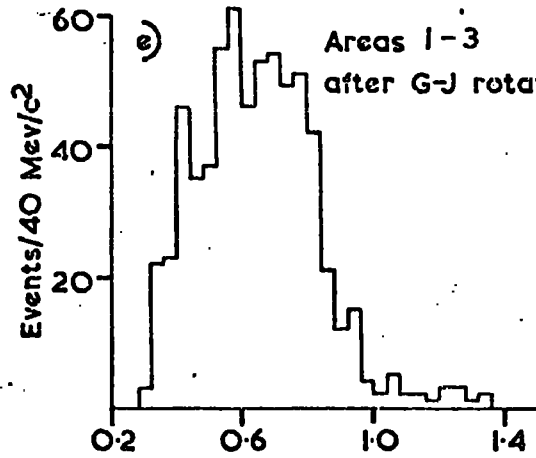
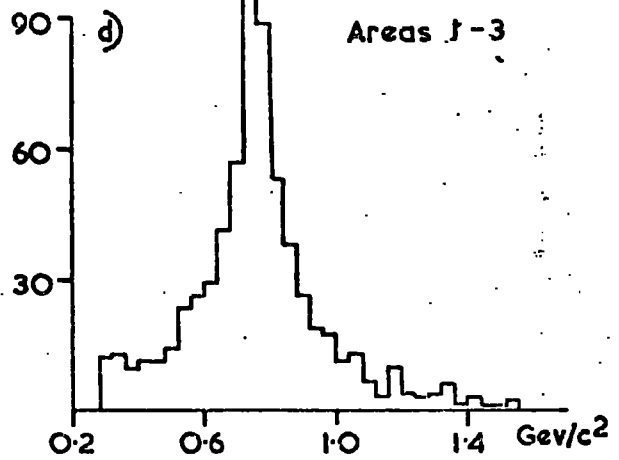
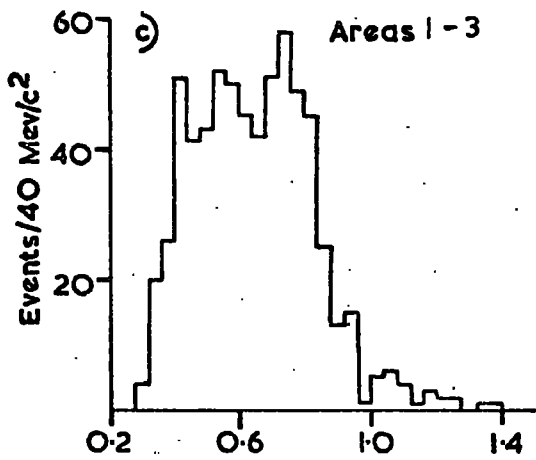
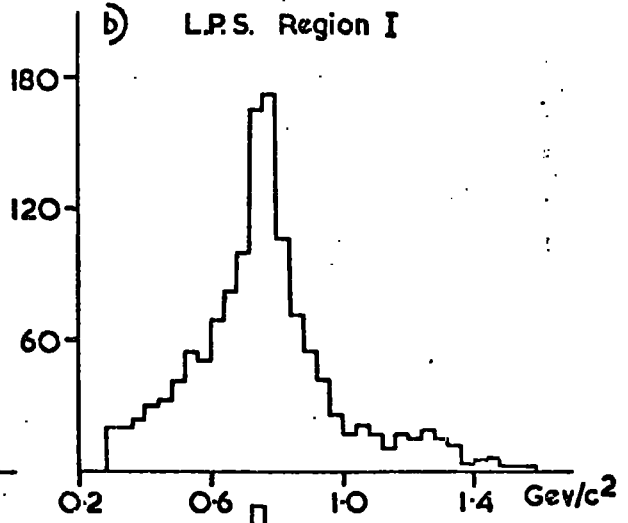
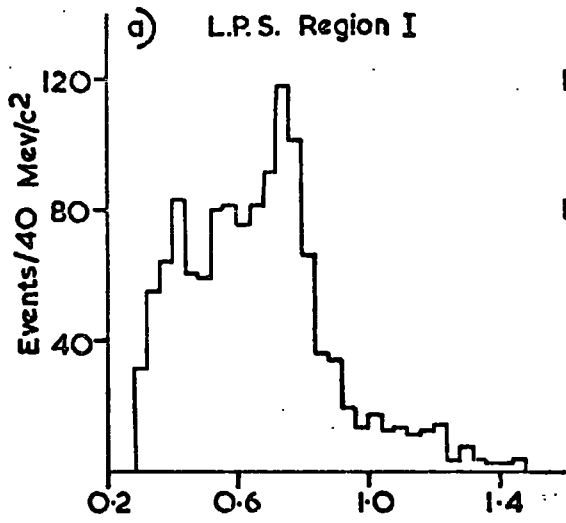
Further characteristics of the events which seem to account for the lack of invariance of L.P.S. can be seen in figure 7.8 where the invariant mass spectra of the $\pi_s^+ \pi^-$ and $\pi_f^+ \pi^-$ combinations are plotted respectively for the whole of the diffractive region (fig. 7.8 (a) and (b)) and for areas 1, 2 and 3 combined both before the rotation (figs. 7.8 (c) and (d)) and after the rotation figs. 7.8 (e) and (f)). The subscripts s and f refer to the slower and faster π^+ in the CMS. It can be seen that areas 1, 2 and 3 show very little ρ^0 production in the $\pi_s^+ \pi^-$ combination in contrast to the remainder of the region. There is also a marked reduction of events in the f^0 region in areas 1, 2 and 3 relative to those for the whole region in both combinations. This can be related to the lack of A_3 events in these three areas.

It is possible to perform the density matrix elements analysis of section 7.1 on the A_1 events from areas 1, 2 and 3, assuming that these are the events responsible for any non-conservation of helicity in the t-channel. The results, however, must be treated with caution since to arbitrarily select various regions of L.P.S. may result in a sample biased towards certain decay angles. The decay angular distributions for these events have been checked and show no obvious sign of bias, but more subtle effects may still be present. The analysis has been performed, however, and the results are shown in figure 7.9 and table 7.3.

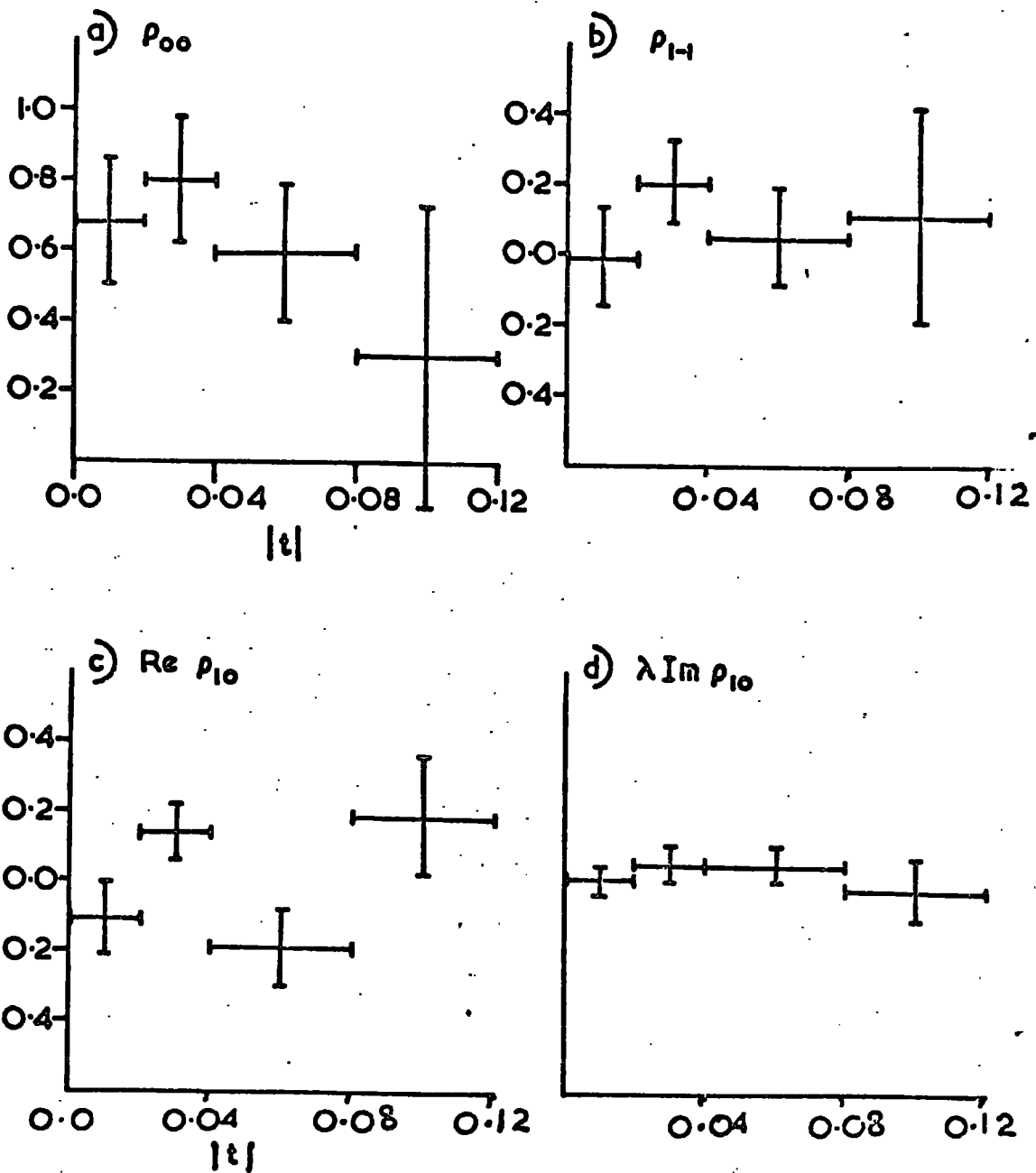
FIG 7.8

$M(\pi_3^+ \pi^-)$

$M(\pi_1^+ \pi^-)$



A₁ DENSITY MATRIX ELEMENTS (G-J FRAME) USING ONLY EVENTS FROM AREAS 1,2,3.



t range (GeV/c) ²	ρ_{00}	ρ_{1-1}	Re ρ_{10}	λ Im ρ_{10}
0.0 -0.02	0.68 \pm 0.18	-0.01 \pm 0.14	-0.11 \pm 0.10	0.01 \pm 0.04
0.02-0.04	0.80 \pm 0.18	0.20 \pm 0.12	0.14 \pm 0.08	0.06 \pm 0.05
0.04-0.08	0.59 \pm 0.19	0.05 \pm 0.14	-0.19 \pm 0.11	0.06 \pm 0.05
0.08-0.12	0.30 \pm 0.43	0.11 \pm 0.30	0.19 \pm 0.17	-0.01 \pm 0.09

TABLE 7.3

Density Matrix Elements of the A_1 meson produced in

Areas 1, 2 and 3 of L.P.S.

Although the non-diagonal elements of the density matrix are compatible with zero (with the possible exception of $\text{Re } \rho_{10}$ which, while its behaviour is rather erratic, is never more than 2 standard deviations away from zero), the trend noted in section 7.1 for ρ_{00} to decrease with increasing $|t|$ is enhanced: in no t region is ρ_{00} compatible with unity and in the range $0.04-0.08 (\text{GeV}/c)^2$ its value is not within 2 standard deviations of the expected value for TCHC; in the highest t region the value of 0.30 is quite incompatible with 1 in spite of the large error. It is concluded that, if no bias is inherent in selecting only those events from certain areas of L.P.S., the change in L.P.S. population upon rotation does indeed correspond to a non conservation of t -channel helicity and that a small amount of helicity flip is present in the t -channel for A_1 production.

7.4. Conclusions

The A_1 meson has been shown not to conserve helicity in the s -channel in this reaction both by the density matrix elements analysis and by the spin-independent method of spherical harmonic moments described in section 7.2, although the results of this latter method have been shown to be rather speculative, and only for $|t| > 0.12 (\text{GeV}/c)^2$ can SCHC be rejected by this method. TCHC cannot be ruled out for the A_1 region, although, all three types of analysis used: density matrix elements, spherical harmonic moments and longitudinal phase space, show some evidence for a slight non-conservation of t -channel helicity and particularly when the density matrix elements analysis is performed in conjunction with the L.P.S. selection of events which are least likely to show TCHC.

All three types of analysis are consistent with TCHC for A_3 production, for which SCHC can be rejected both by the density matrix elements analysis and the spherical harmonic moments analysis. This result is in agreement with that of Ref. 7.6 and suggests that the Gilman

hypothesis of SCHC for all diffractive reactions is invalid, even if the Frautschi rule for diffractive production is true. The non-conservation of s-channel helicity in both A_1 and A_3 production and the conservation, or near conservation, of t-channel helicity for both suggests that the Morrison Rule is acceptable.

For the remainder of the events, the spherical harmonic moments analysis suggests that SCHC may hold above the A_3 and TCHC below the A_1 . Between the A_1 and A_3 neither seem to be conserved.

C H A P T E R E I G H T

POSSIBLE KINEMATICAL INTERPRETATIONS

OF OBSERVED ENHANCEMENTS

Introduction

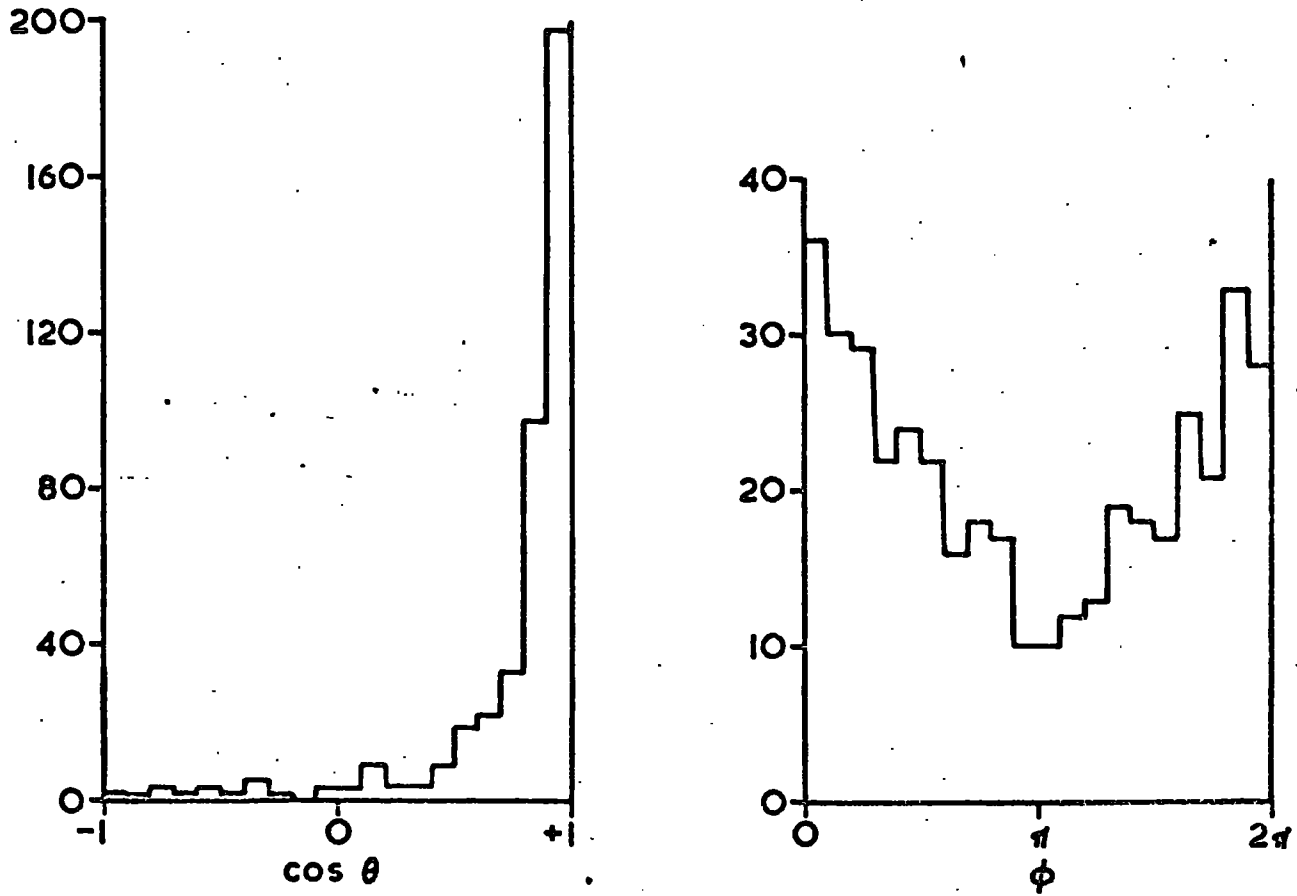
The only prominent effects present in the coherent channel are the ρ^0 and f^0 meson mass peaks in the neutral dipion spectrum, the A_1 and A_3 enhancements in the 3-pion effective mass spectrum, and a $d\pi^+$ mass peak, the d^{*++} . Of these peaks, only the first two, the ρ^0 and f^0 are well established resonant states. While the A_1 and A_3 may be resonant they may also be due to kinematical effects and a model to explain the presence of these peaks will be described in Section 8.2 of this chapter, together with a discussion of the interpretation of the model and a survey of the experimental results on A_1 production which are relevant to the validity of the model. The d^* effect is discussed first, however, in section 8.1.

8.1 The d^{*++} enhancement

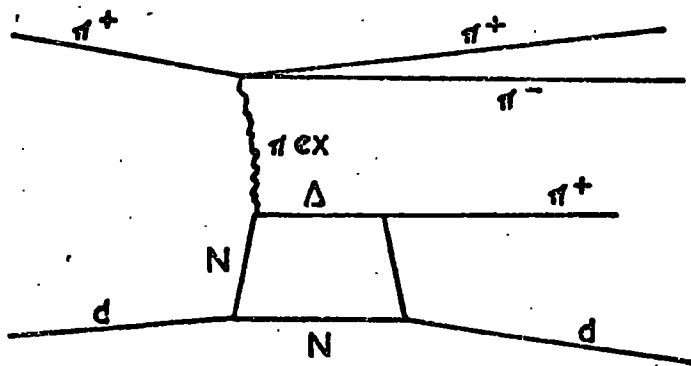
If the peak in the $d\pi^+$ mass spectrum is to be interpreted as a resonant system, then it must have well defined quantum numbers and, in particular, it must have a unique spin parity (J^P) assignment. A study of the decay angular distributions of the d^{*++} events can give information on which spin-parity states are present. The presence of only one J^P state implies that the polar angle distribution ($\cos \theta$) in, for example, the Gottfried-Jackson reference frame should be symmetric around zero. The distribution of this angle and that of the corresponding azimuthal angle for d^* events, defined as those events with $M(d\pi^+) < 2.4$ GeV/c², are shown in figure 8.1 (a). The polar angle distribution is by no means symmetric and, while a certain amount of asymmetry may be

FIG. 8.1

a) d^{*++} decay angles



b) Suggested d^{*} production mechanism



explained by the interference of the dominant J^P state with a state of opposite parity in the background, the magnitude of the observed asymmetry would require a large number of J^P assignments all interfering and it is quite incompatible with the hypothesis of any one state dominating. The d^{*++} is, therefore, not interpreted as a resonance.

The model which is often used to explain the enhancement is as follows: the interaction proceeds by pion exchange and the exchanged virtual pion interacts with one of the nucleons inside the deuteron forming a $\Delta^{++}(1236)$, which subsequently decays in such a way that the deuteron remains intact. The exchange diagram for this model is shown in figure 8.1 (b). The simplest evidence for such a model is the fact that the sum of the masses of the $\Delta(1236)$ and a nucleon is $\sim 2176 \text{ MeV}/c^2$ a value which compares favourably with the central mass of the d^* peak (i.e. $2210 \text{ MeV}/c^2$ in this experiment). The $\cos \theta$ distribution, moreover, need no longer be symmetric since it is complicated by the criterion that the deuteron remains intact. The formation of a $\Delta(1236)$ inside the deuteron without the deuteron breaking up has been used successfully to explain peaks in the cross sections of the reactions:



and it has been shown (Ref. 8.3) that a peak in the $d\pi^+$ effective mass distribution in non-elastic channels will result from such a mechanism.

An interesting aspect of this model is that the exchanged virtual pion interacts with only one of the nucleons inside the deuteron. The coherence condition of low-momentum transfer to the deuteron (see chapter 1) was based on the assumption that the interaction was with the deuteron as a whole, i.e. that the exchanged particle could not

localise any of the deuteron constituents. In the case of d^* production, the reverse is true: the exchanged particle must probe the interior of the deuteron. It might be expected, therefore, that the slope parameter (A) of the deuteron differential cross section, when parametrized by an equation of the type of Eq. 4.2, would be smaller for d^* events than otherwise. Least squares fits to these distributions in the range $0.02 < |t| < 0.12 \text{ (GeV/c)}^2$ yield, the following results:

$$A_{d^*} = 26.1 \pm 1.0 \text{ (GeV/c)}^{-2}$$

$$A_{\text{non}d^*} = 27.8 \pm 2.5 \text{ (GeV/c)}^{-2}$$

Although the value for d^* events is in fact smaller than for non- d^* events, the errors on the results render both values compatible. There is no significant difference between the two results. Evidence that the expected effect does occur, however, can be seen in figures 4,3 (a) and (b) which show, the $d \pi_s^+$ effective mass spectra for 3-prong and 4-prong events, respectively. The 3-prong events correspond to the very lowest values of $|t|$ and are essentially ignored in the determination of the slope parameters since they do not fall in the t range fitted. It is clear, however, from the figures that there is significantly less d^* production in the 3-prong events than for the 4-prong events. In fact 28% of 4-prong events have $M(d \pi_s^+) < 2.4 \text{ GeV/c}^2$, while the corresponding figure for 3-prong events is only 16%. After background subtraction, this difference will be even greater since the only significant signal in the 3-prong events is the narrow spike $\sim 2.2 \text{ GeV/c}^2$, which contains very few events.

The suppression of d^{*0} events can also be understood in the framework of this model, since the formation of a $\Delta(1236)$ with a π^- would necessitate exotic $\pi^+ \pi^+$ scattering at the uppermost vertex of figure 8.1 (b), and this is suppressed relative to the $\pi^+ \pi^-$ scattering

needed for d^{*++} production since there are no known dipion exotic resonances while the $\pi^+\pi^-$ scattering cross section is much enhanced by the presence of the ρ^0 and f^0 mesons.

A model involving $\Delta(1236)$ production inside the deuteron, therefore, seems to explain many features of d^* production. There is evidence, however, that the mechanism for production of the $\Delta(1236)$ is not simple one pion exchange, as was suggested. The distribution of the azimuthal angle of decay of the d^{*++} (fig. 8.1 (a)) is not isotropic, but shows a pronounced dip $\sim \phi = \pi$. This angle, in the Gottfried-Jackson reference frame is equivalent to the Treiman-Yang angle (the angle between the production and decay planes of the system) and must be isotropic if the system is produced by a one pion exchange mechanism. It is therefore, concluded that the $\Delta(1236)$ is produced by a mechanism more complicated than simple one pion exchange.

8.2 The A_1 and A_3 enhancements

In this section a model to explain the A_1 and A_3 enhancements will be described and discussed with respect to the experimental results both from this experiment and from other studies. The emphasis will be on the A_1 enhancement since more information is available about this than for the A_3 . The discussion, however, applies to both effects.

The early observations of the A_1 peak were all in reactions which could be diffractive, i.e. in reactions with no charge, strangeness or baryon exchange and, furthermore, no decay modes other than that into a $\rho\pi$ state have been seen for the A_1 . These facts, together with the great width of the enhancement, a factor of 2 greater than the width of any of the firmly established resonances, suggest that the peak may be kinematic rather than dynamic in origin.

Deck (Ref. 8.4) suggested a model to explain the enhancement

involving pion exchange. Basically the model states that the ρ is formed at the upper vertex by pion exchange and the exchanged virtual pion is diffractively scattered at the lower vertex. The ρ is formed with low momentum transfer and, thus, travels forward in the centre of mass system, while the diffractive scattering, in analogy with on-shell elastic scattering, is forward peaked. The ρ and the π therefore, tend to travel in the same direction and so phase space is distorted to give a low $\rho\pi\pi$ mass enhancement. Detailed calculations of this model show that a peak is predicted at the A_1 mass, but the predicted width is greater than that experimentally determined and the predicted production cross section is substantially smaller than that observed.

Berger (Ref. 8.5) adopted a Reggeised version of the Deck model and this has had more success in explaining the data. This model assumes a diagram of the type of figure 8.2 with the exchange at the upper vertex being the pion trajectory and at the lower vertex being the Pomeron. The four-momenta of the particles, p_1, p_2, q_1, q_2 and q_3 , are defined in this figure and the relativistically invariant variables used in the mathematical construction of the model can be defined in terms of these as follows:-

$$\begin{aligned}
 s_1 &= (q_1 + q_2)^2 = M(\pi d)^2 \\
 s_2 &= (q_2 + q_3)^2 = M(\pi \rho)^2 \\
 s_3 &= q_3^2 = M(\rho)^2 \\
 t_1 &= (q_1 - p_1)^2 = t_{dd} \\
 t_2 &= (q_2 - p_2)^2 = t_{\pi\rho}
 \end{aligned}
 \tag{8.1}$$

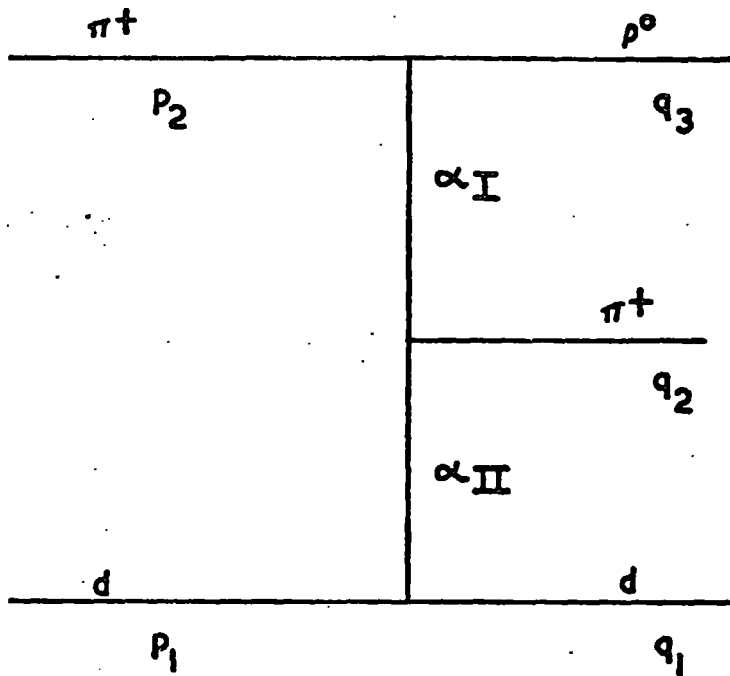
The matrix element (M) associated with this diagram is assumed to factorise:

$$|M|^2 = |M_{\pi\rho}|^2 |S_{\pi}|^2 |M_{\pi d}|^2
 \tag{8.2}$$

where S_{π} is the Reggeised pion propagator and residue:

FIG. 8.2

REGGEISED DECK EXCHANGE MECHANISM



α_I = pion trajectory

α_{II} = pomeron trajectory

P_1, P_2, q_1, q_2, q_3 are the 4-momenta of the respective particles.

$$|S_{\pi}|^2 = \frac{\{\pi(1+\alpha)\}^2}{2\{1-\cos(\pi\alpha)\}} \beta(t_2) \left\{ \frac{1}{s_0} [s_2 - t_1 - \mu^2] - \frac{1}{2t_2} (s_3 - \mu^2 - t_2)(t_1 + t_2 - \mu^2) \right\}^{2\alpha} \quad 8.3$$

s_0 is a constant = 1 GeV²

μ = pion mass

β is a slowly varying function of t_2 and is equal to unity at $t_2 = \mu^2$. It has been set to this value throughout

α is the pion trajectory, taken here as linear:

$$\alpha = t_2 - \mu^2 \quad 8.4$$

Berger does not use a Reggeised form for $M(\pi d)$ (the virtual pion-deuteron scattering matrix element) but assumes that the off shell scattering is similar to the on shell scattering, which gives a pronounced diffraction peak. Hence.

$$|M_{\pi d}|^2 = \left(\frac{d\sigma}{d\Omega} \right)_0 \exp(A t_1) \quad 8.5$$

where $\left(\frac{d\sigma}{d\Omega} \right)_0$ is the forward scattering cross section, which is related to the total cross section by the Optical Theorem:

$$\left(\frac{d\sigma}{d\Omega} \right)_0 = \lambda_0 \sigma_{\pi d}^2 \quad 8.6$$

$$\text{and } \lambda_0 = [s_1 - (md - \mu)^2] [s_1 - (md + \mu)^2]$$

md = deuteron mass.

The slope parameter A is taken as 20 (GeV/c)^{-2} .

$|M_{\pi d}|$ is given by Berger as:

$$|M_{\pi d}|^2 = g^2 (s_3 - 4\mu^2) \quad 8.7$$

and g is the $\pi\pi\rho$ coupling constant.

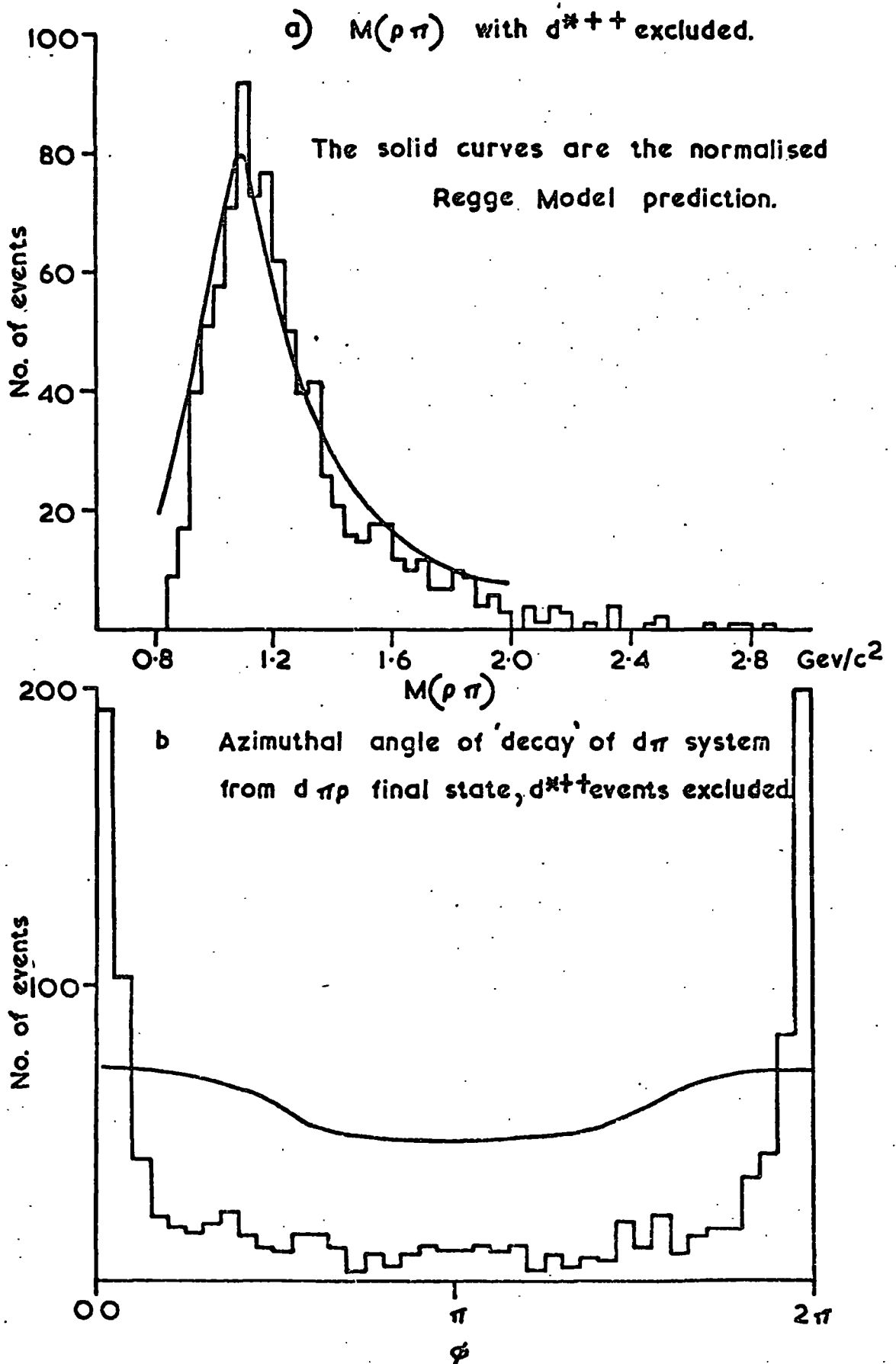
This matrix element has reproduced the A_1 peak very well both with respect to mass and width but the cross section it gives is still found

to be lower than that determined experimentally. Vanderhagen et al (Ref. 8.6) however, found that the predicted cross section could be changed by a factor of 4 without significantly affecting the various mass distributions by using a non linear form for the pion trajectory.

A Monte-Carlo calculation of the expected form of the $d\pi\rho$ final state at 11.7 GeV/c incident pion momentum, shows that the shape of the $\rho\pi$ effective mass distribution is well reproduced (fig. 8.3 (a)) at this energy as was found at lower energies. The figure contains only events where the $d\pi$ mass is greater than $2.4 \text{ GeV}/c^2$ in order to eliminate d^* events, since the lower vertex is more complicated in this case, involving $\Delta(1236)$ production. The same selection was made in the Monte-Carlo calculations. In fact the only distribution for which there is not reasonable agreement between the experimental data and the predicted curve is the azimuthal angle in the Gottfried-Jackson reference frame of the 'decay' of the $d\pi$ system, taken as a composite particle. This is shown in figure 8.3 (b). The non-isotropy of this angular distribution, as noted for d^* events, is increased when the $d\pi$ effective mass is above the d^* region. The model predicts an anisotropy (smooth curve in figure 8.3 (b)) but of a much smaller magnitude than the experimental one. The degree of success of the model in the case of the A_3 enhancement is more difficult to assess, since the statistics are small, but qualitative agreement is found, except again, in the case of azimuthal angular distribution of the $d\pi$ system. This discrepancy does not necessarily invalidate the model but suggests that a better approximation than the one made for the πd vertex is required. It is interesting to note that this discrepancy has not previously been observed

Although in most respects the model seems to reproduce the data quite well, it has been suggested by Chew and Pignotti (Ref. 8.7) that

FIG. 8.3



such a mechanism is not incompatible with a resonant interpretation of the peak. They extended the notion of duality as introduced by Dolen, Horn and Schmidt (Ref. 8.8) from single exchanges to double exchanges of the type of figure 8.2. Duality relates the imaginary part of the t-channel amplitude at high energies to the s-channel amplitude at low energies and states that extrapolation of the high energy t-channel amplitude into the low energy region should explain in an averaged way the low energy reaction. If the t-channel amplitude predicts a high s-channel cross section at low energy then the presence of one or more s-channel resonances at the low energy can be inferred. Chew and Pignotti's extended duality states that if the double exchange mechanism of fig. 8.2 is valid for high $\rho\pi$ masses, then its prediction of a large $\rho\pi$ production cross section at low masses is not incompatible with the possibility of resonances being present.

Cason et al (Ref. 8.9) have argued against the Chew and Pignotti interpretation of the success of the Berger-Regge-Deck (B.R.D) model on the grounds of their results on the reactions:

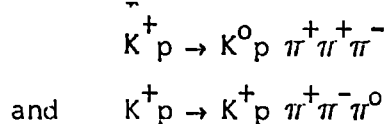


They find an A_1 peak in the former reaction, as might be expected, but also in the latter reaction there is a peak in the A_1 region under the rather strict selection criteria that the mass of the $\pi^- p$ system must be greater than $1.8 \text{ GeV}/c^2$, to eliminate isobar production, and that the 4-momentum transfers from beam pion to the ρ^- and from the target neutron to proton both be less than $0.5 (\text{GeV}/c)^2$; in order to select events which are most likely to be doubly peripheral and to ensure the correct ordering of the exchange chain. In the case of reaction 8.9 the virtual scattering at the lower vertex is not elastic but can be built into the model

nonetheless. They find that the peaks in the A_1 region from both reactions are well described by the B.R.D. model with the same normalisation and argue that, if Chew and Pignotti's extended duality is valid, then there must be resonances in the $\rho^- \pi^-$ system. Such a suggestion is unlikely since it would imply the existence of exotic resonances which are produced with high probability, although previous searches for exotic resonances have indicated that, if they exist at all, they have very low production cross sections. The A_1 enhancement as produced in a coherent channel such as the one being studied here, moreover, cannot be exotic. They suggest that the extended duality argument, involving extrapolation of the whole t-channel amplitude rather than only its imaginary part, is, therefore, invalid and consequently that the A_1 enhancement is purely kinematical.

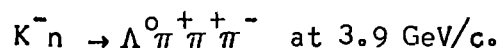
Uhoeda (Ref. 8.10) has contradicted this suggestion, arguing that effects other than the Deck Effect can contribute to the $\rho^- \pi^-$ peak, effects which are not present in diffractive A_1 production. He concludes that there may still be a resonant state in the non-exotic A_1 peak.

No strong evidence for A_1 production in an $I = 1$ state from reactions where the Deck type mechanism cannot occur has been presented. Anderson et al (Ref. 8.11) have seen some evidence for backward production of the A_1 in a missing mass experiment, but it remains inconclusive. Two experiments (Ref. 8.12 and 8.13) on the reactions:

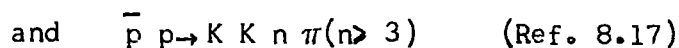


have found both A_1^+ and A_1^0 peaks in the 3-pion system but Rabin et al. (Ref. 8.14) studying the same reactions with far greater statistics and at a very similar energy to that of Ref. 8.12, find no such peaks and

argue against the previous results being anything other than statistical. Grennel et al (Ref. 8.15) have seen a $\rho\pi$ peak in the A_1 region in the reaction:



This reaction involves both charge and strangeness exchange and A_1 production cannot be explained by any simple Deck-type process, but the evidence for the peak is not conclusive. Small A_1 peaks have been seen in $\bar{p} p$ collisions of the type:



but the high background involved, due to many possible 3-pion combinations, particularly in the former of these reactions, renders such peaks rather unconvincing.

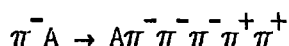
The latter of these two reactions is interesting, however, in that an analysis of the three pion Dalitz Plot shows that, while other spin states are varying smoothly through the A_1 mass region, the $J^P = 1^+$ state shows a distinct peak centred on the A_1 mass. This peak, however, is due to a D-wave $\rho\pi$ decay as opposed to the S-wave decay usually seen in diffractive experiments. Froggatt and Ranft (Ref. 8.18) have made an analysis of the spin states which would occur for events produced by the B.R.D. mechanism, at various energies and find that the dominant state is always S-wave $J^P = 1^+$ and, in particular, that the fraction of D-wave $J^P = 1^+$ should be negligible. Observation of D-wave decay of a $1^+ A_1$ signal would, therefore, confirm the resonant interpretation. The evidence on this point, is however, rather contradictory: Morse et al (Ref. 8.19) and Ballam et al (Ref. 8.20) in $\pi^- p$ experiments at 7 and 16 GeV/c respectively both find considerable D-wave decay, while Ascoli et al (Ref. 8.21) in a compilation of data from several $\pi^- p$ experiments at incident momenta in the range 5-25 GeV/c find that the S-wave decay

is predominant with little or no D-wave decay. The result reported in Chapter 6 for this experiment shows a possibility of D-wave decay of the A_1 enhancement although it cannot be confirmed.

A further possible way of distinguishing between the resonant and non-resonant interpretations of the A_1 enhancement has been suggested by Goldhaber (Ref. 8.22) and Trefil (Ref. 8.23). This depends on the measurement of the cross section of the A_1 with nucleons: if the A_1 is resonant the cross section should be equal to that of the pion, whereas the cross section for an uncorrelated $\rho\pi$ pair should be 1.7 times greater. No direct measurement of the cross section of the A_1 on nucleons is possible, of course, but studies of the A_1 produced coherently with heavy nuclei can yield information on this quantity by comparison with the results of A_1 production in hydrogen. Goldhaber found that:

$$\sigma(A_1 N) \leq 0.5 \begin{matrix} +0.3 \\ -0.2 \end{matrix} \sigma(\pi N)$$

supporting the resonant interpretation and Hwang et al (Ref. 8.24) found the two cross sections to be approximately equal. The most complete study of this problem is by Bemporad et al (Ref. 8.25) in a high statistics missing mass experiment, with a number of complex nuclei as targets. They find that $\sigma(A_1 N)$ is approximately equal to $\sigma(\pi N)$ but suggest that this does not necessarily confirm the resonant interpretation since the cross section is almost constant at this value up to a 3-pion mass of $1.5 \text{ GeV}/c^2$ and rises only slowly for higher masses. The cross section for 5-pion systems, moreover, produced in the reaction:



where A is a complex nucleus, is found to be even smaller than the corresponding 3-pion cross section, suggesting that, perhaps, the model used to predict the non-resonant cross section may be invalid.

The situation is, therefore, rather confused and, as yet, no

definite conclusions as to whether the A_1 enhancement is resonant can be made. More data on non-diffractive A_1 production and more detailed information on the spin-characteristics of the enhancement are needed before the problem can be resolved. There is less data available on the A_3 enhancement and again, no conclusions can be made.

CHAPTER NINE

SEARCH FOR COHERENT A₂ PRODUCTION

Introduction

It has been assumed in the previous chapters that the dominant mechanism responsible for this channel is either diffraction dissociation of the beam pion into the three pion system or pion exchange with an elastic scattering of the virtual pion at the deuteron vertex (fig. 1.1). Many other exchange mechanisms which can produce a correlated 3-pion state (e.g. ρ exchange) are forbidden by the criterion of coherence. The deuteron, however, is a special case of a nucleus in that the spins of the constituent nucleons are aligned and this leads to the possibility of unnatural parity exchange, provided that the isospin of the exchanged object is zero. Exchange of the η meson may, thus, be expected to occur and this will lead to 3-pion states in the natural spin parity series $J^P = 1^-, 2^+, 3^-$ etc. It is possible, therefore to produce the A_2 meson in this channel by η exchange and observation of A_2 production would provide evidence for such a mechanism.

This chapter reports the results of a search for coherent A_2 production. If the production cross section is non-zero, it must be small since no evidence has been presented at lower energies for an A_2 signal in the final state of this channel. No detailed evidence for absence of A_2 production has been presented at lower energies and it is possible that a small amount may have been overlooked. This experiment has higher statistics than any at lower energies and so it may be possible to detect even a very small A_2 production cross section.

9.1 The sample of events used

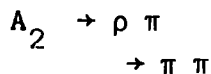
Only a subsample of the total number of events fitting the channel have been used in the search. In the first place, the three prongs events have been rejected from the sample for two main reasons:

(i) The mass resolution of the 3-prong 3-pion effective mass is greatly inferior to that of the 4-prong sample, since the 3-prongs are the results of 1-G fits. A small enhancement in the A_2 region may, therefore, be smeared out and unrecognisable.

(ii) The selection criteria for distinguishing between this channel and other channels are less stringent for the 3-prong sample than for the 4-prongs. It is likely that there is some contamination of the coherent channel by the channel in which the deuteron breaks up into its constituent nucleons in the 3-prong events and, since the A_2 can be produced by ρ exchange if the interaction takes place on only one of the nucleons inside the deuteron any observation of A_2 production in this sample would be evidence for contamination by the break-up reaction rather than η exchange in the coherent channel.

This selection does not seriously effect the number of events in the A_2 region, since the very low values of t for the 3-prong events tends to suppress higher 3-pion masses. It is possible, moreover, that the slope of the $d\sigma/dt$ distribution for η exchange is less steep than that for Pomeron exchange, and if this is the case, antiselecting very low t events will result in an increased A_2/A_1 ratio. This latter consideration is not necessarily valid, however, since the slope of the $d\sigma/dt$ distribution is determined more by the deuteron form factor than the nature of the exchange mechanism.

The second selection consists of using only those events which have at least one neutral dipion effective mass in the ρ^0 region, This is for the simple reason that the A_2 has never been observed to decay directly into three pions. It decays always by the two-step process:



The search was, therefore, carried out on the sample of 763 four pronged events of the type:

$$\pi^+ d \rightarrow d \pi^+ \rho^0.$$

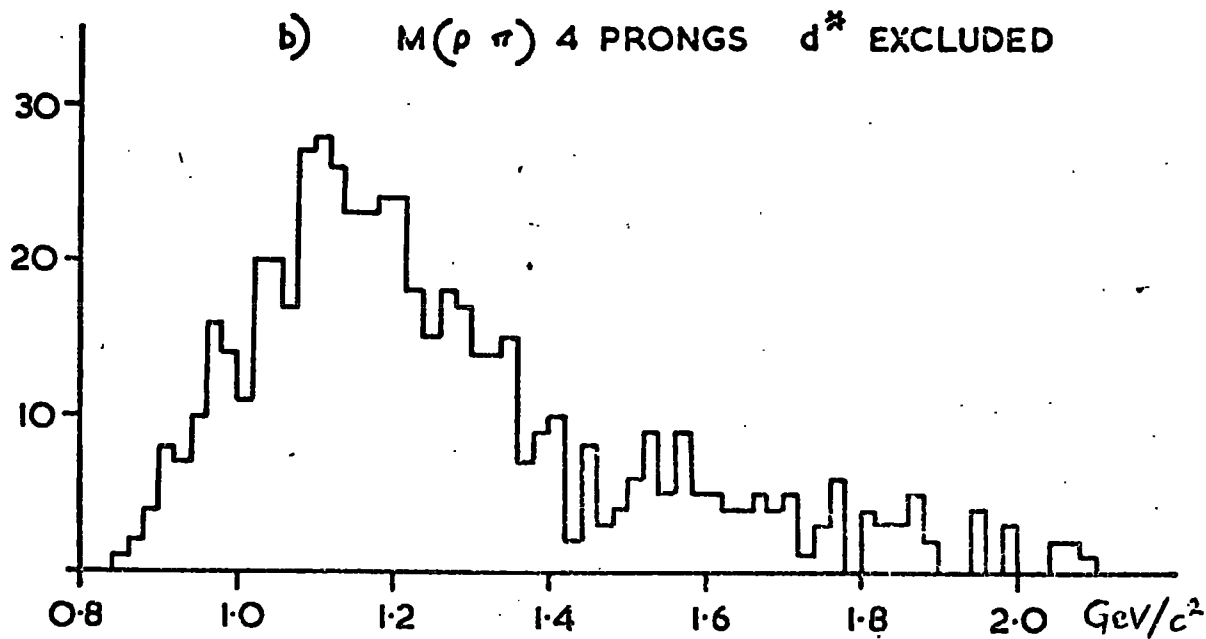
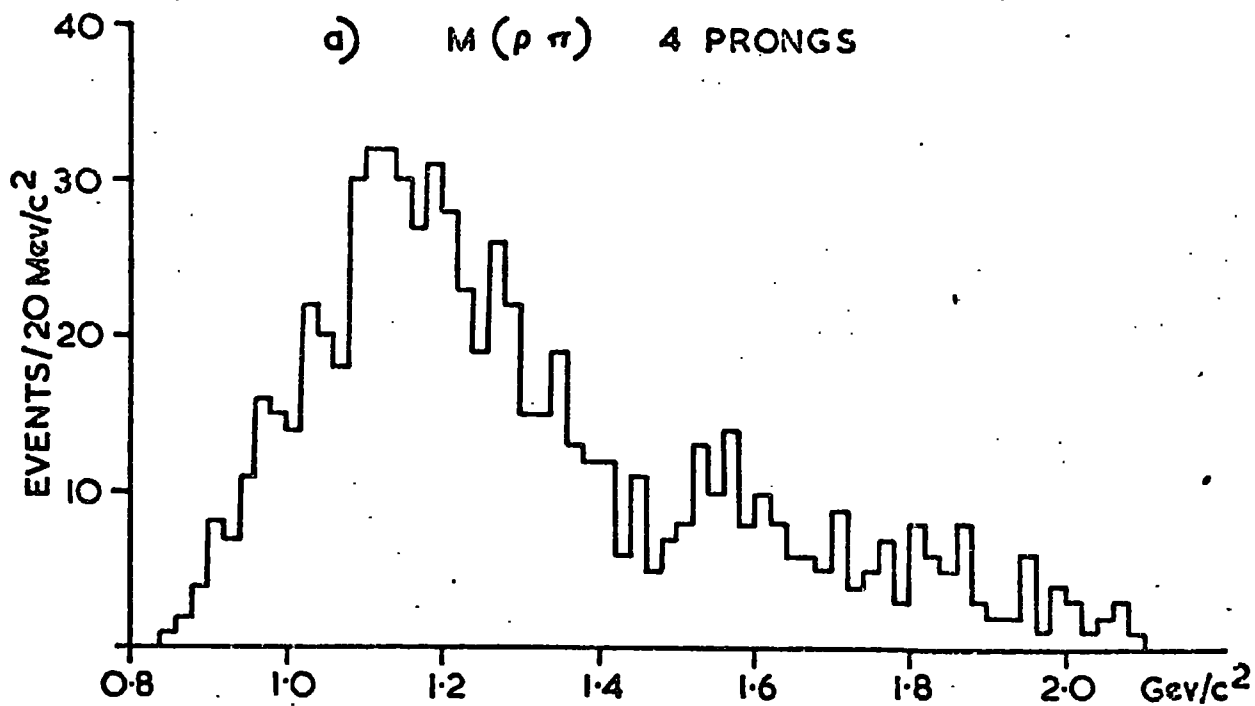
9.2 The results of the search:

The effective mass of the $\rho\pi$ system is shown in figure 9.1 (a) for the events selected as above. The bin width used is $20 \text{ MeV}/c^2$ so that any narrow enhancements may be observable. The small peak which appears in the figure at a mass $\sim 1280 \text{ MeV}/c^2$ can easily be explained in terms of a statistical fluctuation, although if the background is assumed to be a straight line joining the adjacent bins then the effect has a magnitude of more than 2-standard deviations. The same mass spectrum is shown in figure 9.1 (b) after removal of d^* events. The peak is less noticeable in this figure but it is unlikely that d^* reflections would produce a peak so narrow and a statistical explanation must be invoked in order to disregard it.

It is often possible to produce a cleaner A_2 signal by use of the 3-pion Dalitz plot. This arises from the fact that the spin-parity of the A_2 meson ($J^P = 2^+$) is in the natural J^P series and is consequently expected to show a depopulation of the Dalitz plot around the boundary (Ref. 9.1) and no such depopulation is expected for the unnatural spin-parity series. Since the background below any A_2 signal in this channel is due largely to A_1 production ($J^P = 1^+$) or to diffraction dissociation of the beam pion which can only give the unnatural J^P series, the signal to background ratio in the A_2 region can be increased by selecting the central region of the Dalitz plot. To this purpose it is convenient to define the quantity :

$$\lambda = \frac{|P_1 \times P_2|^2}{\frac{3}{4} (M^2 - \mu^2)^2}$$

FIG 9.2



where P_1 and P_2 are the 3-momenta of two of the pions in the 3-pion rest frame, M is the 3-pion effective mass, and μ is the pion mass. λ is constrained to lie between 0 and 1 and effectively measures the distance of an event from the Dalitz plot boundary i.e. $\lambda = 0$ on the boundary and 1 at the centre.

Figures 9.2 (a) and (b) show the $\rho\pi$ mass distributions in the two cases $\lambda < 0.5$ and $\lambda > 0.5$ respectively. It can be seen that for $\lambda < 0.5$ there is a suggestion of a dip in the distribution at $\sim 1300 \text{ MeV}/c^2$ while there may be an enhancement in this same region when λ is greater than 0.5. The hatched histograms in these figures show the same spectra with d^* events excluded, and it can be seen that these features in the A_2 region are not affected by this selection. The small enhancement is more apparent in figure 9.2 (c) where only events with $\lambda > 0.6$ have been plotted. This further reduces the background and leaves a small signal centred on $1300 \text{ MeV}/c$, where the A_2 would be expected to occur. Figure 9.2 (d) shows the spectrum after rejecting all events with $\lambda < 0.85$. The remaining statistics are small and show nothing except an enhancement at $1300 \text{ MeV}/c$.

The distributions of λ for events in the A_2 region (defined as $1.25 < M(\rho\pi) < 1.35 \text{ GeV}/c^2$) and for events in regions $100 \text{ MeV}/c^2$ wide above and below the A_2 region are shown in figure 9.3. While there is some evidence for accumulation of events above $\lambda = 0.5$ in regions other than that of the A_2 (notably for $1.15 < M(\rho\pi) < 1.25$), nowhere is the tendency so marked as in the A_2 region itself. This fact is emphasised in table 9.1 where the number of events with $\lambda > 0.6$ and $\lambda > 0.85$ are given for various regions of 3-pion mass, together with the percentage of the total number in the region. This data is given in the table for all 4-prong events, for those 4-prong events which have a neutral dipion mass in the ρ^0 region and for the subsample of these which do not

FIG 9.2 $M(p\pi)$ 4 PRONGS FOR VARIOUS REGIONS OF λ

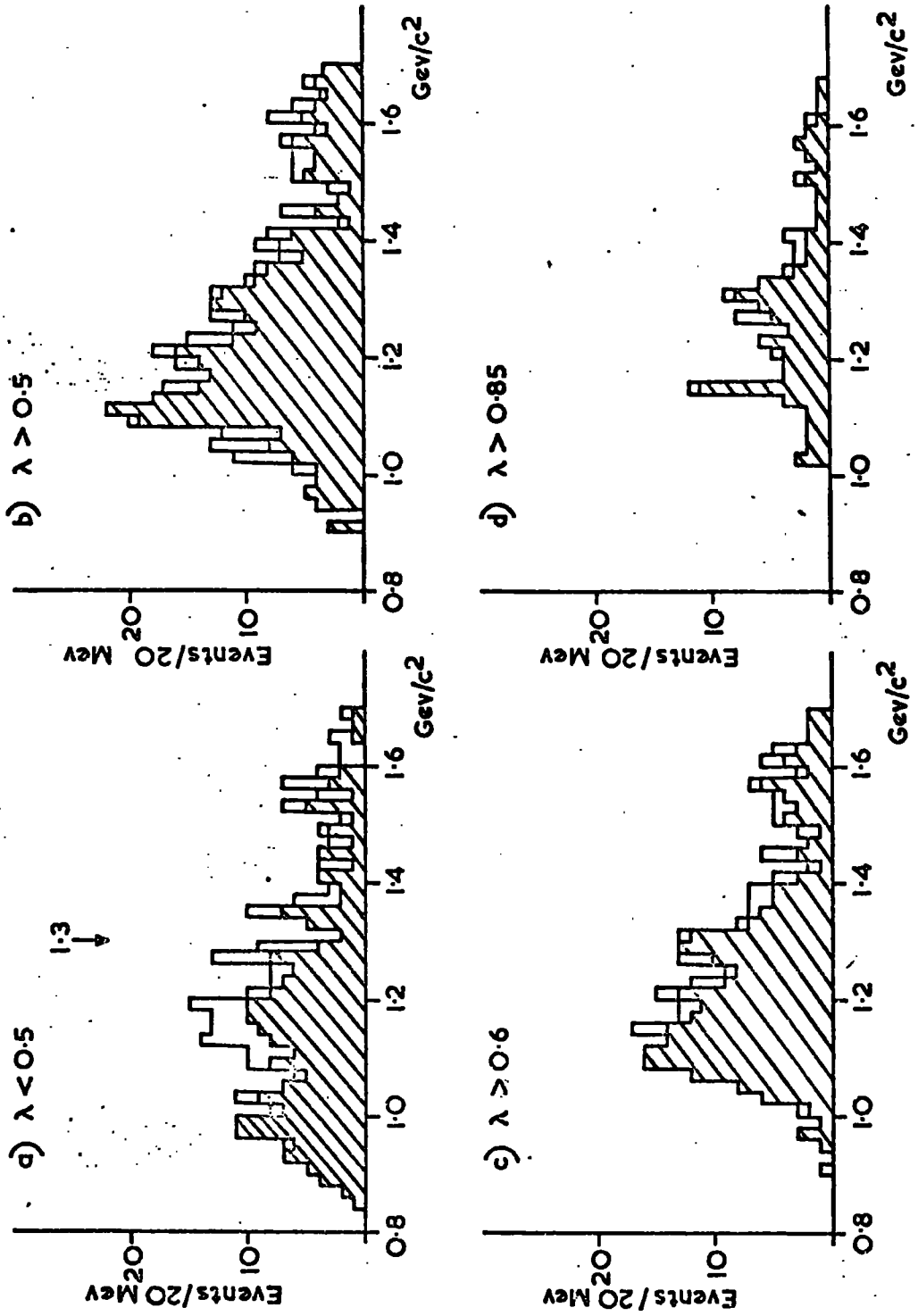
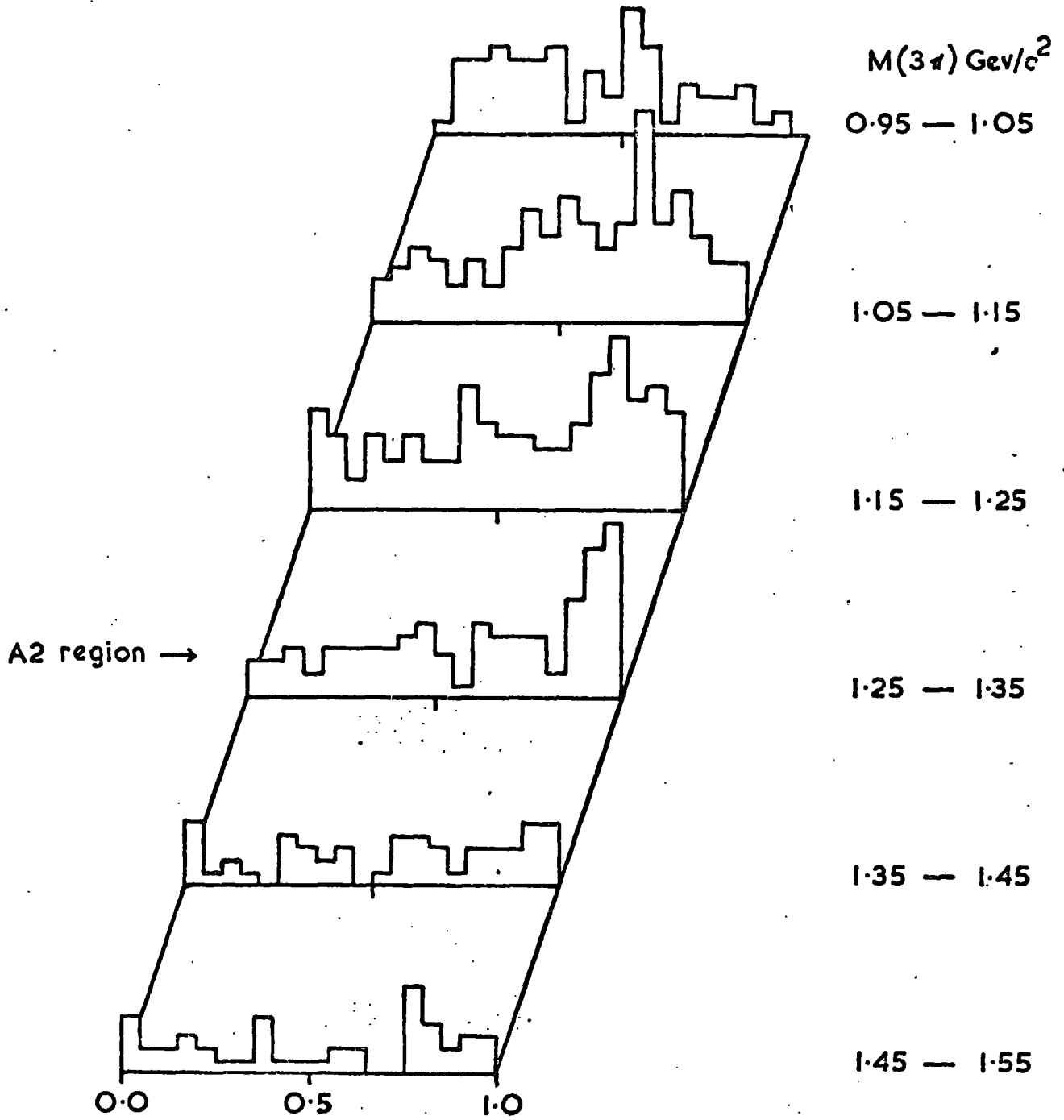


FIG 9.3

DISTRIBUTION OF λ FOR SEVERAL REGIONS OF $M(3\pi)$



3 mass range GeV/c	ALL 4 PRONG EVENTS						4 PRONGS ρ^0 SELECTED						4 PRONGS ρ^0 SELECTED d^* EXCLUDED							
	No. with $\lambda > 0.6$		% with $\lambda > 0.6$		No. with $\lambda > 0.85$		% with $\lambda > 0.85$		Total		No. with $\lambda > 0.6$		% with $\lambda > 0.6$		Total		No. with $\lambda > 0.6$		% with $\lambda > 0.85$	
	Total	No. with $\lambda > 0.6$	% with $\lambda > 0.6$	No. with $\lambda > 0.85$	% with $\lambda > 0.85$	Total	No. with $\lambda > 0.6$	% with $\lambda > 0.6$	No. with $\lambda > 0.85$	% with $\lambda > 0.85$	Total	No. with $\lambda > 0.6$	% with $\lambda > 0.6$	No. with $\lambda > 0.85$	% with $\lambda > 0.85$	Total	No. with $\lambda > 0.6$	% with $\lambda > 0.6$	No. with $\lambda > 0.85$	% with $\lambda > 0.85$
0.95 - 1.05	95	23	24	4	4	83	18	22	3	4	76	17	22	3	4	76	17	22	3	4
1.05 - 1.15	166	71	43	18	11	135	67	50	17	13	119	66	55	17	14	119	66	55	17	14
1.15 - 1.125	172	76	44	27	16	138	69	50	27	20	110	57	52	25	23	110	57	52	25	23
1.25 - 1.35	135	64	47	34	25	100	57	57	34	34	81	51	63	29	36	81	51	63	29	36
1.35 - 1.45	80	32	40	13	16	53	27	50	13	24	25	18	51	8	23	25	18	51	8	23
1.45 - 1.55	71	23	32	8	11	45	21	47	8	18	31	14	45	6	19	31	14	45	6	19

TABLE 9.1

The number of events from various regions of the

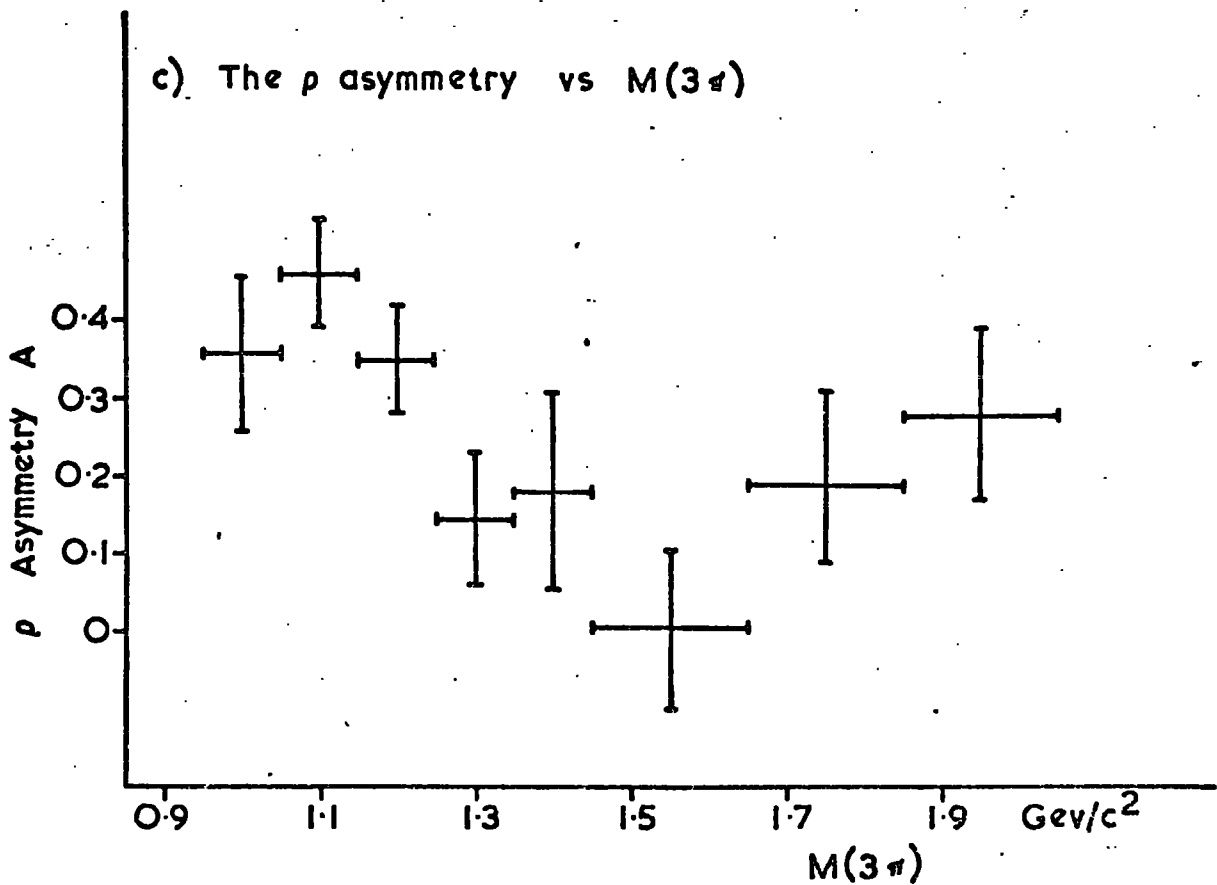
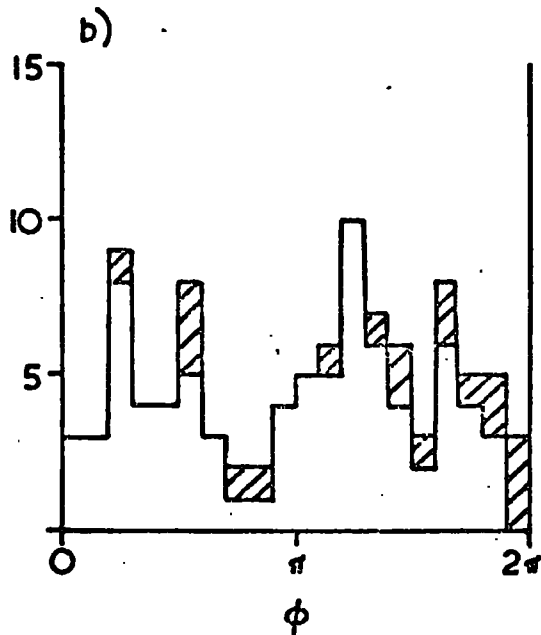
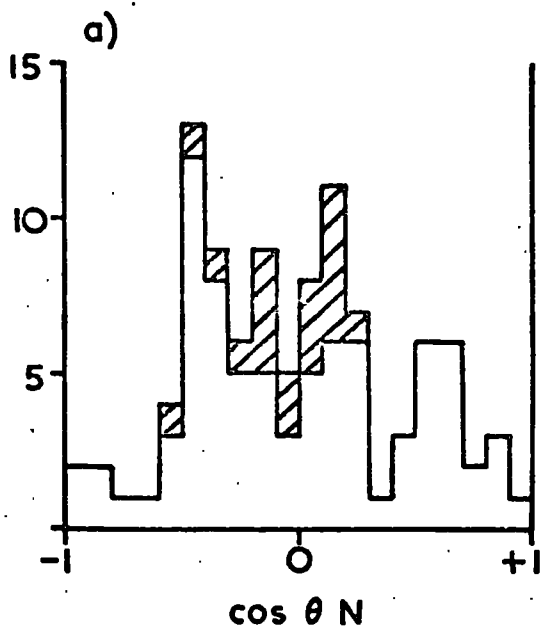
Dalitz plot in different 3π mass ranges.

have a $d\pi^+$ effective mass in the d^{*++} region. In every case the A_2 region shows a higher percentage of events near the centre of the Dalitz plot, and consequently a lower percentage near its border, than do the surrounding 3-pion mass regions.

This method of emphasising the A_2 signal is not entirely legitimate because, having selected ρ events, only one band of the Dalitz Plot is populated and this band does not necessarily cross the centre. In fact a dipion mass of $0.765 \text{ GeV}/c^2$, the ρ mass, corresponds to a line on the Dalitz plot which crosses the centre ($\lambda = 1$) when the 3-pion mass is exactly $1.3 \text{ GeV}/c^2$. The ρ band as defined here ($0.665 < M(\pi^+\pi^-) < 0.865 \text{ GeV}/c^2$), moreover, cannot cross the centre of the Dalitz plot for 3-pion masses below $1.12 \text{ GeV}/c^2$ or above $1.47 \text{ GeV}/c^2$. Selecting the central part of the Dalitz plot and simultaneously selecting ρ^0 's, therefore, leads to the danger of manufacturing a signal in the $\rho\pi$ mass spectrum at $1300 \text{ MeV}/c^2$. While this effect may partly explain the signals in figs. 9.2 (b) (c) and (d), it cannot be entirely responsible since, for example, the whole of the ρ band can have $\lambda > 0.6$ for 3 pion masses greater than $1.13 \text{ GeV}/c^2$. The dip at $1300 \text{ MeV}/c^2$ in fig. 9.2 (a), furthermore, would be expected for a true A_2 signal but need not occur otherwise since the ρ band can always give low values of λ .

The decay angles of the normal to the 3-pion decay plane in the Gottfried-Jackson frame for events in the A_2 region ($1.25\text{-}1.35 \text{ GeV}/c^2$) are shown in figure 9.4 (a) ($\cos \theta_N$) and 9.4 (b) (ϕ_N). Although the statistics are small, the $\cos \theta_N$ distribution does seem to deviate from the $\sin^2 \theta$ shape which would be expected if the signal were merely a fluctuation in the A_1 peak. If the signal were pure A_2 ($J^P = 2^+$) produced by simple η exchange, then the density matrix ought to have $\rho_{00} = 1$ and all other elements zero, so that the distribution of $\cos \theta_N$

FIG. 9.4



should be described by:

$$W(\cos \theta_N) = K (\cos^2 \theta_N - \cos^4 \theta_N)$$

The distribution is not well described by this expression but it is interesting to note in figure 9.4 (a) the dip at $\cos \theta_N = 0$ as would be expected from this expression. No detailed fit of the distribution has been attempted since the statistics are small and if the 2^+ state is present it may interfere with the background, leading to a complicated form for the decay distributions.

A test has been used, however, to see if the observed enhancement is compatible with the spin-parity assignment $J^P = 2^+$. This is based on the asymmetry parameter of the ρ^0 decay angles A defined in Eq. 6.2. As has been seen the A_1 enhancement seems to decay partly into $\rho\pi$ and partly into $\epsilon\pi$ so that the ρ 's from the A_1 decay show the characteristic decay asymmetry. A 2^+ object cannot decay into $\epsilon\pi$, however, and, if the A_2 is produced, the ρ 's resulting from its decay should themselves decay symmetrically. While it may be expected that the background below the A_2 signal will give an asymmetric ρ , the ρ asymmetry from the total number of events in the A_2 region should be smaller than elsewhere. To test this hypothesis the ρ asymmetry from several regions of $\rho\pi$ effective mass has been calculated and the results are shown in figure 9.4 (c). It is clear that in the A_2 region the asymmetry falls significantly below its value at lower $\rho\pi$ masses, in agreement with the interpretation of the effect as being due to A_2 production. Above the A_2 region, the ρ asymmetry remains small, rising again only for masses greater than $1.65 \text{ GeV}/c^2$. The low value of the asymmetry between 1.35 and $1.65 \text{ GeV}/c^2$ can be explained in terms of the background beneath the ρ signals, since it is in this range of $\rho\pi$ mass that this background is particularly high. The background asymmetry has been estimated from the asymmetry of two control regions immediately above and below the ρ^0

region, and, after estimating the amount of background below the ρ signal in each region of $\rho\pi$ mass, A was recalculated with the background subtracted. This procedure has little effect on the results below the A_2 region, but the asymmetry is reduced in the A_2 region to 0.09 while above the A_2 it is increased to 0.35 in the mass range 1.35 - 1.45 GeV/c^2 . After background subtraction there is thus a distinct dip in A at the A_2 mass. The value of A in the $\rho\pi$ mass range

1.45 - 1.65, is similarly increased to 0.10 implying that the ρ asymmetry is smaller when events from the A_2 region are used than in any other mass range.

9.3 Conclusions

A small peak is apparent in the $\rho\pi$ mass spectrum when events taken from the central region of the Dalitz plot are used with a mass $\sim 1.3 \text{ GeV}/c^2$ and a width $< 100 \text{ MeV}/c^2$ as would be expected for an A_2 signal. The peak shows other features which are consistent with interpretation of the peak as the A_2 meson:

(1) It populates only the central region of the Dalitz plot i.e. there is a distinct lack of events at this mass when only events from the boundary of the Dalitz plot are used.

(2) The decay of the ρ^0 meson resulting from the decay of the peak in the A_2 region is more symmetric than it is from any other $\rho\pi$ mass region.

While it is impossible to state categorically that the A_2 meson is produced in this channel, there is, nonetheless, a certain amount of evidence to support that contention. If this result is confirmed, it represents the first observation of η -exchange in coherent deuteron interactions.

C H A P T E R T E N

C O M P A R I S O N S A N D C O N C L U S I O N S

This thesis has presented the results of the analysis of the channel:

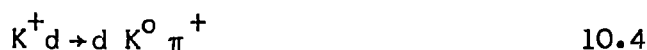


at 11.7 GeV/c incident pion momentum. The total cross section for this reaction was found to be $353 \pm 30 \mu\text{b}$ and this value is compared with the results of previous experiments on this channel in Table 10.1 and figure 10.1 (a). These show, with the exception of the result at 5.4 GeV/c (Ref. 10.3) that the cross section changes only slightly over a wide range of incident momenta, with perhaps a slight tendency to increase with increasing pion momentum. The only experiment with higher incident momentum (Ref. 7.6) quotes no channel cross section and cannot, therefore, confirm this increase.

An increase in cross section for other coherent reactions, is apparent in the published results. In the channel

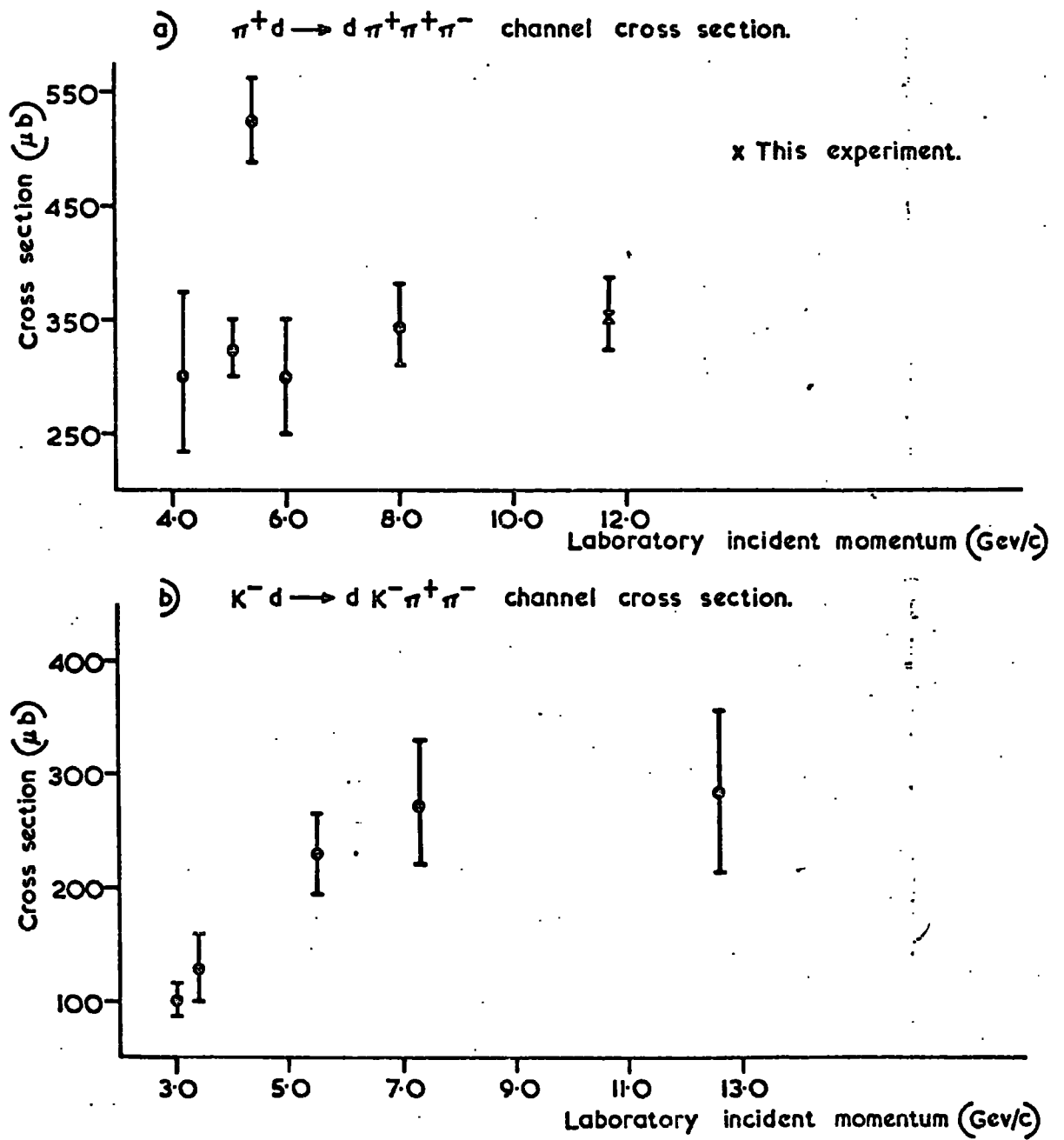


the cross section rises rapidly between 3 and 5.5 GeV/c incident momenta and then rather slowly above this. This can be seen in table 10.2 and figure 10.1 (b). There is less published data on other coherent deuteron reactions, though an increasing channel cross section seems to occur in each of the reactions:



and, furthermore, the same trend is apparent in coherent reactions on complex nuclei as can be seen from the work of Allard et al (Ref. 10.17) using a heavy liquid bubble chamber. The results and references for these

FIG. 10.1



reactions are given in table 10.1 Reaction 10.1 is found to be very peripheral, as expected for coherent reactions, with the slope parameter of the $d\sigma/dt$ distribution equal to 27.6 ± 3.0 . The slope of this distribution at other energies is given in table 10.1 and it can be seen that as the energy increases this parameter also increases, which is equivalent to the statement that the effective size of the deuteron increases with increasing energy.

The final state of the interaction is dominated by ρ^0 production, as was the case at other energies (see table 10.1) with some f^0 production. No f^0 production has been reported at lower energies, except at 5 GeV/c (Ref. 10.2), which may be explained by the fact that very low momentum transfers limit f^0 production when the incident energy is low and the smaller statistics in the other experiments may have caused difficulty in detection.

A non resonant enhancement in the $d\pi^+$ mass spectrum, the d^{*++} , is present in this reaction, but its production cross section falls dramatically with increasing energy, as can be seen in table 10.1. At 11.7 GeV the azimuthal angle of decay of this enhancement in the Gottfried-Jackson reference frame is not isotropic, in contradiction with results at lower energies and with the simple one pion exchange model often described to explain this effect. No corresponding peak in the $d\pi^-$ mass spectrum is seen.

The three pion spectrum is dominated by a broad peak in the A_1 mass region, decaying into a $\rho^0\pi^+$ system. This peak has spin parity 1^+ with some interfering state of opposite parity, perhaps a $0^-\epsilon\pi$ state. The $\rho\pi$ system is predominantly in an S-wave but there is also some evidence for a D-wave state in the A_1 region. The cross section for A_1 production is difficult to determine, but has been calculated at this and other

energies by assuming every event in the three pion mass range 1.0 - 1.24 GeV/c² is due to A₁ production. The results of this are given in table 10.1 and indicate that the cross section is fairly independent of incident momentum, a feature characteristic of diffractively produced states.

A secondary peak in the three pion mass spectrum at ~ 1675 MeV/c² which is attributed to A₃ production, is seen to decay dominantly into an f⁰ π⁺ state. Its decay characteristics indicate that the spin parity is 2⁻, formed by an S-wave f⁰ π⁺ state.

Neither the A₁ nor A₃ enhancements conserve s-channel helicity. While the A₃ is totally compatible with the hypothesis of t-channel helicity conservation, there is some evidence that this hypothesis is not completely valid for A₁ production, although it cannot be disregarded. Outside the A₁ and A₃ mass regions no clear evidence on TCHC or SCHC is present though below the A₁ the former is a better hypothesis and above the A₃ the latter is more compatible with the data.

The analysis has shown that, of the many possible exchange mechanisms which may contribute to the channel (fig. 1.1) only those of figs. 1.1 (a) and 1.1 (e) can explain the data. The latter of these must occur in order to explain the d* enhancement although the decreasing d* production cross section suggests, perhaps, that this mechanism is of decreasing importance. Both mechanisms can explain the general features of the channel, the former by Pomeron exchange and the latter by exchange of the pion trajectory at the upper vertex and diffractive scattering (Pomeron exchange) at the lower vertex. The doubly peripheral diagram is presumably not important outside the A₁ and A₃ regions, since it leads to threshold enhancements and this is not the case in other regions. The possible D-wave decay of the A₁ enhancement, moreover, is incompatible

with such a mechanism. The longitudinal phase space analysis shows that, perhaps, two mechanisms are present, one responsible for A_1 and A_3 production and the other for d^* production.

There is a small indication for A_2 production in this reaction, which, if accepted, implies that exchange of the type of fig. 1.1 (a) does indeed occur, with the exchanged particle being the η meson.

Two other, very small effects are present in the final state of the interaction. The former, a narrow $\rho^0\pi^+$ enhancement with a mass $\sim 1.56 \text{ GeV}/c^2$, has been shown to be probably statistical in origin. The latter, a $\pi^+\pi^-$ peak with a mass $\sim 1.08 \text{ GeV}/c^2$, has been tentatively identified with the η_N meson and shown to have similar characteristics to previous observations of this peak.

Incident Momentum (GeV/c)	Cross Section (μb)	Slope of $d\sigma/dt$ dist. $(\text{GeV}/c)^{-2}$	ρ^0 cross section (μb).	% of ρ^0	d^{*++} cross section (μb)	% of d^{*++}	A_1 cross section (μb)	% of A_1	Ref.
4.2	304 ± 70	~ 18	140	46	158	52	148	49	10.1
5.04	324 ± 25	21.0 ± 0.8	243	75	116	36	154	48	10.2
5.4	528 ± 37	-	396	75	-	-	219	41	10.3
6.0	300 ± 50	32.7 ± 6.5	~ 300	~ 100	< 45	< 15	130	43	10.4
8.0	344 ± 35	-	272	80	34	10	152	44	10.5
11.7	353 ± 30	27.6 ± 3.0	226	64	45	13	134	38	This Expt.
13	-	30.0 ± 2.0	-	-	-	< 10	-	-	6.

TABLE 10.1

Compilation of $\pi^+ d$ experiments

REACTION	BEAM MOMENTUM (GeV/c)	CROSS SECTION (μb)	REFERENCE
$\text{K}^- \text{d} \rightarrow \text{K}^- \pi^+ \pi^-$	3.0	102 ± 14	10.6
"	3.4	130 ± 30	10.7
"	5.5	228 ± 35	10.8
"	7.3	274 ± 56	10.9
"	12.6	285 ± 70	10.10
$\text{K}^+ \text{d} \rightarrow \text{K}^+ \pi^+ \pi^-$	2.3	110 ± 16	10.11
"	3.0	210 ± 22	10.12
"	9.0	~ 332	10.13
"	12.0	331 ± 35	10.14
$\text{K}^+ \text{d} \rightarrow \text{dK}^0 \pi^+$	2.3	150 ± 35	10.11
"	3.0	228 ± 25	10.14
$\bar{\text{p}} \text{d} \rightarrow \text{d} \bar{\text{p}} \pi^+ \pi^-$	5.55	113 ± 38	10.15
"	7.0	260 ± 25	10.16
$\pi^- \text{Nuc} \rightarrow \text{Nuc} \pi^- \pi^- \pi^+$	6.0	26 ± 7 /molecule	10.17
"	18.0	55 ± 15 /molecule	10.17

TABLE 10.2

Compilation of other coherent reactions

A P P E N D I X A

A.1. Peripheral Models

Many strong interactions are found, empirically, to occur in such a way that the final state particles in the centre of mass system have approximately the same direction as one or other of the initial state particles. This lead to the suggestion that collisions were peripheral so that the glancing angle remains small and forms the basis of the peripheral model. Reactions are assumed to proceed by the exchange of a light strongly interacting particle and the range of the interaction, assuming a Yukawa potential, is greater for lighter exchanged particles. The lightest strongly interacting particle is the pion, which, therefore, would give the most peripheral interactions.

A.1.1 One pion exchange

Two body, or quasi-two body reactions of the type:

$$a + b \rightarrow c + d \quad \text{A.1}$$

where c and d may be short lived resonance particles are assumed to proceed by the exchange of a virtual pion and are described by a Feynman Diagram of the type shown in figure A.1, assuming that quantum numbers can be conserved at both vertices. The matrix element for such a diagramme is:

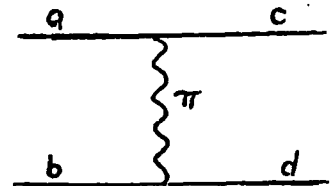


FIG A.1

$$M = V_I \frac{1}{\mu^2 - t} V_{II} \quad \text{A.2}$$

where μ = the pion mass

t = the square of the 4-momentum transfer from particle a to particle c .

V_I and V_{II} are vertex functions for the upper and lower vertices respectively. In the pole approximation, which consists of treating

the exchanged pion as a real or 'on the mass shell' pion, they are equivalent to the matrix elements for the processes:

$$a + \pi \rightarrow c$$

and

$$b + \pi \rightarrow d$$

This mechanism, thus, qualitatively describes the peripherality of the interaction in that the factor $(\mu^2 - t)^{-1}$, the pion propagator, ensures the preponderance of low values of $|t|$. Quantitatively, however, the form of the $d\sigma/dt$ distribution for reactions dominated by pion exchange falls off with increasing t more rapidly than the model suggests.

A.1.2 Other particle exchanges

In some reactions conservation of quantum numbers at the two vertices forbids the exchange of a pion and other exchange particles must be considered. For example, the reaction: $\pi^+ p \rightarrow \pi^0 \Delta^{++}(1236)$ cannot proceed by pion exchange but ρ exchange can be responsible for the interaction. The exchange of a particle with spin predicts, in the framework of the peripheral model, that the total cross section for the reaction will increase as s^{2J} as $s \rightarrow \infty$, where s is the square of the c.m. energy and J is the spin of the exchanged particle. Thus, while the peripheral model for such reactions may describe some features of the final state at relatively low energy, it is clearly invalid at high energy.

A.1.3 Form Factors

In order that one pion exchange may better represent the form of the $d\sigma/dt$ distribution, form factors can be included in equation A.2. These take the form of functions of t which are intended to allow for the spatial dimensions of the particles involved. In theory there are three form factors to consider: one for each vertex and one for the

exchanged virtual pion, but, since no satisfactory theory exists to predict the form factors, all three are combined into one rather arbitrary function. Amaldi and Selleri (Ref. A.1) suggested the form:

$$F(t) = \frac{0.72}{1 + \frac{\mu^2 - t}{4.73 \mu^2}} + \frac{0.28}{1 + \frac{\mu^2 - t}{32\mu^2}} \quad \text{A.3}$$

which while it explains the t distribution in some cases by no means does so in every case. The facts that often the t dependence of the form factors completely masked that of the propagator and, in some cases, that energy dependence needed to be included in the functions, thus rendering them not true form factors, suggest that the form factor approach has little physical meaning.

A.1.4 The Absorption Model

A more refined modification of the one pion exchange model is to include absorption. This is based on the fact that at high energies there are many possible inelastic channels open for the collision of particles a and b . These different channels are assumed to interfere with each other and thus the quasi-two body channel cross section can be reduced by the presence of other more complex final states. The more complex final states may be assumed to be more common for more central collisions, corresponding to lower impact parameters and higher values of t . The absorption of the quasi-two body cross section is, then, likely to be greater at higher t and better agreement with the experimental t -distribution might be expected. The model has had some success but, again, does not well reproduce the differential cross section when the outgoing particles have high spin.

A.2 The Regge-Pole Model

The Regge-pole model is important both in terms of particle classification and of high energy reactions. It relies on the assumption that the scattering amplitude for any particular reaction can be generalised to arbitrary complex values of angular momentum (ℓ) rather than just to positive integers. The amplitude can then be shown to be analytic over the whole complex angular momentum plane with $\text{Re } \ell > -\frac{1}{2}$ except for a finite number of poles which occur in the upper half plane. The position of the pole can vary as a function of energy and in general moves along the real positive ℓ -axis for energies below threshold and in the upper half plane (positive imaginary part) for greater energies. When the real part of the pole is a positive integer, then it corresponds to a bound state if the energy is below threshold and to a resonance, with a width related to the imaginary part of the pole, if the energy is greater than threshold. The path followed by the pole known as the Regge trajectory, can therefore relate several resonances with the same quantum numbers other than angular momentum.

By considering the function:

$$g(\ell) = \frac{\pi(2\ell+1) f(\ell, E) P_\ell(-\cos \theta)}{\sin \pi \ell} \quad \text{A.4}$$

where P_ℓ = the legendre polynomials

$\cos \theta$ = the c.m.s. scattering angle

E = the c.m.s. energy

$f(\ell, E)$ = the ℓ^{th} partial wave scattering amplitude.

and assuming that ℓ can take any complex value, then the total interaction amplitude, as represented by the sum of partial waves, can be related to the residues of this function at the Regge poles of $f(\ell, E)$ by integrating (A.4) around paths in the complex angular momentum plane

chosen to include either, only the Regge poles, or only the poles due to the factor $\sin \pi \ell$ in the denominator, which occur for:

$$\ell = 0, 1, 2, 3 \dots$$

the result of such an operation is to express the total amplitude $F(\cos \theta, E)$ as:

$$F(\cos \theta, E) = \frac{1}{k} \sum_i \text{Res } g(\ell = \alpha_i) + \text{Background Integral} \quad \text{A.5.}$$

where the sum runs over each of the i Regge-poles which contribute and the position of the i^{th} pole is at $\ell = \alpha_i$.

In applications of the Regge-pole model to strong interactions, a form of the scattering amplitude corresponding to (A.5) is assumed for the t -channel process and the principle of crossing symmetry is invoked to describe the s -channel process. The energy dependence of each regge pole contribution is then proportional to $\frac{s}{s_0}^{\alpha(t)}$ for large s where s is the c.m.s. energy squared
 t is the 4-momentum transfer squared
 s_0 is an arbitrary scale factor
 and α is the form of the trajectory for the particular pole.

This energy dependence can be written:

$$\left(\frac{s}{s_0}\right)^\alpha = \left(\frac{s}{s_0}\right)^{R_e \alpha} \exp(i I_m \alpha \log \frac{s}{s_0}) \quad \text{A.6}$$

which shows that a pole with large $R_e \alpha$ will dominate an interaction at high energy. This is equivalent to considering the interaction in the same way as for one particle exchange models, except that it is a Regge-trajectory which is exchanged.

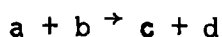
The Regge pole model has proved successful in describing many reactions. In particular, the energy dependence of reactions where

spin zero particles cannot be exchanged can be explained in contrast to the predictions of a one particle exchange model, and the shrinkage of the diffraction peak in pp elastic scattering can be predicted.

A P P E N D I X B

B.1 Reference Frames

In discussing the decay of a resonance, two angles of a suitably chosen decay direction can be defined in terms of a right-handed cartesian co-ordinate system. This co-ordinate system, or reference frame, can, in principle, be any arbitrary system and predictions of the distributions of the decay angles, assuming certain spin-parity assignments of the resonance, can always be made. In practice, these predictions are simpler when certain well defined reference frames are used and two such frames are used in this thesis: the Gottfried-Jackson frame and the Helicity frame. These are defined below for reactions of the type:



where c is a resonance which subsequently decays into two or more particles and d can be one other particle or the combination of all final state particles of an interaction, which do not result from the resonance decay. The direction associated with the decay of the resonance, for which the decay angles are to be determined will be denoted by $\vec{\alpha}$, which in the case of a two body decay will be the direction of one of the decay products. The possible directions for the three body decay are described in Chapter 6.

B.1.1 The Gottfried-Jackson frame

The Gottfried-Jackson frame (G-J frame) (Ref. B.1) is defined in the rest system of the resonance, in which case the directions of particles a , b and d all fall in a plane, shown in figure B.1, known as the production plane. α need not fall in this plane. The z -axis is chosen as the direction of the beam particle b , where this is the beam meson for a mesonic resonance and the target for baryonic resonances. The y -axis is chosen as the normal to the production

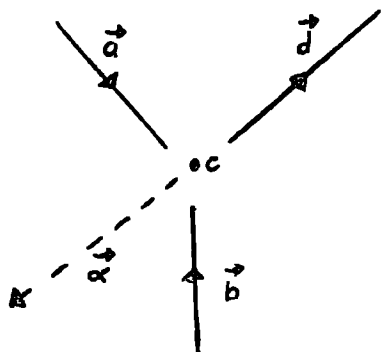


FIG B.1

plane, defined as:

$$\vec{y} = \frac{\vec{a} \times \vec{d}}{|\vec{a} \times \vec{d}|} \quad (\text{B.1})$$

The x-axis is then chosen to give

a right-handed set:

$$\vec{x} \equiv \vec{y} \times \vec{z} \quad (\text{B.2})$$

The decay angles of the resonance are then given by the polar angle (θ) and azimuthal angle (ϕ) of the direction $\vec{\alpha}$ in this co-ordinate system: i.e.

$$\cos \theta = \frac{\vec{b} \cdot \vec{\alpha}}{|\vec{b}| |\vec{\alpha}|}$$

$$\cos \phi = \frac{\vec{a} \times \vec{d} \cdot \vec{b} \times \vec{\alpha}}{|\vec{a} \times \vec{d}| |\vec{b} \times \vec{\alpha}|} \quad (\text{B.3})$$

$$\sin \phi = \frac{\vec{b} \times (\vec{a} \times \vec{d}) \cdot \vec{b} \times \vec{\alpha}}{|\vec{b} \times (\vec{a} \times \vec{d})| |\vec{b} \times \vec{\alpha}|}$$

Thus ϕ is defined between 0° and 360° and $\cos \theta$ between -1 and $+1$.

B.1.2 The Helicity frame

The y-axis of the helicity frame is defined, again, as the normal to the production plane (Eq. B.1). The z-axis or polar axis is defined as the direction of the resonance c in the overall centre of mass system. This is equivalent to the negative of the direction of particle d in the rest system of c .

$$\vec{z} = \frac{-\vec{d}}{|\vec{d}|} \quad (\text{B.4})$$

The x-axis is, again, defined by equation B.2 and the polar and azimuthal angles of the direction $\vec{\alpha}$ are given by equations B.3 with

\vec{b} replaced throughout by $-\vec{d}$.

B.2. The Spin Density Matrix:

The resonance c need not be produced in a pure spin state but will in general be produced in a quantum mechanical mixture of pure spin states with different expectation values of the magnetic quantum number m . The expected distribution of the decay angles depends on the relative amounts of the various possible values of m , which, in turn, depends on the production mechanism. The amounts of each spin state are contained in the spin density matrix. If the mixture contains several pure states $|\mu\rangle$ each with a probability p_μ then the density operator is defined as

$$\rho = \sum_{\mu} |\mu\rangle p_{\mu} \langle \mu| \quad (\text{B.5})$$

Each state $|\mu\rangle$ can be expanded as a sum of eigenstates of the spin operator with magnetic quantum number m , in which case ρ is a square matrix with $(2J + 1) \times (2J + 1)$ elements ρ_{mm}' :

$$\rho_{mm}' = \langle m | \rho | m' \rangle = \sum_{\mu} \langle m | \mu \rangle p_{\mu} \langle \mu | m' \rangle \quad (\text{B.6})$$

The density matrix, then has the following properties:

- (i) It is Hermitian: $\rho_{mm}' = \rho_{m'm}^*$
- (ii) The diagonal elements are positive
- (iii) The trace is unity: $\sum_m \rho_{mm} = 1$
- (iv) The value of ρ_{mm} describes the weight with which the state $|m\rangle$ is contained in the mixture.
- (v) If the spin quantisation axis (z-axis) is chosen to be in the production plane, as is the case for both the G-J frame and the helicity frame, and assuming that the beam is unpolarized, then parity conservation implies that:

$$\rho_{mm}' = (-1)^{m-m'} \rho_{-m-m}'$$

The decay angular distributions for a resonant decay are, in general functions of all the density matrix elements and property (v) consequently simplifies the analysis.

Various production mechanisms can make predictions on the values of the density matrix elements: for example, one pion exchange resulting in a meson resonance which decays into two pions predicts that only $m = 0$ will contribute and hence $\rho_{00} = 1$ and all other elements will be zero. Experimental determination of the density matrix elements can give information on the mechanism for production of the particular resonance, and, since the production mechanism may be different at different values of the momentum transfer, the values of the ρ_{mm} can vary as a function of t .

B.3 The Method of Moments

One method of determining, experimentally, the values of the density matrix elements is the method of moments. The decay angular distribution of a resonance ($W(\cos \theta, \phi)$) can be written:

$$W(\cos \theta, \phi) = \sum_{mm'} f^{mm'}(\rho_{mm'}) g^{mm'}(\cos \theta, \phi). \quad (\text{B.7})$$

where $f^{mm'}$ and $g^{mm'}$ are known functions of the respective variables, assuming a certain spin-parity assignment of the resonance (Ref. B.1 and 6.5). In general the functions $g^{mm'}$ are orthogonal:

$$\int_{-1}^{+1} d \cos \theta \int_0^{2\pi} d\phi g^{mm'} g^{kk'} = C \text{ if } m=k \text{ and } m'=k' \\ = 0 \text{ otherwise} \quad (\text{B.8})$$

The average value of $g^{mm'}(\cos \theta, \phi)$ is given by:

$$\overline{g^{mm'}} = \int_{-1}^{+1} d \cos \theta \int_0^{2\pi} d\phi g^{mm'}(\cos \theta, \phi) W(\cos \theta, \phi) \quad (\text{B.9})$$

and inserting B.7 into B.9 and using the orthogonality B.8 the result is:

$$\overline{g^{mm'}} = f(\rho^{mm'}) \quad G \quad (B.10)$$

and, since $f(\rho^{mm'})$ and G are known and the experimental values of $\overline{g^{mm'}}$ can be determined from the data, the value of $\rho_{mm'}$ can be determined. The error on \overline{g} is given by:

$$\Delta \overline{g} = \left\{ \frac{1}{n} (g^2 - g^{-2}) \right\}^{\frac{1}{2}} \quad (B.11)$$

and hence the error on $\rho_{mm'}$ can be determined.

In some cases, there are two functions $g^{mm'}$ which are not orthogonal and when this occurs results can only be obtained for some linear combination of the two corresponding matrix elements. This occurs, for example, in the case of the ρ^0 meson interfering with an ϵ^0 meson, where ρ_{00} and ρ_{11} of the ρ^0 meson cannot be determined separately but only in the combination $\rho_{00} - \rho_{11}$.

B.4 The Spherical Harmonics

The spherical harmonics are used in this thesis both in connection with spin determination and with the tests of conservation of helicity. The spherical harmonic Y_n^m is defined as:-

$$Y_n^m(\cos \theta, \phi) = e^{im\phi} P_n^m(\cos \theta) \quad (B.12)$$

where the functions P_n^m are the associated Legendre polynomials which are related to the Legendre polynomials P_n by the equation:-

$$P_n^m(\cos \theta) = (-1)^m \sin^m \theta \frac{d^m}{d \cos \theta^m} P_n(\cos \theta) \quad (B.13)$$

$$\text{and} \quad P_n(\cos \theta) = \frac{(2n)!}{2^n n! n!} \left\{ \cos^n \theta - \frac{n(n-1)}{2(2n-1)} \cos^{n-2} \theta + \frac{n(n-1)(n-2)(n-3)}{2 \cdot 4(2n-1)(2n-3)} \cos^{n-4} \theta - \dots \right\} \quad (B.14)$$

The spherical harmonics are orthonormal i.e.

$$\int_{-1}^{+1} \cos \theta \int_0^{2\pi} d\phi Y_{\ell}^m Y_{\ell'}^{m'*} = \delta_{\ell\ell'} \delta_{mm'}$$

and form a complete set of functions. The decay angular distribution of a resonance can therefore be expressed as a sum of the form:

$$W(\cos \theta, \phi) = \sum_{\ell=0}^{\infty} \sum_{m=0}^{\ell} a_{\ell m} Y_{\ell}^m(\cos \theta, \phi)$$

and the coefficients $a_{\ell m}$ can be determined by the method of moments.

LIST OF TABLES

- 2.1 Scanning Data.
- 3.1 The number of coherent fits ambiguous with other channels.
- 3.2 Number of events accepted and rejected in each subsample of the 4-prong data.
- 4.1. Cross Sections for the various final states
- 4.2 Parameters of Resonances and Enhancements produced
- 5.1 Resonances produced in the separate regions of L.P.S.
- 6.1 The ρ^0 spin density matrix elements
- 6.2 The f^0 spin density matrix elements
- 6.3 The A_1 spin density matrix elements
- 6.4 The values of μ , α and β through the A_1 region
- 7.1 The A_1 spin density matrix elements for several t regions
- 7.2 ρ_{00} of the A_3 for several t' regions
- 7.3 Density matrix elements of the A_1 meson produced in Areas, 1,2 and 3 of L.P.S.
- 9.1 The number of events from various regions of the Daltiz plot in different 3π mass ranges.
- 10.1 A compilation of π^+d experiments
- 10.2 A compilation of other coherent reactions.

FIGURE CAPTIONS

- 1.1 Possible exchange mechanisms
- 3.1 (a) Probability for 4 prong events
(b) Probability for 3 prong events
- 3.2 (a) $M(pn)$ for all fits to Reaction 5
(hatched) - ambiguous Reaction 1/5 fits
(b) $\cos \theta_{pn}$ all fits to reaction 5
(hatched) - ambiguous reaction 1/5 fits
- 3.4 (a) Distribution of $R = \frac{N_{mom}}{P_{mom}}$ all ambiguous 4 prongs
(b) $M(pn)$ vs proton momentum for various values of $\cos \theta_{pn}$.
- 3.5 R vs. P_{mom} for various values of $\cos \theta_{pn}$
(a) $M(pn) = 1.8785 \text{ GeV}/c^2$
(b) $M(pn) = 1.880 \text{ GeV}/c^2$
(c) $M(pn) = 1.885 \text{ GeV}/c^2$
- 3.6 Ambiguous 4 prong samples 1, 2 and 3 combined
(a) $M(pn)$
(b) $\cos \theta_{pn}$
(c) $N_{mom}/P_{mom} = R$
- 3.3 Ambiguous 4 prongs
(a) $M(pn)$
(b) $\cos \theta_{pn}$
- 3.7 Sample 9 events (a) $M(pn)$ (b) $\cos \theta_{pn}$ (c) R .
- 3.8 $M(pn)$ for ambiguous 3 prong sample
- 3.9 Deuteron Laboratory momentum - 3 prong sample hatched.
- 4.1 Differential cross sections
(a) $d\sigma/dt$ vs t
(b) $d\sigma/dt$ vs t' .
- 4.2 The $(d\pi^+)$ effective mass. 2 combinations per event.
The hatched histogram shows the $d\pi^+$ slow combination only.
- 4.3 (a) $M(d\pi_s^+)$ - 4 prong events
(b) $M(d\pi_s^+)$ - 3 prong events
(c) $M(\pi_s^+ \pi^-)$ if $M(d\pi_s^+) < 2.4 \text{ GeV}/c^2$ - 4 prong events
- 4.4 (a) $M(d\pi^-)$: the hatched histogram shows only those events
which have no ρ^0 , f^0 and d^{*+++}
(b) $M(\pi^+ \pi^+)$.

- 4.5 The $\pi^+\pi^-$ effective mass distribution. 2 combinations per event.
 The solid curve is a result of a fit to the background + ρ + f mesons
 The dashed curve is the shape of the assumed background
- 4.6 (a) Distribution of angle between 2 positive pions in ρ^0 rest frame
 (b) $M(\pi^+\pi^-)$ when $M(\pi^+\pi^+\pi^-) > 1.4 \text{ GeV}/c^2$.
- 4.7 (a) $M(\pi^+ f_{\ell} \pi^-)$ f_{ℓ} = faster in lab system
 (b) $M(\pi^+ s_{\ell} \pi^-)$ s_{ℓ} = slower in lab system
 (c) $M(\pi^+\pi^-)$ combination formed with lower t
 (d) $M(\pi^+\pi^-)$ combination formed with higher t
 (e) $M(\pi^+ f_c \pi^-)$ f_c = faster in 3π rest frame
 (f) $M(\pi^+ s_c \pi^-)$ s_c = slower in 3π rest frame
- 4.8 Dipion mass for various regions of t' to dipion system
 (a) $t' < 0.04 \text{ (GeV}/c)^2$
 (b) $0.04 < t' < 0.1 \text{ (GeV}/c)^2$
 (c) $0.1 < t' < 0.2 \text{ (GeV}/c)^2$
 (d) $0.2 < t' < 0.5 \text{ (GeV}/c)^2$
- 4.9 $M(d\pi_s^+)$ vs $M(\pi^+ f \pi^-)$
- 4.10 (a) $M(\pi^+ f \pi^-)$ if $M(d\pi_s^+)$ in d^* region
 (b) $M(d\pi_s^+)$ if $0.6 < M(\pi^+ f \pi^-) < 1.0 \text{ GeV}/c^2$
 (c) $M(d\pi_s^+)$ if $1.1 < M(\pi^+ f \pi^-) < 1.5 \text{ GeV}/c^2$
- 4.11 Effective mass of the $\pi^+\pi^+\pi^-$ system
 (4 prong events are shown hatched)
- 4.12 (a) $M(\pi^+\pi^-)$ for $0.95 < M(3\pi) < 1.35 \text{ GeV}/c^2$
 (b) $M(3\pi)$ for $0.665 < M(\pi^+\pi^-) < 0.865 \text{ GeV}/c^2$
 (c) $M(\pi^+\pi^-)$ for $1.4 < M(3\pi) < 1.8 \text{ GeV}/c^2$
 (d) $M(3\pi)$ for $1.12 < M(\pi^+\pi^-) < 1.36 \text{ GeV}/c^2$
- 4.13 $M(d\pi_s^+)$ vs $M(3\pi)$.
- 4.14 (a) $M(\pi^+\pi^+\pi^-)$ for non d^{*++} events: $M(f^0\pi)$ shown hatched
 (b) $M(\pi^+\pi^+\pi^-)$ for d^{*++} events.
- 4.15 $M(\pi^+\pi^+\pi^-)$ for several regions of $M(\pi^+\pi^-)$, ρ events excluded.
- 4.16 (a) $M(d\pi^+\pi^-)$ 2 combinations per event, $M(d^{*++}\pi^-)$ shown hatched
 (b) $M(d\pi^+\pi^+)$
- 5.1 (a) 3 body L.P.S. hexagon for the reaction $a + b \rightarrow c + d + e$
 (b) General 4 body L.P.S. cuboctohedron
- 5.2 Mean transverse momenta for regions of L.P.S.
 (a) $\pi^+ f$ (b) $\pi^+ s$ (c) π^- (d) d.

- 5.3 (a) Unweighted L.P.S. distribution
 (b) Weighted L.P.S. distribution
- 5.4 (a) $M(\pi^+ s \pi^-)$ Region I
 (b) $M(\pi^+ f \pi^-)$ Region I
 (c) $M(\pi^+ \pi^+ \pi^-)$ Region I
 (d) $M(\pi^+ s \pi^-)$ Region IV
 (e) $M(\pi^+ f \pi^-)$ Region IV
 (f) $M(\pi^+ \pi^+ \pi^-)$ Region IV
- 5.5 (a) $M(\pi^+ f \pi^-)$ Region II
 (b) $M(d\pi^+ s)$ for the area of L.P.S. shown shaded in the inset
 The inner histogram shows $M(d\pi^+ s)$ for Region IV
 (c) $M(\pi^+ f \pi^-)$ for the area of L.P.S. shown shaded in the inset
 (d) $M(\pi^+ s \pi^-)$ for the area of L.P.S. shown shaded in the inset
 (e) $M(\pi^+ \pi^+ \pi^-)$ for the area of L.P.S. shown shaded in the inset
- 5.6 (a) Definition of Areas, 1, 2 and 3 of L.P.S.
 (b) $M(d\pi^+ s)$ for Area 2
 (c) $M(d\pi^+ s)$ for Area 3
 (e) $M(3\pi)$ for Area 1
 (f) $M(3\pi)$ for Area 2
 (g) $M(3\pi)$ for Area 3
- 5.7 (a) $M(\pi^+ s \pi^-)$ for Area 1
 (b) $M(\pi^+ s \pi^-)$ for Area 2
 (c) $M(\pi^+ s \pi^-)$ for Area 3
 (d) $M(\pi^+ f \pi^-)$ for Area 1
 (e) $M(\pi^+ f \pi^-)$ for Area 2
 (f) $M(\pi^+ f \pi^-)$ for Area 3
- 6.1 ρ^0 decay angles.
 (a) $\cos \theta$, (b) ϕ . The hatched histograms show only $\pi^+ \pi^-$ combinations in the ρ region.
- 6.2 ρ density matrix elements
- 6.3 (a) f^0 decay angles
 (b) f^0 density matrix elements
- 6.4 η_N decay angles (a) $\cos \theta$, (b) ϕ , (c) $M(\pi^+ \pi^-) \cos \theta < -0.75$
 (d) $M(\pi^+ \pi^-) \cos \theta > 0.75$
- 6.5 Spherical harmonic moments of the normal to the 3π decay plane as a function of 3π mass
- 6.6 Decay angles of the normal to the production plane in the A_1 region

- 6.7 (a) $\cos \theta_\rho$ distribution for A_1 events (hatched histogram is the result of weighting by $\frac{1}{2}$ the A_1 events where both $\pi^+\pi^-$ combinations have a mass in the A_1 region.)
 (b) $\cos \theta_u$ distribution for A_1 events
- 6.8 (a) The distribution of decay angles of normal to production plane for A_3 events. The solid curve shows the result of a fit for $J^P = 2^-$ while the dashed curve is the fit for $J^P = 1^+$.
 (b) polar angle of π^- for A_3 events
 (c) polar angle of f^0 for A_3 events. The hatched part of the histogram corresponds to d^* events
- 6.9 'A_{2.5}' decay distributions
 (a) normal to decay plane
 (b) π^- polar angle
 (c) ρ^0 polar angle
 The hatched part of the histograms correspond to d^* events
- 7.1 The A_1 density matrix elements in the G-J frame and in the helicity frame. The dashed points are the result of excluding d^* events.
- 7.2 ρ_{00} of the A_3 vs t' in (a) the G-J and (b) the helicity frame.
 (c) and (d) show the same distributions when only f^0 events are used.
- 7.3 (a) β_{\min} vs $|t|$ for the A_1 region.
 (b) χ^2 vs β for the A_1 region $|t| > 0.12$ (GeV/c)²
 (c) β_{\min} vs $|t|$ for the A_3 region
 (d) β_{\min} vs $|t|$ for $M(3\pi) < 1.0$ GeV/c²
 (e) β_{\min} vs $|t|$ for $A_1 < M(3\pi) < A_3$
 (f) β_{\min} vs $|t|$ for $M(3\pi) < 1.8$ GeV/c²
- 7.4 (a) Path in LPS taken by several events when rotated round G-J axes
 (b) Path in LPS taken by several events when rotated round Helicity axis
 (c) Definition of Areas 1 - 4 of Region I of L.P.S.
- 7.5 The number of events in various regions of L.P.S. before rotation, after rotation by π round G-J axis and after rotation by π round helicity axis, shown diagrammatically
 (a) all events
 (b) $t > 0.02$ (GeV/c)²
 (c) A_1 region only.
- 7.6 As 7.5 but shown numerically
- 7.7 (a) $M(3\pi)$ for Region I of L.P.S.
 (b) $M(3\pi)$ for Areas 1-3 of L.P.S. before rotation
 (c) $M(3\pi)$ for Areas 1-3 of L.P.S. after G-J rotation

- 7.8 (a) $M(\pi^+ \pi^-)$ for Region I of L.P.S.
 (b) $M(\pi^+_{\text{f}} \pi^-)$ for Region I of L.P.S.
 (c) $M(\pi^+_{\text{s}} \pi^-)$ for Areas 1-3 of L.P.S. before rotation
 (d) $M(\pi^+_{\text{f}} \pi^-)$ for Areas 1-3 of L.P.S. before rotation
 (e) $M(\pi^+ \pi^-)$ for Areas 1-3 of L.P.S. after rotation
 (f) $M(\pi^+_{\text{f}} \pi^-)$ for Areas 1-3 of L.P.S. after rotation
- 7.9 A_1 density matrix elements (G-J) frame using only events from Areas 1-3.
- 8.1 (a) d^{*++} decay angles
 (b) suggested d^* production mechanism.
- 8.2 Reggeised Deck Exchange Mechanism
- 8.3 (a) $M(\rho\pi)$ d^{*++} excluded
 (b) azimuthal angle of 'decay' of $d\pi$ system for $d\pi^0$ final state with d^{*++} events excluded.
- The smooth curves are the B.R.D. model predictions.
- 9.1 (a) $M(\rho\pi)$ 4 prong events
 (b) $M(\rho\pi)$ 4 prong events d^* excluded
- 9.2 $M(\rho\pi)$ for various regions of λ
 (a) $\lambda < 0.5$ (b) $\lambda > 0.5$ (c) $\lambda > 0.6$ (d) $\lambda > 0.85$
- 9.3 Distribution of λ for several regions of $M(3\pi)$
- 9.4 (a) and (b). The decay angular distributions of the normal to the decay plane of the 3-pion system for events in the A_2 mass region, $\cos \theta$ and ϕ .
 (c) The ρ asymmetry vs $M(3\pi)$
- 10.1 (a) $\pi^+ d \rightarrow d \pi^+ \pi^+ \pi^-$ channel cross section vs incident momentum
 (b) $K^- d \rightarrow d K^- \pi^+ \pi^-$ channel cross section vs incident momentum

A C K N O W L E D G E M E N T S

There are numerous people whom I would like to thank for their help and guidance during my work on this thesis. Dr. J.V. Major, who, as head of the High Energy Physics Group at Durham, has provided both the congenial atmosphere and the wherewithal, without which the work would have been impossible, and Dr. S.M. Scarrot, whose guidance and comments have helped me to avoid many of the pitfalls which await unsuspecting, often over-credulous physicists, must both be acknowledged both for their help and reading of the manuscript.

I must thank, also, all other members of the Durham High Energy Physics group for their continual interest in the work, and particularly Mr. A.P. Lotts, Mr. I.G. Bell and Mr. R. Nelson for many interesting and informative discussions. I am grateful to the staff of all the collaborating laboratories, both academic and technical, for provision of their data.

The staff of NUMAC, the computer of the Universities of Durham and Newcastle, have been very helpful in providing an efficient computing system and in solving more specific problems. My thanks are also due to all the scanning and measuring staff at Durham University for their painstaking work on this experiment, and particularly to Mrs. T. Richardson, Mrs. J. Gibson and Mrs. D. Pickles, who in addition to taking charge of the measuring have also assisted in many other ways, the last mentioned especially, since she was responsible to a great extent for making the diagrammes.

I would like to thank, particularly, Mrs. D. Anson for her careful typing of the manuscript and happy acceptance of my often erratic demands.

To these, and to many others, who have helped and encouraged me throughout, I am very much indebted and am pleased to have this opportunity to thank them. In the words of Ernest Hemmingway: "A man alone doesn't stand a bloody chance". (Ref. 500).

REFERENCESCHAPTER ONE

- 1.1 Bellini et al. N.C. 29, 896, (1963).
 1.2 Abolins et al. P.R.L., 15, 125, (1965).
 1.3 Good and Walker, P.R., 120, 1857, (1960).

CHAPTER TWO

- 2.1 See, for example, G.E. Pearson, Ph.D. Thesis, University of Durham
 2.2 " " " " " " " " " "
 2.3 Python)
 2.4 Thresh) CERN T.C. Programme Library
 2.5 Grind)
 2.6 Compilation of cross sections IV, π^+ induced reactions
 CERN/HERE 70-5 (1970).
 2.7 Kemp et al., L.N.C., 3, 257, (1972)
 S.M. Scarrott and D. Kemp, L.N.C., 3, 271, (1972)
 Kemp et al. N.C., 8A, 611 (1972).
 2.8 "A Study of the reactions $\pi^+ d \rightarrow pp \pi^+ \pi^-$ and $\pi^+ d \rightarrow pp \pi^+ \pi^- \pi^0$
 at 11.7 GeV/c" - Nuovo Cimento (to be published).
 2.9 Kemp et al., L.N.C., 2, 471, (1971).

CHAPTER THREE

- 3.1 A.P. Lotts, M.Sc Thesis, University of Durham
 J. Huc, Thèse de Doctorat d'Etat - Ecole Polytechnique.

CHAPTER FOUR

- 4.1 See, for example, Refs. 1.2 and 10.1 - 10.5.
 4.2 J.D. Jackson, N.C., 34, 1645 (1964).
 4.3 "Review of Particle Properties" - The Particle Data Group
 4.4 Miller et al., P.R.L., 21, 1439, (1968).
 4.5 Whitehead et al., N.C. 53A, 817, (1968)
 Oh et al., P.R.L., 23, 331 (1969).
 Oh et al., P.R., D1, 2494 (1970).

- 4.5 J. Pisut and M. Ross, N.P., B6, 325, (1968).
 4.6 Barbaro-Galtieri et al., P.R.L., 22, 1207, (1969).
 4.7 Crennel, et al., P.R.L., 24, 781, (1970).

CHAPTER FIVE

- 5.1 L. Van Hove, P.L., 28B, 429, (1969).
 L. Van Hove, N.P., B9, 331 (1969).
 Kittel, Ratti and Van Hove, N.P., B30, 333, (1971)

CHAPTER SIX

- 6.1 See Refs. 2.8 and 3.1
 6.2 Poirier et al., P.R., 163, 1462, (1967).
 J. Quinquard, Thèse de Doctorat e'Etat, University of Paris VI, (1970).
 6.3 Beaupré et al., N.P., B28, 77, (1971).
 6.4 See Refs. under 4.4.
 6.5 Berman and Jacob, P.R., 139, 1023, (1965).
 6.6 D.R.O. Morrison, P.R., 165, 1699, (1968).
 6.7 Bingham et al., N.P., B48, 589, (1972).

CHAPTER SEVEN

- 7.1 Gilman et al., P.L., 31B, 381, (1970).
 7.2 Ballam et al., P.R.L., 24, 960, (1970).
 7.3 See Ref. 7.1
 7.4 Ascoli et al., P.R.L., 26, 929, (1971)
 Beaupre et al., P.L., 34B, 160, (1971).
 7.5 Carlitz, Frautschi and Zweig, P.R.L., 23, 1134, (1969).
 7.6 Paler et al., L.N.C., 2, 1063, (1971).
 Paler et al., P.R.L., 26, 1675, (1971).
 7.7 Grard et al., Cern, D. Ph. II/Phys. 71-3, (1971).
 and Refs. 7.8 and 7.9.
 7.8 Beaupré et al., N.P., B47, 51 (1972).
 7.9 Beaupré et al., N.P., B49, 441 (1972).

CHAPTER EIGHT

- 8.1 Ramakrishnan et al., N.P., 29, 680, (1962).
- 8.2 M. Month, P.R., 155, 1639, (1967).
- 8.3 Evrard et al., N.P., B14, 69, (1969).
- 8.4 Deck, P.R.L., 13, 169, (1964).
- 8.5 Berger, P.R., 166, 1525, (1968).
- 8.6 Vanderhagen et al., N.P., B13, 329, (1969).
- 8.7 Chew and Fignotti, P.R.L., 20, 1078, (1968).
- 8.8 Dolen, Hom, and Schmidt, P.R., 166, 1768, (1968).
- 8.9 Cohen et al., P.R.L., 28, 1601, (1972).
- 8.10 Uhoeda, L.N.C., 7, 473, (1973).
- 8.11 Anderson, et al., P.R.L., 22, 1390, (1969).
- 8.12 Belinghieri et al., P.R.L., 23, 42, (1969).
- 8.13 Alexander et al., P.R., 183, 1168, (1969).
- 8.14 Rabin et al., P.R.L., 24, 925, (1970).
- 8.15 Crennel et al., P.R.L., 22, 1327, (1969).
- 8.16 Danysz et al., N.C., 51A, 801, (1967).
- Friedman et al., P.R., 168, 1268, (1968).
- 8.17 Atherton et al., P.L., 43B, 249, (1973).
- 8.18 Froggart and Ranft, P.R., D5, 219B, (1972).
- 8.19 Morse et al., N.P., B43, 77, (1972).
- 8.20 Ballam et al., P.R.L., 21, 934, (1968).
- 8.21. Ascoli et al., P.R.L., 26, 929, (1971).
- 8.22 Goldhaber et al., P.R.L., 22, 802, (1968).
- 8.23 Trefil, P.R.L., 23, 1075, (1969).
- 8.24 Hoang et al., N.C., 69A, 327, (1970).
- 8.25 Bemporad, N.P., B33, 397, (1971).

CHAPTER NINE

9.1 Zeemach, P.R., 133, B1201, (1964).

CHAPTER TEN

10.1 Eisenstein and Gordon, P.R., D1, 841, (1970).

10.2 Vanderhagen et al., N.P., B13, 329, (1969).

10.3 Deery et al., P.L., 31B, 82, (1970).

10.4 Vegni et al., P.L., 19, 526, (1965).

10.5 Cnaps et al., P.R.L., 21, 1609, (1968).

Cnaps et al., P.L., 29B, 45, (1969).

10.6 Hoogland et al., N.P., B11, 308, (1969).

10.7 Nicholas et al., N.C., 14A, 363, (1973).

10.8 Werner et al., P.R., 188, 2023, (1969).

10.9 Anderson et al., P.R., D6, 1823, (1972).

10.10 Denegri et al., P.R.L., 20, 1194, (1968).

10.11 Butterworth et al., P.R.L., 15, 500 (1965).

10.12 Buchner et al., N.P. B9, 286, (1969).

10.13 Garfinkel et al., P.R.L., 26, 1505, (1971).

10.14 Firestone et al., P.R., D5, 505, (1972).

10.15 Braun et al., P.R., D2, 1212, (1970).

10.16 Antich et al., Kiev Conference Report (1970).

10.17 Allard et al., P.L., 19, 431, (1965).

APPENDICES etc

A.1. Amaldi and Selleri, N.C., 31, 360, (1964).

B.1 Gottfried and Jackson, N.C., 33, 309, (1964).

Berman and Jacob, P.R., 139, 1023, (1965).

500 Ernest Hemmingway: 'To Have and Have Not'.

Abbreviations

L.N.C. -- Lettere al Nuovo Cimento

N.C. -- Nuovo Cimento

N.P. -- Nuclear Physics

P.L. -- Physics Letters

P.R. -- Physical Review

P.R.L. -- Physical Review Letters

